Measurements for the GDH sum rule on the proton and the neutron

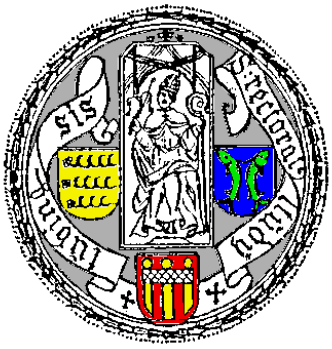

Dissertation

zur Erlangung des Grades eines Doktors
der Naturwissenschaften
der Fakultät für Mathematik und Physik der
Eberhard-Karls-Universität zu Tübingen

vorgelegt von

Jochen Krimmer

aus Waiblingen

2004

Tag der mündlichen Prüfung: 25. Juni 2004

Dekan:	Prof. Dr. H. Müther
1. Berichterstatter:	Prof. Dr. P. Grabmayr
2. Berichterstatter:	Prof. Dr. H. Clement

Zusammenfassung

Die Vermessung helizitätsabhängiger totaler Photoabsorptionswirkungsquerschnitte am Proton und Neutron ist Gegenstand der vorliegenden Dissertation. Diese Messung ist Grundlage für die direkte experimentelle Überprüfung der fundamentalen Gerasimov-Drell-Hearn Summenregel. In dieser Arbeit wird der experimentelle Aufbau und die Analyse der Daten von dem, am Elektronenbeschleuniger ELSA in Bonn durgeführten Experiment, beschrieben.
Zirkular polarisierte Photonen werden durch Bremsstrahlung von longitudinal polarisierten Elektronen erzeugt. Die Energiemarkierung der Photonen erfolgt durch ein sogenanntes *tagging system*. Ein *frozen spin* Targetsystem stellt longitudinal polarisierte Nukleonen zur Verfügung. Durch die horizontale Anordnung ist ein Raumwinkel von $99.6\% \cdot 4\pi$ durch hocheffiziente Detektormodule abgedeckt.
Zum Test des Detektorsystems und der verwendeten Analysemethode wurden unpolarisierte totale Photoabsorptionswirkungsquerschnitte an Kohlenstoff und Beryllium vermessen. Die Ergebnisse sind im Einklang mit bereits veröffentlichten Resultaten und besitzen eine bislang unerreichte statistische Präzission.
Die helizitätsabhängigen totalen Photoabsorptionsquerschnitte am Proton stimmen im Überlappbereich mit vorangegangenen Messungen an MAMI in Mainz überein. Der Beitrag zum GDH Integral beträgt $(45.8 \pm 2.6 \pm 2.3)\mu$b im Energiebereich zwischen 680 MeV und 2.9 GeV, bzw. $(27.3 \pm 2.1 \pm 1.4)\mu$b zwischen 800 MeV und 2.9 GeV. Addiert man zu den vorliegenden Resultaten die Beiträge aus dem Experiment an MAMI und nimmt man theoretische Vorhersagen aus den nicht vermessenen Energiebereichen hinzu, kann keine Verletzung der GDH Summenregel festgestellt werden.
Am Neutron wurden erstmals doppelt polarisierte Photoabsorptionsquerschnitte im Energiebereich zwischen 815 MeV und 1825 MeV vermessen. Dabei wurde ein polarisiertes ^{6}LiD Target verwendet. Die Resultate zeigen einen starken Beitrag im Energiebereich der 3. Resonzregion, was im Widerspruch zu Vorhersagen aus Multipolanalysen steht. Der experimentelle Beitrag zum GDH Integral am Neutron beträgt $(36.8 \pm 5.6 \pm 4.0)\mu$b. Dieser Beitrag sorgt dafür, daß unter Hinzunahme von theoretischen Vorhersagen in den nicht vermessenen Energiebereichen, ebenfalls am Neutron keine Verletzung der GDH Summenregel beobachtet wird.

Abstract

This thesis discusses the measurements of helicity dependent total photoabsorption cross sections on the proton and the neutron. These measurements serve as a test of the fundamental Gerasimov-Drell-Hearn sum rule. The present work describes the experimental setup and the data analysis for the measurement at the electron accelerator ELSA in Bonn.
Circularly polarized tagged photons are generated by bremsstrahlung of longitudinally polarized electrons. Longitudinally polarized nucleons are provided by a *frozen spin* target. Due to the horizontal arrangement of the target cryostat the high efficient detector system covers 99.6% of 4π.
The analysis method and the detector system is tested by the measurement of unpolarized total photoabsorption cross sections on carbon and beryllium. The results are in agreement with published data and the statistical precision is of unattained quality.
Helicity dependent total photoabsorption cross section data on the proton are in agreement with data from MAMI in the energy overlap region. The contribution to the GDH integral is $(45.8 \pm 2.6 \pm 2.3)\mu$b in the energy range from 680 MeV to 2.9 GeV, or $(27.3 \pm 2.1 \pm 1.4)\mu$b from 800 MeV to 2.9 GeV, respectively. Adding the present results to the results from MAMI and including theoretical predictions for the uncovered energy regions, leads to a value which is compatible with the GDH sum rule value.
Doubly polarized photoabsorption cross sections on the neutron have been measured for the first time between 815 MeV and 1825 MeV using a polarized ^{6}LiD target. The results exhibit a strong resonance behaviour in the third resonance region in contradiction to predictions by multipole analyses. The contribution to the GDH integral on the neutron is $(36.8 \pm 5.6 \pm 4.0)\mu$b. Due to this contribution also no violation of the GDH sum rule for the neutron can be observed, if theoretical predictions are included for the uncovered energy regions.

Contents

Chapter 1

Introduction and motivation

More than 70 years ago the magnetic moment of the proton was measured for the first time [Fri33]. The result was not compatible with the expectations for a pointlike (Dirac) particle. This *anomalous* magnetic moment originates from the internal structure of the nucleon. Deep inelastic lepton nucleon scattering experiments in the 1970's revealed the internal structure consisting of quarks and gluons. As a consequence of the internal degrees of freedom a rich excitation spectrum of the nucleon is observed. The *cleanest* probe for the investigation of the nucleon structure and the excitation of the short lived resonance states, is the photon as it contains no internal structure and the interaction is well-known.
Special interest for the spin structure of the nucleon arose in the late 1980's when it was realized that the spin of the quarks only contributes to a small part to the spin of the nucleon. This led to the so-called *spin-crisis* and started a great activity in the field.
In general, sum rules are of special theoretical and experimental interest as they combine dynamical and static properties. In the present case of the Gerasimov-Drell-Hearn sum rule the excitation spectrum of the nucleon is connected to the anomalous magnetic moment. A generalization to virtual photons gives a link to the deep inelastic electron scattering experiments.

1.1 The GDH sum rule

The Gerasimov-Drell-Hearn (GDH) sum rule has already been derived in the mid 1960's. It has first been published by S.B. Gerasimov in [Ger65], the English translation [Ger66] appeared one month before the article of S.D. Drell and A.C. Hearn [Dre66]. In its original form the GDH sum rule has been derived for the photoabsorption cross sections $\sigma_{3/2(1/2)}(\nu)$ of circularly polarized photons on longitudinally polarized nucleons. The subscripts (1/2, 3/2) denote the relative orientation of the photon and the nucleon spin. A total helicity of 3/2 (1/2) is generated by a parallel (antiparallel) orientation of the photon spin 1 and nucleon spin 1/2. The GDH sum rule reads

$$\int_{\nu_0}^{\infty} \frac{\sigma_{3/2}(\nu) - \sigma_{1/2}(\nu)}{\nu} d\nu \;=\; \frac{2\pi^2\alpha}{m^2}\kappa^2 \tag{1.1}$$

An integration over the complete photon energy range ν must be performed from the pion photoproduction threshold ν_0 to infinity. Therefore, the *l.h.s.* contains the complete excitation spectrum of the nucleon. On the *r.h.s* just static properties like the mass m and the anomalous magnetic moment κ appear. The value of the electromagnetic fine structure constant α is 1/137.
The need for polarized nucleon targets and polarized photon beams over a large energy range prevented a direct experimental check of the GDH sum rule for more than 30 years after its theoretical derivation [Ant95].

1.1.1 Derivation of the GDH sum rule

The GDH sum rule can be derived by the use of very fundamental physics principles without the need of any models for the nucleon. In the literature three different methods are given

- Dispersion theory [Ger66] [Dre66]
- Current algebra [Hos66]
- Current algebra on the light cone [Dic72]

All three approaches with their advantages and their drawbacks are discussed extensively in [Pan98]. Here, the main aspects of the derivation based on dispersion theory will be given, as it is comparatively simple and it also follows the original publications of [Ger66] and [Dre66].

Compton scattering

The starting point for the dispersion-theoretical approach is the Compton scattering matrix $F(\nu, \vartheta)$. For the special case of forward scattering $\vartheta = 0$ it reduces to [Dre94]

$$F(\nu, \vartheta = 0) \;=\; \hat{\epsilon}'^{*} \cdot \hat{\epsilon}\; f(\nu) \;+\; i\vec{\sigma} \cdot (\hat{\epsilon}'^{*} \times \hat{\epsilon})\; g(\nu) \tag{1.2}$$

It contains a spinflip amplitude $g(\nu)$ and a non-spinflip amplitude $f(\nu)$. The polarization vectors of the initial and final photon are denoted by $\hat{\epsilon}$ and $\hat{\epsilon}'$, respectively. $\vec{\sigma}$ is the vector of the Pauli spin matrices.
Together with the spinors χ_f and χ_i of the nucleon in the final and the initial state, the scattering amplitude $T(\nu)$ for forward scattering is given by

$$T(\nu) \;= < \chi_f \,|\hat{\epsilon}'^{*} \cdot \hat{\epsilon}\; f(\nu) \;+\; i\vec{\sigma} \cdot (\hat{\epsilon}'^{*} \times \hat{\epsilon})\; g(\nu)|\, \chi_i > \tag{1.3}$$

In a reference frame where the photon beam defines the z-axis, the polarization vectors $\hat{e}_R$ and $\hat{e}_L$ for right- and left handed circularly polarized photons, can be expressed in the following way

$$\hat{e}_R \;=\; -\frac{1}{\sqrt{2}}\,(\hat{e}_x + i\hat{e}_y) \quad \text{and} \quad \hat{e}_L \;=\; \frac{1}{\sqrt{2}}\,(\hat{e}_x - i\hat{e}_y) \tag{1.4}$$

For $\hat{e}' \cdot \hat{e}$ and $\hat{e}' \times \hat{e}$ it follows

$$\hat{e}' \cdot \hat{e} \;=\; \begin{cases} 1 & : \quad \hat{e} = \hat{e}' = \hat{e}_R \\ 1 & : \quad \hat{e} = \hat{e}' = \hat{e}_L \\ 0 & : \quad \text{otherwise} \end{cases} \qquad \hat{e}' \times \hat{e} \;=\; \begin{cases} -i\hat{e}_z & : \quad \hat{e} = \hat{e}' = \hat{e}_R \\ +i\hat{e}_z & : \quad \hat{e} = \hat{e}' = \hat{e}_L \\ 0 & : \quad \text{otherwise} \end{cases} \tag{1.5}$$

With the above relations Eq. 1.3 can be written as

$$T(\nu) \;=\; f(\nu) < \chi_f|\chi_i > \mp g(\nu) < \chi_f|\sigma_z|\chi_i > \quad \text{for} \quad \begin{cases} \hat{e} = \hat{e}' = \hat{e}_R \\ \hat{e} = \hat{e}' = \hat{e}_L \end{cases} \tag{1.6}$$

with the Pauli spin matrix $\sigma_z = \begin{pmatrix} 1 & 0 \\ 0 & -1 \end{pmatrix}$.
For scattering of circularly polarized photons on longitudinally polarized nucleons two relative spin orientations are possible. Both spins can either be parallel or antiparallel generating a total spin of 3/2 or 1/2, respectively. The corresponding scattering amplitudes are $T_{3/2}$ and $T_{1/2}$. Helicity of the photons is conserved in both processes and also the total angular momentum does not change in the scattering process. Therefore, the spin state of the nucleons remains unchanged, i.e. $|\chi_i >= |\chi_f >, < \chi_f|\chi_i >= 1$.

- $\boxed{T_{3/2}:}$

  The two possibilities for a parallel orientation of both spins are[1]:

$$\hat{\epsilon} = \hat{\epsilon}_R \text{ and } |\chi_i >= \begin{pmatrix} 1 \\ 0 \end{pmatrix} \quad \text{or} \quad \hat{\epsilon} = \hat{\epsilon}_L \text{ and } |\chi_i >= \begin{pmatrix} 0 \\ 1 \end{pmatrix} \tag{1.7}$$

$$\text{Therefore:} \quad < \chi_f|\sigma_z|\chi_i > \;=\; \pm 1 \quad \text{for} \quad \begin{cases} \hat{\epsilon} = \hat{\epsilon}_R \\ \hat{\epsilon} = \hat{\epsilon}_L \end{cases} \tag{1.8}$$

  Together with equation 1.6 one obtains for the scattering amplitude $T_{3/2}$:

$$T_{3/2}(\nu) \;=\; f(\nu) - g(\nu) \tag{1.9}$$

- $\boxed{T_{1/2}:}$

  In complete analogy for an antiparallel orientation of both spins:

$$\hat{\epsilon} = \hat{\epsilon}_R \text{ and } |\chi_i >= \begin{pmatrix} 0 \\ 1 \end{pmatrix} \quad \text{or} \quad \hat{\epsilon} = \hat{\epsilon}_L \text{ and } |\chi_i >= \begin{pmatrix} 1 \\ 0 \end{pmatrix} \tag{1.10}$$

$$\text{Therefore:} \quad < \chi_f|\sigma_z|\chi_i > \;=\; \mp 1 \quad \text{for} \quad \begin{cases} \hat{\epsilon} = \hat{\epsilon}_R \\ \hat{\epsilon} = \hat{\epsilon}_L \end{cases} \tag{1.11}$$

  and the scattering amplitude $T_{1/2}$ reads

$$T_{1/2}(\nu) \;=\; f(\nu) + g(\nu) \tag{1.12}$$

According to Eqs. 1.9 and 1.12 the amplitudes $f(\nu)$ and $g(\nu)$ can be written in terms of $T_{3/2}(\nu)$ and $T_{1/2}(\nu)$

$$f(\nu) \;=\; \frac{1}{2}\left(T_{1/2}(\nu) + T_{3/2}(\nu)\right) \tag{1.13}$$

$$g(\nu) \;=\; \frac{1}{2}\left(T_{1/2}(\nu) - T_{3/2}(\nu)\right) \tag{1.14}$$

[1] The nucleon spinors $\chi = \binom{1}{0}$ and $\binom{0}{1}$ represent the two possible polarization directions $|\rightarrow>$ and $|\leftarrow>$.

Optical theorem

The optical theorem relates the imaginary part of scattering amplitudes to experimental accessible total absorption cross sections[2]. For the forward amplitudes $f(\nu)$ and $g(\nu)$ the following equations hold

$$\Im\mathrm{m}\ f(\nu) = \frac{\nu}{8\pi}(\sigma_{3/2}+\sigma_{1/2}) \equiv \frac{\nu}{4\pi}\sigma_T \tag{1.15}$$

$$\Im\mathrm{m}\ g(\nu) = \frac{\nu}{8\pi}(\sigma_{3/2}-\sigma_{1/2}) \equiv \frac{\nu}{4\pi}\sigma'_{TT} \tag{1.16}$$

Crossing symmetry

Crossing symmetry requires the scattering amplitude $T(\nu)$ (Eq. 1.3) to be invariant under the transformation $\hat{\epsilon}' \leftrightarrow \hat{\epsilon}$ and $\nu \leftrightarrow -\nu$ with the result that $f(\nu)$ is an even and $g(\nu)$ is an odd function

$$f(\nu) = f(-\nu) \quad \text{and} \quad g(\nu) = -g(-\nu) \tag{1.17}$$

Dispersion relations

From *causality* it follows that the scattering amplitude can be analytically continued to the complex plane. Starting from a Cauchy integral one can setup dispersion relations for $f(\nu)$ and $g(\nu)$. Application of crossing symmetry and the optical theorem leads to [Dre03]

$$\Re\mathrm{e}\ f(\nu) = \frac{1}{2\pi^2}\mathcal{P}\int_{\nu_0}^{\infty}\nu'^2\frac{\sigma_T(\nu')}{\nu'^2-\nu^2}d\nu' \tag{1.18}$$

$$\Re\mathrm{e}\ g(\nu) = \frac{\nu}{4\pi^2}\mathcal{P}\int_{\nu_0}^{\infty}\frac{\sigma_{1/2}(\nu')-\sigma_{3/2}(\nu')}{\nu'^2-\nu^2}\nu' d\nu' \tag{1.19}$$

With ν_0 the threshold for pion photoproduction ($\nu_0 \approx 150$ MeV)[3]. If the above integrals exist they can be expanded in a power series around the origin ($\nu \to 0$) [Dre03]. In this case the singularities are outside the integration limits ($\nu \ll \nu_0$) and the principle value integrals reduce to ordinary integrals. Furthermore, the amplitudes on the *l.h.s.* are always real as no photoabsorption is possible. According to the crossing-symmetries, only even (odd) powers of ν appear in the expansions of $f(\nu)$ and $g(\nu)$, respectively.

$$f(\nu) = \frac{1}{2\pi^2}\int_{\nu_0}^{\infty}\sigma_T\left(1+\frac{\nu^2}{\nu'^2}+\mathcal{O}(\nu^4)\right)d\nu' \tag{1.20}$$

$$g(\nu) = \frac{1}{4\pi^2}\int_{\nu_0}^{\infty}\left(\sigma_{1/2}(\nu')-\sigma_{3/2}(\nu')\right)\left(\frac{\nu}{\nu'}+\frac{\nu^3}{\nu'^3}+\mathcal{O}(\nu^5)\right)d\nu' \tag{1.21}$$

[2] A derivation of the optical theorem for photoabsorption cross sections is given in [Pan98].

[3] Photons with energies below ν_0 cannot be absorbed on free nucleons.

Low theorem

The scattering of low energy photons on spin 1/2 particles has been calculated within a quantum field theoretic approach by Low [Low54] Gell-Mann and Goldberger [Gel54]. Requiring Lorentz- and gauge invariance, the forward scattering amplitudes $f(\nu)$ and $g(\nu)$ can be expanded in a power series of the photon energy ν.

$$f(\nu) = -\frac{\alpha}{m} + \left(\bar{\alpha} + \bar{\beta}\right)\nu^2 + \mathcal{O}(\nu^4) \tag{1.22}$$

$$g(\nu) = -\frac{\alpha}{2m^2}\kappa^2\nu + \gamma_0\nu^3 + \mathcal{O}(\nu^5) \tag{1.23}$$

This Low-theorem describes the scattering of low energetic photons on structureless spin 1/2 particles. The 0th order in the expansion of $f(\nu)$ is the Thomson limit with α, the electromagnetic fine structure constant, and m, the mass of a nucleon. The next order describes Rayleigh scattering with the scalar electric and magnetic polarizabilities $\bar{\alpha}$ and $\bar{\beta}$.
The expansion of $g(\nu)$ includes the anomalous magnetic moment κ and the spin polarizability γ_0.
The derivation of the Low-theorem holds at least to order α^2 and to all orders of the strong interaction [Roy68].

Sum rules

Comparing the coefficients of the 0th order terms of Eq. 1.20 and Eq. 1.22 results in an equation which cannot be fulfilled

$$-\frac{\alpha}{m} = \int_{\nu_0}^{\infty} \sigma_T(\nu) d\nu \tag{1.24}$$

The *l.h.s.* is negative and the *r.h.s.* with the total unpolarized photoabsorption cross section $\sigma_T(\nu)$ is always positive, because the first term of Eq. 1.20 does not converge, actually $\sigma_T(\nu)$ increases for very high energies [Der94] [Aid95] [Der92]. This behaviour complies with Regge-phenomenology where an increase of the total photoabsorption cross section is expected according to $\sigma_T(\nu') \sim \nu'^{0.8}$ [Don92]. It is therefore necessary to introduce a subtraction constant $f(0) = -\alpha/m$ in Eq. 1.18. This once subtracted dispersion relation reads

$$\Re\mathrm{e}\, f(\nu) = f(0) + \frac{1}{2\pi^2}\mathcal{P}\int_{\nu_0}^{\infty} \nu'^2 \frac{\sigma_T(\nu')}{\nu'^2 - \nu^2} d\nu' \tag{1.25}$$

A Comparison of the second order terms of Eqs. 1.20 and Eq. 1.22 leads to the Baldin sum rule [Bal60] [Lap63]

$$\bar{\alpha} + \bar{\beta} = \frac{1}{2\pi^2}\int_{\nu_0}^{\infty} \frac{\sigma_T(\nu')}{\nu'^2} d\nu' \tag{1.26}$$

Unpolarized photoabsorption data are precise enough to pin down the sum $\bar{\alpha} + \bar{\beta}$ [Bab98]. Differential Compton scattering cross sections[4] are proportional to the difference $\bar{\alpha} - \bar{\beta}$. From free and quasi-free Compton scattering experiments [Wis04] the individual electric

[4]For an experiment covering a large energy and angular range see e.g. [Wol01].

and magnetic polarizabilities of the proton [Olm01] and the neutron [Lun03] [Kos03] can be extracted.

Combining the relations for the spin dependent amplitude $g(\nu)$, Eqs. 1.21 and 1.23, one directly finds the Gerasimov-Drell-Hearn sum rule [Ger65] [Dre66]

$$\boxed{\int_{\nu_0}^{\infty} \frac{\sigma_{3/2}(\nu') - \sigma_{1/2}(\nu')}{\nu'} d\nu' \;=\; \frac{2\pi^2\alpha}{m^2}\kappa^2} \tag{1.27}$$

By comparing the orders ν^3 a relation for the forward spin polarizability γ_0 is obtained

$$\gamma_0 \;=\; -\frac{1}{4\pi^2}\int_{\nu_0}^{\infty} \frac{\sigma_{3/2}(\nu') - \sigma_{1/2}(\nu')}{\nu'^3} d\nu \tag{1.28}$$

In contrast to σ_T the sign of $\sigma_{3/2} - \sigma_{1/2}$ is a priori not known. The use of an unsubtracted dispersion relation for $g(\nu)$ (Eq. 1.19) implies that this cross section difference converges fast enough for $\nu \to \infty$ so that the integral remains finite. This so-called *no-subtraction hypothesis* is the most crucial point in the derivation of the GDH sum rule. Physically, this assumption means that Compton scattering becomes spin-independent for high energies. The no-subtraction hypothesis is supported by Regge phenomenology which claims that $\big(\sigma_{3/2}(\nu') - \sigma_{1/2}(\nu')\big) \sim \nu'^{-1.3}$ [Bia99]. Checking this high-energy behaviour is one strong motivation for an experimental verification of the GDH sum rule.

1.1.2 Results from multipole analyses

On the *r.h.s.* of Eq. 1.27 constants appear which are well known from other experiments. The anomalous magnetic moment κ is the difference between the measured magnetic moment of the nucleon μ_{meas} and the expectation for a structureless Dirac particle μ_D.

$$\kappa = (\mu_{meas} - \mu_D) \tag{1.29}$$

In units of the Bohr magneton $\mu_N = e\hbar/2m_p$, μ_D is 0 and 1 for the proton and the neutron, respectively. Together with μ_{meas} from [PDG00] one obtains for the anomalous magnetic moments $\kappa_{p,n}$

$$\kappa_p = 1.79\ \mu_N \quad \text{and} \quad \kappa_n = -1.91\ \mu_N \tag{1.30}$$

Application of the other constants on the *r.h.s.* of Eq. 1.27 results in the GDH sum rule values denoted in the first line of Table 1.1.

A direct experimental check of the GDH sum rule is possible only with doubly polarized experiments. Prior to these experiments, estimates have been given from multipole analyses. Due to the ν^{-1} weighting, the largest contribution to the GDH sum rule is expected in the energy region of the nucleon resonances. Multipole analyses use (unpolarized) differential cross sections of single pion production to extract the electric and magnetic multipole amplitudes of the contributing resonances. These multipoles can be converted to helicity amplitudes $A_{1/2(3/2)}$ [Arn90] which are directly proportional to the helicity dependent total cross sections $\sigma_{1/2(3/2)}$. A simple Breit-Wigner parametrization will be given in Section 5.2.2. An increase of the data base, where nowadays also single and doubly polarized [Ahr02] observables are available, led to an improvement of the extracted amplitudes. Nevertheless, all

	$I_p[\mu b]$	$I_n[\mu b]$	$I_p - I_n[\mu b]$
GDH sum rule	205	233	-28
Karliner [Kar73]	261	183	78
Workman [Wor92]	260	191	69
Burkert [Bur93]	223		
Sandorfi [San94]	289	160	129
Drechsel [Dre98]	261	180	81
Arndt [Arn02]	187	137	50
modified sum rule [Cha94]	294	185	109

Table 1.1: GDH sum rule value and predictions for the GDH integral from various multipole analyses. The multi-pion contribution from [Kar73] is also used in [Wor92] [San94] [Dre98], whereas in [Arn02] just the single pion contribution is given. The values of a modified sum rule [Cha94] are closer to the multipole analyses but are in disagreement with the original GDH sum rule values.

multipole analyses are based on single pion production data. However, in the total helicity dependent cross sections also the production of two and more pions has to be taken into account together with the production of other mesons. In [Kar73] the contribution of these channels to the GDH sum rule of the proton has been estimated to 65 μb.
In contrast to the GDH sum rule (Eq. 1.1) which requires an integration to infinitely high energies, all available data bases have a certain maximum energy ν_{max}. In the definition of the GDH integral I_{GDH} the upper integration limit is ν_{max}

$$I_{GDH} = \int_{\nu_0}^{\nu_{max}} \frac{\sigma_{3/2}(\nu) - \sigma_{1/2}(\nu)}{\nu} d\nu \tag{1.31}$$

The ν^{-1}-weighting enhances saturation of I_{GDH} for higher energies. Predictions from various multipole analyses for the GDH integral on the proton I_p, the neutron I_n and the difference $I_p - I_n$ are given in Table 1.1. The multi-pion contribution from [Kar73] has also been used in [Wor92] [San94] and [Dre98], whereas in [Arn02] just the single pion part is given. The most recent analysis includes data up to 2 GeV, for earlier analyses only data up to 1.6 GeV or 1.2 GeV have been used, respectively. The value of the GDH integral denoted in Table 1.1 is obtained by integration up to the maximum energy of the data set. All multipole analyses agree well with each other but all have a significant deviation from the GDH sum rule value. In particular, they all fail to reproduce the sign for the difference $I_p - I_n$.

1.1.3 Modifications of the GDH sum rule

Shortly after its derivation it was realized that a fixed pole at $J = 1$ in the angular momentum plane would generate a modification of the GDH sum rule [Aba68]. In such a case the spin dependent amplitude $g(\nu)$ does not vanish for $\nu \to \infty$ and a subtraction of the constant value $g(\infty)$ would be introduced.

The existence of an anomalous charge density commutator would modify the GDH sum rule

for the proton and the neutron in the following way [Cha94]

$$\int_{\nu_0}^{\infty} \frac{\left[\sigma_{3/2}(\nu) - \sigma_{1/2}(\nu)\right]_{p,n}}{\nu} d\nu \;=\; \frac{2\pi^2\alpha}{m^2}\kappa_{p,n}^2 \;+\; S_{p,n} \;\equiv I_{p,n}^{mod} \tag{1.32}$$

where the additional constant on the *r.h.s.* is $S_p = 89\mu$b for the proton and $S_n = -48\mu$b for the neutron [Cha94]. The numerical values of this modified sum rule, which come very close to the results from multipole analyses, are given in the last line of Tab. 1.1.
The theoretical background of possible modifications of the GDH sum rule has been studied in [Pan98] where strong evidence for the validity of the original, unsubtracted, sum rule (Eq. 1.1) has been found.

1.2 Related sum rules

The GDH sum rule has been derived for the absorption of real photons on polarized nucleons. It can be generalized to the photoabsorption on nuclei. Furthermore, it can be extended to virtual photons (polarized electron-nucleon scattering) which allows a comparison to fundamental QCD sum rules.

1.2.1 GDH sum rule for nuclei

The extension of low energy theorems to arbitrary spin [Lap61] [Sai69] [Fri77] allows the definition of a GDH sum rule for nuclei. It reads for a particle with mass M, charge eQ anomalous magnetic moment κ and spin S

$$\int_0^{\infty} \frac{\sigma_P(\nu) - \sigma_A(\nu)}{\nu} d\nu \;=\; 4\pi^2\kappa^2\frac{e^2}{M^2}S \tag{1.33}$$

where $\sigma_{P,A}$ are the photoabsorption cross sections for circularly polarized photons on longitudinally polarized nuclei with both spins parallel or antiparallel, respectively.
For the deuteron, for example, the anomalous magnetic moment $\kappa_d = -0.143$ is very small, leading to a sum rule value of -0.65 μb. The GDH integral for the deuteron I_d can be separated into two energy regions, above ($I_{d>}$) and below ($I_{d<}$) the pion threshold. For higher energies the nucleons inside the deuteron can be treated as quasifree, so that $I_{d>} \approx I_p + I_n$, where the contributions for the free proton and neutron are $I_p = 205$ μb and $I_n = 233$ μb, respectively. If the GDH sum rule is to be valid, $I_{d<} \approx -437$ μb where this large negative contribution comes from the photodisintegration of the deuteron which is the only possible photoabsorption process below the pion threshold. Indeed, such large negative contributions have been predicted by calculations [Are98], and an experimental verification is on the way [Wel03]. An indirect measure was extracted from beam asymmetries close to the deuteron breakup at 2.2 MeV [TUNL03].

1.2.2 Generalized GDH sum rule

Scattering polarized lepton beams off polarized nucleon targets has been used for more than 25 years to examine the spin structure of the nucleon which is described by the spin

structure functions $g_1(x, Q^2)$ and $g_2(x, Q^2)$. These depend on the Bjorken scaling variable $x = Q^2/2m\nu$ and on the four-momentum transfer Q^2. In the *Breit-frame*[5] $g_1(x)$ represents the quark distribution inside the nucleon

$$g_1(x) \;=\; \sum_{i=u,d,s,...} e_i \left(q_{i+}(x) - q_{i-}(x)\right) \tag{1.34}$$

where q_{i+} and q_{i-} are the probability-densities to find a quark with spin parallel or antiparallel to the nucleon spin, respectively, and x is the fraction of the nucleon momentum carried by the quarks. The sum runs over all quark flavours $i = u, d, s, ...$ and e_i is the charge of a quark.
The first moment $\Gamma_1(x) = \int_0^1 g_1(x)dx$ can be calculated in a simple quark model [Ell74]. Experimental results of Γ_1 from CERN [Ash89] and SLAC [Bau83] were well below the predictions of this *Ellis-Jaffe* sum rule. In fact, these results were compatible with a zero contribution of the quark spin to the nucleon spin[6]. This led to the so-called *spin-crisis*. Later it has been realized that also the angular momenta of the quarks and the gluons have to be taken into account. Various experiments at DESY, CERN and JLAB are on the way to disentangle the magnitude of the different contributions [Lam00].
The *Bjorken sum rule* [Bjo66] has first been derived within current algebra in the limit $Q^2 \to \infty$. In this limit it predicts a constant value for the difference of the first moments of the proton and the neutron $\Gamma_1^p - \Gamma_1^n$. Later it has been generalized to finite Q^2 within QCD. Including corrections to third order in the strong coupling constant $\alpha_s(Q^2)$ it reads [Tho01]

$$\Gamma_1^p - \Gamma_1^n \;=\; \left[1 - \frac{\alpha_s(Q^2)}{\pi} - 3.583\left(\frac{\alpha_s(Q^2)}{\pi}\right)^2 - 20.215\left(\frac{\alpha_s(Q^2)}{\pi}\right)^3\right]\frac{g_A}{g_V} \tag{1.35}$$

where the ratio of the axial and the vector coupling constant of the weak interaction g_A/g_V is determined from β-decay and equals to [PDG00] 1.267 ± 0.004. The *running* coupling constant $\alpha_s(Q^2)$ is given by [Pov94]

$$\alpha_s(Q^2) \;=\; \frac{12\pi}{(33 - 2n_f)\ln\left(Q^2/\Lambda\right)} \tag{1.36}$$

with n_f, the number of quark flavours, and Λ, a constant ranging from 200 to 300 MeV, which has to be determined from experiment. The Q^2 dependence of the Bjorken sum rule is found to be in agreement with experiment (see e.g. [Ade98]).
The spin structure function $g_2(x)$ describes the distribution of the quark spins transverse to the nucleon spin. The Burkhardt-Cottingham sum rule [Bur70] gives for the first moment $\Gamma_2 = \int_0^1 g_2(x)dx = 0$, which is in agreement with recent experiments [Ant03] [Ama04].

In 1989 Anselmino [Ans89] was the first to generalize the GDH sum rule to finite photon virtualities Q^2. This connects the GDH sum rule at the real photon point ($Q^2 = 0$) and QCD sum rules for large Q^2.
Following [Dre01] $\sigma'_{TT} = 1/2\left(\sigma_{3/2} - \sigma_{1/2}\right)$ and the longitudinal transverse interference cross

[5] In this reference frame the incoming electron and the nucleon have equal but opposite momenta.
[6] Recent experiments [Ade98] give a contribution of about 20% of the quark spin to the nucleon spin [Hug99] [Fil01].

section σ'_{LT} can be written in terms of the spin structure functions

$$\sigma'_{LT} = -\frac{4\pi^2\alpha}{mK}\gamma(g_1+g_2) \tag{1.37}$$

$$\sigma'_{TT} = -\frac{4\pi^2\alpha}{mK}(g_1-\gamma^2 g_2) \tag{1.38}$$

with K the virtual photon flux factor which reads in the Hand-convention $K=\nu(1-x)$. In the literature [Pan98] [Dre01] three different generalisations of the GDH sum rule exist which only include the transverse cross sections and which differ by kinematical factors.

$$\begin{aligned} I_A(Q^2) &= \frac{m^2}{8\pi^2\alpha}\int_{\nu_0}^{\infty}(1-x)(\sigma_{1/2}-\sigma_{3/2})\frac{d\nu}{\nu} \\ &= \frac{2m^2}{Q^2}\int_0^{x_0}\left(g_1-\gamma^2 g_2\right)dx \end{aligned} \tag{1.39}$$

$$\begin{aligned} I_B(Q^2) &= \frac{m^2}{8\pi^2\alpha}\int_{\nu_0}^{\infty}\frac{1-x}{\sqrt{1+\gamma^2}}(\sigma_{1/2}-\sigma_{3/2})\frac{d\nu}{\nu} \\ &= \frac{2m^2}{Q^2}\int_0^{x_0}\frac{1}{\sqrt{1+\gamma^2}}\left(g_1-\gamma^2 g_2\right)dx \end{aligned} \tag{1.40}$$

$$\begin{aligned} I_C(Q^2) &= \frac{m^2}{8\pi^2\alpha}\int_{\nu_0}^{\infty}(\sigma_{1/2}-\sigma_{3/2})\frac{d\nu}{\nu} \\ &= \frac{2m^2}{Q^2}\int_0^{x_0}\frac{1}{1-x}\left(g_1-\gamma^2 g_2\right)dx \end{aligned} \tag{1.41}$$

where $x_0 = Q^2/(2mm_\pi + m_\pi^2 + Q^2)$ is the threshold for one pion production. All three integrals reduce to the GDH sum rule value at the real photon point and they show the same asymptotic behaviour for $Q^2 \to \infty$. But, the integrals give different values for the slope at the real photon point and they differ at intermediate Q^2. Experiments are on the way to measure $I(Q^2)$ over a large Q^2 range. In Fig. 1.1 results from the HERMES experiment [Air03] for $I_B^{p,n}(Q^2)$ for the proton and the neutron are given. The line is a parametrization for the proton [Ans89] to demonstrate how $I(Q^2)$ has to change sign from the positive values for the proton at large Q^2 to the negative value at $Q^2=0$ defined by the GDH sum rule. The HERMES data of $I_B^p - I_B^n$ (Fig. 1.2) are in agreement with the Bjorken sum rule [Bjo66] if the QCD corrections up to third order in $\alpha_s(Q^2)$ (Eq. 1.35) are applied.

Recently, data for the spin structure functions and the generalized GDH integral on the neutron have been published [Ama02] [Ama04][7]. The experiment covers the Q^2 range from 0.1 to 0.9 GeV^2, and the data are compatible with the HERMES-data [Air03]. This intermediate Q^2 gives the connection from partonic degrees of freedom at large Q^2, which is well described by perturbative QCD, down to resonance behaviour of nucleons at low Q^2, which can be treated by chiral perturbation theory (χPT) for example. At the real photon point the slope of $I(Q^2)$ can be calculated. Calculations in the framework of χPT give a different sign of the slope when going from O(p^3)[Ber93] to O(p^4)[Ji00]. Recent calculations [Ji01] [Ber03] predict a negative sign of the slope, which is in agreement with the data from JLAB. The phenomenological model MAID [Dre99] [Dre01] gives a good description of the Q^2 dependence of the data but it fails to reproduce the absolute values of the data points. The

[7] Results for $g_1(x,Q^2)$ on the proton have also become available [Fat03]

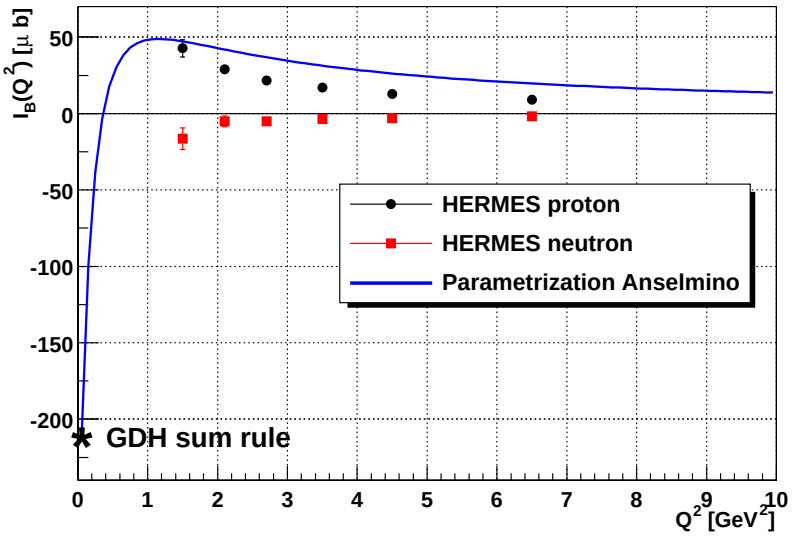

Figure 1.1: HERMES data [Air03] for $I_B(Q^2)$ for the proton and the neutron. The Q^2 dependence down to the GDH sum rule value is given by a parametrization [Ans89].

missing strength of the multipole analyses for the GDH Integral on the neutron is already obvious in Table 1.1. A possible solution to this problem will be given in Section 5.2.5.

1.3 Experimental program

Several motivations for a direct experimental check of the GDH sum rule have been given in the preceding chapters:

- Validity of the no-subtraction hypothesis (Section 1.1.1)
- Multipole analyses (Table 1.1)
- Connection to the *spin crisis* (Section 1.2.2)

The experimental requirements are

- Circularly polarized photons covering a large energy range
- Longitudinally polarized nucleons
- Detector systems covering almost 4π of the solid angle

In 1991 the first meeting of the GDH-Collaboration took place. It was decided to perform the experiment at the tagged photon facilities of the electron accelerators MAMI in Mainz and ELSA in Bonn.
The low energy part at MAMI covered the photon energy range 200 MeV $\leq \nu \leq$800 MeV.

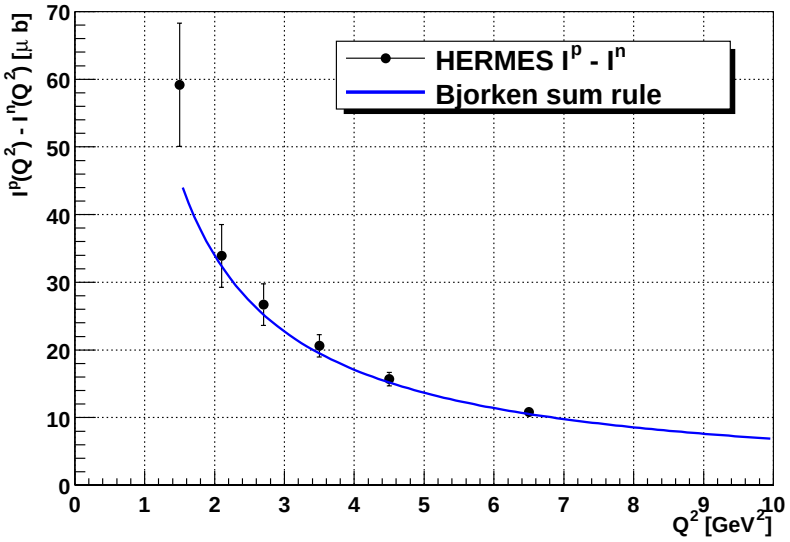

Figure 1.2: $I_B^p - I_B^n$ from HERMES data [Air03] in comparison with the Bjorken sum rule [Bjo66] including QCD corrections (Eq. 1.35).

The measurement on the proton was performed in 1998 using the DAPHNE-detector [Aud91] which allows tracking and particle identification. Besides the measurement of the total helicity dependent photoabsorption cross sections [Ahr01] also the helicity dependence of all partial reaction channels was investigated. These are, single [Ahr00] and double pion production [Ahr03] as well as η production [Ahr03b] within a limited kinematical range. Furthermore, doubly polarized observables have been available for the first time, giving more information about the resonance behaviour of the nucleon [Ahr02].
In the years 2001-2002 doubly polarized data on the proton have been taken at ELSA in Bonn covering the photon energy range from 680 MeV to 2.9 GeV. The low energies have some overlap with the MAMI experiment for a cross check of both experimental parts, whereas the upper energy limit allows some extrapolation to infinity. The polarized target used at MAMI has also been used at ELSA. The design of the detector system was optimized for a high efficient and fast measurement of total photoabsorption cross sections [Hel02], without the possibility of tracking and particle identification. After the measurements on the proton have been finished, a limited amount of data have been taken with a polarized ^{6}LiD target from 815 MeV to 1825 MeV.
The whole experimental program has been finished in 2003 with measurements on a polarized deuterium target at MAMI. The data are currently being analysed [Ros04].

The present work deals with the analysis of doubly polarized data on the proton and the neutron from the GDH experiment at the electron accelerator ELSA in Bonn. The thesis is structured as follows:
In Chapter 2 the main ingredients of the experimental setup at ELSA will be described. These are, a polarized electron beam producing circularly polarized photons, a longitudinally polarized nucleon target and a 4π detector system.
In Chapter 3 all the steps of the analysis are given. These include calibrations and corrections before cross sections can be extracted.
After that, systematic studies and a search for false asymmetries follows in Chapter 4.

Finally, results for cross sections and experimental contributions to the GDH integral for the proton and the neutron will be presented in Chapter 5.

Chapter 2

The GDH experiment at ELSA

The high energy part of the GDH experiment has been carried out at the Electron Stretcher Accelerator (ELSA) at the University of Bonn. The major components of the experiment will be described in the following sections: A longitudinally polarized electron beam (Section 2.1) producing a circularly polarized tagged photon beam (Section 2.2), a longitudinally polarized nucleon target (Section 2.3) and a 4π detector system (Section 2.4).
Figure 2.1 gives an overview of the experimental setup. Longitudinally polarized electrons produce circularly polarized photons on an amorphous radiator. The energy of the photons is determined via a tagging system. After passing an active collimator system (Section 2.2.3) and a dipole magnet (called *Sweepy*) the photons hit the polarized target. The reaction products are detected with a high efficient 4π detector system where electromagnetic background events are rejected by a threshold Čerenkov detector (Section 2.4.3). The parameters of the photon beam are constantly monitored with two independent systems (Section 2.2.4) right in front of the gamma beamdump with the leadglass detector (Section 2.2.5).
The polarization of the electron beam is determined with a 2-arm Møller polarimeter (Section 2.1.2). A lead-mineral oil Čerenkov detector (due to its shape called *V6*) detects the photons which are produced via bremsstrahlung at the moeller radiator. The primary electron beam finally ends in the electron beamdump with a Faraday cup.

2.1 The electron beam at ELSA

Fig. 2.2 shows the floor plan of the electron accelerator ELSA which consists of 2 Linacs[1] with corresponding electron sources, a synchrotron and the stretcher ring.
Electrons coming from one of the three available electron sources (2 polarized and 1 unpolarized) are preaccelerated in Linac 1 (120 keV polarized source or thermionic gun) or Linac 2 (50 keV polarized source), respectively. This continuous electron beam is converted by a *prebuncher* into a 50 Hz pulsed beam before it is injected into the synchrotron where it is accelerated up to a maximum energy of 1.6 GeV (here 1.2 GeV are used). The electrons are then injected through the transfer channel into the stretcher ring. 7-28 *shots* of the synchrotron, which corresponds to an injection time of 140-480 ms, guarantee a homoge-

[1] Linear accelerator

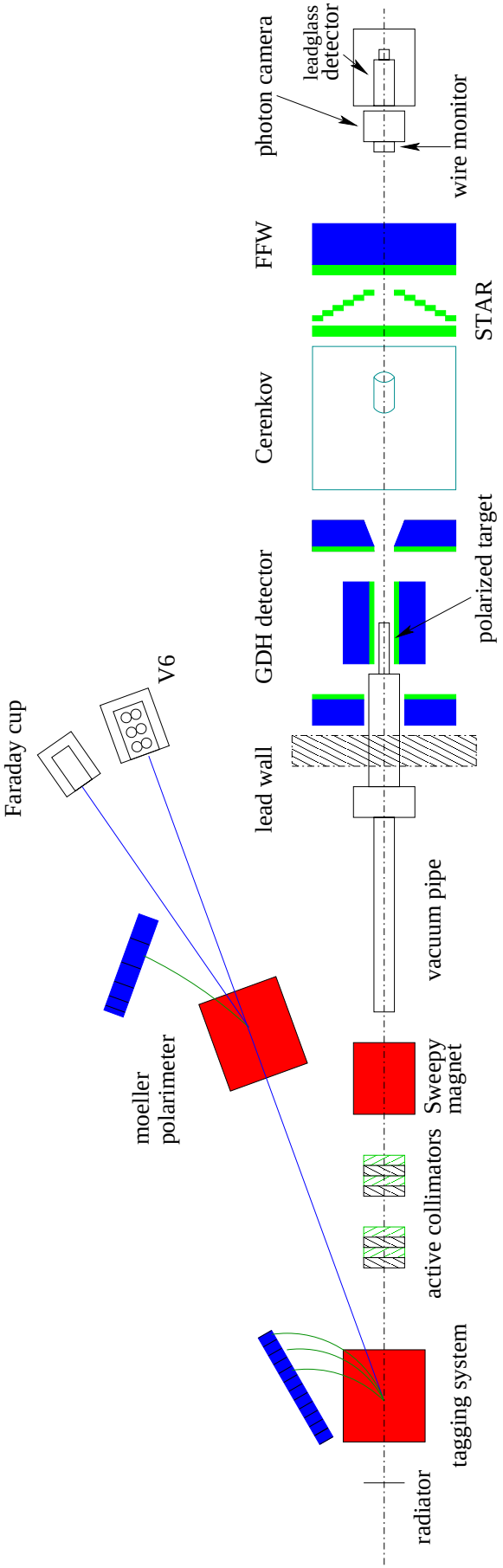

Figure 2.1: Sketch of the experimental setup.

nous filling of the stretcher ring. After injection, the electrons are further accelerated (up to 3.5 GeV) and the magnets of ELSA are ramped synchronously to the electron energy with max. 7 GeV/s (here 4.5 GeV/s). During acceleration inside the ring, the electrons loose their 50 Hz time structure as the energy loss due to synchrotron radiation is compensated by cavities (500 MHz) leading to a period of 2 ns, where the electron bunches have a width of 50 ps. As the circumference of the ring is 164.4 m, the electrons need 548 ns for one turn. The electrons in the stretcher ring can either be kept inside the ring for experiments with synchrotron light or can be extracted to external experiments. For extraction the phase space of the electrons is increased by magnetic air-quadrupoles. Electrons at the edge of the beam are *peeled off* by 2 septum magnets which operate as magnetic blades. The extraction time can be chosen between 1 and 60 s, generating a macroscopic duty cycle between 50 % and nearly 100 %.

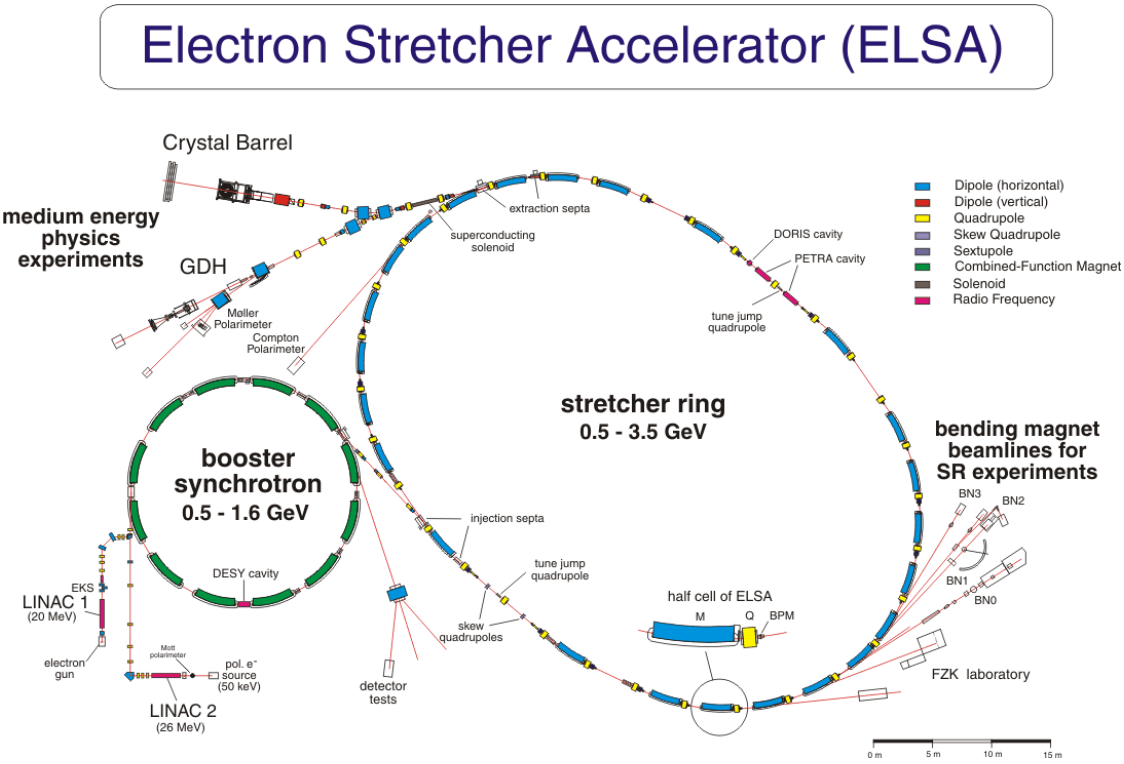

Figure 2.2: The floorplan of the electron accelerator ELSA.

2.1.1 Production and acceleration of polarized electrons

For studies and optimization of the transport of polarized electrons through ELSA the 120 keV electron source of Linac 1 (20 MeV) [Nak98] has been used between 1997 and 2000. This source provided electrons with a maximum polarization of 66 %.
Since 2000 Linac 2 with the 50 keV source for polarized electrons is available [Hil00]. This source has been used exclusively for the measurement of the helicity dependent photoabsorption cross sections. Its working principle will be explained in the following.

E_0 [GeV]	1.0	1.4	1.9	2.4	2.9	3.02	3.2
el. pol. [%]	72.4±0.4	72.4±0.4	72.4±0.4	64.6±1.0	50.7±0.9	44.9±1.0	43.8±1.8

Table 2.1: The maximum electron polarization in ELSA at several energies [Hof01].

Impinging circularly polarized laser light ejects linearly polarized electrons from a BeInGaAs/BeAlGaAs superlattice crystal through the photo-electric effect. The polarization direction of the laser light coming from a tunable titan-saphire laser (700-900 nm) [Gow01] can be varied through the high voltage applied to a Pockels cell. The helicity of the emitted electrons is determined by the polarity of the voltage at the Pockels cell. The present crystal provided electrons with a maximum polarization of 80 % a quantum efficiency of 0.2 % and a peak current of about 100 mA [Gow01].
Leaving the source, the longitudinally polarized electrons enter an electrostatic deflector, where the momentum of the electrons is turned by 90°, whereas the spin keeps its direction. Solenoid magnets finally rotate the spin perpendicular to the acceleration plane. This direction is kept during acceleration and transport through ELSA. Due to the structure of ELSA depolarizing resonances occur at specific energies which decrease the polarization. The spin usually precesses perpendicular to the accelerator plane with an energy dependent precession frequency. Horizontal fields with a frequency close to the precession frequency (or a multiple of it) of the electron spin lead to a widening of the precession cone and therefore to an increase of the horizontal spin component. This horizontal spin component vanishes due to slightly different precession frequencies of the electrons caused by a certain energy spread. It remains the (decreased) vertical spin component and therefore a decreased polarization. In a storage type accelerator like ELSA two different types of depolarizing resonances can occur:

- Intrinsic resonances:
  Through vertical betatron oscillations the electrons do not pass the quadrupole magnets in their magnetic middle, i.e. they experience horizontal field components.
- Imperfection resonances:
  Misalignment of the magnets and imperfect fields causes horizontal field components experienced by the electrons.

Extensive studies have been performed to minimize the effect of the depolarizing resonances [Hof01]. Intrinsic resonances are compensated by the use of fast air-quadrupoles (*tunejumps*) to cross the critical working points. Closed-orbit correction minimizes the influence of imperfection resonances. The track of the electrons is optimized so that they pass the magnets in the magnetic middle without the influence of horizontal field components. Table 2.1 gives an overview of the maximum electron polarization in ELSA that is available for several primary electron energies. As the energy of the depolarizing resonances is very well defined, they can be used for energy calibration. It has been shown [Hof01] that the measured energy in ELSA slightly differs from the nominal energy (Table 2.2).
The spin of the electrons is still vertical at extraction, a superconducting solenoid bends it to the horizontal plane, where it then precesses to the longitudinal direction in two dipole magnets, due to Larmor precession. The superconducting solenoid possesses an effective field length of max. 12 Tm which is sufficient to completely turn the spin to the horizontal plane

nominal el. energy [GeV]	1.00	1.40	1.90	2.40	2.92	3.02	3.20
measured el. energy [GeV]	0.9962	1.3947	1.8890	2.3843	2.8990	3.0017	3.1760

Table 2.2: The measured electron energy in ELSA in comparison to the nominal values.

for electrons with a maximum energy of 2.3 GeV. For higher energetic electrons a vertical and therefore transverse component of the spin remains.
The polarization of the electrons which is measured at the Møller-polarimeter (Section 2.1.2) is not identical to the polarization at the tagging radiator. After extraction, the electrons are passing two dipole magnets and the tagging magnet before they reach the Møller radiator. As the flight path of the electrons is fixed, the fields of the magnets have to be adapted for different primary electron energies. Therefore, the spin rotation is energy dependent and has to be taken into account when evaluating the polarization at the tagging radiator from the measured values at the Møller polarimeter [Mic96] [Kie99] [Spe02].

2.1.2 The Møller-polarimeter

Møller scattering is a widely used tool to determine the polarization of electron beams. The scattering of longitudinally polarized electrons off the electrons of a magnetized ferromagnetic foil is polarization dependent and can be factorized as follows

$$\left(\frac{d\sigma}{d\Omega}\right)^{pol}(\Theta) = \left(\frac{d\sigma}{d\Omega}\right)^{unpol}(\Theta)\left(1 + \sum_{j=x,y,z}\sum_{k=x,y,z} a_{jk}(\Theta)P_f^j P_e^k\right) \tag{2.1}$$

where $\left(\frac{d\sigma}{d\Omega}\right)^{unpol}$ is the unpolarized Møller cross section, P_f^j and P_e^k are the Cartesian components of the polarizations of the target foil and the electron beam and $a_{jk}(\Theta)$ are the asymmetry coefficients which can be calculated from QED. The *Møller asymmetry* A^M can be defined by the following combination of polarized cross sections with beam and target polarization parallel $(\frac{d\sigma}{d\Omega})^{\uparrow\uparrow}$ or antiparallel $(\frac{d\sigma}{d\Omega})^{\uparrow\downarrow}$, respectively.

$$A^M = \frac{\left(\frac{d\sigma}{d\Omega}\right)^{\uparrow\uparrow} - \left(\frac{d\sigma}{d\Omega}\right)^{\uparrow\downarrow}}{\left(\frac{d\sigma}{d\Omega}\right)^{\uparrow\uparrow} + \left(\frac{d\sigma}{d\Omega}\right)^{\uparrow\downarrow}} \tag{2.2}$$

For symmetric scattering which corresponds to a scattering angle Θ in the CM[2] system of 90° the asymmetry coefficient $a_{zz}(\Theta)$ is -7/9, whereas the other components are small. The asymmetry can be approximated to

$$A^M \approx a_{zz} P_f P_e \cos\alpha \tag{2.3}$$

with P_f and P_e the target-foil and beam polarizations. As the target foil can only be polarized in the plane of the foil it has to be tilted by an angle α to the beam direction (Fig. 2.3).
The asymmetry A^M can also be written in terms of the experimentally accessible count rates for beam and target polarization parallel $N^{\uparrow\uparrow}$ and antiparallel $N^{\uparrow\downarrow}$, respectively, as the helicity of the electron beam is flipped frequently.

$$A^M = \frac{N^{\uparrow\uparrow} - N^{\uparrow\downarrow}}{N^{\uparrow\uparrow} + N^{\uparrow\downarrow}} \tag{2.4}$$

[2] Center of Mass

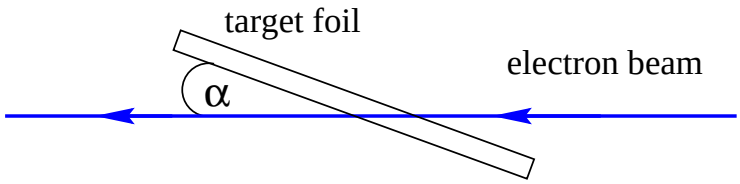

Figure 2.3: Side view of the Møller target foil for the longitudinal polarization component.

Using Equation 2.3 the polarization of the electron beam can be determined by

$$P_e = \frac{1}{a_{zz} P_f \cos\alpha} \frac{N^{\uparrow\uparrow} - N^{\uparrow\downarrow}}{N^{\uparrow\uparrow} + N^{\uparrow\downarrow}} \tag{2.5}$$

For a realistic polarimeter, the asymmetry coefficients have to be divided by the acceptance which is obtained by simulations [Spe02]. This so-called effective asymmetry coefficient $\tilde{a}_{zz}$ [Mic96] replaces a_{zz} in Eq. 2.5.
A foil of magnetized supermendur which consists of 49% iron, of 49% cobalt and of 2 % vanadium is used as Møller target. It is polarized by Helmholtz coils to $P_t = 8\%$ and tilted by an angle $\alpha = 20°$. The original and the Møller electron are deflected in a dipole magnet according to their energy. Both electrons are detected in coincidence by two rows of 7 leadglass detectors which are mounted above and below the middle plane of the magnet (Figure 2.4).

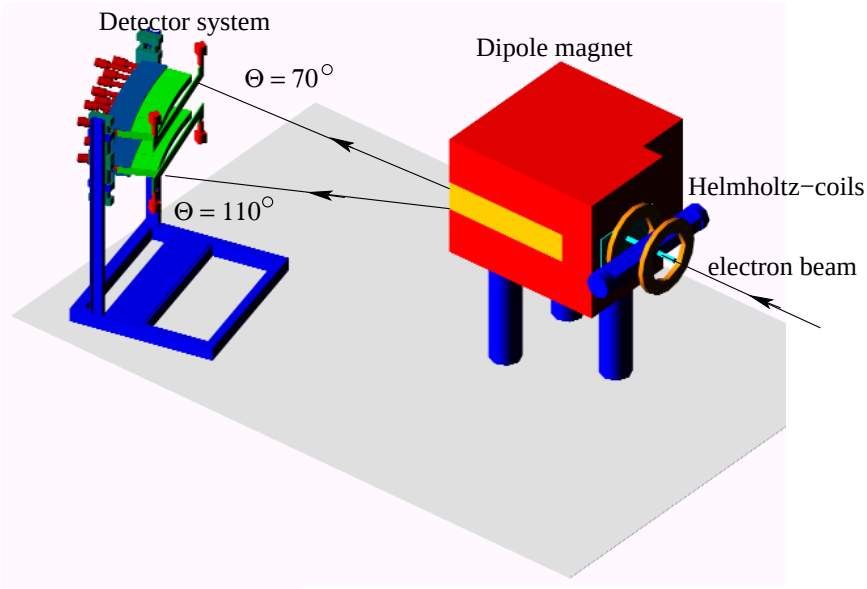

Figure 2.4: The Møller polarimeter [Spe04] [Spe02] [Kie99].

A Møller event is separated from the background by energy conservation. The sum of the energies of both electrons has to be equal to the primary beam energy. The 7 pairs of leadglass detectors cover an angular range $\Theta_{CM} = [65°,115°]$ and represent 7 independent measurements of the electron polarization P_e. The large acceptance minimizes systematic error sources like the Levchuk effect [Spe02].
Additional to the measurement of the longitudinal polarization component, further Møller foils for the transverse components exist which can be magnetized by corresponding

Helmholtz coils. Therefore, the measurement of all 3 spatial components of the electron polarization is possible. For the longitudinal component a statistical precision better than 1% can be obtained within 10-15 minutes whereas the measurement of the transverse components needs several hours to reach a statistical error of 2%. The Møller data for the determination of the electron polarization are taken in parallel to the data of the GDH-detector as both systems have their own data acquisition system. The Møller and the detector data contain a *timestamp* which allows a correct assignment of the beam polarization to the detector events during data analysis.

2.2 The photon beam

In this section the path of the photons will be followed from their production (Section 2.2.1) to their *end* in the photon beamdump with the leadglass detector (Section 2.2.5). The energy of the photons is determined by a tagging system (Section 2.2.2) and they have to pass an active collimator system (Section 2.2.3) before they reach the target. The position and the width of the beam is constantly monitored via two separate systems (Section 2.2.4) right in front of the gamma beamdump.

2.2.1 Production of polarized photons

The generation of high energy polarized photon beams is possible via a variety of methods. For example coherent bremsstrahlung from a crystalline radiator [Nat00] or compton laser backscattering [Bab91] can be used. As the present experiment requires a high flux of circularly polarized photons, bremsstrahlung of longitudinally polarized electrons at a radiator foil is used. The helicity transfer to the photons depends solely on the photon energy and can be calculated from QED [Ols59]. The circular polarization P_γ of the photons as a function of the photon energy E_γ can be written in terms of the electron polarization P_e and the primary electron energy E_0

$$\frac{P_\gamma}{P_e} = \frac{k\,(1+(1-k))}{1-(2(1-k))+3(1-k)^2} \quad \text{with} \quad k = \frac{E_\gamma}{E_0} \tag{2.6}$$

The polarization transfer from the electrons to the photons P_γ/P_e according to Eq. 2.6 is plotted versus the ratio E_γ/E_0 in Figure 2.5. The electron polarization is transferred completely if the electrons loose all their energy in the bremsstrahlung process ($E_\gamma = E_0$) and the polarization transfer drops to zero for $E_\gamma \to 0$.
The value of the electron polarization which is measured at the Møller polarimeter (Section 2.1.2) has to be transformed to the value at the tagging radiator by use of the spin-transport [Spe02]. With the knowledge of the photon energy E_γ (Section 2.2.2) the polarization of each individual photon is determined via Equation 2.6.

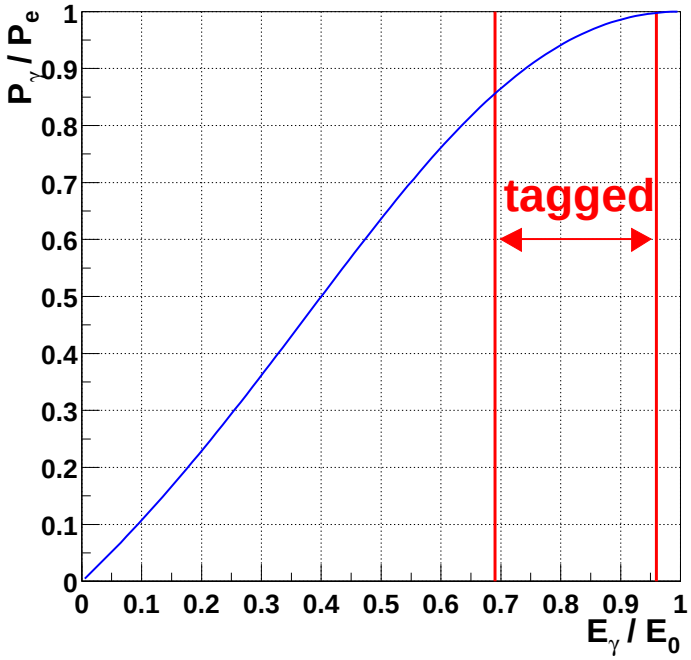

Figure 2.5: The polarization transfer according to Eq. 2.6.

2.2.2 The tagging system

As the energy spectrum of the photons produced in the bremsstrahlung process is continuous one has to *tag* the photons so that a later assignment of the measured cross section to the according photon energy is possible. Figure 2.6 shows the principle of the tagging system. Electrons that loose energy due to the radiation of a bremsstrahlung photon are separated in energy by the field of a dipole magnet. With this spectrometer setup the electron energy E_e is measured. As the primary electron energy E_0 is well known the photon energy E_γ can simply be obtained by

$$E_\gamma = E_0 - E_e \tag{2.7}$$

Figure 2.7 gives an impression of the technical realisation of the tagging system (for more details see [Nau01], [Wei02], [Nau03]). Inside the vacuum tank four different radiator foils are mounted, which can be brought into the beam via a stepping motor. With these foils (10 μm Al, 20 μm Al, 15 μm Cu, 50 μm Cu) different intensities of the photon beam can be generated for rate studies without changing the intensity of the primary electron beam. The dipole magnet (C-type 0.5-2.0 T) deflects the primary electron beam by 9° to the Møller spectrometer and the electron beamdump. Electrons that have undergone a bremsstrahlung process are bent to a ladder of 65 scintillation counters. These counters are mounted alternatively from top and from bottom with some overlap, where two successive counters define one tag channel. This coincidence reduces background of electrons which have not produced a bremsstrahlung photon but come for example from a scattering process. The 65 scintillator counters form 64 tag-channels which cover 68 % - 97 % of the primary electron energy E_0. As can be seen from Fig. 2.5 the energy range covered by the tagging system guarantees the circular polarization of the photons to be greater than 85 % of the longitudinal electron polarization. To cover the desired photon energy range 680 MeV $\leq E_\gamma \leq$ 3 GeV the mea-

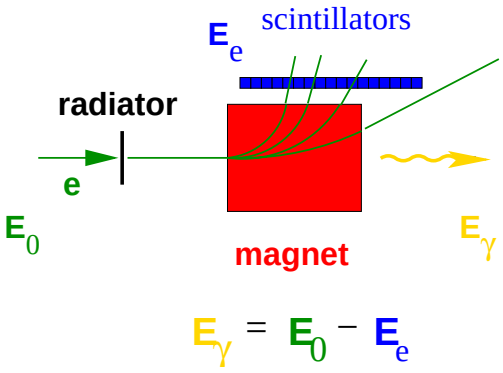

Figure 2.6: Principle of the tagger.

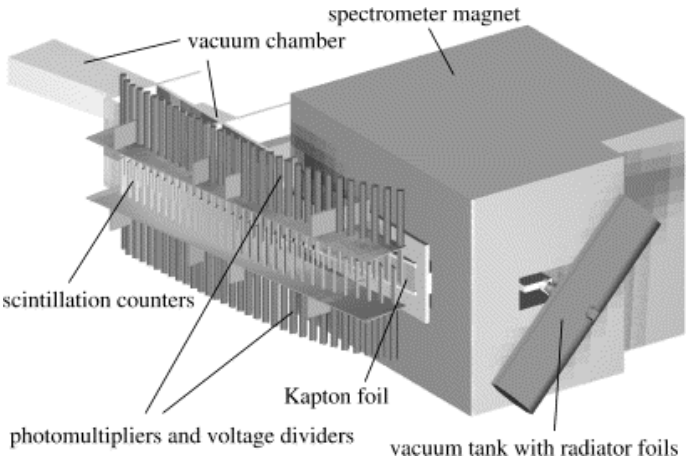

Figure 2.7: 3-D view of the tagging system [Nau03].

surements have been performed at 5 primary electron energies: 1.0 GeV, 1.4 GeV, 1.9 GeV, 2.4 GeV and 3.02 GeV. The bars in Figure 2.8 indicate the energy ranges covered by the 64 tag channels for the 5 primary electron energies[3]. The width of a tag channel is obtained from the distance between two successive bars. The width of the scintillators vary from 5 cm for the low photon energy channels to 2 cm for the channels at the upper end of the energy range. Therefore, the energy resolution varies between 0.2% $\cdot E_0$ and 0.6% $\cdot E_0$ [Nau03]. The two lowest photon energy channels are much broader to provide a small statistical error in the overlap region of two primary electron energies.

2.2.3 The active collimator system

The bremsstrahlung photons are emitted within a cone with a characteristic critical opening angle Θ_c. In the ultrarelativistic limit ($E_0 \gg m_e c^2$) Θ_c solely depends on the energy [Hei54].

$$\Theta_c = \frac{E_0}{m_e c^2} \tag{2.8}$$

50 % of the radiated photons are emitted inside this cone. The divergence of the primary electron beam causes an additional broadening of the photon beam. Therefore, the photon beam has to be limited in its size and divergence to meet the given constraints at the nucleon target ($\sigma_{x,y} \leq 4$mm). A broader beam would either prevent a correct determination of the photon flux or would interact with material of the target cryostat.
The limitation of the size of the photon beam is usually done with a passive collimator which simply consists of a lead block with a drill hole of the required diameter. This passive collimation causes some problems especially if the tagged photon energy range is small compared to the complete photon spectrum (as in our case).
If the photons interact with the collimator material they can produce an electromagnetic shower which consists of charged particles (e^+e^-) and secondary photons. The charged particles are removed from the photon beam by a dipole magnet (*Sweepy*) while the secondary

[3]for technical reasons data have also been taken at 2.9 GeV which is not plotted in Fig. 2.8

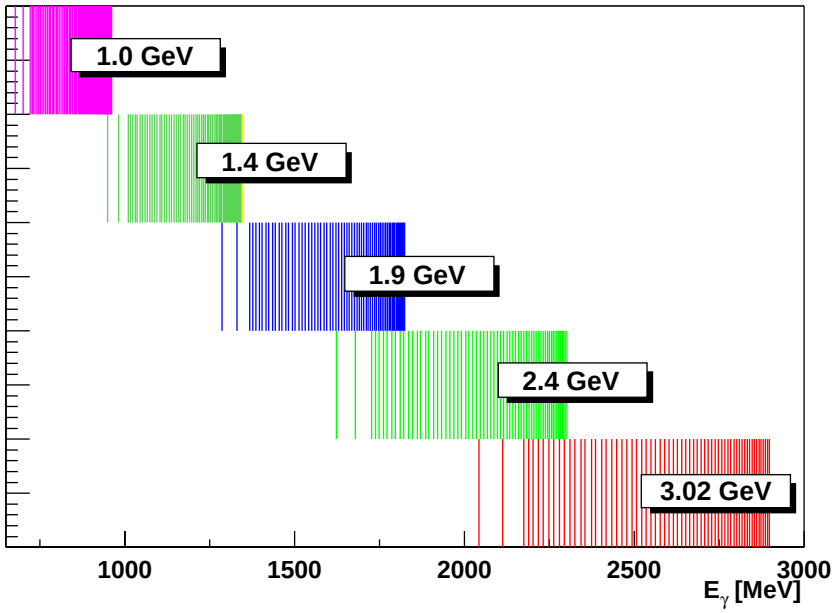

Figure 2.8: Photon energy ranges covered by the tagging system for 5 different primary electron energies.

photons still could reach the target region and might produce a hadronic reaction. This reaction would then be assigned to the wrong photon energy, as the primary (tagged-)photon lost energy through the interaction with the collimator material and the GDH-detector is not designed to measure the photon energy independent from the tagging system.
These problems have first been recognized during the pilot experiment with the GDH-detector at the PHOENICS-areal at ELSA [Hel97] [Sau98]. During this experiment a first prototype of an active collimator system has been tested successfully. For the double polarized measurements the design of the active collimator system has been optimized by simulations and test measurements [Zei98] [Zei01].
The active system consists of two modules (Figure 2.9) where each module consists of 4 lead-scintillator double layers. The photon beam is curtailed to its design values by the first lead layer of the first module. Photons interacting with the collimator material produce an electromagnetic shower which causes light output in the scintillator layers. The light of each module is read out by two photomultipliers via silicone pads and fishtail lightguides. The signals of the photomultipliers are then used as a veto for the experimental trigger (Section 2.5.4).
The first module possesses a bore hole of 5 mm in diameter to limit the photon beam. The second module is used to increase the efficiency of the collimator system. It has a hole with 6 mm in diameter to not further decrease the size of the beam. The rate of the photomultipliers of the first module is kept at moderate rates ($\approx$ 3 MHz) by a passive collimator right in front of the first module. This collimator is used to absorb low energetic, untagged, photons which are emitted from the tagging radiator under a large angle. It is, however, possible that in this *pre-collimator* secondary photons are produced which are not detected by the active collimator system. To prevent these photons from reaching the target, another *post-collimator* is installed in front of the target. The complete setup in the gamma beamline,

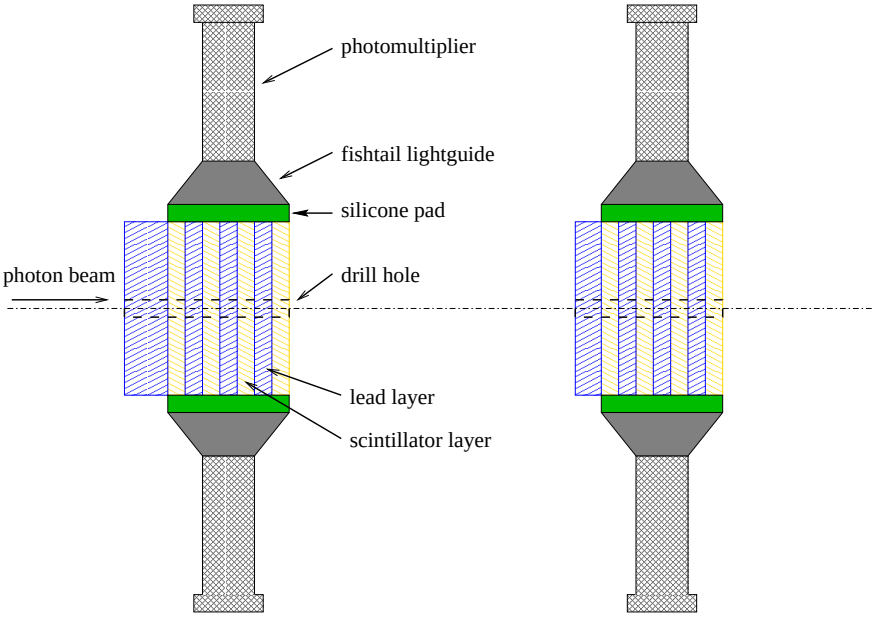

Figure 2.9: The active collimator modules.

including the two active collimator modules and the pre- and post-collimator, is displayed in Figure 2.10.
More details about the performance of the active collimator system can be found in [Zei01] [Zei02].

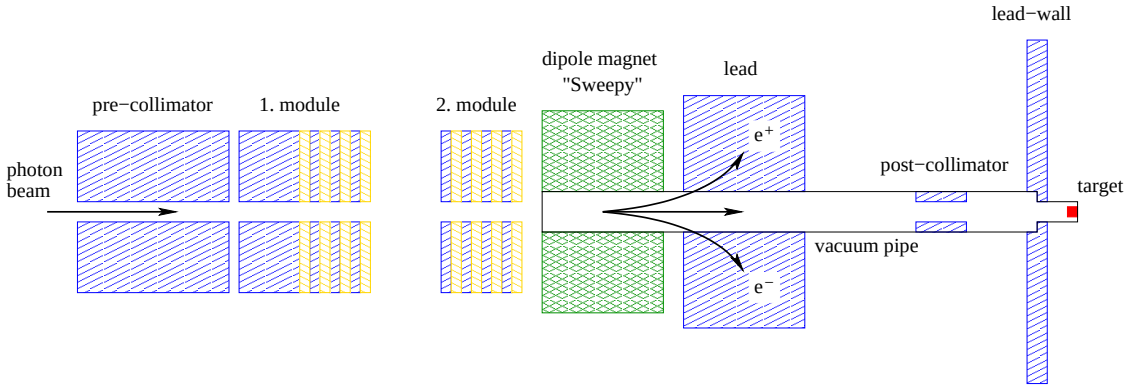

Figure 2.10: The gamma beamline with the collimator setup (not to scale).

2.2.4 Monitoring the photon beam

Right in front of the photon beamdump with the leadglass detector, two systems for monitoring the parameters of the photon beam are mounted. Both systems work independently, and as they use different detection methods, they are sensitive to different energy ranges of the photon beam.

The wire scanner

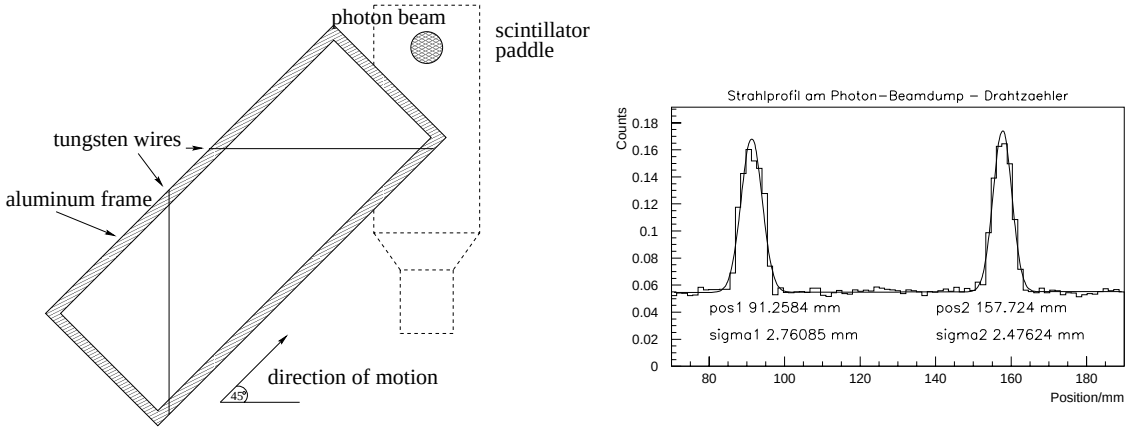

Figure 2.11: left: Principle of the wire scanner; right: Registered intensity versus the position of the frame.

Figure 2.11 (left side) gives an impression of the working principle of the wire scanner [Are91]. Two orthogonal tungsten wires are mounted on an aluminum frame which is moved at 45° through the photon beam. A scintillator paddle (with a hole for the primary beam) which is placed behind this arrangement, registers the intensity as a function of the wire position. If one of the wires reaches the photon beam, electron-positron pairs are produced. These additional charged particles lead to an increase of the measured intensity in the scintillator paddle. The frame is moved through the beam by a stepping motor[4], where each position is maintained for a certain amount of time. This dwell time can be selected together with the step width via software to match the actual requirements. A typical result of such a scan is shown in the right half of Figure 2.11, where the number of counts of the scintillator paddle is plotted against the position of the frame. Two maxima appear which correspond to the positions where the photon beam is crossed by the horizontal or vertical wire, respectively. The step width of the motor (1.8°) corresponds to a linear movement of 0.01 mm. After taking into account a factor $1/\sqrt{2}$ due to the movement at 45°, the beam position and width can be given in mm.
The calibration of the absolute position can be performed with the aid of an adjusted theodolite. The position of the wires is reproducable within a precision better than 0.01 mm [Are91], i.e. the position of the photon beam can in principle be measured with this precision. The statistical fluctuations in Figure 2.11 result from a measuring time of about 10 min. for the complete scan.

The photon camera

As the previously described system needs about 10 min. before any information from the photon beam can be extracted, a photon camera [Kri98] has been developed which allows *online* monitoring of the photon beam during data taking. This device is also used during the beam development phase. Especially at an early stage of the experimental buildup, when

[4]Isel Automation, Germany

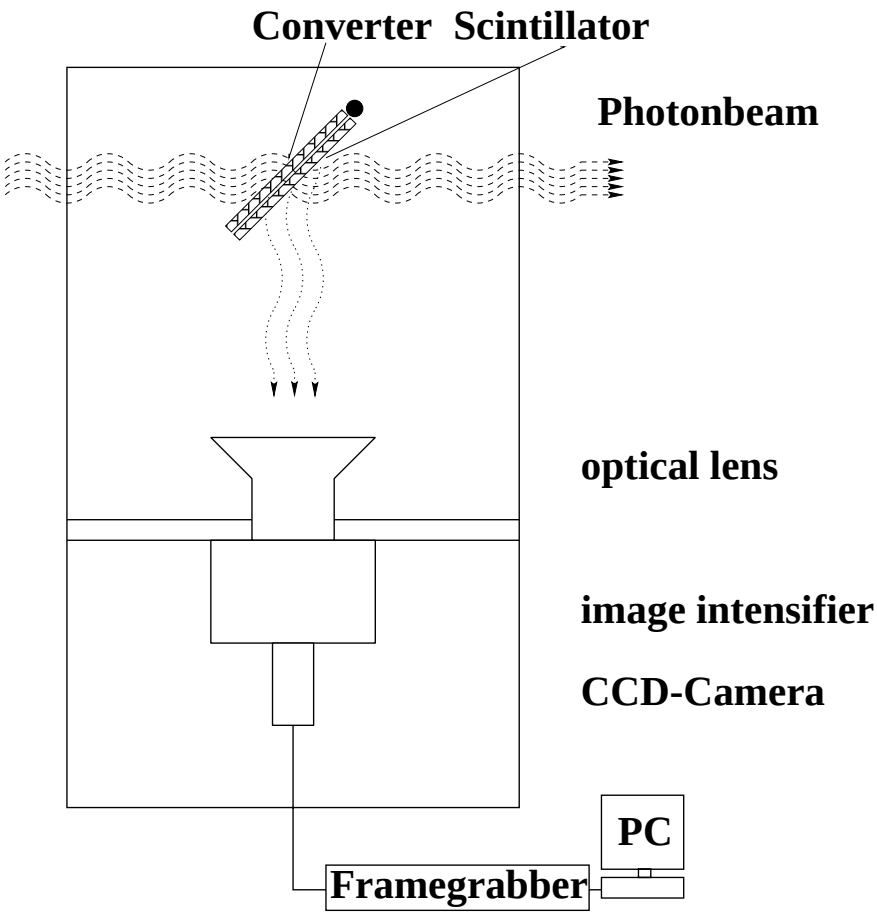

Figure 2.12: A schematic sketch of the photon camera.

the new external beamline for the GDH experiment has been installed [Kie96], the photon camera demonstrated its flexibility as it has also been used in the electron beam.
The principle of the photon camera is based on the conversion of high energy photons to visible light which can be detected via standard optical devices. The structure is displayed in Figure 2.12. It consists of a thin scintillator which is placed at 45° in the beam. The beamspot is *viewed* by a ccd-camera[5] via an optical lens and an image intensifier[6]. The image is digitized by a framegrabber so that further image processing can be performed with the help of a PC in order to extract the parameters of the photon beam.
For the scintillation process the production of charged particles is necessary as an intermediate step. These can be produced anywhere on the flightpath of the photons or in the scintillator itself, through photo effect, Compton effect or pair production. To increase the number of electron positron pairs, a high Z converter is placed right in front of the scintillator. Its thickness has been optimized to give an optimal light output of the scintillator without disturbing the measurement of the photon flux with the leadglass detector. Various scintillator materials have been tested and it turned out that a thin foil (≈ 1 mm) of terbium doped gadoliniumoxisulfide (Gd_2O_2S:Tb) is ideal for the present purpose. This material is well known from intensifier foils in medical X-ray diagnostics. Test measurements have shown that it has a higher light output in a photon beam than plastic scintillators of comparable

[5]Hamamatsu C3077 756 x 580 pixel
[6]Hamamatsu C2400-80

thickness [Kri98].
The framegrabber[7] is housed in a PC as an extension card and it provides the connection between the camera and the software. It digitizes the incoming camera signal which complies with the CCIR standard[8], and it also generates the synchronization pulses for driving the camera. The integration time for one picture can be varied via these synchronization pulses. Exposure times between 0.04 to 1 s are possible, which determine the statistical quality of one image and which limit in principle the number of images which can be taken within a certain time interval. In the system used for the GDH measurements in Bonn, the exposure time was not the limiting factor for the number of images per time, but the available computer power.

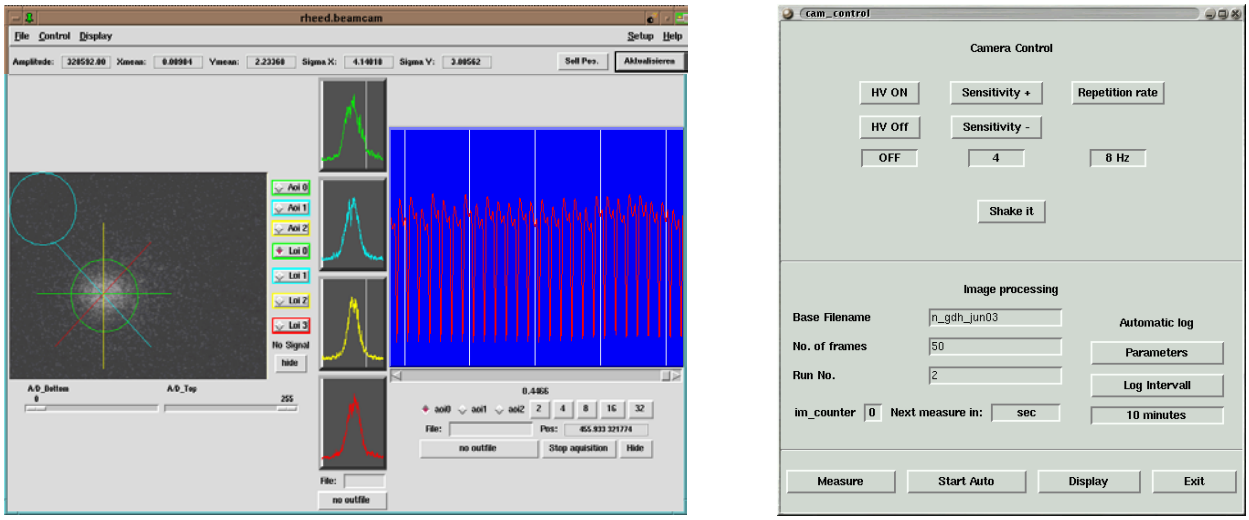

Figure 2.13: Left: A screen copy of the graphical interface which displays the measured data. Right: A panel to control both the camera and the image intensifier and to select parameters for automatic protocoling.

The software for the framegrabber card is based on a driver [Kar96] [Drv96] for the multitasking operating system Linux. The driver is implemented as a loadable kernel module, as it has to manage resources and to supervise interprocess communication. Functions of the driver can either be activated through standard calls from C-libraries or through extensions to the script language Tcl/Tk [Ous94]. The integration time of the ccd-chip and the sensitivity (amplification) of the image intensifier can be adjusted via a graphical interface (Figure 2.13 right). Moreover the parameters for the automatic protocoling can be selected within the same panel (lower half). For display of the measured data and of the results from the online analysis, a real-time graphical widget was created (Figure 2.13 left). The actual image taken by the CCD camera is displayed on the left side and updated regularly. The bright spots indicate the light produced by beam particles and thus represent the beam spot on the scintillator. A circular area-of-interest (AOI) can be selected for integration. The time sequence of this intensity is displayed on the right side. The observed structures in the histogram result from the macro pulsing of the ELSA accelerator (extraction period $\approx$ 2 s). Furthermore, four lines-of-interest (LOI) can be defined. The projections of the intensity onto these lines are displayed in the four histograms in the middle of the interface. This

[7] Mutec MV-1000
[8] Comitté Consultativ International des Radiocommunication

allows a quick visual check of the beam profile.

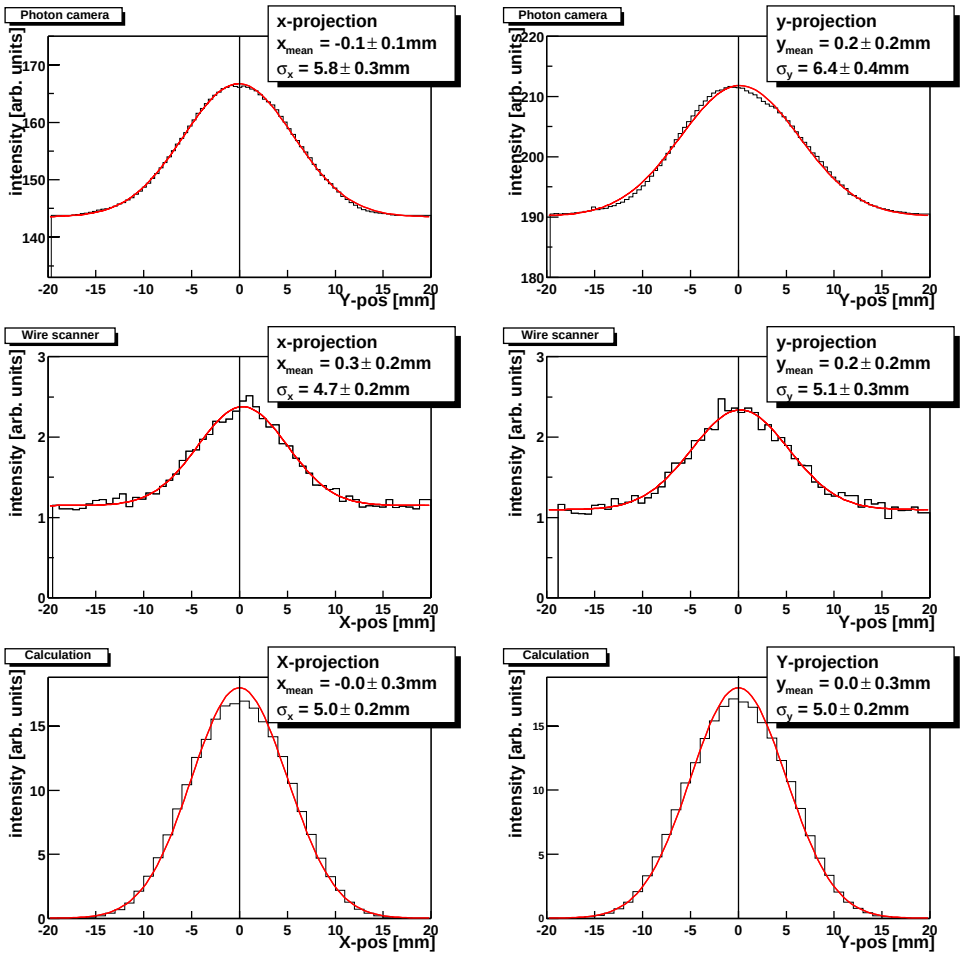

Figure 2.14: Comparison of measured beam profiles in horizontal (x)- and vertical (y)-direction. Upper panels: taken by the photon camera; middle taken by the wire scanner; bottom: calculated by MCB [Nat03].

To obtain a *mean image* with sufficient statistical precision, a certain number of frames (typically 50-100) is accumulated by software. The projections onto the x- and y-axes are fitted by Gaussians to obtain the position and the width of the beam. A comparison of the performance of this system to the wire scanner is displayed in Figure 2.14. The upper part displays the x- and y-projections of the beam spot taken with the photon camera. The lines represent a Gaussian fit to the data (histograms). The middle section shows for comparison the beam distribution when recorded with the wire scanner. Despite the different background intensities (note the zero suppression in Fig.2.14 top) both systems show consistently the same centroid position. For comparison a Monte Carlo prediction of the bremsstrahlung process is presented in the bottom of Fig. 2.14. For input to the MCB code [Nat03] realistic electron beam parameters have been taken as e.g. the beam spot size of 1 x 1 mm^2 and a divergence of 0.3 mrad. The photon beam produced on the Al radiator of 20 μm thickness was limited by a collimator of 5 mm diameter at 3.51 m distance. The simulations assume a Gaussian profile of the electron beam. Despite the slight deviation from the Gaussian profile they can reproduce the wire scanner data quite well. The slight differences observed for the shapes

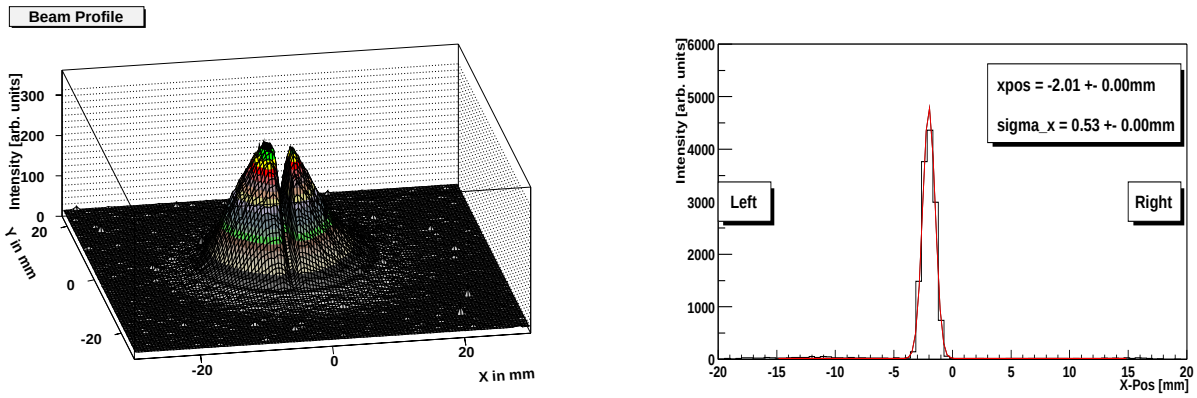

Figure 2.15: a) Vertical tungsten wire in front of the scintillator produces a dip in the intensity distribution. b) After subtraction a peak at the wire position remains.

and the widths is associated with the different methods and sensitivities for photon detection of the two instruments. The tungsten wires mainly produce electron positron pairs which are detected by a scintillation detector as a function of wire position, whereas the present CCD system makes use of all photoabsorption processes in the scintillator material directly. Therefore, both systems are sensitive to different parts of the bremsstrahlung spectrum.
As described above about 10 minutes are required for the wire scanner to complete one scan. The photon camera has been operated for the GDH experiment at ELSA with a 200 MHz pentium processor. With a selected exposure time for one image of 0.125 s and an accumulation of 100 frames for the *mean image* a complete cycle including the image processing needs less than 2 min, even then the statistics is better than that of the wire scanner (see Fig. 2.14). The calibration of the photon camera can be performed via a cross hair which is placed at the demand position of the photon beam with the aid of a theodolite. As the cross hair can be illuminated by a LED, the demand position can be depicted to the CCD-chip (see also [Kri98]).
A second method for calibration uses the wire scanner. If placed in the photon beam, the tungsten wires produce a *shadow* in the measured intensity distribution of the photon camera. Figure 2.15 a) shows the measured intensity distribution, while the vertical tungsten

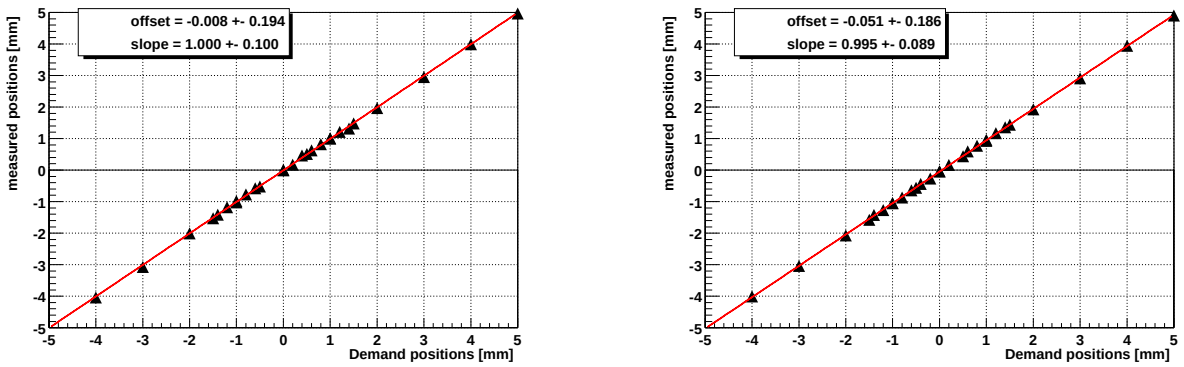

Figure 2.16: Measured positions versus demand values after application of conversion factors for the photon camera.

wire is in front of the scintillator. The dip in the intensity reflects the position of the wire. For analysis, the image with the wire in front is subtracted from an image with beam but without wire. The result of this operation can be seen in Figure 2.15 b). At the position of the wire, a peak remains. This procedure has been repeated several times with known values for the positions of the horizontal and vertical wires, respectively. From the analysis of the measured positions, conversion factors from pixels on the CCD-chip to absolute position values in mm have been extracted. For the setup at ELSA they are 0.108 pixel/mm for the x-direction and 0.123 pixel/mm for the y-direction. The demand positions are 388 pixel for x and 230 pixel for y. With the application of these factors and demand positions, the measured positions are plotted versus the demand positions of the wires in Figure 2.16. A straight line fitted to the measured points gives, within error bars, a slope of 1 with offset 0.

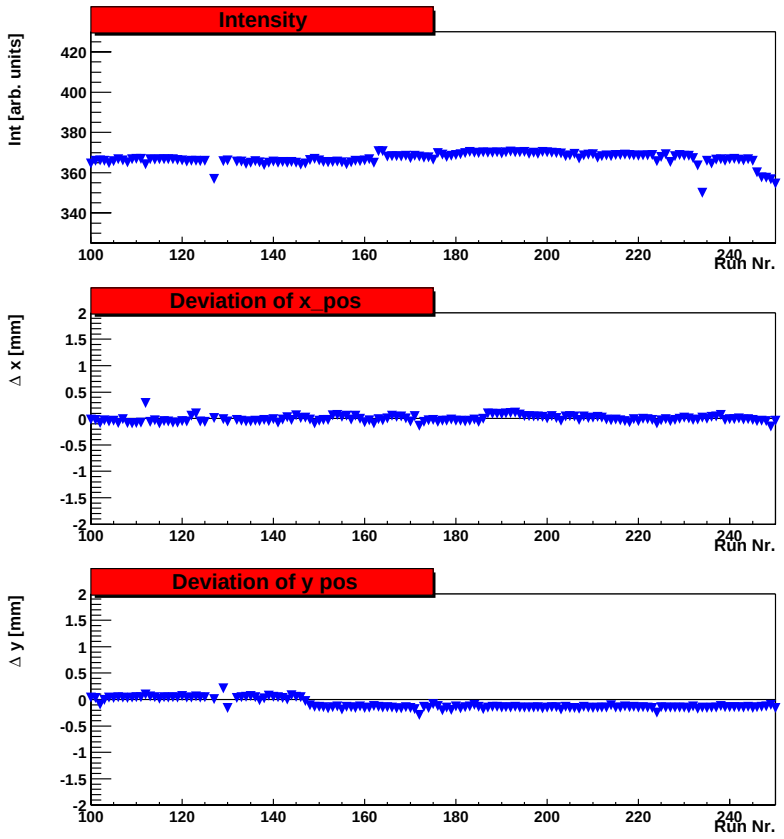

Figure 2.17: The measured intensity (top) and the x- (middle) and y-position (bottom) of the photon beam over a period of ≈ 5 days.

During routine data taking the measured positions and intensities are written to a log-file, e.g. every 2 minutes. For the beamtimes in 2002 the position information has been used as a feedback signal to ELSA control. If a deviation from the demand position occurs, the current of one of the ELSA magnets is automatically adapted to steer the beam back to the demand position [Fro02]. Since 2002 a stabilization system is also used for the intensity. Figure 2.17 shows the intensity (top) together with the measured x- and y-position (middle and bottom) over the run number for a beamtime in 2002. The displayed period of time is about 5 days. Relative intensity variations have been less than 1 % and the position has been kept stable

to better than 0.1 mm during this period.
In the second half of 2002 first test measurements have been performed for the experimental check of the GDH sum rule on the neutron with the DAPHNE detector at the tagged photon facility of the electron accelerator MAMI in Mainz. The photon beam in the A2 hall is made visible on a TV monitor by a system which has been built by the nuclear physics group of the university of Glasgow [McG97] and which gave the basic principles of the photon camera described in this section. In former times a certain number of frames were accumulated by a hardware device (called *framestore*) before displayed on a TV monitor. The beam position has just been checked *by eye* without any quantitative analysis of the images. From a certain time on, spare parts for the *framestore* have not been available any more so it has been decided to buy the same framegrabber card (Mutec MV-1000) which is used at ELSA, also for the experiment at MAMI. The framegrabber card is operated in a PC with a 1.6 GHz AMD K6 processor and the software for image processing has been adapted for the requirements at MAMI. With this faster computer system 50 frames can be accumulated and analysed within 20 seconds. The calibration was performed with an illuminable cross-hair at the demand position. The conversion factor for this system is 0.1 pixel/mm. Figure 2.18 shows a contour plot of the intensity distribution of the photon beam in the A2 hall of the MAMI accelerator.

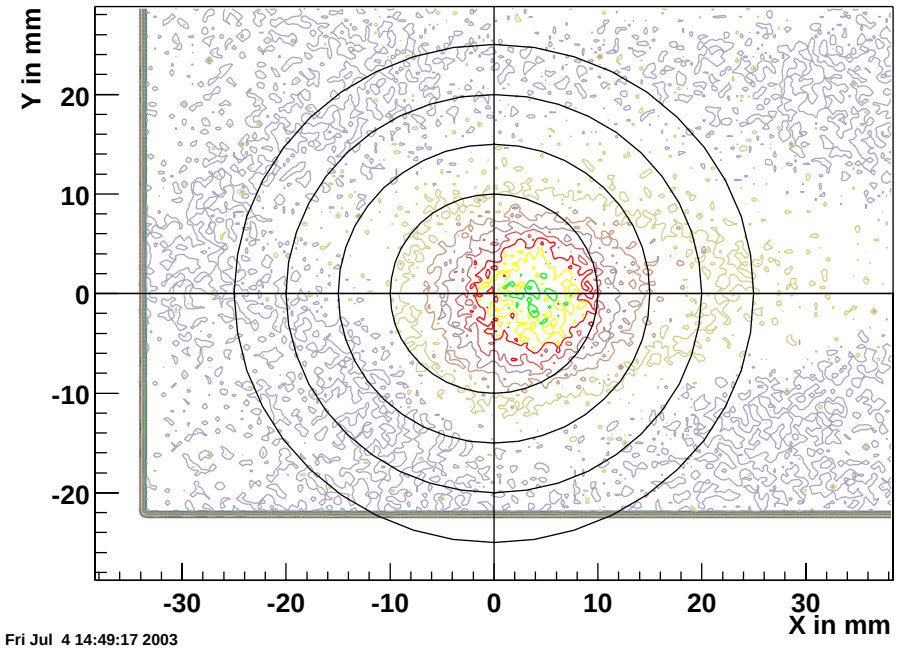

Figure 2.18: The photon beam in the A2 hall of the MAMI accelerator.

2.2.5 The photon veto detector

At the end of the photon beam line, inside the gamma beamdump, a leadglass detector is situated which shall be called *photon veto detector*. For photons in the energy range of the

present experiment it can be treated as total absorptive because its dimensions (13.8cm x 13.8cm x 28.8cm) [Zei98] correspond to more than 12 radiation lengths. It has two tasks:

1. During ordinary data taking it acts as a veto. Photons have to pass a lead layer (2.5 cm or 5 cm depending on primary electron energy) before they reach this detector. If a tagged photon reaches the detector, it cannot have undergone a hadronic reaction in the target, therefore these events have to be rejected. Also background events from electromagnetic reactions which have not been detected in the Čerenkov detector (Section 2.4.3) can reach the leadglass detector and have to trigger a veto signal. No hadronic reactions are falsely rejected as it is extremely unlikely that photons coming from meson decay have the proper direction to reach the photon veto detector nor do they have the energy to pass the lead layer right in front of the leadglass detector.

2. The second task is the determination of the tagging efficiency ϵ_{tag} which is the fraction of produced tagged photons that reach the target area. It can be determined by demanding only hits of the tagger in the trigger electronics and then to count the number of coincident events between the leadglass detector and the tagger ($N_{Pb} \wedge N_{tag}$). Finally, this number is normalized to the number of produced tagged photons (N_{tag}).

$$\epsilon_{tag} \approx \frac{N_{Pb} \wedge N_{tag}}{N_{tag}} \tag{2.9}$$

   As one has also to take into account the influence of the active collimators and shadowing effects which occur at high rates, a more elaborated method (see Section 3.6.1) has to be used for the exact determination of the tagging efficiency.

The thickness of the lead layer and the high voltage (HV) of the photomultiplier are optimized by maximizing the tagging efficiency and keeping the rate of the photomultiplier as low as possible. Due to radiation damage the leadglass detector gets *brown* after a certain amount of accumulated charge. This effect can be cured by application of ultraviolet light. If the leadglass detector gets *brown*, the tagging efficiency for the low energy photons drops and the HV for the photomultiplier has to be increased to compensate for this effect. A method for correcting the tagging efficiency values that have been obtained with a *brown* leadglass detector will be described in Section 3.6.1.

2.3 The polarized nucleon target

For the experimental check of the GDH sum rule, helicity dependent total photoabsorption cross sections have to measured which results in the following requirements for the polarized nucleon target:

- Longitudinally polarized nucleons
- Minimal loss of solid angle for outgoing hadrons
- Large maximum polarization with long relaxation times

For this purposes a new *frozen spin* target has been built by the Bonn-Bochum-Nagoya target groups [Bra99]. It is based on a horizontal ^{3}He/^{4}He dilution refrigerator with an internal superconducting holding coil which allows emitted particles to be detected within an angular range of nearly 4π.
The principle of nucleon polarization will be described in Section 2.3.1. In Section 2.3.2 the apparatus of the polarized target is explained together with the measurement of the nucleon polarization. Finally, the properties of the target materials (butanol and ^{6}LiD) like target density, maximum polarization values and relaxation times will be given in Section 2.3.3.

2.3.1 Polarized nucleons

In thermal equilibrium the polarization P_{TE} of a system with spin J under the influence of a magnetic field B is given by the Brillouin-function

$$P_{TE}(J) = \frac{2J+1}{2J}\coth\left(\frac{2J+1}{2J}\frac{\mu B}{k_B T}\right) - \frac{1}{2J}\coth\left(\frac{1}{2J}\frac{\mu B}{k_B T}\right) \tag{2.10}$$

which reduces for a spin-$\frac{1}{2}$ system to

$$P_{TE} = \tanh\left(\frac{\mu B}{k_B T}\right) \tag{2.11}$$

with the magnetic moment μ, the Boltzmann constant k_B and the temperature T. Consider now for example $B = 2.5$ T and $T = 300$ mK. With the magnetic moment for the electron ($\mu_e = 5.788 \cdot 10^{-11}\frac{MeV}{T}$) and the proton ($\mu_p = 3.152 \cdot 10^{-14}\frac{MeV}{T}$) an electron polarization $P_e = 99.99$ % is obtained whereas the protons are just polarized to $P_p = 0.85$ %. In order to obtain useful proton polarizations in thermal equilibrium one would need magnetic fields greater than 10 T and temperatures below 20 mK. As these conditions are hard to achieve technically and as in some cases it would even need months to reach thermal equilibrium at these conditions, these so called *brute force* targets are not widely spread for experimental use.
A commonly used technique in solid state targets is the dynamic nuclear polarization (DNP) which shall shortly be described here. For a more detailed depiction of DNP and its description via various models (e.g. resolved solid state effect, equal spin temperature (EST) theory) see for example [Goe02] and references therein.
Through the application of microwaves with a frequency close to the electron Larmor frequency ω_e the high electron polarization can be transferred to the nucleus. Due to dipole-dipole interaction of the electron spin with the spin of the nucleus it is possible to stimulate the *forbidden* transition with a simultaneous spin-flip of the electron and the nucleus. The electron flips then back again as its relaxation time τ_e is much shorter than the nuclear relaxation time τ_N. Thus, many nuclear spins can be flipped by a single electron.
The relative orientation of the nuclei can be chosen via the frequency of the microwave field (ω_{mw}). With $\omega_{mw} = \omega_e \mp \omega_N$[9] the polarization of the nuclei can be orientated parallel (antiparallel) to the electron polarization.
Paramagnetic centers as donators of free electrons have to be brought into the diamagnetic target materials. This can either be achieved with the help of chemical methods or

[9] ω_N denotes the Larmor frequency of the nucleus

by irradiation with charged particles. The butanol target which was used for the polarized measurement on the proton was doped with porphyrexide, whereas ^{6}LiD for the neutron measurement was exposed to 20 MeV electrons at the Bonn preaccelerator [Goe95].

2.3.2 Technical realisation

The ^{3}He/^{4}He dilution refrigerator

As described in the previous section, the DNP process requires a large magnetic field (2.5 T) and low temperatures (300 mK). For the experimental check of the GDH sum rule the angular acceptance for the detection of outgoing particles should be nearly 4π in the laboratory frame. To fulfill these requirements a horizontal ^{3}He/^{4}He dilution refrigerator is used, where the cryogenic components which are mounted in the backward direction just cover an angular range of $6\% \cdot 4\pi$. A schematic sketch of the dilution refrigerator is given in Figure 2.19.

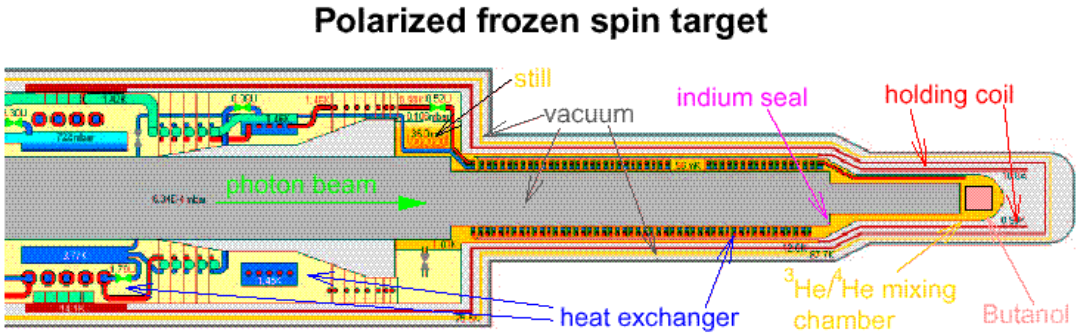

Figure 2.19: Schematic sketch of the dilution refrigerator.

Polarization

The polarization is performed at 300 mK and 2.5 T with an external magnet. The homogenity of the magnetic field is better than $\Delta B/B < 10^{-4}$ over the whole target region in order to uniformly polarize the target sample.
Microwaves for the DNP are provided by a carcinotron and are conducted to the target probe via an oversized rectangular waveguide and a stainless-steel tube. The frequency of the microwaves ≈ 70 GHz (the Larmor frequency of the electron at 2.5 T) has to be tunable by several hundred MHz ($w_p = 106$ MHz at 2.5 T) in order to obtain the selected direction of the nuclear polarization.
After reaching the desired polarization value the magnetic field is transferred to the internal holding coil and the temperature is lowered to ≈ 70 mK. In this *frozen spin* mode the protons have a relaxation time of 200 hours at a field of 0.4 T. The internal superconducting holding coil has a thickness of 780 μm [Bra99] [Roh03] which enables scattered particles to pass through without excessive energy loss.

Polarization measurement

The polarization of the target material is a crucial quantity as its value directly effects the magnitude of helicity dependent cross sections. For its measurement the continuous wave nuclear magnetic resonance NMR is used [Rei95]. The target material is surrounded by a coil which is part of a RF circuit driven at the Larmor frequency of the nucleus. The area under an absorption curve detected with a series Q-Meter is directly proportional to the target polarization. For calibration the area A_{TE} is determined in thermal equilibrium (TE), at a known temperature T and magnetic field B of the target, without application of microwaves. These TE measurements are typically performed in the ^{4}He mode of the cryostat at temperatures of ≈ 1 K. The polarization P_{TE} is then given by equation 2.11. The polarization P_{dyn} after the DNP process (and also in *frozen spin* mode) is related to the measured area under the absorption curve A_{dyn} via

$$P_{dyn} = \frac{A_{dyn}}{A_{TE}} P_{TE} \tag{2.12}$$

The polarization is measured at the beginning of the data taking period (at the end of the polarization period) and at the end of the data taking period before repolarization. In between, an exponential decay is assumed, where the relaxation time is calculated from the start and end values (Figure 2.20).
The homogenity of the internal holding coil allows an online NMR measurement of the polarization during data taking. However, this feature was not available for the GDH measurements at ELSA as probably electromagnetic radiation from the synchrotron disturbed the NMR measurement [Roh03].
To suppress systematic effects the direction of the nuclear polarization was reversed from time to time by tuning the microwaves at the DNP process to the corresponding frequencies. To eliminate further sources of *false asymmetries* the field direction of the polarizing magnet and the internal holding coil was once changed for a systematic study (see Section 4.1).

2.3.3 Target materials

The target materials used in double polarization experiments with real photons should meet the following requirements in order to minimize the measuring time and to suppress systematic uncertainties:

- They should easily be polarizable (short polarization buildup times) with long relaxation times and large maximum polarization values.
- The dilution factor $f_d = \frac{\#\ of\ polarized\ nucleons}{\#\ of\ all\ nucleons}$ should be large.
- Besides the interesting nuclei (here: p and D) all other nuclei in the material should be unpolarizable (spin 0).
- The polarization should not be destroyed by the photon beam.
- The target material should be easy to handle at extreme low temperatures.
- The target density should be sufficiently high.

Butanol

In principle molecular hydrogen would be the ideal proton target but as it reaches a para-state at low temperatures it is unpolarizable. Butanol (C_4H_9OH) was used for the GDH measurements on the proton. It has a dilution factor $10/74 \approx 0.135$ and the residual nuclei carbon and oxygen are spinless. The radiation damage is negligible at a tagged photon beam of $5 \cdot 10^5 \gamma/s$ [Bra99]. The paramagnetic centers, necessary for the DNP process were provided by 0.5 wt% porphyrexide dissolved in 5 wt% water. The target material was frozen into spherical beads of 2 mm size obtained by shock freezing in liquid nitrogen. This procedure guarantees a homogenous distribution of the paramagnetic centers. The butanol beads were placed in a PTFE-container with a length $l = (28.77 \pm 0.25)$ mm and a diameter of 2 cm. The filling factor f_f denotes the fraction of the container volume $V_{container}$ which is occupied by the butanol beads (with a total volume $V_{butanol}$).

$$f_f = \frac{V_{butanol}}{V_{container}} \tag{2.13}$$

As this quantity is not constant over the target volume (in the middle the beads are packed more dense than at the boundaries of the container), extensive studies [Roh03] have been performed including simulation calculations and counting experiments with glass beads. The filling factor in the target region which is hit by the photon beam has been determined to $f_f = (64.4 \pm 1.2)$ % [Roh03].
For the target preparation 1 part porphyrexide is dissolved in 10 parts water which are then mixed with 200 parts butanol in order to obtain a sufficient number of paramagnetic centers. For the determination of the dilution factor it has to be taken into account that also the protons in the water and the porphyrexide can be polarized. The dilution factor is therefore given by

$$f_d \;=\; 0.947868 \cdot \frac{10}{M_{but}} + 0.047393 \cdot \frac{2}{M_{H_2O}} + 0.004739 \cdot \frac{9}{M_{porph}} \;=\; 0.13344 \frac{mol}{g} \tag{2.14}$$

with M_x the molar mass of the ingredients x (x = butanol, H_2O, porphyrexide).
The target density F_t which gives the number of polarized nucleons per area is defined by

$$F_t \;=\; \rho \cdot l \cdot N_A \cdot f_d \cdot f_f \tag{2.15}$$

With $\rho = (0.94 \pm 0.01) g/cm^3$ the density of butanol at low temperatures [Rob90] and N_A the Avogadro constant. All other quantities have already been defined above and thus the target density amounts to

$$F_t \;=\; (1.3996 \pm 0.032) \cdot 10^{23} cm^{-2} \tag{2.16}$$

The obtained relaxation times with the butanol target ranged from 20 to more than 100 hours with a maximum polarization of about 80 %. In Figure 2.20 two examples for time sequences of the target polarization are given. Fig. 2.20 a) shows an example where the relaxation time amounts to 100 hours and the polarization direction has been changed several times in order to study systematic effects. At a later beamtime in 2001 (Fig.2.20 b)) a daily repolarization was necessary as the relaxation times were just about 20 hours due to *high* temperatures in the cryostat.

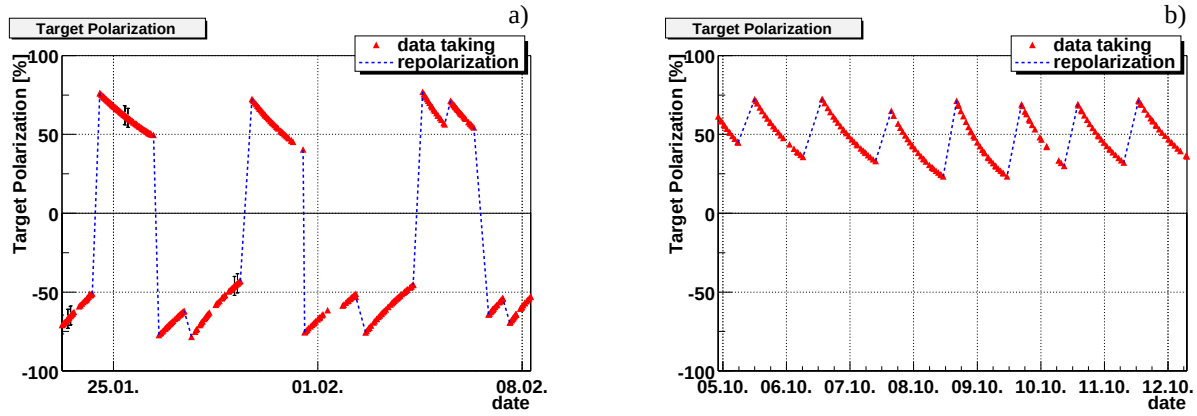

Figure 2.20: Target polarization as a function of time for 2 beamtimes in 2001. a) Relaxation times $\approx$ 100 hours; reversal of polarization direction. b) Relaxation times $\approx$ 20 hours.

Lithium-deuteride

Recent studies [Bue99] [Goe95] have shown that ^{6}LiD is an attractive polarized deuteron target material owing to its large dilution factor $f_d \approx 0.5$. ^{6}Li can be approximated in a very simple model as an (unpolarizable) α-core plus a neutron-proton pair.
The paramagnetic centers were produced by irradiating the target material with 20 MeV electrons of the Bonn preaccelerator at a temperature between 180 and 190 K. To produce the required density of paramagnetic impurities of 10^{19} spins per cm^3 an electron dose of 10^{17} e$^-$/cm^2 has been applied [Goe95].
The nucleons (p and n) are bound in nuclei (D and ^{6}Li) and their polarizations (P_p and P_n) are different from the nuclear polarizations (P_N) which are measured with the NMR method. The fraction $x^{p,n}$ to which the nucleons are aligned in the nucleus ($P_{p,n} = x^{p,n} P_N$) can be obtained from theoretical calculations.
For the isosinglets D and ^{6}Li the magnetic moment μ and the angular momentum I can be written in terms of the spin $S_z^{(p,n)}$ and orbital $L_z^{(p,n)}$ components as [Ron99]:

$$\mu = g_s^p < S_z^{(p)} > + g_s^n < S_z^{(n)} > + g_l^p < L_z^{(p)} > \tag{2.17}$$

$$I = < S_z^{(p)} > + < S_z^{(n)} > + < L_z^{(p)} > + < L_z^{(n)} > \tag{2.18}$$

where $g_s^{p(n)}/2 = \mu_{p(n)} = 2.793$ (-1.91) are the g-factors of the free nucleons. With $g_l = 1$ and using isospin symmetry, these equations can be solved for the spin component

$$< S_z^{(p)} > = < S_z^{(n)} > = \frac{\mu - I/2}{0.76} \tag{2.19}$$

After inserting the experimental values for μ, the spin and orbital components can be extracted (see Table 2.3). The polarization of the unpaired nucleons (p or n) in D or ^{6}Li is the fraction of the nuclear polarization ($x^{p,n}$) shown in column 3 of Table 2.3.
The above calculation is model independent and will be compared to model dependent results. The principle will be shown for deuterium and results of similar calculations will be given for ^{6}Li and ^{7}Li.
Deuterium has $I^\pi = 1^+$ so only even components of the orbital angular momentum are allowed. The relative S- and D-state probabilities are 95% and 5%, respectively. In

Nuclide	Magnetic moment $[\mu_N]$	Spin component	Orbital component (x 1/2)
D	0.857	0.94	0.03
^6Li	0.822	0.847	0.077

Table 2.3: Nucleon polarizations in D and ^{6}Li [Ron99].

[Ron99] an average value of several calculations is given for the D-state probability to be $\omega_D = 0.0490 \pm 0.0104$. In the relative S-state the proton and neutron spins are aligned parallel to add up their spins to $I = 1$. In the D-state with orbital angular momentum $L = 2$ the nucleon spins are antiparallel to the deuteron spin 50% of the time which will be calculated now.
Under the influence of a magnetic field the deuteron splits into a triplet

$$|I, M> = \ |1,1>,\ |1,0>,\ |1,-1> \tag{2.20}$$

With the Clebsch-Gordon (CG) coefficients and the notation CG$|m_L, m_S; M>$ the $M = \pm 1$ substates of the D-state are given by [Ron99]

$$\begin{aligned} &\sqrt{\tfrac{3}{5}}|2,-1;1> \quad + \quad \sqrt{\tfrac{3}{10}}|1,0;1> \quad + \quad \sqrt{\tfrac{1}{10}}|0,1;1> \\ &\sqrt{\tfrac{3}{5}}|-2,1;-1> \quad + \quad \sqrt{\tfrac{3}{10}}|-1,0;-1> \quad + \quad \sqrt{\tfrac{1}{10}}|0,-1;-1> \end{aligned} \tag{2.21}$$

By looking at the relative sign between m_S and M one sees that the nucleons in the deuteron D-state are antiparallel to the deuteron spin 3/5 of the time and parallel 1/10 (first and third terms). The nucleon polarization $x_D^{p,n}$ of the D-state is given by

$$x_D^{p,n} \ = \ \frac{N_D^{\uparrow\uparrow}}{N_D} \ - \ \frac{N_D^{\uparrow\downarrow}}{N_D} \ = \ \frac{1}{10} \ - \ \frac{3}{5} \ = \ -\frac{1}{2} \tag{2.22}$$

With the absolute S- and D-state numbers $N_S = \omega_S N$ and $N_D = \omega_D N$ and $N = N_S + N_D$, the effective nucleon polarization in the deuterium denotes

$$\begin{aligned} x_{^2H}^{p,n} \ &= \ \omega_S x_S^{p,n} \ + \ \omega_D x_D^{p,n} \ &= \ \tfrac{1}{N}\left(N_S - \tfrac{1}{2}N_D\right) \\ &= \ 1 \ - \ 1.5\ \omega_D \ &= \ 0.926 \pm 0.016 \end{aligned} \tag{2.23}$$

where $\omega_D = 0.0490 \pm 0.0104$ has been used from Ref. [Ron99]. The effective nucleon polarization is therefore reduced to $\approx 93\%$ of the deuteron polarization, in agreement with the model independent approach. The model dependency of the present calculation enters through the D-state probability.
For ^{6}Li the situation is more complex as now also P- and P'- states can be occupied. The effective three body problem[10] has been treated in a Faddeev approach for various αN and NN potentials by [Sch93]. The results for the occupation probabilities of the orbital angular momentum states have been summarized in [Ron99] to give a nucleon polarization for the *free* nucleons of

$$x_{^6Li}^{p,n} \ = \ 0.866 \pm 0.012 \tag{2.24}$$

[10] ^{6}Li can be approximated as $\alpha \ + \ p \ + \ n$

	a	x^p	x^n	α^p	α^n		$M\ [g/mol]$
^{6}Li	0.9535	0.866	0.866	1	1	^{6}LiD	8.0292
^{7}Li	0.0465	0.58	-0.03	1	2	^{7}LiD	9.0301
D	0.997	0.926	0.926	1	1	^{6}LiH	7.0229
H	0.003	1	0	1	0	^{7}LiH	8.0238

Table 2.4: Constants used in Equations 2.26 and 2.27.

The lithium used for the GDH experiment consists of 95.35% ^{6}Li and 4.65% ^{7}Li [Roh03]. Therefore, also the nucleon polarization in ^{7}Li has to be taken into account. ^{7}Li can be approximated as an *alpha triton* pair [Wal85] or as a neutron pair plus proton plus alpha. The results of the relative proton and neutron polarization from [Pud97] and [Ron99] agree very well with each other so that for the following analysis the mean values of both authors will be used[11]

$$x^p_{^7Li} = 0.58 \qquad x^n_{^7Li} = -0.03 \tag{2.25}$$

The occurance of ^{7}Li breaks the symmetry between the relative proton and neutron polarizations. For an exact treatment of the target material one also has to take into account the 0.3 % hydrogen in the deuterium. Therefore, the target consists of ^{6}LiD, ^{7}LiD, ^{6}LiH and ^{7}LiH which all have different dilution factors f_d. It is useful to separate f_d from the target density F_T (Equation 2.15) and to define effective polarizations P_{eff} instead [Roh03]. These effective polarizations now include the dilution factors and they have slightly different values for the proton and the neutron due to the presence of ^{7}Li.
Neutron:

$$\begin{aligned} P^n_{eff} = \quad & a_{^6Li} a_D M^{-1}_{^6LiD} && (\alpha^n_{^6Li} x^n_{^6Li} P_{^6Li} + \alpha^n_D x^n_{^2H} P_D) \\ + \quad & a_{^7Li} a_D M^{-1}_{^7LiD} && (\alpha^n_{^7Li} x^n_{^7Li} P_{^7Li} + \alpha^n_D x^n_{^2H} P_D) \\ + \quad & a_{^6Li} a_H M^{-1}_{^6LiH} && (\alpha^n_{^6Li} x^n_{^6Li} P_{^6Li} + \alpha^n_H x^n_H P_H) \\ + \quad & a_{^7Li} a_H M^{-1}_{^7LiH} && (\alpha^n_{^7Li} x^n_{^7Li} P_{^7Li} + \alpha^n_H x^n_H P_H) \end{aligned} \tag{2.26}$$

Proton:

$$\begin{aligned} P^p_{eff} = \quad & a_{^6Li} a_D M^{-1}_{^6LiD} && (\alpha^p_{^6Li} x^p_{^6Li} P_{^6Li} + \alpha^p_D x^p_{^2H} P_D) \\ + \quad & a_{^7Li} a_D M^{-1}_{^7LiD} && (\alpha^p_{^7Li} x^p_{^7Li} P_{^7Li} + \alpha^p_D x^p_{^2H} P_D) \\ + \quad & a_{^6Li} a_H M^{-1}_{^6LiH} && (\alpha^p_{^6Li} x^p_{^6Li} P_{^6Li} + \alpha^p_H x^p_H P_H) \\ + \quad & a_{^7Li} a_H M^{-1}_{^7LiH} && (\alpha^p_{^7Li} x^p_{^7Li} P_{^7Li} + \alpha^p_H x^p_H P_H) \end{aligned} \tag{2.27}$$

with a being the fraction of the corresponding isotope, $x^{p,n}$ the probability for the nucleon spin to be parallel to the nucleus and P the polarization of the corresponding nucleus. The dilution factor is given by the quotient of the polarizable nucleons in the nucleus $\alpha^{p,n}$ and the molar mass M. The used constants are summarized in Table 2.4.
To calculate $P^{p,n}_{eff}$ the polarizations of all nuclei involved have to be known. For practical purposes it is sufficient to measure the polarization of one nucleus, for example the deuteron. As already mentioned the dynamical nuclear polarization can be explained via the equal spin temperature (EST) concept. In this model it is assumed that all involved nuclei share one common spin temperature T_s. The polarization of one isotope is measured, and the spin temperature is calculated with the Brillouin function (Equation 2.10). The polarizations of all other nuclei can then also be calculated with this function by replacing the temperature

[11] the slightly different value $x^p_{^7Li} = 0.63$ quoted in [Bue99] comes from the usage of the model independent value for $x^p_{^3H}$ of the triton which deviates by 8% from the model dependent values used by the other authors.

T with the spin temperature T_s.
For spin 1 (deuteron and ^{6}Li) and spin 3/2 (^{7}Li) nuclei the Brillouin function simplifies to

$$P_1 = \frac{4 \tanh\left(\frac{g\mu_N B}{2k_B T}\right)}{3 + \tanh^2\left(\frac{g\mu_N}{2k_B T}\right)} \tag{2.28}$$

$$P_{3/2} = \frac{1}{3}\frac{\tanh^3\left(\frac{g\mu_N B}{2k_B T}\right) + 5 \tanh\left(\frac{g\mu_N B}{2k_B T}\right)}{1 + \tanh^2\left(\frac{g\mu_N B}{2k_B T}\right)} \tag{2.29}$$

where g denotes the g-factor and $\mu_N = 3.152 \cdot 10^{-14}$ MeV/T is the nuclear magneton.
The validity of the EST concept has been confirmed experimentally for ^{6}LiD targets [Bue99] and very recently [Bal03]. For this purpose, the polarizations of the deuterons, ^{6}Li and ^{7}Li have been measured explicitly. The results are in agreement with the calculated values from the EST theory.
Figure 2.21 a) shows the polarizations of ^{6}Li and ^{7}Li with respect to the deuteron polarization

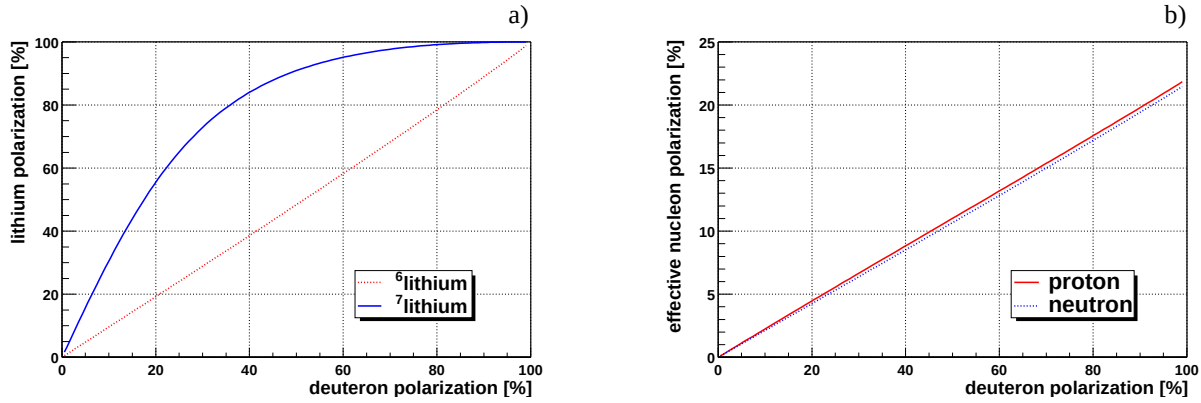

Figure 2.21: a) ^{6}Li and ^{7}Li polarizations versus the deuteron polarization. b) Effective neutron and proton polarizations as a function of the measured deuteron polarization.

as calculated from Equations 2.28 and 2.29. The following g-factors are used: for the deuteron: $g_D = 0.856438$, for ^{6}Li: $g_{^6Li} = 0.822051$ and for ^{7}Li: $g_{^7Li} = 2.170961$. In Figure 2.21 b) the effective neutron and proton polarizations according to Eqs. 2.26 and 2.27 are plotted against the deuteron polarization.
The target density (F_t') is now defined as (without the dilution factor f_D)

$$F_t' = \rho \cdot l \cdot N_A \cdot f_f \tag{2.30}$$

With the length of the target $l = (25.90 \pm 0.25)$ mm, the density for lithium deuteride of $\rho = 0.820\ g/cm^3$, and the filling factor $f_f = (54.5 \pm 1.6)\%$ [Roh03], F_t' results in

$$F_t' = (6.970 \pm 0.24) \cdot 10^{23} cm^{-2} \tag{2.31}$$

2.4 The detector

In this section the concept (Section 2.4.1) and the technical realisation (Section 2.4.2) of the GDH detector will be described. The main features are a high detection efficiency and

an almost complete angular acceptance with an effective suppression of electromagnetic background events (Section 2.4.3).

2.4.1 The concept

For the experimental check of the GDH sum rule, total photoabsorption cross sections have to be measured. In the photon energy range relevant for ELSA (680 MeV $\leq E_\gamma \leq$ 3 GeV) several multiple-particle final-states are open. Smaller systematic errors are expected when the total photoabsorption cross section is not determined by identifying and summing up all partial reaction channels, but by an inclusive measurement of all hadronic processes. The principle is to detect at least one product of a photohadronic reaction. The detector system was designed [Hel93] [Nag95] to cover almost the complete angular range (99.6% of 4π) with a high detection efficiency. It was not intended to allow the identification of partial reaction channels, however within a limited kinematical range the single η-meson production can be identified ([Mic01] [God02] and Section 5.1.2).

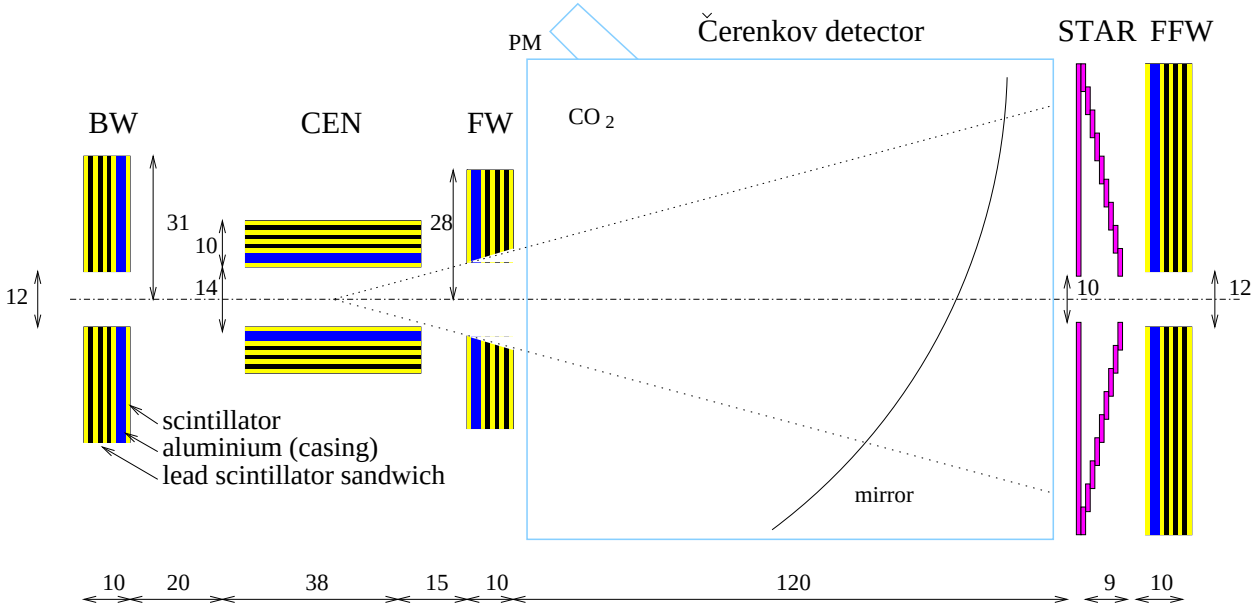

Figure 2.22: Schematic side view of the detector system, all numbers are given in cm.

Secondly, the detector design aims at the effective suppression of electromagnetic background events. The cross section of pair production in the Coulomb field of the nuclei is two orders of magnitude larger than the interesting photohadronic cross section, Compton scattering off atomic orbital electrons is still one order of magnitude larger. As these electromagnetic processes are independent of the target polarization their contribution would in principle cancel in the difference of the helicity dependent cross sections which enters the integrand of the GDH sum rule. But the magnitude of these background processes would cause large systematic uncertainties. An effective suppression is possible as the angular distribution of the electromagnetic processes deviates significantly from the hadronic events. Due to the Lorentz boost the distribution of electromagnetic events is not isotropically, but peaked in the forward direction ($\vartheta < 15°$). This angular range is covered by a threshold Čerenkov detector (Section 2.4.3) to detect electromagnetic processes. A hit in this detector initiates

a veto-signal in the trigger electronics and the event is not recorded. For pair production it is sufficient to identify the lepton with the smaller angle. This triggers a veto-signal which prevents the other lepton from misidentification as a hadron.

The modular design of the detector system can be seen in Figure 2.22. It consists of the central and forward parts (Section 2.4.2) for the detection of hadronic events and the Čerenkov detector for the suppression of electromagnetic background. In order to identify all hadronic events, charged particles have to be detected as well as photons coming from the decay of neutral mesons (e.g. $\pi^0 \rightarrow \gamma\gamma$). One module consists of a scintillator plate (called *trigger plate*) for the detection of charged particles and a lead-scintillator sandwich where the pho-

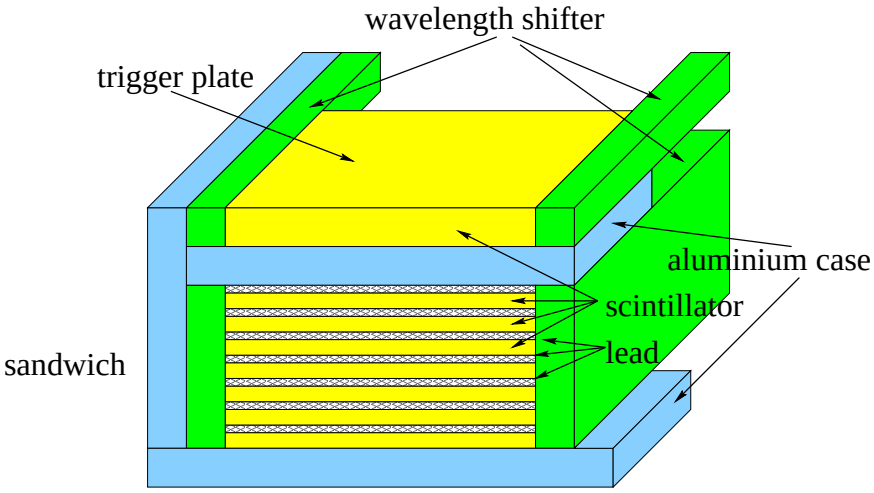

Figure 2.23: Sketch of a detector module to detect charged particles and decay photons.

tons produce an electromagnetic shower which generates a signal in the scintillator layers. Figure 2.23 shows such a CAD-module[12]. In the trigger plate charged particles (p, π^+, π^-, ...) are registered with an efficiency of almost 100%. The trigger plates consist of 10 mm plastic scintillator, with exception of the FFW part where 20 mm plastic scintillator have been used. The number of layers for the sandwich part has been optimized via simulation calculations [Hel97]. 10 layers of plastic scintillator, each with a thickness of 5 mm, are mounted between the 2.5 mm thick lead layers, so that a total of 2.5 cm lead is available for conversion of the photons into an electromagnetic shower. The efficiency for detecting a photon with an energy of 50 MeV is 88 % [Hel02]. A process like $\pi^0 \rightarrow \gamma\gamma$ can be registered with a probability of more than 98 % since the two decay photons can be detected independently.
The light produced in the trigger plate and the sandwich part is read out separately via wavelength shifters, which are mounted at the lateral faces and coupled optically to the photomultipliers. The light which is absorbed in the wavelength shifter is reemitted isotropically with a longer wavelength so that it cannot be reabsorbed by the scintillator material. To guarantee light transport via total reflexion, a small gap between the scintillator and the wavelength shifter exists. The photomultipliers are coupled via a small air gap (for the trigger plate) or via a fishtail light guide (for the sandwich part) to the wavelength shifter. In order to monitor and to adjust the amplification of all photomultiplier tubes to the same value, light emitting diodes (LEDs) are placed in front of the photo cathodes [Mic01].

[12] Charged particle And Decay photon counter

	BW	CEN	FW	STP	FFW
dimensions [cm^2]	62 x 62	28 x 38	56 x 56	112 x 112	108 x 108
dist. to target [cm]	39	7	34	164	174
hole diameter [cm]	12	-	18 - 24	10	12
ϑ acceptance [°]	155 - 174	20 - 160	15 - 20	1.5 - 15	1.5 - 15
ϕ acceptance [°]	0 - 360	0 - 360	0 - 360	0 - 360	0 - 360

Table 2.5: Dimensions and angular acceptances of the detector modules.

2.4.2 The hadron detectors

The central part of the detector system consists of the backward detector (BW), 4 central detectors (CEN1..CEN4) and the forward detector (FW), see Fig. 2.22. All modules consist of a trigger plate and a lead scintillator sandwich as described in the previous section. The backward wall has a hole in the center for the target cryostat. The wavelength shifters are read out via photomultipliers on both ends. The 4 central parts cover the target in the azimuth angle completely. Due to geometrical reasons the wavelength shifters are read out just on one side. The forward wall has a conical hole with $\vartheta = 15°$ as the following Čerenkov counter covers this angular range for the detection of the electromagnetic background events. Behind the Čerenkov counter further detector modules cover the remaining angular range. These consist of the STAR trigger plate (STP), the STAR rings and the far-forward detector (FFW). With exception of the STAR rings (see separate paragraph) all wavelength shifters of the forward modules are read out on both sides, and they all have a hole for the passage of the primary beam.
All dimensions of the various modules and the angles of coverage are listed in Table 2.5.

The STAR-detector

The STAR[13]- detector [Fuc94] [Sau96] consists of a 1 cm thick scintillator plate (called STAR Trigger Plate *STP*) and a hodoscope of 9 concentric plastic scintillator rings. The trigger plate is read out via two wavelength shifters, each coupled to two photomultipliers. The hodoscope is made of 18 scintillator half rings with a thickness of 1 cm, which are read out via lightguides and photomultipliers on one side. The cutting angles of the rings and the angle between the lightguide and a ring segment have been optimized by Monte Carlo simulations.
Figure 2.24 gives a front view of the STAR-detector. The rings have a certain overlap and cover the range $\vartheta = 2.8°$ to $\vartheta = 16.5°$. Two STAR-segments forming one ring are shown in Figure 2.25. The parameters of the rings are given in Table 2.6. The detector was designed to allow an extrapolation of the measured cross sections to $\vartheta \to 0$. Results will be shown in Section 4.3. Furthermore, the segmentation allows the identification of partial reaction channels via the missing mass method within a limited kinematical range ([Mic01] [God02] and Section 5.1.2).

[13] Scintillators from Tübingen for Angle Reconstruction

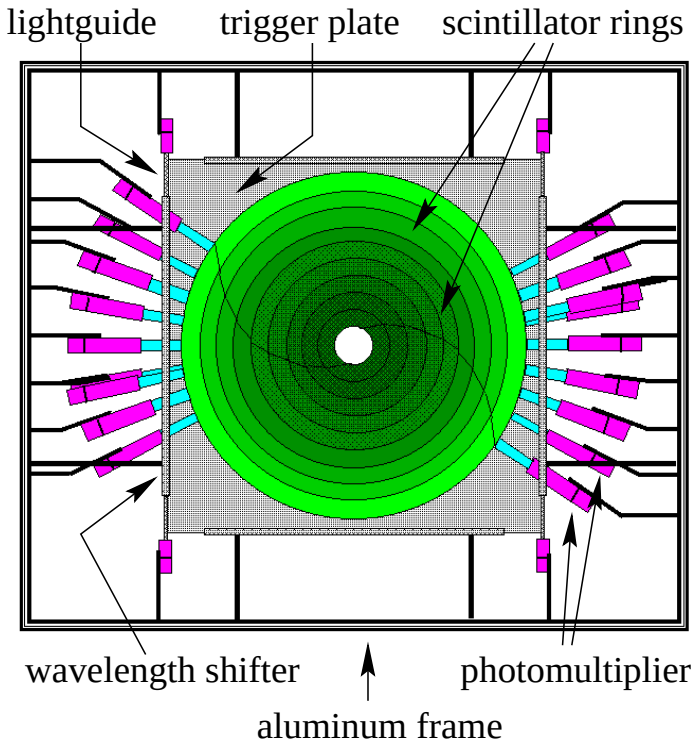

Figure 2.24: Front view of the STAR-detector.

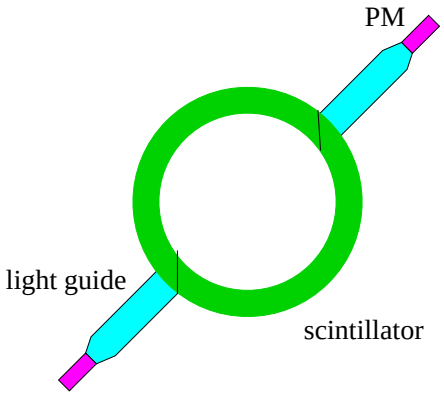

Figure 2.25: Two STAR segments forming one ring.

2.4.3 The Čerenkov-detector

The task of the Čerenkov-detector is to give a veto signal if an electromagnetic background process has occurred in the target region. In this case at least one fast electron or positron is emitted in forward direction under a small angle ($\vartheta < 15°$). This angular range is covered by the gas Čerenkov counter built by the university of Gent.

Čerenkov-light is emitted if a charged particle moves faster through a medium than the speed of light in this medium, i.e. $v > c/n$ with n the index of refraction. The opening angle α of the lightcone is given by $\cos\alpha = c/(v \cdot n)$.

Ring	r_{in} [mm]	r_{out} [mm]	$\vartheta_{min}[°]$	$\vartheta_{max}[°]$	$\vartheta_{mean}[°]$
1	459	519	15.5	17.5	16.5
2	411	471	13.9	15.8	14.9
3	362	422	12.2	14.2	13.2
4	313	373	10.5	12.5	11.5
5	263	323	8.82	10.8	9.85
6	212	272	7.10	9.11	8.08
7	160	220	5.33	7.33	6.36
8	108	168	3.61	5.56	4.58
9	55	115	1.83	3.78	2.81

Table 2.6: The radii and angular ranges of the individual STAR-rings.

With

$$\beta \;=\; \frac{v}{c} \quad \text{and} \quad \gamma \;=\; \frac{1}{\sqrt{1 \;-\; \beta^2}} \tag{2.32}$$

it follows for the threshold of the Lorentz factor γ_{thr}

$$\gamma_{thr} \;=\; \frac{n}{\sqrt{n^2 \;-\; 1}} \tag{2.33}$$

If $\gamma > \gamma_{thr}$ Čerenkov radiation is emitted. For the purpose of the present experiment the index of refraction n, i.e. the medium, has to be chosen in such a way that the lightest charged hadrons are always below the Čerenkov threshold. For our experimental conditions these are the charged pions with $m_{\pi^\pm} = 139.57$ MeV/c^2 and a maximum possible energy $E_{max} = 3000$ MeV. The corresponding $\gamma_{\pi^\pm}$ reads

$$\gamma_{\pi^\pm} \;=\; \frac{E_{max}}{m_{\pi^\pm} c^2} \;=\; 21.5 \tag{2.34}$$

which results in the condition for the index of refraction n

$$n \;\leq\; \frac{\gamma_{\pi^\pm}}{\sqrt{\gamma_{\pi^\pm}^2 - 1}} \;=\; 1.0011 \tag{2.35}$$

Besides n, other properties of the gas have to be considered: It should be easy to handle, inflammable, intoxic, the chosen n should be achieved at normal pressure and it should not be too expensive. Furthermore, it should not scintillate, as scintillation light could also be produced by hadrons which must not trigger a veto-signal. For the present experiment CO_2 was chosen with an index of refraction $n = 1.000382$ at normal pressure and room temperature. The threshold energy $E_{e,thr}$ for electrons to produce Čerenkov light in this gas is

$$E_{e,thr} = m_e c^2 \; \frac{n}{\sqrt{n^2 \;-\; 1}} \;=\; 18.5 \text{ MeV} \tag{2.36}$$

Electrons or positrons above this energy cause a signal in the Čerenkov detector. Electromagnetic background events below this threshold cannot be rejected by the Čerenkov detector. These events can, however, be identified through their entries in the timing spectra (Section 3.3.1). Furthermore, due to their low energy they cause entries at small values in the QDC[14] spectra of the detectors. An effective suppression of these background events is therefore possible by applying cuts in the pulseheight spectra (Section 3.3.2).

A side view of the Čerenkov detector can be seen in Fig. 2.22. It has a cubical shape with a volume of (1.2 m)^3. The gas volume is enclosed in a light tight aluminum casing where the entrance and exit windows consist of a thin foil. The Čerenkov light is focused via an ellipsoidal mirror onto a 5 inch photomultiplier tube. The mirror, made out of perspex with an aluminum layer, has a hole with a diameter of 5 cm for the passage of the photon beam. This hole is covered by a highly reflecting Mylar-foil to avoid the loss of Čerenkov light. More technical details can be found e.g. in [Lan00].

The efficiency of the Čerenkov detector has been determined with 1.2 GeV electrons to $(99.990 \pm 0.003)\%$ [Hel02].

[14] Charge to digital converter

2.5 The electronics

The complete electronics of the GDH-experiment is separated into two independent parts, the *Møller-electronics* and the *experiment-electronics*. The *Møller-electronics* for the determination of the electron polarization is not described here, details can be found in [Kie99] [Spe02].
The *experiment-electronics* is divided into the following parts:

- The tagger electronics (Section 2.5.1) which forms coincidences of two adjacent tag counters to define 64 energy channels out of the 65 counters. An OR (the TAG-OR) of the 64 channels goes into the *experimental trigger*.
- The detector electronics (Section 2.5.2), where an OR of all detector modules is generated (the DET-OR) which enters the *experimental trigger*.
- The veto electronics (Section 2.5.3), which combines the signals of the active collimators, the Čerenkov-detector and the leadglass-counter into the VETO-OR, which is inverted before it reaches the *experimental trigger*.

The pulsed structure of the ELSA accelerator with an accumulation and an extraction phase requires a machine dependent trigger, the *extraction phase trigger* (Section 2.5.5).

2.5.1 The tagger electronics

The signals of the 65 tagging counters are transported via RG213-cables from the experimental hall to the counting room. Low frequency noise is filtered with a 22 nF capacitor which is discharged via a grounded resistor (see Figure 2.26). The signal is then passively split into two branches. One branch leads directly to VME[15]-QDCs[16] to measure the respective charge.
The other branch is connected to constant fraction (CF) discriminators[17] which generate logic NIM-pulses[18] out of the incoming analog signals. The CF-discriminators strongly suppress timewalk effects, which are reduced further by the fact that the incoming pulseheights just vary in a small range (the electrons are minimum ionizing and pass always more or less the same amount of scintillator material).
The discriminators have two output channels with pulse lengths of 10 ns and 40 ns, respectively. A coincidence is then formed with the short pulse of discriminator i and the long pulse of discriminator $i+1$. This coincidence defines one energy channel and will in the following be called a *tag-channel*. The signals are connected to scalers to measure the photon flux, and to the STOP-input of VME-TDCs[19] [20].

[15] Versa Module Europe
[16] CAEN VN1465S
[17] CAEN N415
[18] Nuclear Instrument Module
[19] Time to digital converter
[20] CAEN VN1488

Next an OR of the 64 tag-channels (the TAG-OR) is generated which produces the QDC-gate and the TDC-start through the *major trigger* (MT). More details about the tagger electronics can be found in [Nau01] and [Wei02].

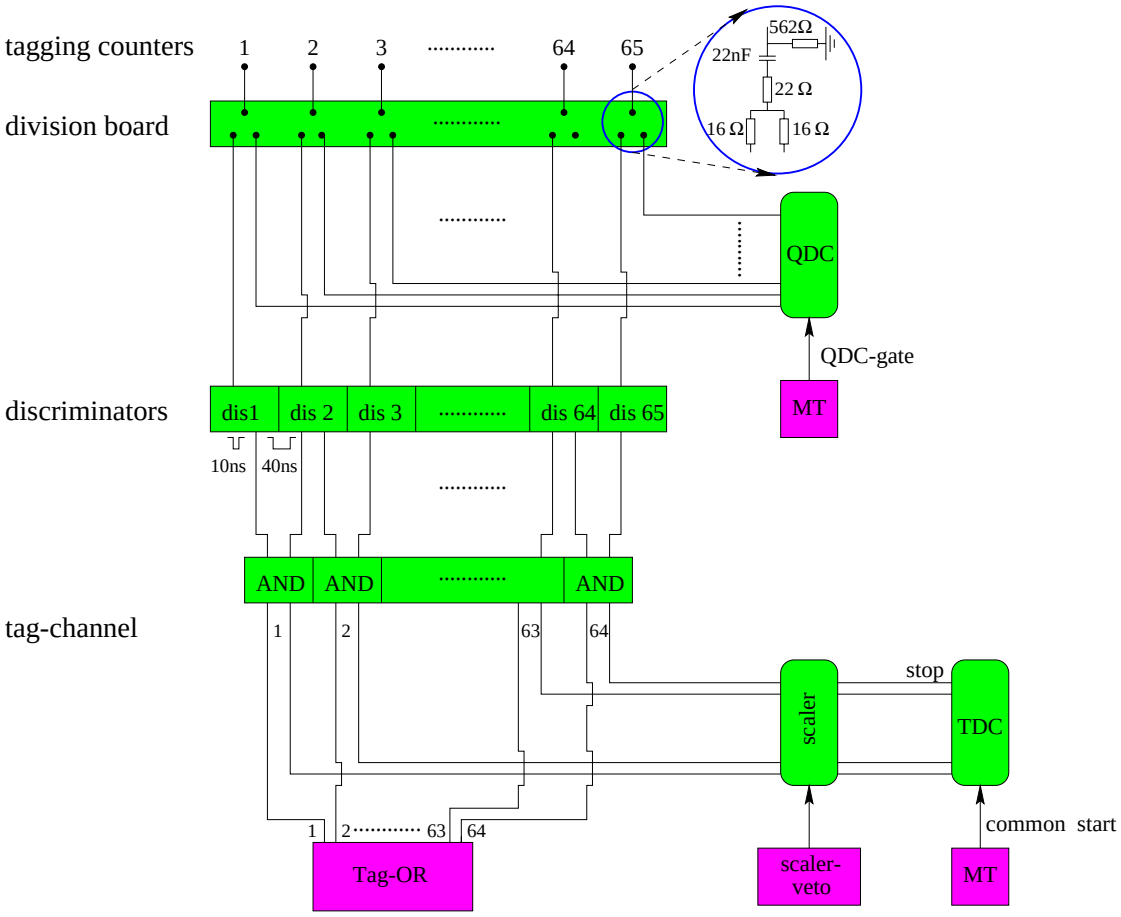

Figure 2.26: The tagger electronics.

2.5.2 The detector electronics

Similar to the tagger electronics each signal from the hadron detectors (BW_T, BW_S, ..., FFW_S) is divided into a QDC- and TDC-branch after the low frequency noise is filtered with a 22 nF capacitor. The division board has the same components as the one displayed in Figure 2.26.
One output of the division board is connected to VME-QDCs (see Figure 2.27) for measuring the accumulated charge of the detector signals. The other output enters leading edge discriminators which generate a NIM-pulse if the input signal is larger than a threshold value. The time the NIM-pulse is generated depends on the pulseheight of the incoming signal. This *timewalk* effect can be corrected in the data analysis (Section 3.1.2) if the TDC and QDC information is available. One output channel of the discriminator is connected via a second discriminator, reshaping the signal after a second delay line, to the STOP-input of VME-TDCs.
The other output channel is connected to coincidence units called *majority coincidences*.

These modules generate a pulse if a chosen number of incoming signals arrives at the same time at the input. These *majority coincidences* suppress the generation of an experimental trigger by the noise of the photomultiplier tubes. Separate coincidence units exist for the trigger plate and the sandwich part of all detector modules. With exception of the FW-detector, for all modules the maximum possible multiplicity is required (4/4 for BW_T, BW_S, STP, FFW_T, FFW_S and 2/2 for the central parts CEN_T 1-4 and CEN_S 1-4). As the FW-detector has a large conical hole, part of the scintillation light may not be seen by all four photomultiplier tubes so that for the FW_T and FW_S detectors only three out of four tubes have to fire to generate an output-signal of the majority coincidence. This guarantees an optimum detection efficiency without any loss of events.

Because the STAR-rings do not cover an angular range which is not already covered by

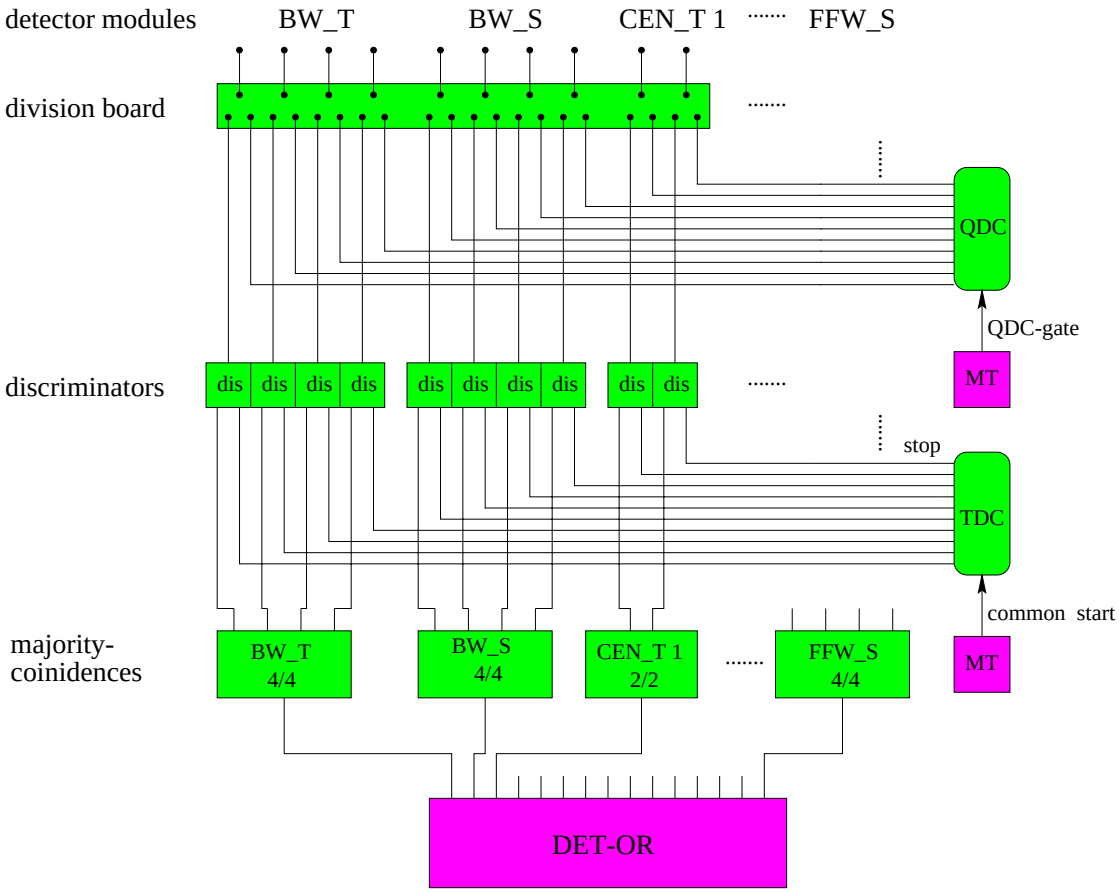

Figure 2.27: The detector electronics.

any other detector module, and as they cannot detect different particles than the STP, their signals are not connected to the trigger logic. The corresponding TDCs and QDCs are running freely which is sufficient for the extrapolation of the cross sections to $\vartheta \to 0$ and the determination of partial reaction channels. The delay lines of the STAR-rings have been adjusted relative to the other detector modules.

The 15 output channels of the majority coincidences are connected to another coincidence module where an OR is generated. This unit gives an output signal if at least one of the detector modules possesses the required multiplicity. This DET-OR is one part of the *experimental trigger*.

2.5.3 The veto electronics

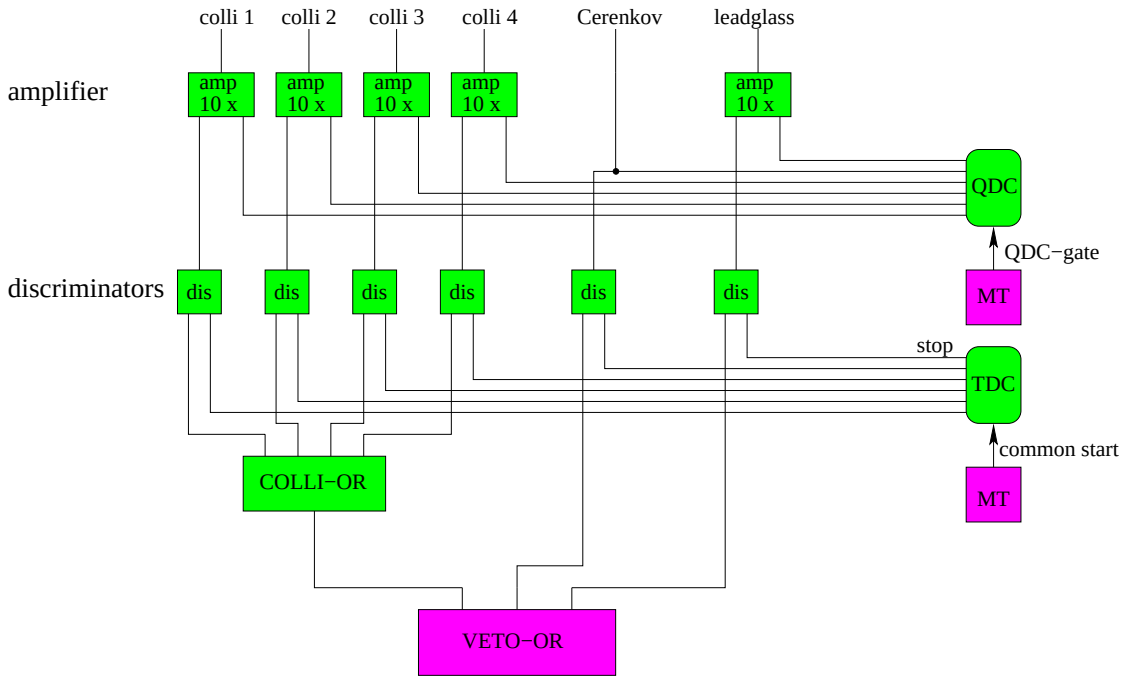

Figure 2.28: The veto electronics.

The veto electronics (Figure 2.28) forms an OR of the 3 veto detectors: the active collimators, the Čerenkov-detector and the leadglass-detector. If one of the veto detector fires the event must be rejected. The three veto detectors have the following functions:

- *Active collimators*: If a photon looses energy during the interaction with the collimator material and still produces a hadronic event in the target region, its energy cannot be assigned to the tag channel that fired. Since the GDH detector does not determine the incoming photon energy from the outgoing hadrons, these events have to be rejected.
- *Čerenkov-detector*: In case of an electromagnetic interaction of a photon in the target region, a fast electron or positron is emitted under forward directions which causes a signal in the Čerenkov-detector. This detector therefore suppresses electromagnetic background events.
- *Leadglass detector*: If a photon still reaches the leadglass detector it cannot have been absorbed in the target region. Events with a simultaneous signal in the tagging system, the GDH-detector and the leadglass-detector originate from a random coincidence with an untagged photon. Rejection of the leadglass events causes a reduction of this random background.

The signals of the 4 active-collimator tubes and the leadglass-detector are amplified in the counting room by a factor 10. The use of amplifiers allows the photomultiplier tubes to be operated with a relative low high voltage. Especially for high rates (several MHz for the tubes of the active collimators) the use of a lower operating voltage is preferable. The rate of the Čerenkov counter is much lower so it can be operated with a higher voltage to give a

similar gain as the tubes of the active collimators and the leadglass-detector in combination with the amplifiers. Owing to the high rates the signals of the veto detectors are not filtered with a capacitor as not enough time for charging and discharging would be available.
One exit channel of the amplifiers (or one part of the split signal in case of the Čerenkov counter) is connected to VME-QDCs. The other signals are fed to leading edge discriminators. One output signal of this discriminator is used for time measurements with VME-TDCs. The other signals form the VETO-OR, where first a COLLI-OR is generated from the 4 active-collimator modules. After inversion, the VETO-OR is also one part of the experimental trigger (see next Section).
Furthermore, the VETO-OR can be used to measure the deadtime produced by the veto detectors (see Section 3.4.2 for more details and the correction to this deadtime).

2.5.4 Experimental and major triggers

A valid event is characterized by a coincident hit in the tagger and the GDH-detector with no hit in the veto counters. The coincidence of these three signals forms the *experimental*

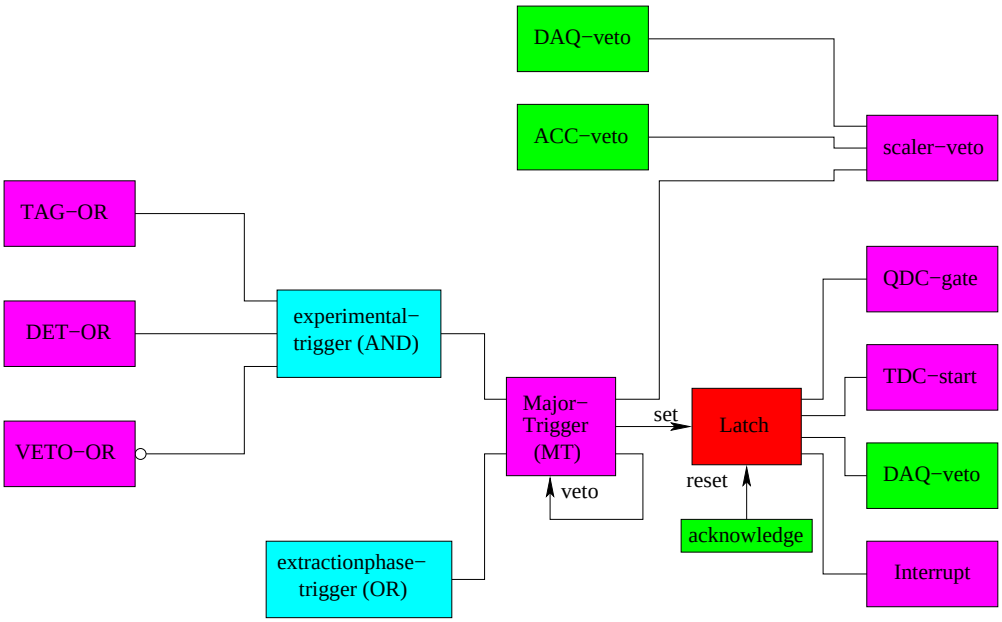

Figure 2.29: The trigger electronics.

trigger (see Figure 2.29). The delay lines are adjusted in such a way that the 13 ns wide signal of the tagger generates the timing. The tagging signal is embedded in the inverted colli- and leadglass signals with a width of 30 ns each. The Čerenkov veto has a length of 120 ns to reject random electromagnetic background and is therefore longer than the DET-OR with 100 ns. An illustration of these signals is given in Figure 2.30.
The experimental trigger causes a major trigger (MT) which sets the latch register. This generates the TDC start, opens the QDC gate and after some delay generates an interrupt to initiate the readout of all modules. After a normal event the QDCs, TDCs and an I/O register are readout, the information of the scalers is only extracted every 100 events. The use of the latch register guarantees that no further triggers are accepted during the readout

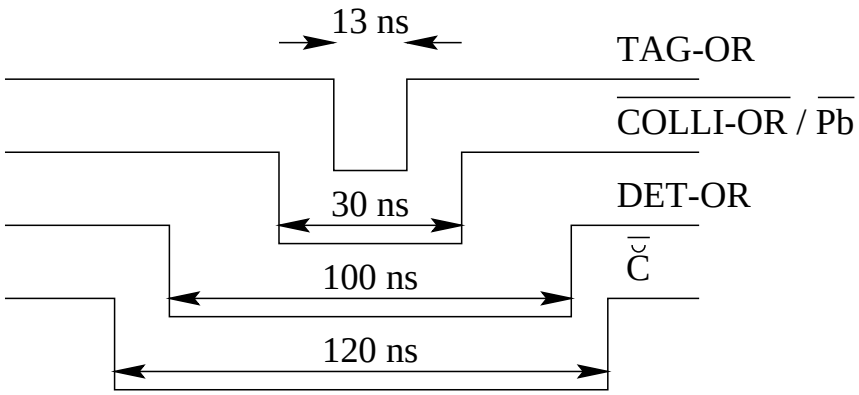

Figure 2.30: Sketch of the signals entering the major trigger coincidence.

process. In order to not produce further triggers during the latch register is set, the major trigger module is *vetoed* by its own signal. The scalers are inhibited by the scaler-veto which is formed from the DAQ-veto together with the accumulation veto (ACC-veto) (Section 2.5.5). The DAQ-veto prevents the scalers from counting during the data acquisition process, and the ACC-veto is set during the accumulation phase of the accelerator when no beam is extracted to the experiment (see also Fig. 2.31).
When the readout of all modules is completed, the data acquisition system (Section 2.5.7) generates an acknowledge signal which resets the latch register to accept the next major trigger.
The major trigger can either be initiated by the experimental trigger or by the extraction-phase trigger (see next section). Depending on the component that generated the major trigger, different bits of an I/O register[21] are set.

2.5.5 Machine dependent electronics

The extraction phase trigger

The electron accelerator ELSA has alternative phases of accumulation where the stretcher ring is filled, and of extraction where the beam is extracted to the experiment. As previously mentioned, the scalers are read out only every 100 events. For experiments with polarized electrons the polarization direction can change between two extraction phases. At the end of an extraction phase a readout of the scaler modules is required to not mix phases with different polarization directions. As the data acquisition might be busy at the end of an extraction phase the wiring displayed in Figure 2.31 has to *memorize* the extraction phase trigger.
In absence of a DAQ-veto an extraction phase trigger is generated directly at the end of an extraction phase. If the data acquisition is busy at that time, a latch register is set. After completion of the readout of all modules the acknowledge signal resets the latch register which produces via its inverted output channel an extraction phase trigger. A major trigger is generated and also the readout of the scalers is initiated.
The extraction start also generates a trigger, however this requires no special treatment as

[21] CAEN V513

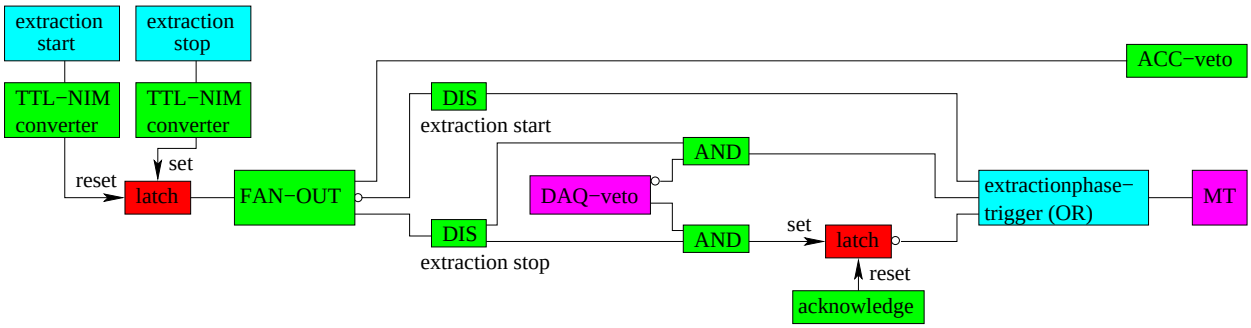

Figure 2.31: The extractionphase trigger electronics.

the data acquisition cannot be busy at that time.
During the accumulation phase of the accelerator the scalers are inhibited by the accumulation veto (ACC-veto) which is formed through the FAN-OUT.

The polarization signal

The polarization direction of the electrons is determined by the sign of the high voltage applied at the Pockels cell (Section 2.1.1). The information-signal passes a TTL-NIM converter and a discriminator before a certain bit of the I/O register is set. With this information the helicity of the photons can be assigned to every event.
At the beginning and the end of an extraction phase, also specific bits of the I/O register are set. It is possible to check if the polarization direction of the electrons has changed during one extraction phase which normally should not happen. The sign of the electron polarization is usually fixed at the end of the accumulation phase to make sure that the data acquisition at the end of the extraction phase is finished.

The HF-electronics

Electrons from ELSA are coming in bunches with an interval of 2 ns between the bunches and a width of 50 ps. This structure originates from the acceleration with a 500 MHz field. The information of the HF generator can be used to improve the starting times of the TDCs.

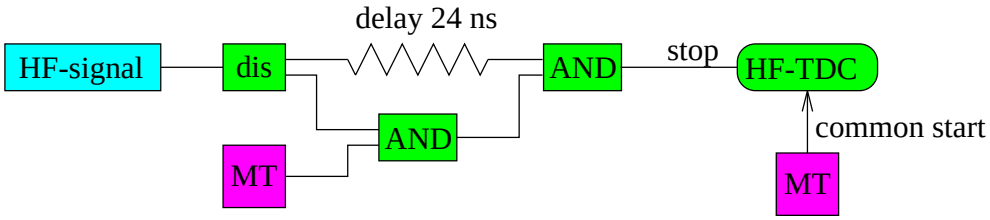

Figure 2.32: The HF-electronics.

The 500 MHz signal passes a discriminator and is then scaled down by 1:15 before it reaches the electronics shown in Figure 2.32. The signal undergoes a two-fold coincidence with the major trigger before it stops the HF-TDC which has been started by the major trigger. The

two-fold coincidence is necessary to guarantee that the HF-TDC is stopped by the HF-signal and not by the major trigger.

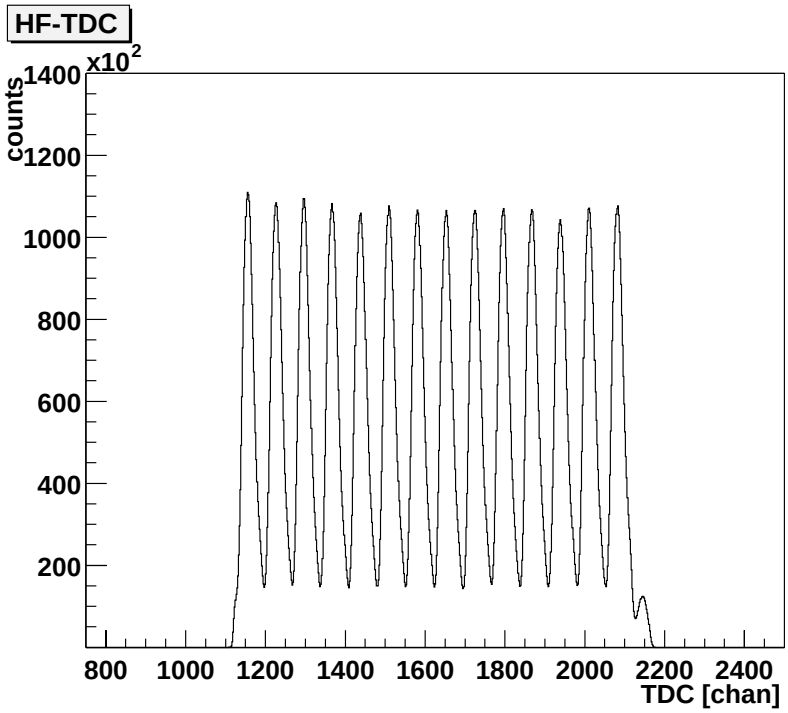

Figure 2.33: The raw HF-TDC spectrum

The start of the HF-TDC is directly correlated to the time when the photon is produced at the bremsstrahlung process. In the TDC spectrum 15 peaks appear with a distance of 2 ns (Fig. 2.33). The OR of 64 tag channels determine the start of all TDCs. Their limited time resolution causes broader peaks in the HF-TDC spectrum than the 50 ps expected from the electron bunches. With the knowledge of the difference to the next HF peak it is possible to shift the start to the middle of an electron bunch for a fine correction (cf. Section 3.1.3).

2.5.6 Time calibration

The 12 bit VME TDCs have a nominal value of 25 ps per channel. For calibration a time calibrator[22] is used which generates start and stop signals where the time between start and stop varies by a multiple of 10 ns in the range 10 ns to 160 ns. In the measured TDC spectrum *needle*-peaks appear with an interval of (real) 10 ns. From the measured distance between the peaks one gets a calibration factor for each TDC which is around 26 ps/chan (see also Section 3.1.1). Details about the electronics for the time calibration measurement can be found in [Wei02] and [Nau01].

[22] Ortec 462

2.5.7 Data Acquisition

The data acquisition has been performed with the program ACQU [Ann96] which consists of two parts. The *frontend* part runs on a VME computer[23] under the operating system LynxOS. It is responsible for reading out the modules. A header is put to each event and the events are collected in a buffer. Full buffers are transmitted to the *workstation*[24]. Through a code on this *workstation* a minimal set of histograms is filled for online monitoring and the data are written to hard disk. For storage and backup the data are written to Exabyte-tapes. Prior to the experiment, investigations have been performed with the VME-QDCs and TDCs [Wei96] [Wei97]. These modules have been integrated together with other new modules like the I/O register into the *frontend* part of ACQU [Nau01] [Wei02].
Zero-suppression is applied for the TDCs and QDCs, i.e. the TDCs that have no entry are not digitized. All QDCs are digitized but only the non-zero entries are written to the buffer. With this technique one event has a size of about 100 byte. The QDCs and TDCs are read out for each event, however, the scalers can be read out after a selected number of events (here 100 was chosen). With a tag-rate of 1 MHz a trigger rate of approximately 700 Hz was obtained while the deadtime of the data acquisition system remained at a level of about 15% [Nau01].

[23] CES RIO 8062, processor: PowerPC 604r, 300 MHz
[24] An ordinary PC with a 400 MHz Pentium II processor

Chapter 3

Data analysis

The present chapter describes the necessary steps in the data analysis to obtain physical results, i.e. cross sections and missing mass spectra, from the raw experimental data.

The offline analysis of the experimental data is performed with the version 3v3 of ACQU [Ann96] which has also been used for data acquisition. The program consists of a system part and a user part. In the system part data are unpacked, events are accumulated and histograms are filled. The user part allows the definition of functions for the specific analysis via so called *user defined spectra* (UDS). Furthermore, parameter files with calibration constants for each beamtime period can be read.
The unpolarized pilot experiment has been performed with a similar detector setup so that some of the existing UDSs [Sau98] have been reused. The main task of this work was the development of routines to analyze polarized data and an improvement of the analysis method.

3.1 Calibrations and corrections

General calibrations (Section 3.1.1) include the time calibration of the TDCs and the pedestal subtraction of the QDCs. The corresponding calibration constants are determined for every beamtime period separately as their values can change.
Electronics effects have an influence on the raw experimental data. Knowledge about the behaviour of these effects allows the application of corrections to increase the quality of the data. Corrections to the TDC start and stop will be given in Sections 3.1.2 and 3.1.3.

3.1.1 General calibrations

Time calibration

At the beginning and/or the end of each beamtime period a *time calibration run* (Section 2.5.6) is performed. In each TDC 15 *needle*-peaks appear as shown in Figure 3.1 a). The distance between two peaks corresponds exactly to 10 ns. To obtain the time calibration constants the peak positions are determined via fit. In Figure 3.1 b) the actual time in ns

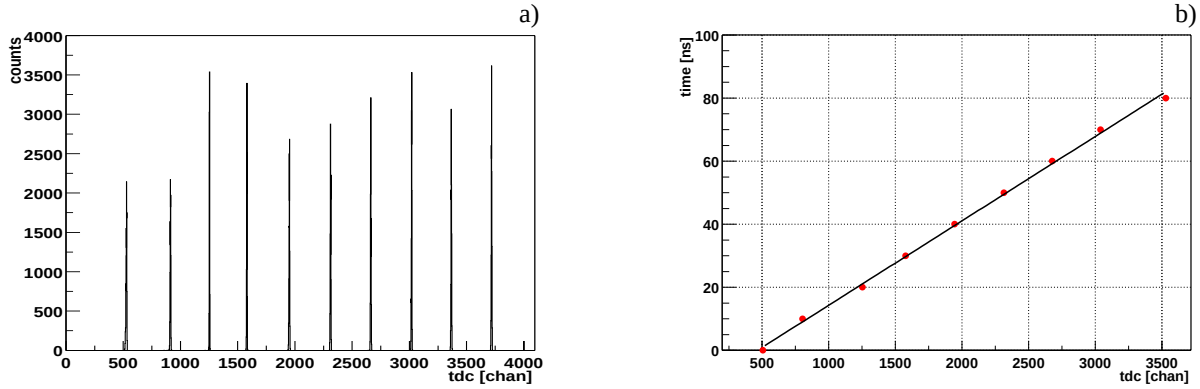

Figure 3.1: a) TDC spectrum of a time calibration run where the distance between the peaks corresponds to 10 ns. b) time [ns] versus the measured positions [chan], the slope gives the timecalibration factor.

is plotted versus the measured peak positions in channels. The slope of a fitted straight line gives the the timecalibration factor f_{tc} in ps/chan. Typical values are $\approx$ 26 ps/chan. As for the further analysis no absolute time information is required, a relative calibration is sufficient to obtain the time calibrated values TDC_{tc} from the measured TDC information TDC_{meas}[1]

$$TDC_{tc}[chan] \;=\; \frac{f_{tc}[ps/chan]}{25ps/chan} \;\cdot\; TDC_{meas}[chan] \tag{3.1}$$

In the TDC spectra which are generated after this time calibration, one channel in the spectrum corresponds exactly to 25 ps.

Pedestal subtraction

The QDCs measure the charge of the incoming photomultiplier signals during the time the QDC-gate is open. During this time a constant offset value, the *pedestal*, is registered by all QDC modules even if the corresponding detector component is not hit by a particle. This pedestal can be caused by noise picked up by the signal cables or by an internal offset of the QDC modules. The QDC value of the pedestal peak is subtracted in the analysis as it represents an effective charge of zero Coulomb. *Pedestal runs* have been performed during each beamtime period. For these runs the major trigger is initiated by a clock so that mainly the pedestal values are registered in the QDCs. The same conditions as during ordinary data taking are guaranteed by a running accelerator without the extraction of an electron beam to the experiment.
The pedestal peaks exhibit two different shapes depending on the frequency of the noise that causes the pedestal. The DC-part of the arriving tagger- and detector signals is filtered via a capacitor. The remaining high frequency noise causes a Gaussian like pedestal peak (Fig. 3.2 a)). A saddle like structure (Fig. 3.2 b)) is generated by low frequency noise. This structure can be explained under the assumption of a sinusoidal shape of the noise signal. If the width of the QDC-gate is smaller than the period of the noise signal, the probability to

[1] In the analysis just the raw TDC values TDC_{meas} are treated as *integers*, all other corrected informations, so also TDC_{tc}, are treated as *doubles*.

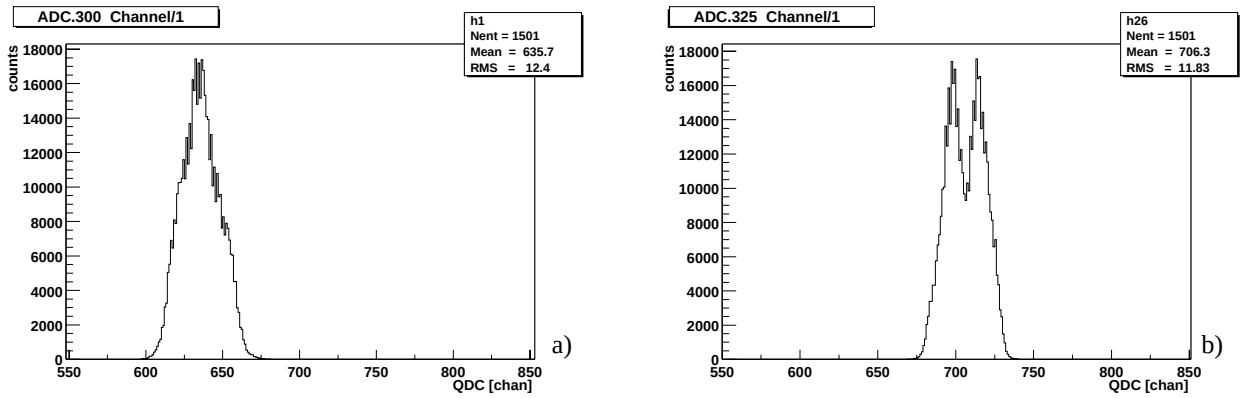

Figure 3.2: Pedestal peaks for a) high b) low frequency noise.

be inside the gate is larger at the maximum and minimum values of the noise than at the zero crossing. The interesting value of zero Coulomb is therefore right in the middle of the two peaks of the saddle structure.
The occurrence of both peak shapes shows that the low frequency noise could not be filtered completely for all detector modules.

3.1.2 Correction to the TDC stop

The only electronics effect which has an influence on the TDC stop is the timewalk effect.

Timewalk correction

The TDC branch of the detector and veto signals is connected to leading edge discriminators. These generate a NIM pulse if the incoming signal is larger than an adjustable threshold. The time at which the NIM pulse is created depends on the pulseheight of the incoming signals. This *timewalk* effect is illustrated in Figure 3.3, where pulses A and B arrive at the same time at the discriminator but have different pulseheights. Pulse B passes the threshold at a later time and therefore also the outgoing pulse is generated at a later time.
With the knowledge of the corresponding QDC value the timewalk effect can be corrected. As normally the threshold is much lower than shown in Fig. 3.3, the assumption of a quadratic rise of the photomultiplier signals is valid. This leads to the following correction formula

$$TDC_{corr}^{walk} \;=\; TDC_{TC} \;-\; \frac{c_{walk}}{\sqrt{QDC}} \tag{3.2}$$

The constant c_{walk} is determined by plotting the TDC information versus $1/\sqrt{QDC}$, where QDC means the pedestal subtracted value. The slope of a fitted straight line gives c_{walk}.
Figure 3.4 shows the influence of the walk correction. In the left part the QDC is plotted versus the raw TDC of the Čerenkov detector. For small QDC values, the discriminator threshold is passed at a later time producing the curvature. The lines left and right to the prompt peak (middle of the spectrum) are generated by the pulse structure of the ELSA accelerator. After application of the walk correction according to Eq. 3.2, the curvature disappears, and straight vertical lines with a distance of 2 ns show up (Fig. 3.4 b)).

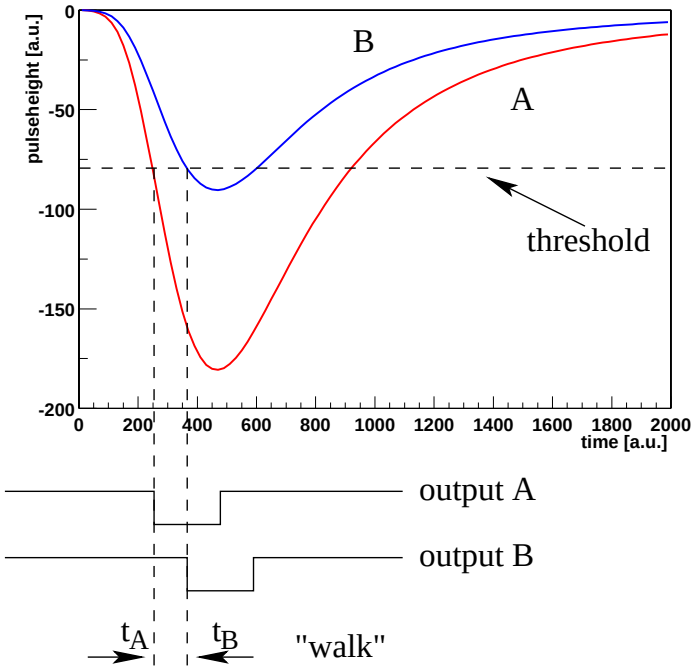

Figure 3.3: Illustration of the walk effect.

3.1.3 Corrections to the TDC start

The delay lines are adjusted in such a way that usually the tagging system is responsible for the timing, i.e. the TAG-OR initiates the TDC start. This case can be forced in the trigger logic by setting the input channels for DET-OR and $\overline{\text{VETO-OR}}$ to logic '1'[2].
The TDCs of the tagger are stopped, after passing delay lines, by their own signal. As the time between the start and the stop just depends on the length of the delay lines, a sharp peak appears in each TAG-TDC spectrum. This is the so-called *self-stop-peak* (SSP).
Even in the simplest case when the tagger initiates the TDC start one has to correct for **cable shifts** and one has to take into account **multiple hits**. For the real **data taking trigger** also the cases when the detector or the veto counters initiate the TDC start, have to be treated. Finally, the **HF correction** can be used to shift the TDC start to the middle of an electron bunch.

Cable shifts

For the 64 tag channels the flight paths of the electrons are different, they have varying lengths of the delay lines and the processing times of the electronics modules differ. This causes the TDC start time to be dependent on the tag channel.
This effect can be visualized by plotting the (walk corrected) TDC of a detector for each tag channel separately. To be independent from different time of flights, a detector is used which only registers $\beta = 1$ particles. In the present case the Čerenkov detector has been used as it has a better time resolution than the leadglass detector.

[2]This trigger setup is used to determine the tagging efficiency (Section 3.6.1).

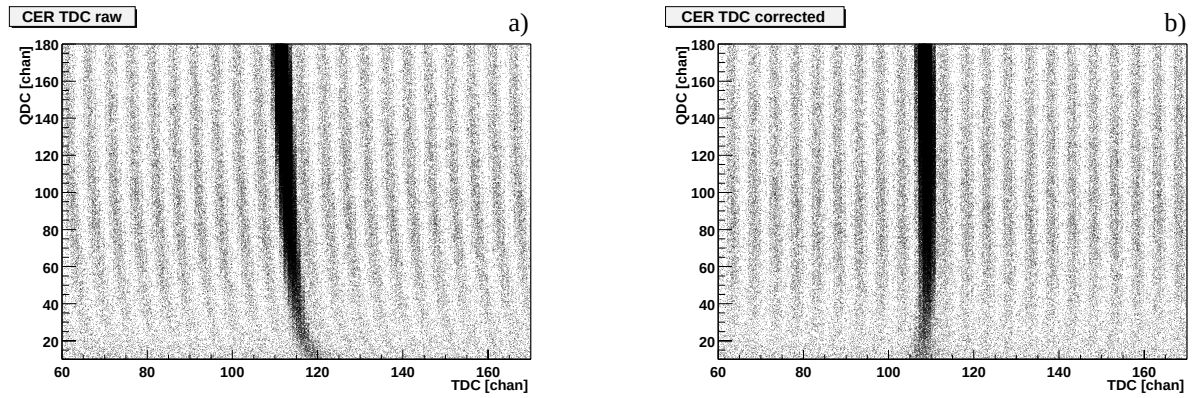

Figure 3.4: Influence of the walk correction. QDC versus TDC for a) the raw and b) the walk corrected Čerenkov-TDC.

Due to the different start times, the positions of the prompt peak slightly vary in the CER-TDC spectra for each tag channel. To correct for this effect all spectra are shifted relative to the spectrum for a reference tag channel. The shifts $cable^i_{cer}$ are obtained from

$$cable^i_{cer} \;=\; (\text{CER-TDC})^i \;-\; (\text{CER-TDC})^{63} \tag{3.3}$$

where $(\text{CER-TDC})^i$ is the prompt peak position of the Čerenkov-TDC for each each tag-channel i (obtained via fit) where i runs from 0 to 63. In the above equation tag channel 63 has been used as reference.

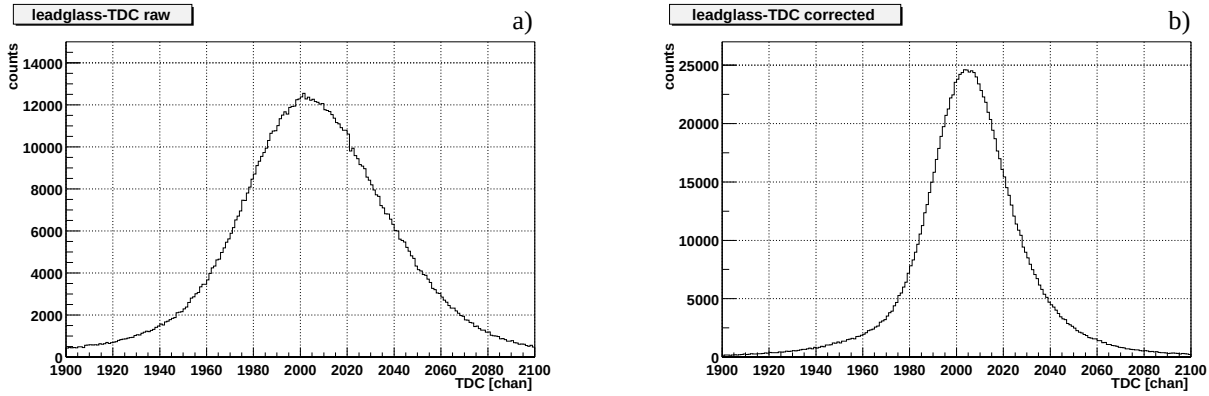

Figure 3.5: The leadglass TDC a) before and b) after the correction to the cable shifts.

The HF-TDC provides the most exact time information. This can be used for a fine correction of the cable shifts on top of the previous. After adding $cable^i_{cer}$, the same procedure as previously described is performed for the 15 peaks of the HF-TDC (Fig. 2.33). The difference of each peak to its corresponding peak of the reference channel is calculated, and finally the mean value of the 15 peaks gives the value of the additional constant $cable^i_{HF}$.

$$cable^i_{HF} \;=\; \frac{1}{15}\sum_{j=1,15} (\text{HF-TDC})^{i,j} \;-\; (\text{HF-TDC})^{63,j} \tag{3.4}$$

$(\text{HF-TDC})^{i,j}$ is the jth peak of the HF-TDC plotted for tag-channel i.
The use of $cable^i_{cer}$ prior to the fine correction with the HF-TDC is necessary as otherwise

shifts by multiples of 2 ns would be possible.
The final cable-shift correction value for tag-channel i ($i = 0$ ... 63) $cable^i_{final}$ is the sum of both values.

$$cable^i_{final} \;=\; cable^i_{cer} \;+\; cable^i_{HF} \tag{3.5}$$

The influence of the cable shift correction is displayed in Figure 3.5. The left part shows the raw TDC of the leadglass detector whereas in the right part the cable shifts $cable^i_{final}$ have been applied for each tag-channel i. Due to this correction the width of the prompt peak decreases from 33 to 22 channels (this corresponds to 0.825 ns and 0.55 ns, respectively)[3].

Multiple hits

If a single tag channel initiates the TDC start, an entry at the position of the SSP is generated in its TDC spectrum. Each tag channel has a certain geometrical overlap with its neighbour in order to prevent acceptance gaps. Geometrical double hits can occur where the entries in the TDC spectra of the two tag channels that fired are not exactly in their SSP but have a characteristic time interval in between.
The other kind are *real* multiple hits where either two electrons of a single electron bunch have undergone a bremsstrahlung process or where electrons from different bunches produced a bremsstrahlung photon each. In this latter case only one TAG-TDC is in its SSP the other has some time difference $(\text{tag-diff})^i$ to it.

$$(\text{tag-diff})^i \;=\; (\text{TAG-TDC})^i \;-\; (\text{TAG-SSP})^i \tag{3.6}$$

$(\text{TAG-TDC})^i$ denotes the TDC value of tag-channel i and $(\text{TAG-SSP})^i$ its corresponding self-stop-peak.
Adding $(\text{tag-diff})^i$ changes the timing in such a way that the start is effectively shifted to the tag channel that was not in its SSP.

Data taking trigger

For the real data taking the coincidence of TAG-OR $\wedge$ DET-OR $\wedge$ $\overline{\text{VETO-OR}}$ is required to generate a major trigger, i.e. the TDC start can be produced by

- The tagging system (TAG-OR)
- The detector (DET-OR)
- The veto counters (VETO-OR)

The delay lines are adjusted in such a way that usually the TAG-OR is responsible for the timing, i.e. the TAG-OR generates the TDC-start. For random coincidences it is however possible that the falling edge of the DET-OR or the inverted VETO-OR signal generates the start. The TDC of the detector- or veto-counter that arrives last to complete the coincidence

[3]The shown example is from a run in 1999. For later runs additional delay lines have been installed in the tagger electronics to minimize the influence of the cable shifts.

has a sharp peak (the SSP) in its TDC spectrum. The tag-TDCs in such a case are not in their SSPs. By adding $(\text{tag-diff})^i$ (Eq. 3.6) to the detector or veto TDC the timing is the same as if the tagger would have generated the TDC start.

HF-correction

The quality of the start can further be increased by using the information of the HF-TDC. If all corrections are applied to the HF-TDC, a spectrum like in Figure 3.6 is obtained. It is filled with peaks which have a distance of 2 ns coming from the 500 MHz HF structure of the ELSA accelerator. The additional peaks in comparison to the raw HF-TDC spectrum (Fig. 2.33) are generated by the correction according to equation 3.6. The peaks should have

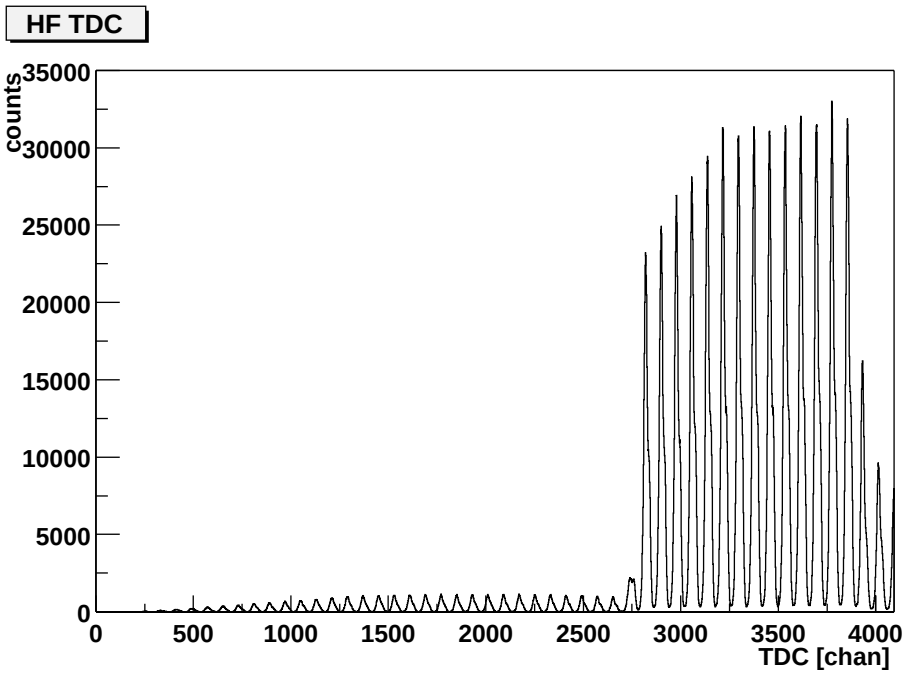

Figure 3.6: HF-TDC spectrum after the application of corrections.

a width of 50 ps, the width of a single electron bunch. The limited time resolution of the tagging system causes a width of 250 ps of the peaks, i.e. the uncertainty of the TDC start is 250 ps. With the HF-TDC spectrum the time resolution can be increased to 50 ps. In a first step the position of each peak is determined. In the analysis the difference of the actual HF-TDC value to the nearest peak $(\text{HF-peak})^j$ is calculated

$$(\text{HF-diff}) \;=\; (\text{HF-TDC}) \;-\; (\text{HF-peak})^j \tag{3.7}$$

By adding (HF-diff) to all TDC values the start is effectively shifted to the middle of an electron bunch. Application of this correction to the HF-TDC changes each peak of Fig. 3.6 to a *needle* peak with a width of one channel.

3.1.4 Application of the corrections

In the previous sections corrections affecting the start and stop of TDCs have been described. For practical reasons all corrections are applied to the stop of the detector- and veto-TDCs. If several tag channels i fired, the corrections are done for each channel i. The corrected TDC value of photomultiplier tube k reads:

$$(TDC)^{i,k} = TDC^k_{TC} - \frac{c^k_{walk}}{\sqrt{QDC^k}} - cable^i_{final} - (\text{tag-diff})^i - (\text{HF-diff}) \tag{3.8}$$

The quantity $(\text{tag-diff})^i$ is always subtracted. If the tag-TDC is in its SSP it is zero. If there was a multiple hit in the tagger or another detector initiated the start, the timing is corrected appropriately.

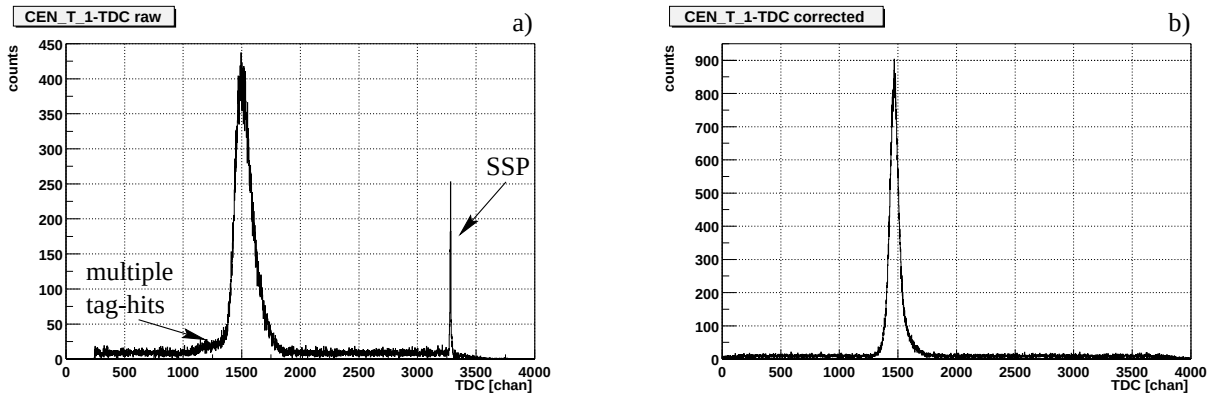

Figure 3.7: Detector TDC for one photomultiplier tube for a) the raw TDC and b) after all TDC corrections.

For the analysis the constants c^k_{walk} have to be determined for every photomultiplier tube k. The cable-shifts $cable^i_{final}$ are determined for each beamtime period separately as for example processing times might vary. It is possible that the tag-SSPs drift or jump during a single beamtime period. Therefore, their values are determined in a first analysis step for each run. A parameter file is generated for each run with these values. This file is then read in at the beginning of the next analysis step.
In Figure 3.7 the influence of the TDC corrections is displayed. The left part shows the raw TDC of one photomultiplier tube of a central detector module. The small plateau left to the prompt peak is generated by multiple hits in the tagging system. The sharp self stop peak at large TDC values is caused by events where this detector module generated the start at the major coincidence. After application of the described corrections the small plateau and the SSP vanish (Figure 3.7 right part).

3.2 Position independent information

Due to the structure of the detector modules the QDC and TDC information of a single photomultiplier tube depends on the position where the scintillator was hit. For the following analysis just one TDC and QDC information per module is required, which can be formed in such a way that it becomes position independent.

3.2.1 Mean TDC information

A position independent time information is obtained by taking the arithmetic mean of the TDCs of a detector module.

$$TDC_{mean} = \frac{1}{n}\sum_{i=1}^{n}(TDC)^i \tag{3.9}$$

where $n = 2$ for the 8 central modules (CEN_T 1..4, CEN_S 1..4) which are read out via two photomultiplier tubes, and $n = 4$ for all other modules[4].

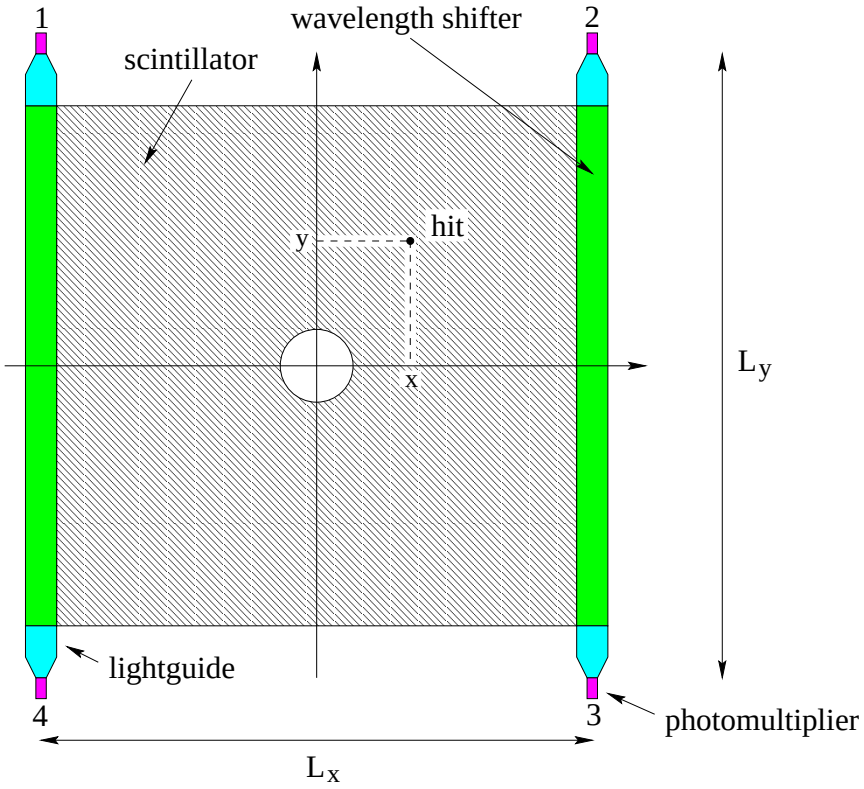

Figure 3.8: Detector module with a hit at position (x,y).

Figure 3.8 shows such a module which is read out via two wavelength shifters and four photomultipliers, e.g. the STAR-triggerplate. A hit at position (x,y) produces light which needs different times t_i to arrive at the photomultiplier tubes i, $i = 1, 2, 3, 4$. These times are given by the following equations.

$$\begin{aligned}
t_1 &= \tfrac{1}{c_x^{eff}}(\tfrac{L_x}{2} + x) + \tfrac{1}{c_y^{eff}}(\tfrac{L_y}{2} - y) \\
t_2 &= \tfrac{1}{c_x^{eff}}(\tfrac{L_x}{2} - x) + \tfrac{1}{c_y^{eff}}(\tfrac{L_y}{2} - y) \\
t_3 &= \tfrac{1}{c_x^{eff}}(\tfrac{L_x}{2} - x) + \tfrac{1}{c_y^{eff}}(\tfrac{L_y}{2} + y) \\
t_4 &= \tfrac{1}{c_x^{eff}}(\tfrac{L_x}{2} + x) + \tfrac{1}{c_y^{eff}}(\tfrac{L_y}{2} + y)
\end{aligned} \tag{3.10}$$

where $c_{x,y}^{eff}$ are the effective speeds of light in the module for the x- and y-direction. The arithmetic mean t_{mean} leads to a quantity which is independent of the position and just

[4]For FW_T and FW_S also $n = 3$ is possible (Section 2.5.2).

depends on constants of the detector module

$$t_{mean} = \frac{L_x}{c_x^{eff}} + \frac{L_y}{c_y^{eff}} \tag{3.11}$$

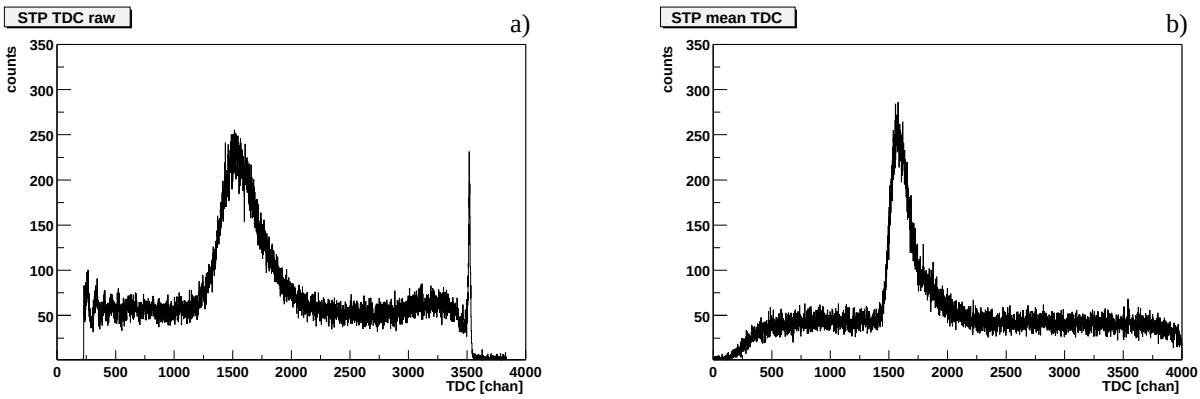

Figure 3.9: a) raw TDC signal of a single photomultiplier tube, b) mean TDC of the STP after the timing corrections according to eq. 3.8.

Figure 3.9 demonstrates the quality of a position independent TDC signal. In the left part the raw TDC spectrum of a single photomultiplier tube of the STAR-triggerplate is shown. In the right part the arithmetic mean of all 4 TDC values is displayed. This value is calculated after the application of all timing corrections according to equation 3.8. Compared to the single tube the prompt peak of the mean TDC spectrum is more narrow. In such a case the width of the prompt region for the TDC cuts (Section 3.3.1) can be decreased which improves the statistical quality.

3.2.2 Mean QDC information

The attenuation of light in the scintillators obeys an exponential law. Similar to the arithmetic mean for the time information, a position independent value for the QDC information can be defined by the geometric mean:

$$QDC_{mean} = \sqrt[n]{\prod_{i=1}^{n}(QDC)^i} \tag{3.12}$$

To demonstrate that this quantity is independent of the position a two dimensional example is regarded. Figure 3.10 shows for example one central detector module which is just read out via two photomultiplier tubes. A hit at position (x) produces an amount of light which corresponds to a certain QDC value (QDC_0). Due to the exponential attenuation in the scintillator the amount of light seen by the photomultiplier tubes with respect to the position (x) is given by

$$\begin{aligned} QDC_1 &= QDC_0 \cdot e^{\frac{L_x+x}{2}\frac{1}{X_0}} \\ QDC_2 &= QDC_0 \cdot e^{\frac{L_x-x}{2}\frac{1}{X_0}} \end{aligned} \tag{3.13}$$

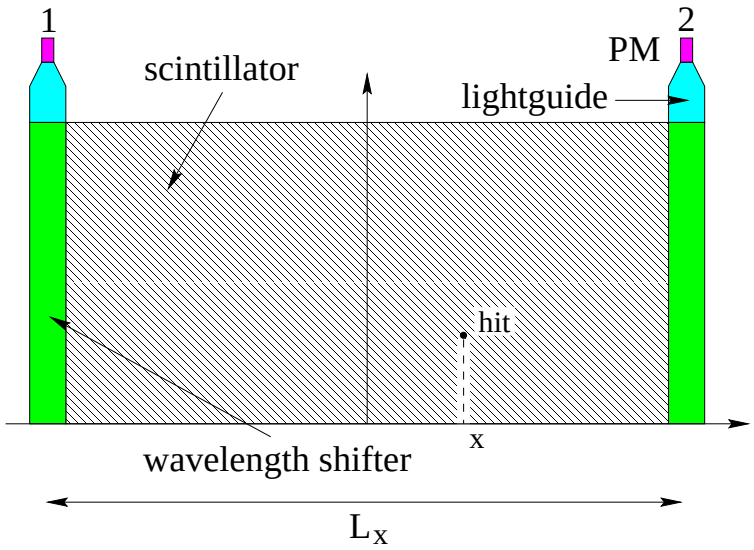

Figure 3.10: Detector module read out via two photomultiplier tubes with a hit at position x.

The geometric mean of these two values

$$QDC_{mean} = QDC_0 \sqrt{e^{\frac{L_x}{X_0}}} \tag{3.14}$$

just depends on constant values like the length L_x and and the attenuation length X_0 and is therefore independent on the position (x).

3.3 Cuts in the time and pulseheight spectra

A valid event is characterized by the absorption of a tagged photon in the target region. A photohadronic reaction leads to the production of a particle, e.g. a meson which is registered in the detector system. Additionally to these *desired* reactions, background exists which can come from reactions of untagged photons or random coincidences. By application of cuts in the timing and pulseheight spectra these background events can be separated from the *real* events and the statistical error can be minimized.

3.3.1 TDC cuts

A time spectrum as shown in Figure 3.11 may be divided into three regions:

- An early random region, left to the prompt peak
- A prompt peak
- A late random region, right to the prompt peak

In the **prompt region** a peak appears, as a fixed relation between the TDC start and stop exists. These events are mainly produced by tagged photons. The start is generated by the

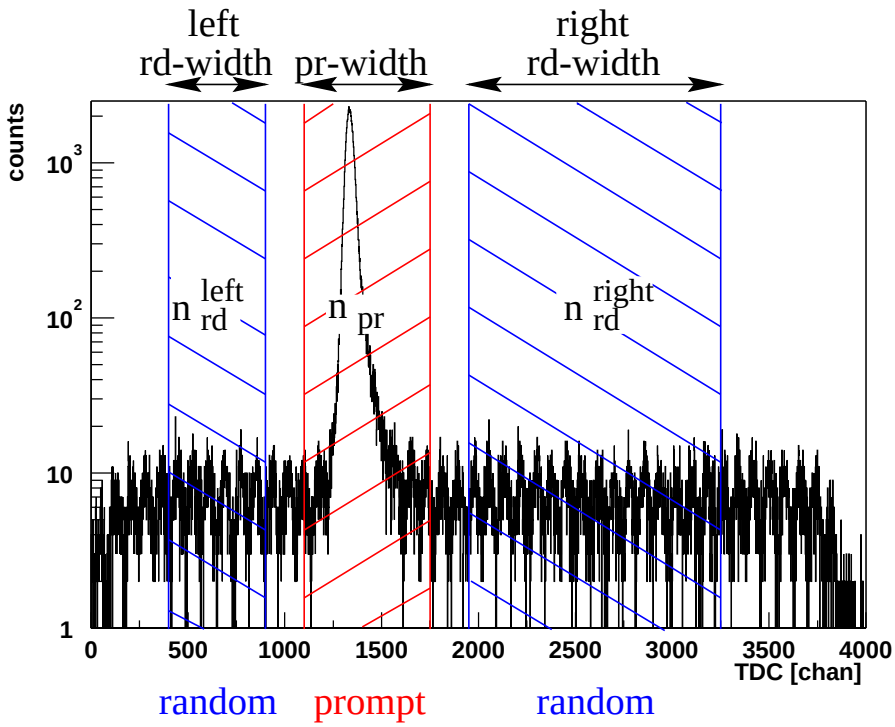

Figure 3.11: Mean TDC spectrum of a CEN_S module to display the prompt and random regions.

tagger and the stop in a detector module by reaction products of the same photon. The width of the prompt peak depends on the flighttime of the hadrons produced. In Figure 3.11 the mean TDC of a sandwich module of the central detector is displayed which has a narrow prompt peak as it is very close to the target. In the far-forward parts STP and FFW_T the prompt region is more extended as the time of flight of heavy hadrons varies in a wider range. To reach the sandwich part of the far-forward detector, hadrons have to pass the mirror of the Čerenkov counter, the STAR-triggerplate, the STAR-rings and the far-forward-triggerplate with its aluminum casing. Therefore, only high energy hadrons reach the FFW_S-detector producing a prompt peak which has a smaller width than that of the FFW_T and the STP.

Random events are mainly produced by untagged photons. A tagged photon generates the TDC start but passes the target region without interaction. An untagged photon is absorbed in the target and produces a hadron which reaches the detector and stops the TDC. As no fixed time relation between the two photons exists, such events generate the continuous background in the TDC spectra which is modulated by the 2 ns bunch structure of ELSA (Fig. 3.11). This random background also occurs under the prompt peak.

For the analysis the background events under the prompt peak have to be corrected for. For this purpose prompt and random regions (as indicated in Figure 3.11) are defined for each detector module. For some modules the amount of background is different for the early and late random region, the reason is the shadowing effect which will be explained in Section 3.6.1. To account for this effect a left and right random region is defined and the mean value of both is assumed to be under the prompt peak. The true number of events n_{true} can be obtained from the number of events in the prompt peak n_{pr} and the number of events in the

	BW_T	BW_S	CEN_T	CEN_S	FW_T	FW_S	STP	FFW_T	FFW_S
pr-width	9	9	6	6	6	7	12	10	9
rd-width	21	21	24	26	24	25	17	19	22

Table 3.1: The prompt and random widths (in bunches) of all detector modules.

left and right random regions n_{rd}^{left} and n_{rd}^{right}, via

$$n_{true} \;=\; n_{pr} - (\text{pr-width}) \cdot n_{rd}^{mean} \tag{3.15}$$

where the background per channel n_{rd}^{mean} is defined by

$$n_{rd}^{mean} \;=\; \frac{1}{2}\left(\frac{n_{rd}^{left}}{(\text{left-rd-width})} + \frac{n_{rd}^{right}}{(\text{right-rd-width})}\right) \tag{3.16}$$

The random regions are chosen as wide as possible to minimize the statistical error. The upper boundary of the left random region and the lower boundary of the right random region are 2 bunches (160 channels) away from the boundaries of the prompt region. For statistical reasons the width of the prompt region should be as small as possible. But one has to make sure that no nonrelativistic hadrons are lost in the far-forward components. For this reason the prompt width of the STP is for example much wider than that of a CEN module. All prompt and random widths are summarized in Table 3.1 where rd-width denotes the sum of the left and right random widths.

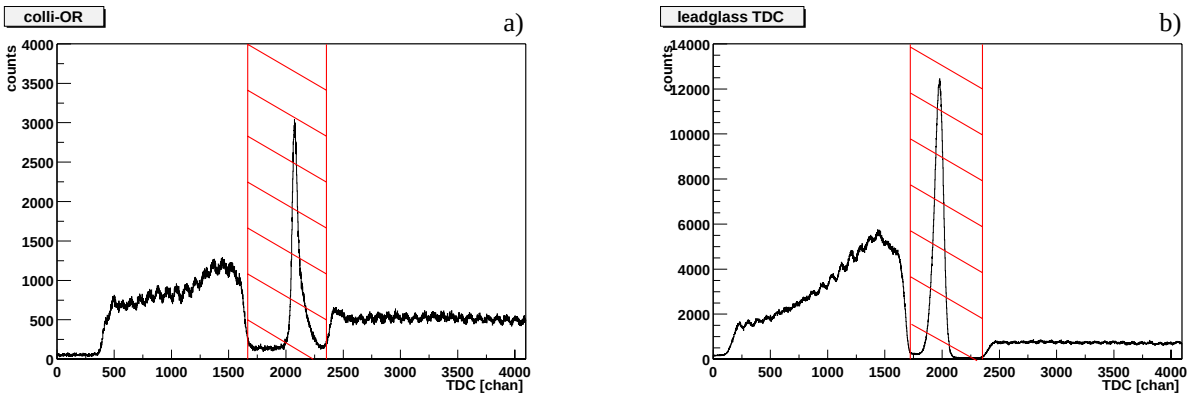

Figure 3.12: Corrected TDC spectra for a) a software generated colli-OR b) the leadglass detector. Events in the hatched areas have to be rejected.

In the **veto-detectors** additional cuts have to be applied. Figure 3.12 shows TDC spectra for two different veto detectors after the timing corrections. In Fig. 3.12 a) a software OR is generated from the four active collimator photomultipliers whereas in b) the TDC spectrum of the leadglass detector is shown. The *dip region* in both spectra represents the pulsewidth of 30 ns of these veto detectors. In principle no events should appear in this region, but due to multiple hits in the tagger it is possible that the coincidence condition is fulfilled for one tag channel, i.e. a major trigger is generated although a veto signal should prevent a readout. These events cause a peak in the time corrected spectra of the veto counters. In the analysis the (sub)event is rejected where one of the veto counters has an entry in the hatched area. For the Čerenkov-detector this effect can also occur, but due to the lower rate very few events are rejected by the application of these software cuts.

3.3.2 QDC cuts

In Figure 3.13 a 2-D gmean-QDC[5] versus mean-TDC spectrum of the STP is shown. This plot indicates that it is not possible to suppress background events completely with the veto detectors. As mentioned above these background events are mainly caused by untagged photons. If such a photon produces an electron or positron through electromagnetic interaction where the energy is below the Čerenkov-threshold (see Section 2.4.3) no veto can be generated. Such an event is recorded if it occurs within a certain time window before or after the TDC start. As the stop of these events is uncorrelated to the TDC start and as it is mainly minimum ionizing low energy particles that generate the TDC stop in such a case, the horizontal band at low QDC values is generated in Fig. 3.13.

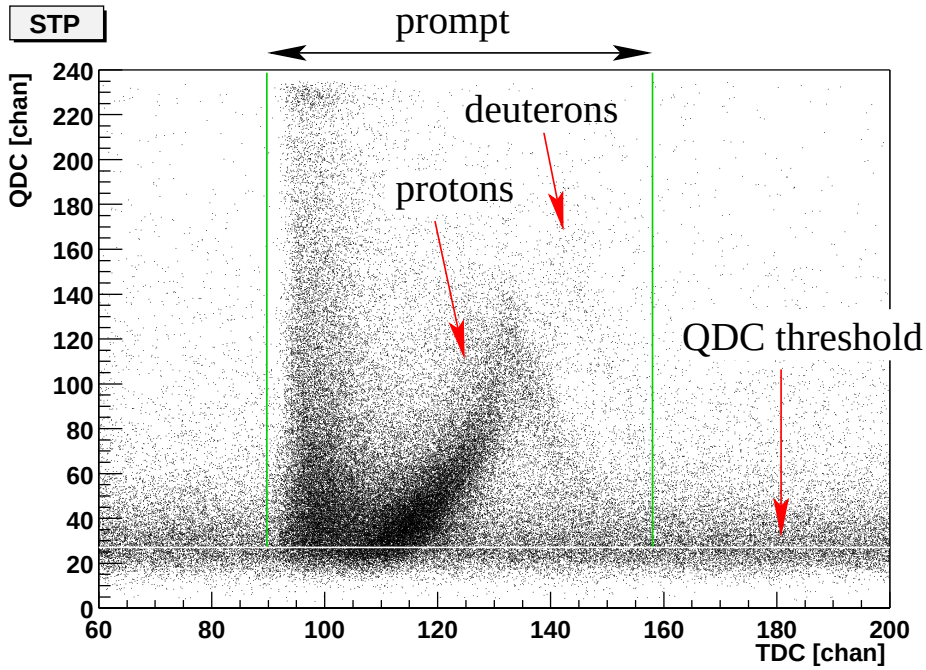

Figure 3.13: Gmean QDC versus mean TDC spectrum of the STP. Due to different time of flights protons and deuterons are separated from β=1 particles. The horizontal line indicates the software QDC threshold.

The HV of the photomultipliers is adjusted in such a way that the background is as low as possible and that all hadronic events are above the discriminator threshold [Mic01]. To improve the statistical quality of the data it is possible to set a software threshold in the gmean-QDC spectrum (horizontal line in Fig. 3.13). This threshold can be set more accurately than the hardware thresholds, as gmean-QDC is independent of the impact position. The influence of the threshold-value to the cross-section will be investigated in Section 4.2. Increasing the threshold reduces background and improves the statistical quality, but from a certain value on also hadronic events are rejected which leads to a decrease of the cross section.
In Figure 3.13 the heavy hadrons, proton and deuteron, can clearly be discriminated through their hook-like structure from β=1 particles which generate the vertical band. The *proton*

[5]gmean is the geometric mean (Section 3.2.2)

hook can be explained as follows: Starting from the right side of the hook, low energetic protons (large time of flight) are stopped in the scintillator and deposit their complete energy. Decreasing TDC values correspond to increasing energy and therefore also to increasing QDC values as more energy is deposited in the detector. At a certain point (the tip of the hook) the energy of the protons is high enough so that they *punch through* the detector. With further increasing energy the protons pass the detector. The faster the protons are, the less time they have to interact with the scintillator, the less energy is deposited, generating the decreasing QDC values of the left half of the hook.
For deuterons the mechanism is identical. According to the Bethe-Bloch formula deuterons can deposit more energy in the scintillator than protons of the same kinetic energy, generating higher QDC values in the *deuteron hook*.
Particles with $\beta \approx 1$ appear in the vertical band in Fig. 3.13, these are electrons or fast pions. It is obvious that pions cannot be discriminated from electrons with this detector setup. But the identification of protons allows the investigation of η-meson production via the missing mass method (Section 5.1.2).

3.4 Rate dependent corrections

In this section the pseudorandom (Section 3.4.1) and the veto deadtime (Section 3.4.2) correction will be described. The magnitude of these corrections directly depends on the tagging rate.
One goal of the optimization of the electron beam is to obtain a constant electron current during the extraction phase. Figure 3.14 shows the measured tagging rates for one extraction phase at a beamtime period with 1.4 GeV primary electron energy. This figure has been produced by using the scaler information of the TAG-OR and a 10 MHz clock. The scalers are read out every 100 events and at the beginning and the end of each extraction period. For the given example 31 blocks are read out during one extraction phase, block number 1 represents the extraction start and block nr. 31 the extraction end. The statistics is obtained by accumulation of 150 extraction phases. For rate investigations with a more accurate time resolution of $\approx 100\mu$s extra scalers are used, the electronics and the results are described in [Nau01].
Even with the present method it is obvious that the tagging rate varies significantly during an extraction phase. The effects which will be discussed in the next two sections are directly dependent on the tagging rate. For the data analysis the corresponding correction values are calculated separately for each scaler block (see Section 3.5).

3.4.1 Pseudorandom correction

During the pilot experiment with the GDH detector [Hel97] [Sau98] an enhancement of random background under the prompt peak was recognised. This effect which is purely statistical is called *pseudorandom effect*. Due to the chosen parameters of the electron beam current and the thickness of the tagging radiator the treatment of this effect was of major importance for the analysis of the pilot experiment.
In the following, first the mean number of electrons per bunch will be calculated. This value

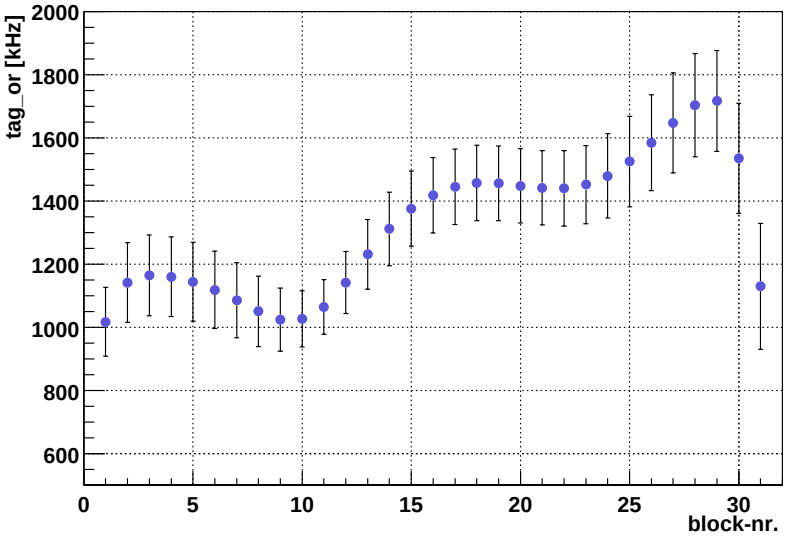

Figure 3.14: Tag-rate during one extraction phase at 1.4 GeV.

determines the magnitude of the pseudorandom effect, which will be derived afterwards.

Filling of the electron bunches

The electrons are provided in bunches with a width of 50 ps at an interval of 2 ns. The number of tagged photons γ_{tag} depends on the current of incoming electrons, the tagging radiator and the tagging range. From these parameters the mean number of electrons per bunch can be calculated.
Electrons in the GeV energy range mainly loose energy due to radiative processes. After passage of material with the length l the electrons have the energy $E(l)$ according to

$$E(l) \;=\; E_0 \cdot e^{-\frac{l}{X_0}} \tag{3.17}$$

Where X_0 is the radiation length, i.e. the length which reduces the energy to 1/e. The energy loss E_{loss} is given by

$$E_{loss} \;=\; E_0 - E(l) \;=\; (1 - e^{-\frac{l}{X_0}}) \cdot E_0 \tag{3.18}$$

The energy flux $d\Phi_{brems}$ due to bremsstrahlung in a photon energy interval dE_γ at an energy E_γ can be treated as a constant under the assumption of an $1/E_\gamma$ behaviour of the bremsstrahlung cross section $d\sigma_{brems}/dE_\gamma$

$$d\Phi_{brems} \;\sim\; \frac{d\sigma_{brems}}{dE_\gamma} E_\gamma dE_\gamma \;=\; const. \tag{3.19}$$

The energy E_{tag} which is emitted via tagged photons can be calculated directly from the tagging range r_{tag} (= 29 %) and from the number of incoming electrons N_e

$$E_{tag} = N_e \cdot r_{tag} \cdot E_{loss} \tag{3.20}$$

radiator	Al10	Al20	Cu15	Cu50
l [μm]	10	20	15	50
X_0 [cm]	8.9	8.9	1.43	1.43
E_{loss} [E_0]	$1.123 \cdot 10^{-4}$	$2.246 \cdot 10^{-4}$	$1.048 \cdot 10^{-3}$	$3.490 \cdot 10^{-3}$

Table 3.2: Parameters of the tagging radiators.

The probability distribution for the emission of a photon in a certain energy range is proportional to the cross section $d\sigma_{brems}/dE_\gamma$. The expectation value of this distribution gives, after normalization to the tagged photon range, the mean energy $\overline{E_\gamma}$ of the tagged photons. The energy E_{tag} which is emitted via N_γ photons reads

$$E_{tag} = \overline{E_\gamma} \cdot N_\gamma = \frac{\int_{E_{min}}^{E_{max}} E_\gamma \frac{1}{E_\gamma} dE_\gamma}{\int_{E_{min}}^{E_{max}} \frac{1}{E_\gamma} dE_\gamma} \cdot N_\gamma \tag{3.21}$$

where $E_{min} = 0.68 \cdot E_0$ and $E_{max} = 0.97 \cdot E_0$ are the minimum and maximum tagged photon energy values.

$$E_{tag} = \frac{0.29 \cdot E_0}{\ln(0.97) - \ln(0.68)} \cdot N_\gamma = 0.816 \cdot E_0 \cdot N_\gamma \tag{3.22}$$

The number of incoming electrons N_e can be written in terms of the number of produced tagged photons N_γ (Eqs. 3.20 and 3.22)

$$N_e = \frac{0.816 \cdot E_0}{r_{tag} \cdot E_{loss}[E_0]} \cdot N_\gamma = \frac{2.814}{1 - e^{-\frac{l}{X_0}}} \cdot N_\gamma \tag{3.23}$$

$E_{loss}[E_0]$ is given together with the length l and the radiation length X_0 of the tagging radiators in Table 3.2.
With the known interval of 2 ns between two successive bunches the mean number of electrons μ in a single bunch is given by

$$\mu = \dot{N}_e \cdot 2 \cdot 10^{-9} s \tag{3.24}$$

As Equation 3.23 is also valid for the rates $\dot{N}_e$ and $\dot{N}_\gamma$ Eq. 3.24 can be written as

$$\mu = \frac{5.628 \cdot 10^{-9} s}{1 - e^{-\frac{l}{X_0}}} \dot{N}_\gamma \tag{3.25}$$

As will be seen at the end of the next section this quantity μ determines the magnitude of the pseudorandom effect.

Derivation of the pseudorandom effect

Random coincidences are mainly caused by untagged photons. It is useful to distinguish two different cases which are illustrated in Figure 3.15 a) and b). A filled circle denotes here a bunch which is filled with one ore more electrons.

- Case a): The photon that generates a start in the tagger and the untagged photon are produced by different electron bunches. If these untagged photons interact in the target (Figure 3.15 c)) they are responsible for the flat background in the TDC spectrum (see e.g. Fig. 3.16).

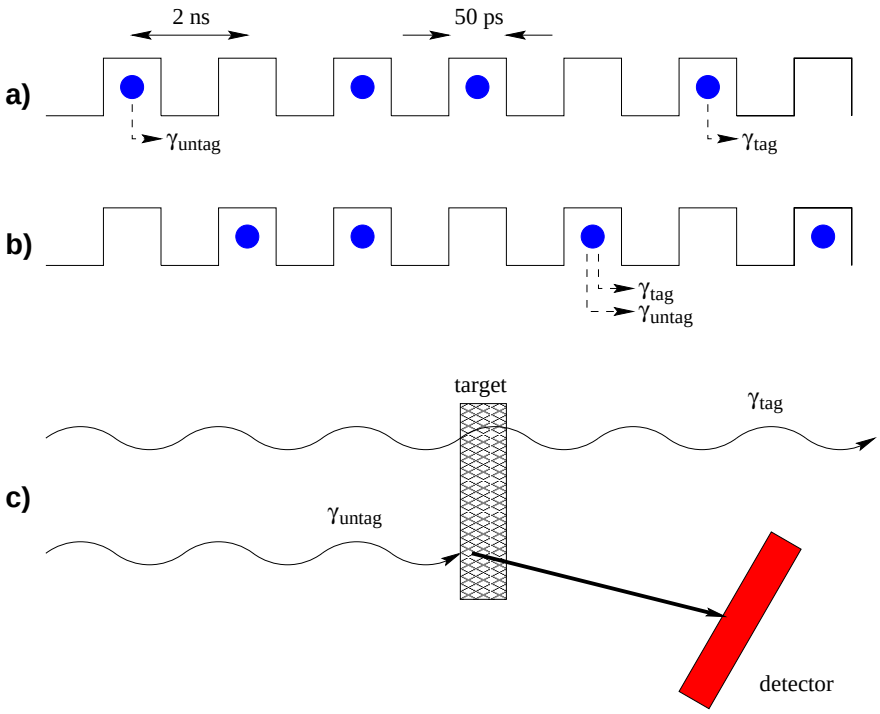

Figure 3.15: Sketch to illustrate the different types of random coincidences.

- Case b): The tagged and the untagged photon are generated within the same bunch. The untagged photon can either be produced from the same electron that emitted the tagged photon or from another electron within the same bunch. Both photons arrive at the same time at the target and an interaction generates entries in the prompt region of the TDC spectrum.

The number of electrons per electron bunch obey a Poisson distribution. If the mean number of electrons in a bunch is μ, the probability f_{arb} to find n electrons in an arbitrary bunch is given by

$$f_{arb}(n) \;=\; \frac{\mu^n \cdot e^{-\mu}}{n!} \tag{3.26}$$

The probability to emit a photon in the tagged energy range is proportional to the number of electrons in the bunch. A tagged photon has to be emitted by an electron bunch which is filled at least with one electron. These electron bunches can therefore be distinguished from arbitrary bunches. The probability f_{tag} that such a *tagged* bunch is filled with n electrons can be written in terms of f_{arb} as

$$f_{tag}(n) \;=\; \frac{1}{\mu} \cdot n \cdot f_{arb}(n) \;=\; \frac{\mu^{n-1} \cdot e^{-\mu}}{(n-1)!} \tag{3.27}$$

where the factor $1/\mu$ is required to guarantee the normalization $\sum_{n=0}^{\infty} f_{tag}(n) = 1$.
The cross section to produce a low energetic photon via a bremsstrahlung process can be treated in a good approximation to be independent of the electron energy. The probability $f_{\gamma_{low}}$ to produce a low energetic photon is therefore also independent of the electron energy E_0. This implies that an electron that already emitted a tagged photon has the same chance to emit a low energetic photon as an electron with the full primary energy. The probability

radiator	Al10	Al20	Cu15	Cu50
μ	50.1	25.06	5.37	1.61
$1/\mu$ [%]	2.0	3.99	18.62	62.11

Table 3.3: Values of μ and $1/\mu$ for the different radiators at a tag-rate of 1 MHz.

to emit a low energetic photon is proportional to n the number of electrons in the bunch. The ratio of the probability that such a photon is emitted by a *tagged* bunch P_{tag} to the probability that it is emitted by an arbitrary bunch P_{arb} is given by:

$$\frac{P_{tag}}{P_{arb}} = \frac{\sum_{n=0}^{\infty} n f_{tag}}{\sum_{n=0}^{\infty} n f_{arb}} = \frac{\sum_{n=0}^{\infty} \frac{n^2}{\mu} f_{arb}}{\sum_{n=0}^{\infty} n f_{arb}} = 1 + \frac{1}{\mu} \tag{3.28}$$

This implicates that the random background under the prompt peak is increased by a factor $(1+1/\mu)$. Figure 3.16 illustrates this effect. For simplicity it is assumed that the random

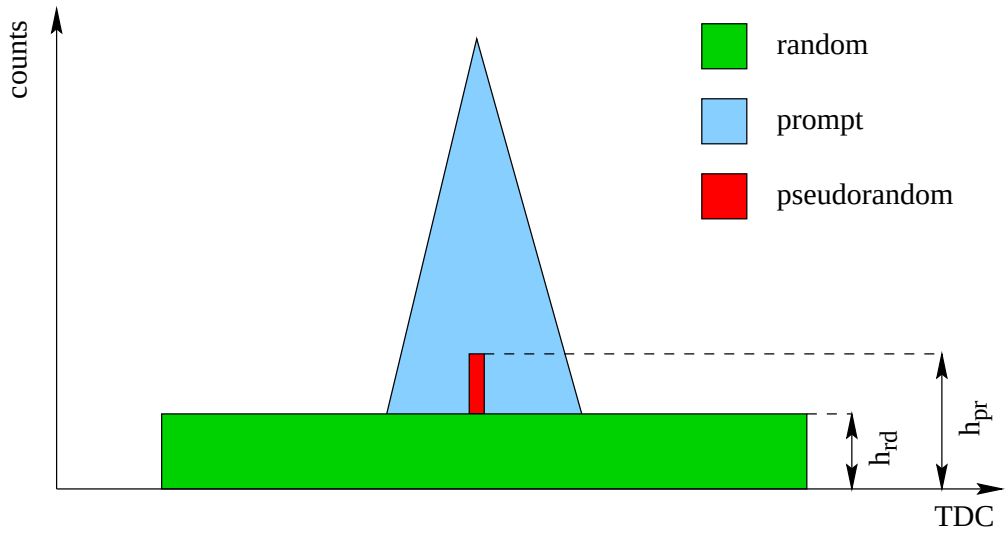

Figure 3.16: Sketch to illustrate the enhanced background caused by the pseudorandom effect.

background is flat and constant over the complete TDC region. The enhancement of the background under the prompt peak due to the pseudorandom effect can be calculated via:

$$h_{pr} = h_{rd} \cdot (1 + \frac{1}{\mu}) \tag{3.29}$$

where h_{rd} is the *height* of the random background and h_{pr} the *height* of the background in the prompt bunch caused by the pseudorandom effect.
Table 3.3 gives examples of the quantities μ and $1/\mu$ for the various radiators at a tag-rate $\dot{N}_\gamma = 1$ MHz. These values are calculated using Equation 3.25 and Table 3.2. The GDH measurements on the proton have been performed for all primary energies with a Cu15 radiator and the tag-rates were between 1.0 and 1.3 MHz. In this case $1/\mu \approx 19$ %. It has however to be pointed out that the pseudorandom effect just appears for a single bunch (*the* prompt bunch). In the detector TDCs the resolution is much worse, e.g. due to time of flight effects, so that the prompt window has a width between 6 and 12 bunches for the different

detector modules (Table 3.1). In order to calculate the enhancement of random events in this prompt window one has to divide h_{pr} by the width of the prompt window (in bunches). Compared to the pilot experiment the pseudorandom correction plays here a minor role but as a systematic correction in the order of 2 % it still has to be taken into account.

3.4.2 Veto deadtime correction

A major trigger is generated from the coincidence of the tagger, the detector and the inverted signal of the veto detectors. In this case it is very likely that a hadronic event has occurred. Due to the high rates of the veto counters it is possible that a real hadronic event is rejected by a random coincidence of the veto counters. This deadtime effect has to be measured and the hadronic rate has to be corrected accordingly.

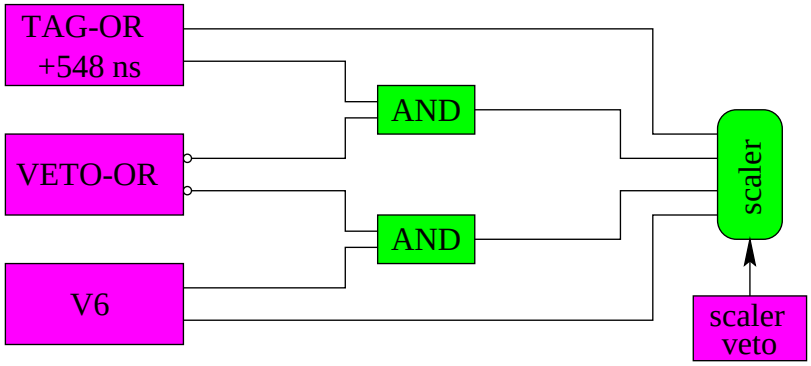

Figure 3.17: Electronics to measure the veto deadtime.

For the measurement of this deadtime a signal is needed which is uncorrelated to the veto signals. This signal shall be called monitor signal. It is measured on the one hand free and on the other hand in coincidence with the inverted VETO-OR signal. The livetime t_{live} is calculated from the ratio of the rate of the monitor signal in anticoincidence with the vetos $\dot{N}_{mon\wedge\overline{veto}}$ and the free rate $\dot{N}_{mon}$

$$t_{live} = \frac{\dot{N}_{mon\wedge\overline{veto}}}{\dot{N}_{mon}} \tag{3.30}$$

The deadtime t_{dead} which is generated by the veto signals reads

$$t_{dead} = 1 - t_{live} \tag{3.31}$$

If the livetime t_{live} is known the real hadronic yield is obtained by dividing the measured hadronic yield by t_{live}.
The electronics to measure the veto deadtime is displayed in Figure 3.17. The monitor signal should be proportional to the beam intensity and it should be uncorrelated to the veto signals. Two different monitor signals have been used:

- The signal of the V6-detector [Spe98] [Zei98] which registers photons that are produced at the Møller-target. As it is in the electron beamline its signal is uncorrelated to the veto signals and its rate is proportional to the beam intensity.

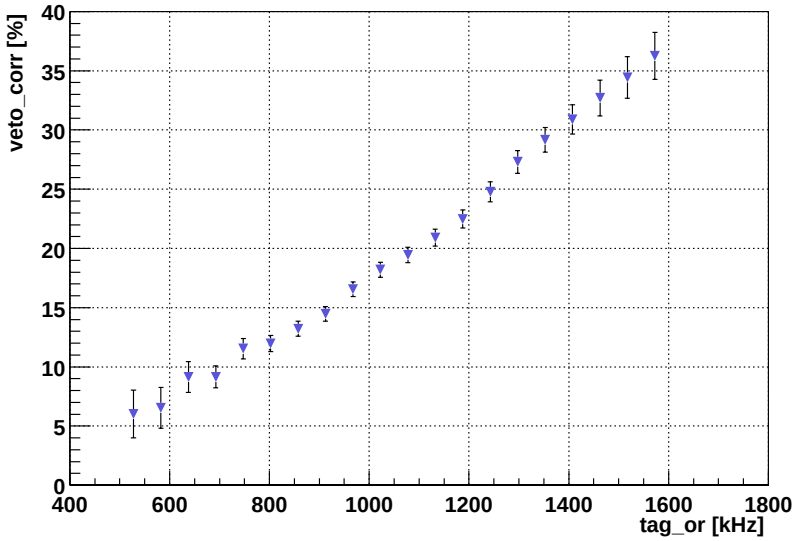

Figure 3.18: Veto deadtime as a function of the tag-rate.

- The delayed signal of the TAG-OR. This signal has exact the same distribution of the pulses as the original TAG-OR signal. The delay is necessary as the TAG-OR and the VETO-signals are highly correlated. The delay of 548 ns corresponds exactly to the time an electron bunch needs for one turn in ELSA.

The task of the electronics in Fig. 3.17 is to simulate the deadtime effects that occur at the major trigger (MT) coincidence. The pulse widths of the monitor signals are adjusted to the same value as the TAG-OR signal. Furthermore, the same coincidence units as for the MT coincidence are used.
The deadtimes measured with the V6 and the delayed TAG-OR produce identical results within error bars [Mic01]. Figure 3.18 shows the veto deadtime obtained with the TAG-OR signal as a function of the tag-rate. Even at very high rates no deviation from a linear behaviour can be observed. This implicates a constant beam position during the extraction phase.
For the analysis of the hadronic events the deadtime obtained with the TAG-OR signal has been used for all beamtime periods.

As the deadtime has a priori not to be identical for both polarization directions of the electrons and therefore for both helicity states of the photons it has been determined for both directions separately.

3.5 Analysis procedure

In this section the steps in the analysis are described which are necessary to obtain physical results from the raw experimental data.

Prelude

At the beginning and/or the end of each beamtime period, time calibration and pedestal runs are performed. The first step is to determine these constants for all TDC and QDC channels. The next step is to extract the values necessary for the walk correction, the correction to the cable shifts and the HF-correction. All these constants are written to parameter files which are produced for every beamtime period separately. In principle these constants should be the same for all periods but they might slightly vary due to e.g. temperature variations or influences of the different primary electron energies.
For the correction of the TDC start the self-stop-peaks of the tagging channels have to be known. As these values sometimes drift or jump during a beamtime period, a parameter file with these values is generated for each run.
The correction values for the pseudorandom effect and the veto deadtime directly depend on the tagging rate. As has been shown in Section 3.4 this rate is usually not constant during an extraction phase. Therefore, a file is generated for each run which comprises these values together with the polarization state and the entry of the I/O register for every scaler block.
For the determination of cross sections the flux of incoming photons has to be known at the target position. For this purpose so called *tagging efficiency* runs are performed every few hours during ordinary data taking. For these runs the experimental trigger is generated by the TAG-OR and the fraction of produced photons which arrive at the leadglass detector is counted. The analysis of these runs will be described in Section 3.6.1.

Event by event analysis

After this preparatory work is finished the *real* analysis can start. The data have been taken in runs which lasted between 30 and 60 minutes. For the analysis an arbitrary number of files can be selected which are analysed in one turn. The parameter files previously described are read in at the beginning or when a new run is reached[6], respectively.
The following steps are performed *event by event*. First the helicity of the photon is determined. Then it is checked if the trigger was caused by a real detector event or if it was initiated by the extraction phase trigger. In the case of the extraction start the event is rejected together with the entries of the scalers in this block. At the end of an extraction phase just the event where the readout was initiated is rejected, but all other events of this scaler block are used. If the data acquisition was busy at the end of an extraction phase the electronics shown in Figure 2.31 *memorizes* the extraction end and initiates a scaler readout. This event is rejected together with the corresponding scaler block. In all other cases the event is further analysed.
For such *good* events all calibrations and corrections described in Section 3.1 are applied to the raw QDC and TDC information of the photomultipliers that fired at this event. If more than one tag channel fired during one event these corrections, especially to the TDC start, are performed for each tag-channel separately. As the QDC modules do not provide information about overflows, such cases can be identified if there is a hit in the TDC spectrum but no hit in the corresponding QDC spectrum. These events can be used for the analysis

[6] for the file with the veto deadtime corrections

by generating an entry at QDC-value 4095 (the last channel), via software.
If the number of photomultipliers per detector module that fired, is above the required multiplicity, the mean TDC and gmean QDC is calculated (Section 3.2). For the further analysis only these mean values are used.
In the next step it is checked if one of the corrected VETO-TDCs has an entry in its prompt regions (hatched areas in Figure 3.12) for one or more tag channels that fired. In such a case this (sub)event is rejected. For each detector module with a valid hit and a gmean QDC value above the selected threshold (Section 3.3.2) it is tested if the TDC value lies inside the prompt or one of the random windows (Section 3.3.1). The number of hits in the prompt and the random regions are counted for each detector module and each tag-channel. The detector multiplicity *det_multi* denotes the number of detector modules that have hits inside the required TDC regions, for each tag channel. For one tag-channel it is very unlikely that one detector module has a hit in the prompt region whereas another module has a random entry (about 1 in 1000) therefore, no special treatment is necessary for such cases.
To take into account the effect of the veto deadtime, each hit in the prompt region is weighted by the corresponding correction factor vc_tag(l) of this scaler block l. The running sum of prompt hits $N_{i,j}^{pr,k}$ of detector module k for tag-channel i and detector multiplicity j reads

$$N_{i,j}^{pr,k} \;=\; \sum_{l} \text{vc\_tag}(l) \tag{3.32}$$

The entries in the left and right random region are accumulated separately. For both also the pseudorandom correction has to be treated. The running sum of random entries $N_{(left,right),i,j}^{rd,k}$ is given by

$$N_{(left,right),i,j}^{rd,k} \;=\; \sum_{l} \text{vc\_tag}(l) \cdot \left(\frac{\text{pr\_fac}(l) - 1}{(\text{pr-width})^k} + 1 \right) \tag{3.33}$$

where pr_fac(l) is the pseudorandom correction factor of scaler block l and (pr-width)^k the prompt width of detector module k given in bunches (see Table 3.1).

Hadronic rate

At the end of a run the hadronic rate is extracted. For this purpose the random background has to be corrected. This background subtraction is performed for each detector module and each tag-channel separately. The number of hadronic events $N_{i,j}^{k,hadr}$ of detector module k ($k = 0...14$) tag-channel i ($i = 0...63$) and detector multiplicity j ($j = 1...15$) is given by

$$N_{i,j}^{k,hadr} \;=\; N_{i,j}^{pr,k} - N_{i,j}^{rd,k} \tag{3.34}$$

with

$$N_{i,j}^{rd,k} \;=\; \frac{1}{2} \left(\frac{N_{(left),i,j}^{rd,k}}{(\text{left-rd-width})^k} + \frac{N_{(right),i,j}^{rd,k}}{(\text{right-rd-width})^k} \right) \cdot (\text{pr-width})^k \tag{3.35}$$

The total number of hadronic events N_i^{tot} is obtained by summing the contributions of all detector modules k and all detector multiplicities j.

$$N_i^{tot} \;=\; \sum_{k=0}^{14} \sum_{j=1}^{15} \frac{1}{j} \, N_{i,j}^{k,hadr} \tag{3.36}$$

The factor $1/j$ in the summation over the detector multiplicities is necessary to compensate for multiple counting.
The hadronic rate $Y(i)$ is defined as the number of total hadronic events N_i^{tot} divided by the flux of electrons ϕ_i^{el} in tag-channel i

$$Y(i) \;=\; \frac{N_i^{tot}}{\phi_{el}^i} \tag{3.37}$$

The scaler entries of the tagging system, summed over all *good* scaler blocks, gives ϕ_{el}^i. The hadronic rate Y is directly proportional to the total photoabsorption cross section. The missing factors will be calculated in the following sections.

3.6 The photon flux

For a correct determination of cross sections the flux of tagged photons at the target region $\phi_{\gamma,tag}^i$ has to be known for each tag channel i. Due to collimation of the photon beam this flux is lower than the number of produced photons at the tagging radiator.

$$\phi_{\gamma,tag}^i \;=\; \epsilon_{tag}^i \;\cdot\; \phi_{el}^i \tag{3.38}$$

Where ϕ_{el}^i is obtained from scalers which are connected to the tag-channels (Section 2.5.1). The *scaler veto* (see Fig. 2.26) guarantees that the incoming flux is just counted when the data acquisition is able to process experiment triggers.
The tagging efficiency ϵ_{tag}^i also takes into account events where an electron was detected in a tag-channel but no photon was radiated. This can be caused by Møller-scattering in the tagging radiator or by effects of the electron beam halo.

3.6.1 The tagging efficiency

For the determination of the tagging efficiency a detector is needed which detects $\approx 100\%$ of the photons in the tagged energy range. For this purpose the leadglass detector in the photon beamdump is used. For practical applications the number of photons that reach this detector is equal to the number of photons in the target region. In principle it is possible that a photon converts into an electron-positron pair between the target and the leadglass detector. In such a case it is however very likely that a fast lepton is emitted under a small angle with respect to the beam axis so that it reaches the leadglass detector and causes a signal there.
The measurement of the tagging efficiency is performed every few hours between ordinary data taking runs. As trigger condition at the experimental trigger (Section 2.5.4) only a TAG-OR signal is required, the signals of the DET-OR and the $\overline{\text{VETO-OR}}$ are set to logic '1'. The tagging efficiency is the number of photons that reach the leadglass detector without interaction in the active collimators $N^i_{tag \wedge Pb \wedge \overline{colli}}$, normalized to the number of hits in the tagger N_i^{tag}, i.e. the number of produced photons in the tagged energy range.

$$\epsilon_{tag}^i \;=\; \frac{N^i_{tag \wedge Pb \wedge \overline{colli}}}{N_{tag}^i} \tag{3.39}$$

This quantity has to be determined for each tag-channel i separately. Multiple hits in the tagger are analysed independently because the leadglass detector cannot distinguish simultaneous single and multiple photon hits. Furthermore, each hit in the tagger generates an entry in the corresponding TAG-TDC. The number of entries N^i_{tag} is used for normalization in Eq. 3.39.
The tagging efficiency runs are performed at the same conditions as the data taking runs, i.e. at the same photon fluxes. Therefore, the leadglass detector and the active collimators are exposed to high rates which makes the correction to the *shadowing effect* necessary which will be explained in the following.

Shadowing correction

Here the main aspects of the shadowing correction shall be given, a more detailed treatment can be found in [Zei02].
The shadowing effect is important for the leadglass detector and the active collimators. In this section *detector* means one of these components. Random events are responsible for the shadowing effect. These events occur if a tagged photon does not reach the detector but a second untagged photon generates a hit in the detector. In such a case no fixed time between the TDC start (from the tagged photon) and the TDC stop (from the untagged photon) exists, so such events generate the random background in the regions I, III and IV in Figure 3.19.

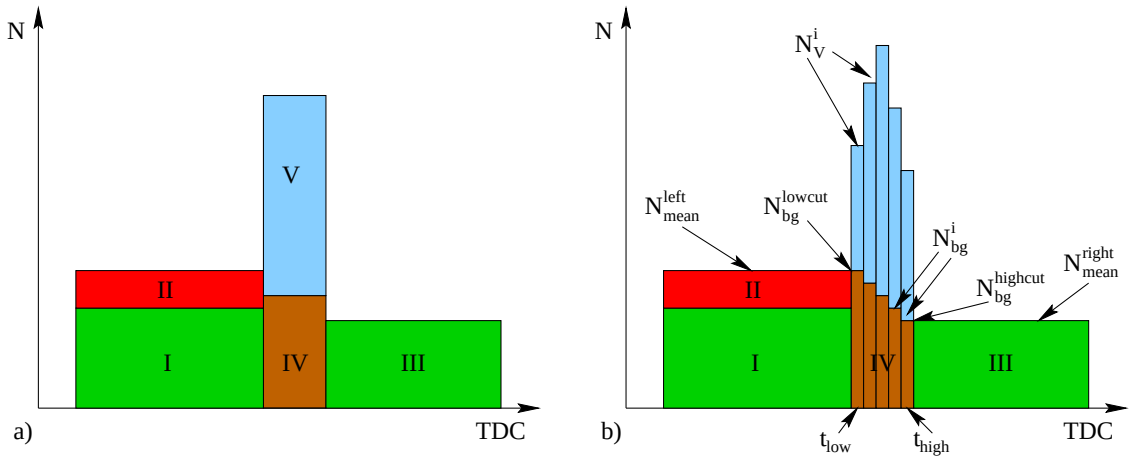

Figure 3.19: Schematic TDC spectra for a) a single prompt peak and b) an extended prompt peak

If an untagged photon generates a hit in the detector and if at a later time a tagged photon occurs which would produce an entry in the prompt region of the TDC spectrum, then this prompt event cannot be detected properly as the TDC was already stopped by the untagged photon. This effect causes entries at low TDC values and the events in region II are actually prompt events. The prompt events are so to say *shaded* by the stops generated by untagged photons. This effect increases with increasing tagging rate and also with the ratio of untagged to tagged photons. This shadowing effect can be seen in the leadglass TDC spectrum (Figure 3.20) obtained during a tagging efficiency run at a tagging rate of approximately 1.3 MHz.
Following [Zei98] a procedure will now be described to obtain the *true* number N_{true} of

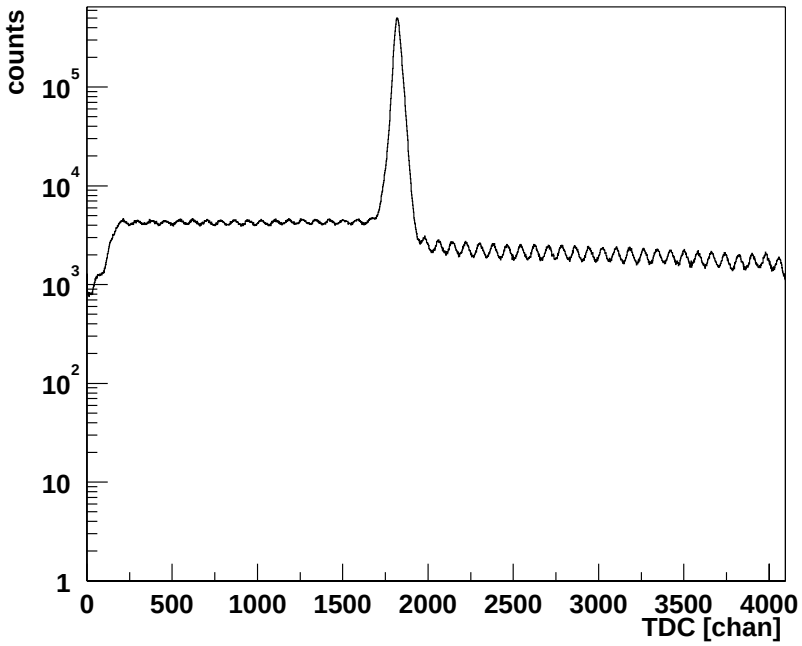

Figure 3.20: Leadglass TDC during a tagging efficiency run at a tagging rate of 1.3 MHz.

prompt events. According to Figure 3.19 N_{true} is the sum of N_{II} and N_V

$$N_{true} \;=\; N_{II} \;+\; N_V \tag{3.40}$$

The probability P_{shadow} for a prompt event to be shaded is the ratio of the number of stops that occurred too early, to the number of true events

$$P_{shadow} \;=\; \frac{N_{II}}{N_{true}} \tag{3.41}$$

Inserting equation 3.41 into 3.40

$$N_{true} \;=\; N_V(1 \;-\; P_{shadow})^{-1} \tag{3.42}$$

As the probability P_{shadow} is equal to the total probability P for a TDC stop prior to the prompt peak, when N_{tot} TDCs have been started.

$$P_{shadow} \;=\; P \;=\; \frac{N_I + N_{II}}{N_{tot}} \tag{3.43}$$

the number of true events N_{true} is given by

$$N_{true} \;=\; N_V \left(1 \;-\; \frac{N_I + N_{II}}{N_{tot}}\right)^{-1} \;=:\; N_V \cdot S \tag{3.44}$$

Where S denotes the shadowing factor. N_{tot} includes the total number of started TDCs, it is obtained from the entries in the TAG-TDCs. The other quantity necessary for the determination of N_{true}, $N_I + N_{II}$ can directly be extracted from the corresponding detector TDC

spectrum.
For the realistic situation of an extended prompt peak (Figure 3.19 b)) the described correction has to be applied for every channel i in the prompt region. It has to be taken into account that for the correction of channel i also the background up to channel $i-1$ contributes to the shadowing effect.

$$N^i_{true} \;=\; N^i_V \left(1 \;-\; \frac{N_I + N_{II} + \sum_{k=lowcut}^{i-1} N^k_{bg}}{N_{tot}} \right)^{-1} \tag{3.45}$$

where the background N^k_{bg} is determined via linear interpolation between the left N^{left}_{mean} and right N^{right}_{mean} part

$$N^k_{bg} \;=\; N^{left}_{mean} \;+\; \frac{N^{right}_{mean} - N^{left}_{mean}}{t_{high} - t_{low}} \, (t_k - t_{low}) \tag{3.46}$$

For high rates the background in a TDC spectrum should in principle decrease exponentially [Owe90]. In the present case (Fig. 3.20) the background can be treated as flat, because the rates are not high enough to show this exponential behaviour.

Determination of the tagging efficiency

The tagging efficiency Eq. 3.39 can be rewritten [Zei02] in such a way that just coincidences instead of anticoincidences appear

$$\epsilon^i_{tag} \;=\; \frac{N^i_{tag \wedge Pb \wedge \overline{colli}}}{N^i_{tag}} \;=\; \frac{N^i_{tag \wedge Pb}}{N^i_{tag}} \;-\; \frac{N^i_{tag \wedge Pb \wedge colli}}{N^i_{tag}} \tag{3.47}$$

Where the first term denotes the standard tagging efficiency $\epsilon^i_{tag,standard}$ and the second term a correction $corr^i$ to it

$$\epsilon^i_{tag} \;=\; \epsilon^i_{tag,standard} \;-\; corr^i \tag{3.48}$$

Both terms have to be treated differently in the analysis.
The **standard tagging efficiency** is obtained by generating TDC spectra of the leadglass detector for each tag-channel i separately. All corrections described in Section 3.1 are applied and prompt and random regions are defined. The shadowing effect and the random subtraction are treated according to equation 3.45 with the exception that the background is enhanced due to the pseudorandom effect. Equation 3.46 therefore modifies to

$$N^k_{bg} \;=\; \left(N^{left}_{mean} + N^k_{pseudo} \right) \;+\; \frac{N^{right}_{mean} - N^{left}_{mean}}{t_{high} - t_{low}} \, (t_k - t_{low}) \tag{3.49}$$

Where N^k_{pseudo} is the additional background generated by the pseudorandom effect which can be calculated from the tagging rate, the tagging radiator and the width of the prompt TDC window (see Section 3.4.1).
After these corrections $N^i_{tag \wedge Pb}$ is known and the standard tagging efficiency $\epsilon^i_{tag,standard}$ can be calculated via

$$\epsilon^i_{tag,standard} \;=\; \frac{N^i_{tag \wedge Pb}}{N^i_{tag}} \tag{3.50}$$

Where N^i_{tag} are the entries in the TAG-TDCs for each tag-channel i.
The analysis of the **correction term** $corr^i$ requires a different analysis method. To handle the signals of the four photomultiplier tubes of the active collimators an OR is generated via software. First all timing corrections are applied before the signals of the four tubes are shifted to one reference tube. Now all prompt peaks are on top of each other and it can be decided which tube was the first to fire. This TDC value is then written to a new software generated TDC spectrum, called COLLI-OR (see Fig. 3.12 a)).
To treat the three-fold coincidence $tag \wedge Pb \wedge colli$ it is useful to plot a two-dimensional time spectrum (Figure 3.21) where the two-fold coincidences $tag \wedge colli$ and $tag \wedge Pb$ are plotted versus each other. In this spectrum different regions of the three-fold coincidence can

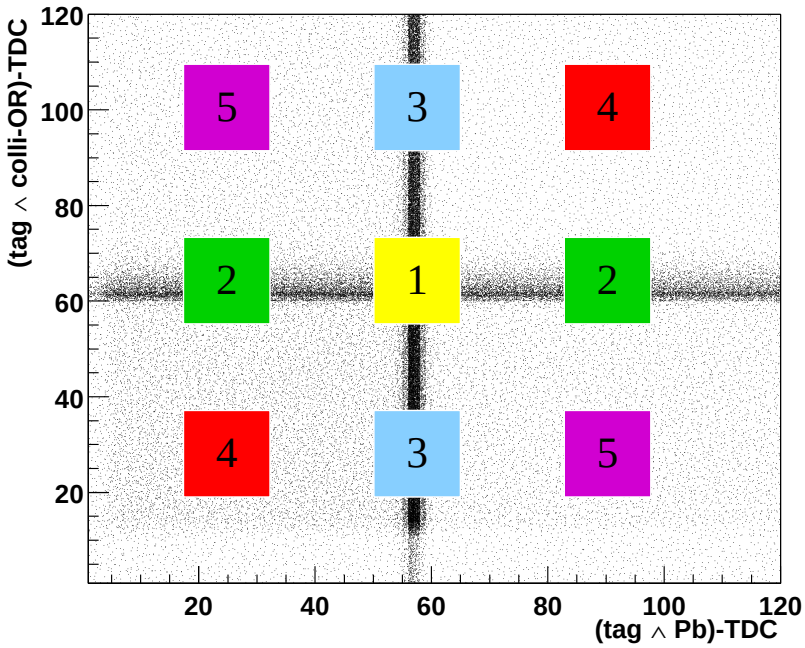

Figure 3.21: 2D-time-spectrum of the ($tag \wedge colli$)-TDC versus the ($tag \wedge Pb$)-TDC. In region 1 the events of the 3-fold coincidence $tag \wedge Pb \wedge colli$ are located, all other regions are necessary for background determination (see text).

be identified:

- In the complete spectrum a homogeneous background of random entries can be found which are uncorrelated to the tagger, the leadglass detector and the active collimators.
- Three bands exist where two out of the three signals are correlated to each other.
  - A horizontal band where the COLLI-OR is correlated to the tagging signal but the leadglass-TDC is uncorrelated to the tagger.
  - A vertical band where the leadglass-TDC is correlated to the tagger and the COLLI-OR is uncorrelated to it.
  - A diagonal band (which is not visible in Fig. 3.21) where the COLLI-OR is correlated to the leadglass-TDC but both are uncorrelated to the tagger.

- In region '1' the prompt events of the required three-fold coincidence of the COLLI-OR, the leadglass-TDC and the tagger are located. Besides the prompt events which have to be counted, the three bands crossing in this region generate background. Furthermore, also completely random background appears here.

In order to correct for the background in region '1' rectangles '2'...'4' are defined in the different bands and rectangles '5' are defined in regions where only uncorrelated entries exist. With the entries in these rectangles $N^i_{tag\wedge Pb\wedge colli}$ can be obtained via

$$N^i_{tag\wedge Pb\wedge colli} \;=\; N^i_1 \;-\; N^i_2 \;-\; N^i_3 \;-\; N^i_4 \;+\; 2\cdot N^i_5 \tag{3.51}$$

Where N^i_1 are the number of entries in the prompt region '1' for each tag-channel i. N^i_j (j=2..5) are the number of entries in the regions 'j' where the mean has been calculated for each j to take into account the differences between the early and late random regions. These values have been normalized to the respective areas.
The totally uncorrelated background appears everywhere in the spectrum, thus it has to be subtracted from '1' just once, however it has been subtracted three times together with '2','3','4'. To treat this background correctly, two times N^i_5 has to be added in Eq. 3.51. Up to now the pseudorandom effect has been neglected. This effect appears in the prompt region and also in the horizontal, vertical and diagonal bands in Figure 3.21. For regions '2','3','4' it is automatically taken into account. In regions '5' no pseudorandom effect occurs but this background also appears in regions '2','3','4' where the pseudorandom effect occurs. As N^i_5 has to be added twice, Eq. 3.51 modifies to

$$N^i_{tag\wedge Pb\wedge colli} \;=\; N^i_1 \;-\; N^i_2 \;-\; N^i_3 \;-\; N^i_4 \;+\; 2\cdot N^i_5 \;+\; 2\cdot N^i_5\cdot R^1_{pseudo} \tag{3.52}$$

With $R^1_{pseudo} = c_{window}/\mu$ the pseudorandom correction factor according to equation 3.25 where c_{window} guarantees that the pseudorandom correction is just applied for one bunch.
Finally, also the shadowing correction has to be treated. Therefore, TDC spectra are generated for $colli \wedge tag$ and $Pb \wedge tag$ for each tag-channel i. With these spectra the shadowing correction factors S^i_{colli} and S^i_{Pb} are extracted according to equation 3.44. $N^i_{tag\wedge Pb\wedge colli}$ is now finally defined as

$$N^i_{tag\wedge Pb\wedge colli} \;=\; \left(N^i_1 \;-\; N^i_2 \;-\; N^i_3 \;-\; N^i_4 \;+\; 2\cdot N^i_5 \;+\; 2\cdot N^i_5\cdot R^1_{pseudo}\right)\cdot S^i_{Pb}\cdot S^i_{colli} \tag{3.53}$$

and the correction term $corr^i$ can be calculated via

$$corr^i \;=\; \frac{N^i_{tag\wedge Pb\wedge colli}}{N^i_{tag}} \tag{3.54}$$

Figure 3.22 shows the tagging efficiencies versus tag-channel i for several primary electron energies obtained with the described method. Tag-channel 0 denotes the tag-channel which corresponds to the lowest photon energy. The tagging efficiency increases with increasing primary electron energy E_0 as the opening angle of the bremsstrahlung cone Θ_c is proportional to $1/E_0$. Therefore, at higher primary energies less photons are removed by the collimators and thus they can reach the leadglass detector to generate a larger tagging efficiency.
For a single primary energy the tagging efficiency slightly depends on the photon energy, i.e. on the tag-channel i. This effect is caused by the geometry of the tagging system and the influence of the active collimators.

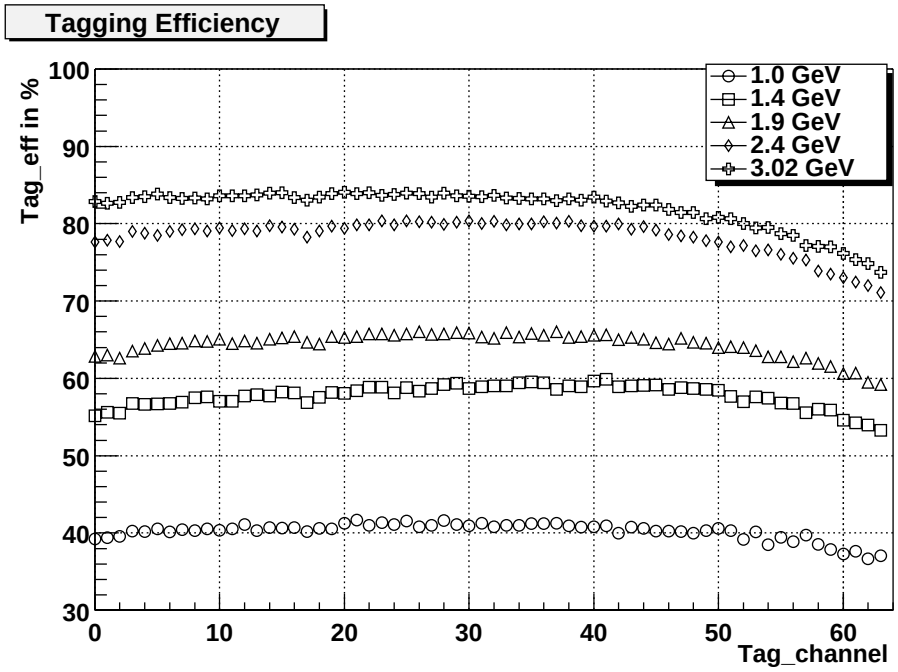

Figure 3.22: Tagging efficiency versus tag-channel i for several primary electron energies.

Correction to radiation damage of the leadglass detector

After a certain time in the beam the leadglass detector gets *brown* due to radiation damage[7]. Owing to the radiation damage the leadglass crystal becomes less transparent which causes a decrease of the detection efficiency for low energetic photons and therefore a decrease of the measured tagging efficiency for the low tag-channels. This effect can be visualized by plotting the ratio of the tagging efficiency of a reference run, taken e.g. at the begin of a beamtime period with a good detector, to an ordinary tagging efficiency run. An increasing ratio for low tag-channels (Figure 3.23 top) indicates radiation damage. In such a case normally the HV of the photomultiplier tube is increased to compensate for this effect. In some cases this radiation damage was however recognized too late so that a correction via the analysis software became necessary.
To the ratio plotted in Fig. 3.23 top, a polynomial is fitted. The corrected tagging efficiency values are obtained by dividing the measured values by the polynomial. As the absolute value of the tagging efficiency might be different, the coefficient for the absolute normalization is set to one in the polynomial. After correction the ratio is plotted again in the lower part of Fig. 3.23. A polynomial fitted to it results in a straight line. For the example shown, the corrections are on the order of 3 % for the lowest tag-channels and they reach zero around tag-channel 30.

[7]This effect can be cured after a beamtime period by the irradiation with UV light.

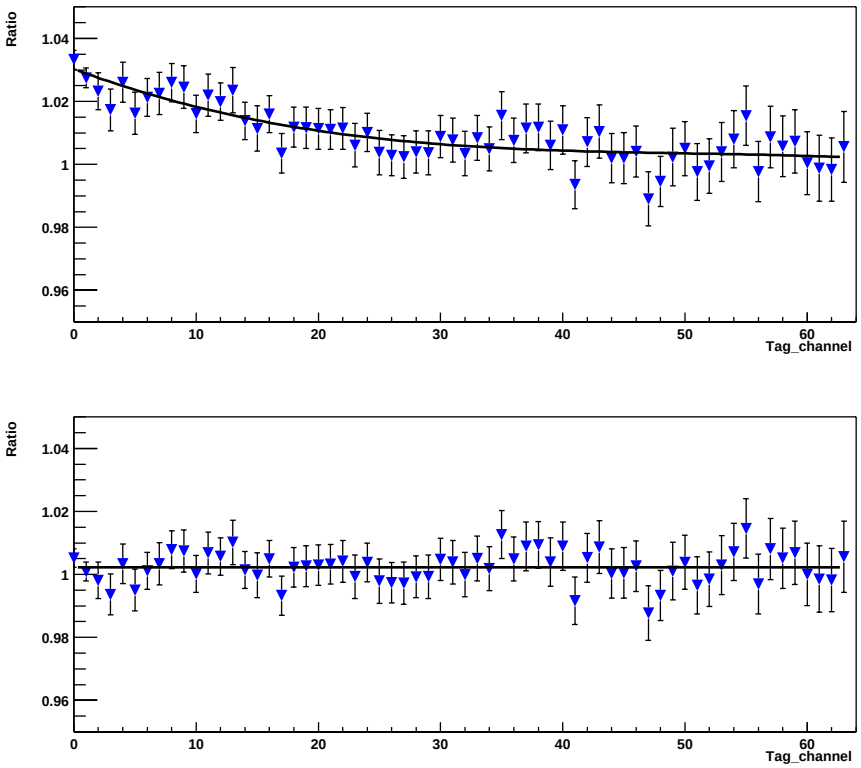

Figure 3.23: Top: ratio of tagging efficiencies of a reference run to the tagging efficiency measured with a *brown* leadglass detector; Bottom: same ratio after correction as described in the text.

3.6.2 Attenuation of the photon flux

The flux of tagged photons $\phi^i_{\gamma,tag}$ reaching the target is obtained via equation 3.38. Electromagnetic interactions (mainly pair production) attenuate the photon flux which is *seen* by the target atoms with increasing target length L. After passing a distance x in material with a radiation length X_0 the incoming flux ϕ_0 decreases to

$$\phi(x) \;=\; \phi_0 \cdot e^{-\frac{x}{X_0}} \tag{3.55}$$

This effect has to be taken into account for the determination of cross sections and can be treated via a mean flux $\phi_{mean}(L)$

$$\phi_{mean}(L) \;=\; \frac{1}{L}\int_0^L \phi(x)\,dx \;=\; \frac{1}{L}\int_0^L \left(\phi_0 \cdot e^{-\frac{x}{X_0}}\right) dx \;=\; \phi_0 \cdot \frac{X_0}{L}\left(1 \;-\; e^{-\frac{L}{X_0}}\right) \tag{3.56}$$

Which can be written in terms of a correction factor c_ϕ as

$$\phi_{mean}(L) \;=\; \phi_0 \cdot c_\phi \tag{3.57}$$

For the butanol target an effective attenuation length X_0^{mean} has to be calculated out of the attenuation lengths X_0^i of its constituents $i = C, H, O$.

$$\frac{1}{X_0^{mean}} \;=\; \frac{P^C}{X_0^C} \;+\; \frac{P^H}{X_0^H} \;+\; \frac{P^O}{X_0^O} \tag{3.58}$$

		^{12}C	^{9}Be	butanol	^{6}LiD
length	L[mm]	15.00	10.00	28.77	25.90
eff. density	ρ_{eff} [g/cm^3]	1.706	1.848	0.605	0.447
radiation length	X_0 [g/cm^2]	42.70	65.19	42.19	90.05
eff. rad. length	$X_0^{eff} = X_0/\rho_{eff}$ [mm]	250	353	697	2014
corr. factor	c_ϕ	0.971	0.986	0.979	0.993
target density	F_t [$10^{-7}\mu$barn^{-1}]	1.2824	1.2348	1.3996	6.97

Table 3.4: Parameters for the flux attenuation in the targets. The effective density ρ_{eff} for ^{12}C is from [Sau98], for butanol and ^{6}LiD $\rho_{eff} = \rho \cdot f_f$ where f_f is the filling factor (see Section 2.3) . The radiation lengths are from [Tsa74]. The correction factors c_ϕ are calculated via equations 3.56 and 3.57. The target density F_t for ^{12}C and ^{9}Be is $F_t = \rho_{eff} \cdot L \cdot N_A/M$ with N_A the Avogadro constant and M the molar mass. The target densities for butanol and ^{6}LiD have been calculated in Section 2.3.3. Note that for ^{6}LiD the dilution factor is included in the effective nucleon polarizations.

Where the weighting factors P^i are given by

$$P^i = \frac{n^i \cdot M^i}{M_{but}} \tag{3.59}$$

With n^i the number of atoms $i = C, H, O$ in the butanol molecule C_4H_9OH, M^i their molecular weights, and M_{but} the molecular weight of butanol.
Data have also been taken with carbon and beryllium targets for the measurement of unpolarized photoabsorption cross sections. Furthermore, a double polarized measurement has been performed with a ^{6}LiD target. The parameters of all targets are given in table 3.4 where the effective attenuation length of ^{6}LiD has been calculated analog to equation 3.58.
The described attenuation of the photon flux is dominated by pair production. The use of an (energy independent) radiation length X_0 corresponds to the absorption coefficient for pair production at infinite energy $\mu_p(\infty)$. In the ELSA energy range μ_p deviates between 3% and 8% from the asymptotic value [EPD97]. As the corrections c_ϕ are on the order of 2%, a 5% change of this value due to the energy dependence of μ_p would generate a variation of the cross section by 1 per mill which can be neglected with respect to other systematic uncertainties (Section A.1).

3.7 Calculation of cross sections

Now all terms have been discussed which are necessary to define a total photohadronic cross section $\sigma(\nu)$.

$$\sigma(\nu) = Y(\nu) \cdot \Phi_\gamma(\nu) \cdot \frac{1}{F_t} \tag{3.60}$$

With $Y(\nu)$ the hadronic rate, $\phi_\gamma = (\epsilon_{tag} \cdot c_\phi)^{-1}$ and F_t the target density.

Calculation of unpolarized cross sections

Prior to the double polarized experiment the GDH-detector was tested by measurements with unpolarized carbon and CH_2 targets. The total photoabsorption cross section per nucleon is e.g. given for carbon as

$$\sigma_C(\nu) \;=\; \left(\left(\frac{Y(\nu)}{\epsilon_{tag}(\nu)} \right)_C \;-\; \left(\frac{Y(\nu)}{\epsilon_{tag}(\nu)} \right)_{empty} \right) \cdot \frac{1}{c_\phi^C} \cdot \frac{1}{F_t^C \cdot n_N^C} \tag{3.61}$$

Here the hadronic rate is measured with a target, in this case carbon, and without. The *empty* measurement is necessary to subtract the number of events which have not produced in the target but somewhere else along the photon beamline.
As already mentioned, the tagging efficiency has been measured routinely every few hours and especially if something in the beamline changed. For the analysis a parameter file exists which assigns to each data-run its corresponding tagging efficiency run. Therefore, the tagging efficiency values for the target and empty term in equation 3.61 do not have to be necessarily identical.
The constants c_ϕ^C and F_t^C are given in Table 3.4, and n_N^C is the number of nucleons. The target consists of natural carbon which has an 1.1% admixture of ^{13}C to ^{12}C. The effective number of nucleons is $n_N^C = 12.011$ in this case.
From the measurements on CH_2 and C the photoabsorption cross section on the proton $\sigma_p(\nu)$ can be extracted via

$$\sigma_p(\nu) \;=\; \frac{1}{2} \left(\sigma_{CH_2}(\nu) \;-\; \sigma_C(\nu) \right) \tag{3.62}$$

Results of these measurements can be found in [Mic01]. [Hel97] and [Sau98] give the results from the pilot experiment which was performed with the same detector in the PHOENICS areal at the ELSA accelerator.
For systematic checks during the double polarized experiment, some data were taken with an additional carbon or beryllium target which was placed behind the tip of the cryostat of the polarized target. Similar to equation 3.61 the carbon or beryllium cross section per nucleon is now given by

$$\sigma_{Be,C}(\nu) \;=\; \left(\left(\frac{Y(\nu)}{\epsilon_{tag}(\nu)} \right)_{(Be,C)+but} \;-\; \left(\frac{Y(\nu)}{\epsilon_{tag}(\nu)} \right)_{but} \right) \cdot \frac{1}{c_\phi^{Be,C}} \cdot \frac{1}{F_t^{Be,C} \cdot n_N^{Be,C}} \tag{3.63}$$

Where now the runs with the butanol target alone serve as *empty* measurements. For beryllium $n_N^{Be} = 9.00$ as the isotope ^{9}Be is the only stable one.
Results of these unpolarized measurements will be given in Section 5.1.1[8].

Double polarized cross sections for the proton

The major task of this thesis is the determination of helicity dependent total photoabsorption cross section differences $\sigma_{3/2}(\nu) - \sigma_{1/2}(\nu)$ of the proton and the neutron. Here the proton

[8] Runs with the additional beryllium and carbon targets can also be used in the double polarized analysis, as the nuclei in these external targets cannot contribute to $\sigma_{3/2} - \sigma_{1/2}$.

part will be discussed.

$$\left(\sigma_{3/2}(\nu) - \sigma_{1/2}(\nu)\right)_p \;=\; \left(Y_{3/2}(\nu) \;-\; Y_{1/2}(\nu)\right) \cdot \frac{1}{\epsilon_{tag}(\nu) \cdot c_\phi^{but}} \cdot \frac{1}{F_t^{but} \cdot P_t} \cdot \frac{1}{P_{circ}(\nu)} \tag{3.64}$$

With $Y_{3/2,1/2}(\nu)$ the hadronic rate for photon and nucleon spin parallel or antiparallel, respectively. As the veto-deadtime correction and the pseudorandom correction are applied for each scaler block separately, possible differences of these corrections for the two helicity states are automatically taken into account.
The target polarization is measured at the begin and the end of a polarization period, in between an exponential decay is assumed. For each beamtime period a parameter file exists with the starting time of a data run and the corresponding longitudinal target polarization at this time. With this information and the value of a system clock which was also written to the data file, the target polarization P_t can be calculated for each single event during a run. The previously mentioned parameter file contains besides the polarization information of the target, also the longitudinal electron polarization at the tagging radiator for each run. With the knowledge of the primary electron energy E_0, the circular polarization of the photons $P_{circ}(\nu)$ can be calculated via equation 2.6.
The tagging efficiency is not applied for the both helicity states separately as it does not depend on the photon helicity (see Section 4.1). The constants c_ϕ^{but} and F_t^{but} can be found in Table 3.4.

Double polarized cross sections for the neutron

The double polarized measurement on the neutron has been performed with a ^{6}LiD target. As has been shown in Section 2.3.3 not just the neutrons are polarized in ^{6}LiD but also the protons. The GDH-detector can not discriminate between events that were produced on the proton or the neutron, respectively. The experimentally obtained difference of hadronic rates $\Delta Y(\nu) = Y_{3/2}(\nu) - Y_{1/2}(\nu)$ is the sum of the proton and the neutron contribution

$$\Delta Y(\nu) \;=\; \Delta Y^p(\nu) + \Delta Y^n(\nu) \tag{3.65}$$

The cross section differences $\Delta\sigma(\nu) = \sigma_{3/2}(\nu) - \sigma_{1/2}(\nu)$ are given by

$$\Delta\sigma^p(\nu) \;=\; \Delta Y^p(\nu) \cdot \frac{1}{\epsilon_{tag}(\nu) \cdot c_\phi^{LiD}} \cdot \frac{1}{F_t' \cdot P_{eff}^p} \cdot \frac{1}{P_{circ}(\nu)} \tag{3.66}$$

and

$$\Delta\sigma^n(\nu) \;=\; \Delta Y^n(\nu) \cdot \frac{1}{\epsilon_{tag}(\nu) \cdot c_\phi^{LiD}} \cdot \frac{1}{F_t' \cdot P_{eff}^n} \cdot \frac{1}{P_{circ}(\nu)} \tag{3.67}$$

In these three equations four unknowns appear: $\Delta\sigma^p(\nu)$, $\Delta\sigma^n(\nu)$, $\Delta Y^p(\nu)$ and $\Delta Y^n(\nu)$, so it is not possible to obtain $\Delta\sigma^n(\nu)$ from these equations alone. However, $\Delta\sigma^p(\nu)$ has been measured at the same experiment with the polarized butanol target so that it can be inserted in the above equations. $\Delta\sigma^n(\nu)$ now reads [Roh03]

$$\Delta\sigma^n(\nu) \;=\; \Delta Y(\nu) \cdot \frac{1}{\epsilon_{tag}(\nu) \cdot c_\phi^{LiD}} \cdot \frac{1}{F_t' \cdot P_{eff}^n} \cdot \frac{1}{P_{circ}(\nu)} \;-\; \Delta\sigma^p(\nu) \cdot \frac{P_{eff}^p}{P_{eff}^n} \tag{3.68}$$

The target density F_t' is given in Table 3.4 and the effective proton and neutron polarizations $P_{eff}^{p,n}$ have been defined in equations 2.26 and 2.27.
The above formula for the extraction of $\Delta\sigma^n$ is valid only if the nucleons in the deuteron can be treated as *quasifree*. The binding energy of the deuteron is just about 2.22 MeV. Nevertheless, calculations [Are97] show that pion photoproduction on the deuteron deviates significantly from the process on the free nucleon in the energy region of the Δ-resonance. *Caveats* have been formulated [Are00] that one can extract in a simple manner the spin asymmetry on the neutron from the spin asymmetry on the deuteron. For the present experiment the situation is different as the lowest photon energy is 680 MeV. Calculations, including final state effects, have been performed up to photon energies of 550 MeV [Dar03]. These calculations show that above 450 MeV the pion production on the deuteron cannot be distinguished from the quasifree process. This statement remains valid for higher energies [Fix04]. The doubly polarized cross sections on the neutron have therefore be extracted according to Eq. 3.68 without corrections to nuclear effects of the deuteron.

3.8 Identification of η-mesons

It has already been mentioned that the detector system has not been designed to identify partial reaction channels. However, it is possible to identify the production of single η-mesons within a limited kinematical range as will be shown in this section.
In Figure 3.13 it is demonstrated that in the forward detectors STP and FFW_T protons and deuterons can be separated from $\beta = 1$ particles. For the photoproduction of a single particle X on the proton, $\gamma p \rightarrow pX$, the four-momentum conservation reads

$$\begin{pmatrix} \nu \\ \vec{p_\gamma} \end{pmatrix} + \begin{pmatrix} m_p \\ 0 \end{pmatrix} = \begin{pmatrix} E_p \\ \vec{p_p} \end{pmatrix} + \begin{pmatrix} E_X \\ \vec{p_X} \end{pmatrix} \tag{3.69}$$

Particles which cannot be detected directly can be identified via the *missing mass* method. From the above equation the missing mass m_{miss} is defined as

$$\begin{aligned} m_{miss}^2 &= E_X^2 - p_X^2 \\ &= (\nu + m_p - E_p)^2 - p_\gamma^2 - p_p^2 + 2p_\gamma p_p \cos\vartheta_p \end{aligned} \tag{3.70}$$

If a single particle X is produced and if all kinematic quantities of Eq. 3.70 are known, m_{miss} is then equal to the mass of particle X.
For the present detector system all kinematical quantities can be determined for the special case of the outgoing proton hitting the far forward detectors.

- The photon energy ν and the momentum p_γ are determined by the tagging system.
- A hit in one of the STAR-rings gives the proton angle ϑ_p. If a hit occurs in two adjacent rings the proton angle can be obtained by taking the arithmetic mean of the ϑ angles of the two rings. Such an event is valid as the STAR-rings have a certain geometrical overlap. If two non-neighbouring rings have an entry or if more than two rings fired, the event cannot be reconstructed uniquely.

- The total energy of the proton E_p and its momentum p_p is determined by the mass of the proton m_p and the relativistic γ-factor

$$E_p = \gamma m_p \quad \text{and} \quad p_p = \sqrt{E_p^2 - m_p^2} \tag{3.71}$$

The corresponding β of the protons can be written in terms of the distance between the target and the detector d_t, the time-of-flight t_{tof} and the proton angle ϑ_p.

$$\beta = \frac{v}{c} = \frac{d_t}{t_{tof} \cdot \cos\vartheta_p \cdot c} \tag{3.72}$$

t_{tof} is the time the protons need from the target to the detector. It is obtained via $t_{tof} = t_{\beta=1} + t_{diff}$ where $t_{\beta=1} = d_t/c$ is the time $\beta = 1$ particles need to travel the distance d_t. These particles lead to a vertical line in the QDC versus TDC spectrum (Fig. 3.13), t_{diff} is the time difference between an entry in the TDC spectrum and this vertical line.

The selection of protons in the forward direction is performed by a two-dimensional cut in the QDC versus TDC spectrum of the STP (Fig. 3.24). Here just the increasing part of the proton-hook is selected as the protons have to cross the STP to reach one of the STAR-rings for a determination of ϑ_p. β is then calculated according to the above equations. If the energy of the protons is high enough they can reach the FFW_T. In such a case β is calculated for both detectors and the arithmetic mean of both values is used for further analysis. Now it is

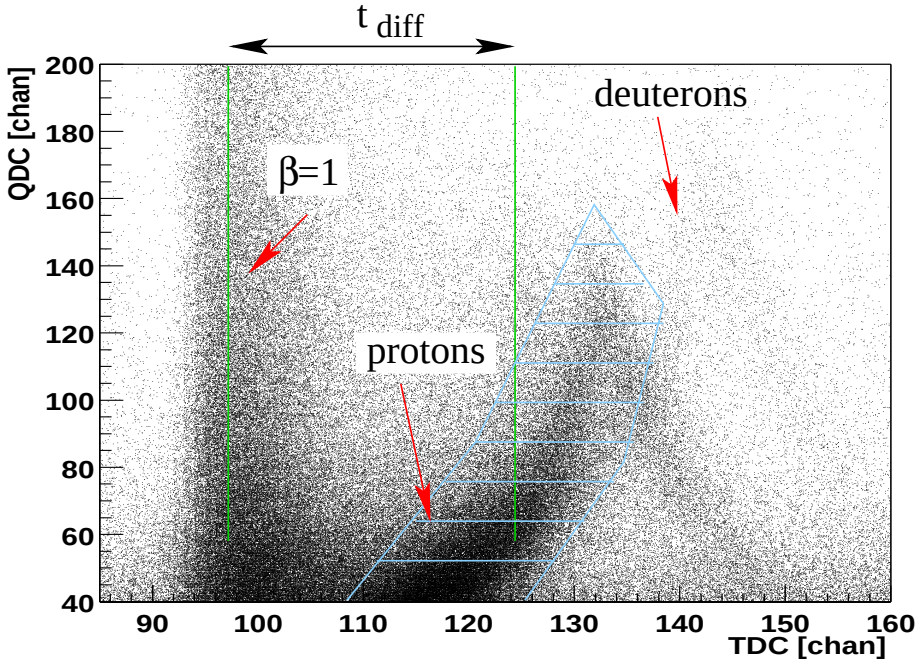

Figure 3.24: QDC versus TDC spectrum of the STP. The vertical band denotes β =1 particles. Protons are selected via a 2-D cut (hatched area).

possible to generate a missing mass spectrum. For single particle production, peaks should appear at the masses of the produced particles. In the ELSA energy range it is possible

decay mode	Branching ratio	# of TP's	# of SW's
$\eta \rightarrow \gamma\gamma$	39.2 %	0	2
$\eta \rightarrow \pi^0\pi^0\pi^0$	32.2 %	0	≥ 3
$\eta \rightarrow \pi^+\pi^-\pi^0$	23.1 %	2	2

Table 3.5: η decay modes with branching ratios ([PDG00]) and the corresponding characteristic hitpatterns.

to produce multiple particles (e.g. two or more pions) with a single photon. This multi-particle partial reaction channels generate background in the missing-mass spectrum. The information of the other detector modules can be used to reduce this background.
Each module of the GDH detector consists of a trigger plate (TP) and a sandwich part (SW). With this arrangement it is possible to distinguish charged and uncharged particles. The η-meson has three major decay modes, which are given together with their branching ratios in Table 3.5. Each of the η decay modes leaves a characteristic signature in the hitpattern of the detector modules. The modules used for the detection of the decay particles are BW, CEN, and FW. The characteristic hitpattern, i.e. the number of trigger plates and sandwich parts that have to be fired, is summarized for the three decay channels in Table 3.5.

The two photon decay of the η-meson has the largest branching ratio and it gives also the cleanest signature with the hits in two sandwich modules.
For the 3 π^0 decay mode only uncharged decay particles occur. The uncharged pions cannot reach any detector module before they decay into two gammas because of their mean livetime of $8 \cdot 10^{-17}s$. Altogether 6 gammas are produced in this decay mode. Due to very bad granularity of the detector (two or more gammas can hit a single module) and the limited angular acceptance (the far forward parts are used for the proton identification) a hit in three or more sandwich modules is used as a signature of this decay channel.
In the last decay channel with the two charged and one uncharged pion the limited granularity of the detector again causes some problems. Simultaneous hits in the TP and the SW of a single module can be caused by charged particles which have enough energy to reach the sandwich part. The same signature can also be caused by the interaction of a charged pion in the TP and the detection of a photon from the π^0 decay in the SW. Therefore, the background of this decay channel can only be reduced partially.

The missing mass method presented in this section has been used for the identification of η-mesons. The same method has also been applied by [Mic01] for the identification of ρ- and ω-mesons near their production threshold. The acceptance of the GDH detector for the identification of η-mesons has been obtained via simulation calculations by [God02].
Results of missing mass spectra for the three decay channels of the η-meson will be given in Section 5.1.2.

Chapter 4

Systematic studies

In this chapter the influence of various quantities to the final cross section results will be studied.
Possible sources of *false asymmetries* will be investigated first (Section 4.1). In Section 4.2 the influence of the QDC cuts on the cross sections will be discussed. After that, an extrapolation to the missing solid angles in the forward and backward directions will be given in Section 4.3. Finally, Section 4.4 will deal with systematic studies in dependence of the tagging rate.

4.1 Spin studies

It has to be assured that the measured helicity dependent cross section difference $\sigma_{3/2}(\nu) - \sigma_{1/2}(\nu)$ is generated by the interaction of polarized photons with the polarized target and does not come from any intrinsic asymmetries of the experimental setup. For this purpose all possible sources of such *false asymmetries* have been investigated.

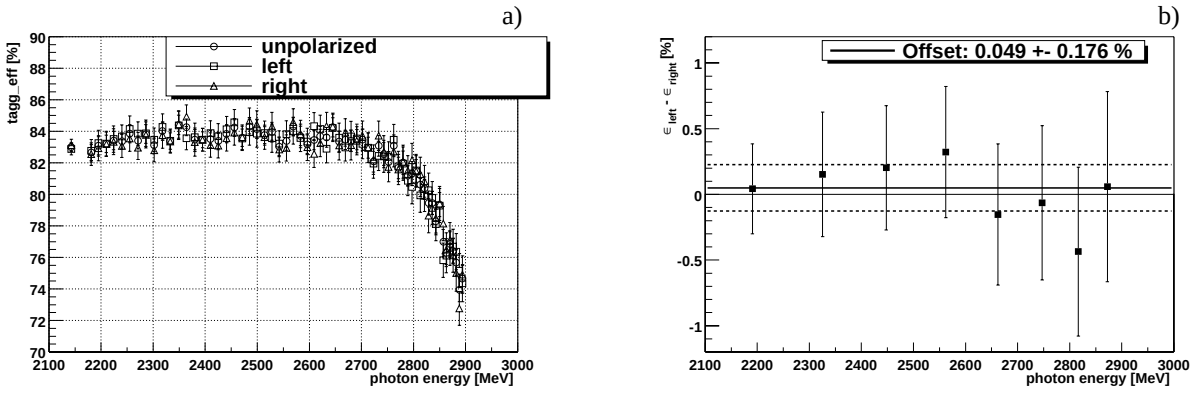

Figure 4.1: a) The tagging efficiencies for the both helicity states of the photon ϵ_{left} and ϵ_{right} together with the unpolarized case ϵ_0. b) The difference $\epsilon_{left} - \epsilon_{right}$ plotted versus the photon energy. The dashed lines give the statistical error band of a fitted straight line.

The **tagging efficiency** is the first possible source. In principle it might be possible that electrons are deflected differently when passing an inhomogeneous magnetic field, according

to their polarization direction. This would cause a helicity dependence of the tagging efficiency ϵ. This quantity has been extracted for both helicity states of the photons +1 and -1 (right and left handed circular polarized photons), separately. The corresponding tagging efficiencies are denoted ϵ_{right} and ϵ_{left}, they are shown for a primary electron energy of 3.02 GeV, together with the unpolarized case ϵ_0, as a function of the photon energy in Figure 4.1 a). No difference can be seen *by eye* between the three data samples. Figure 4.1 b) quantifies this result. The difference $\epsilon_{left} - \epsilon_{right}$ is compatible with zero as is indicated by the offset value of a fitted straight line. The dashed lines denote the statistical error band of the fit. For the data analysis it is therefore sufficient to use one *unpolarized* tagging efficiency ϵ_0 for both helicity states. For its determination (Section 3.6.1) the polarization information of the electrons is simply ignored, and its value is the mean of ϵ_{left} and ϵ_{right}.

The next possible source of *false asymmetries* is the **polarized target**. If the target is unpolarized the helicity dependent cross section difference has to vanish. For this purpose some data have been taken with a polarized beam at a primary electron energy of 1.9 GeV with an unpolarized butanol target, however under the same conditions as during ordinary double polarized data taking. This means that the target was running in frozen spin mode, and that in particular, the field of the internal holding coil was switched on. The cross section difference $\sigma_{3/2}(\nu) - \sigma_{1/2}(\nu)$ extracted under these conditions is shown in Figure 4.2. The data

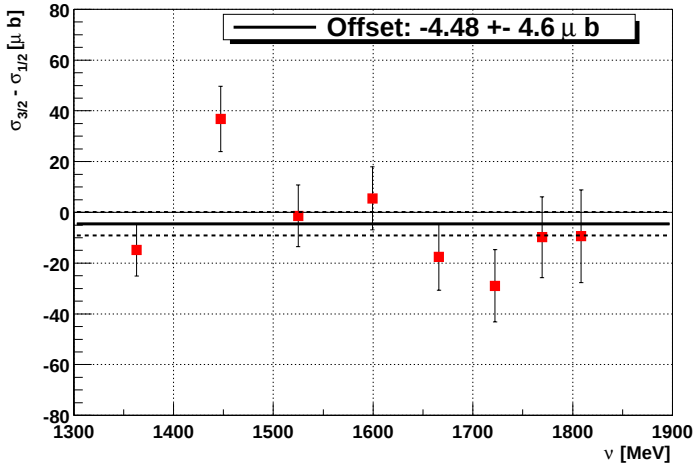

Figure 4.2: The cross section difference $\sigma_{3/2}(\nu) - \sigma_{1/2}(\nu)$ extracted for an unpolarized target, plotted versus the photon energy ν. A fitted straight line is compatible with zero within the error band.

are compatible with zero, furthermore, a change in the direction of the holding field had no influence to this result.

Finally, the polarization direction of the longitudinally polarized protons has been reversed for systematic studies. The possible directions are either *downstream* or *upstream* with respect to the incoming photon beam. If $\sigma_+(\nu) - \sigma_-(\nu)$ denotes the cross section difference for photons with helicity +1 minus photons with helicity -1, this difference should change its sign if the relative nucleon polarization is reversed. Figure 4.3 a) shows this difference versus the photon energy for the two possible directions of the target polarization. A contrary shape can be seen. If the sum $\Delta(\sigma_+(\nu) - \sigma_-(\nu))$ of both data samples is taken, a distribution compatible

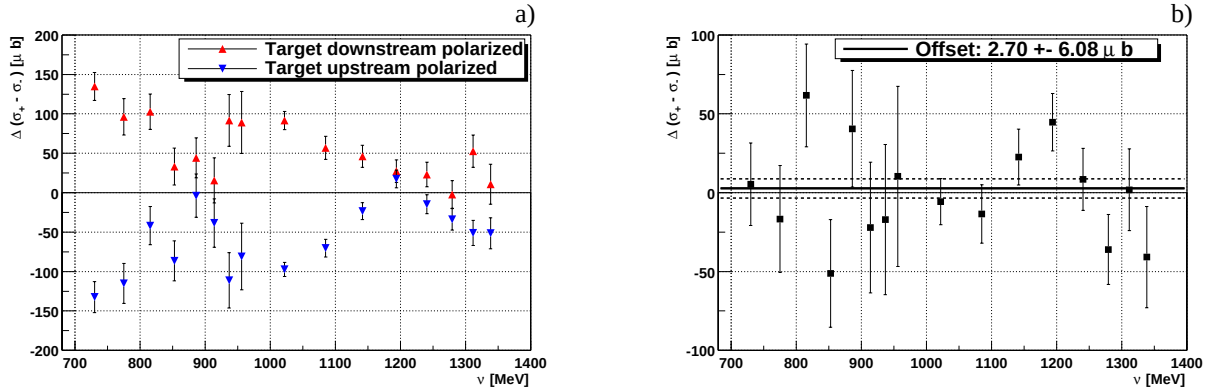

Figure 4.3: a) $\sigma_+(\nu) - \sigma_-(\nu)$ for both possible directions of the target polarization. b) The sum $\Delta(\sigma_+\nu - \sigma_-(\nu))$ of these two samples.

with zero remains (Figure 4.3 b)).
To conclude this section, no asymmetry coming from the experimental setup has been found within the statistical precision.

4.2 Influence of cuts

The cuts in the (mean)-TDC spectra (Section 3.3.1) have been chosen in such a way that for

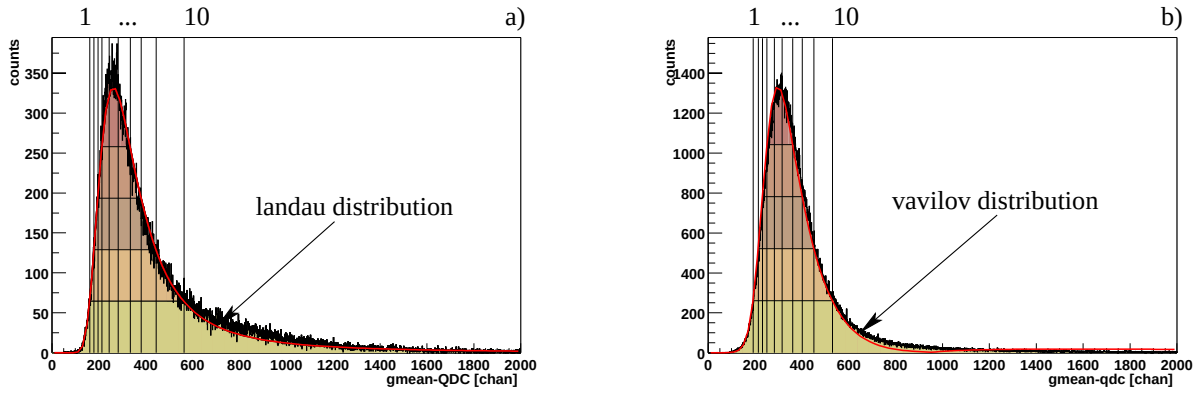

Figure 4.4: Gmean-QDC spectra with 10 cut values (vertical lines) relative to the maximum. In a) a Landau-distribution is fitted to the gmean-QDC spectrum of a central trigger plate whereas in b) a Vavilov-distribution is better suited to fit the spectrum of the STAR trigger plate.

the prompt region no hadronic events are lost and that the random regions are as wide as possible to minimize the statistical error. For a consistency check the width of the random windows has been decreased which caused, besides an increase of the statistical error, no effect. The same effect was obtained by an increase of the prompt windows.
With the cuts in the QDC spectra (Section 3.3.2) the fraction of the electromagnetic background can be limited and therefore the statistical error can be reduced. From a certain value of the QDC threshold on, hadronic events are rejected also, which results in a decrease of

the cross sections. To obtain a quantitative criterion for the cuts, (gmean)-QDC spectra for each detector module are generated under the condition that the corresponding (mean)-TDC has an entry outside the prompt window. In this case electromagnetic background events are enhanced in the QDC spectra. For each detector module these (gmean)-QDC spectra have a different shape. The spectra are divided into five vertically equal spaced regions (see Figure 4.4). The ten QDC cut values (vertical lines) are placed at the intersections of the contour lines with the spectrum. This guarantees that going from one QDC cut to the next, a constant number of entries is rejected and that in all QDC spectra a certain cut number always denotes the same fraction relative to the peak maximum. For practical purposes to obtain the contour lines, Landau- or Vavilov-distributions are fitted to the spectra. Figure 4.4 shows two gmean-QDC spectra where in a) a Landau-distribution is fitted to the spectrum of a central triggerplate whereas in b) a Vavilov-distribution is better suited to fit the spectrum of the STAR triggerplate.
For a systematic study, cross sections have been extracted where the ten different cut values have been applied for the trigger plates of the detector modules. As in the sandwich parts less random background appears, a constant and relative low QDC cut value has been used for these modules. Figure 4.5 displays the influence of the QDC cuts to the cross sections. In a)

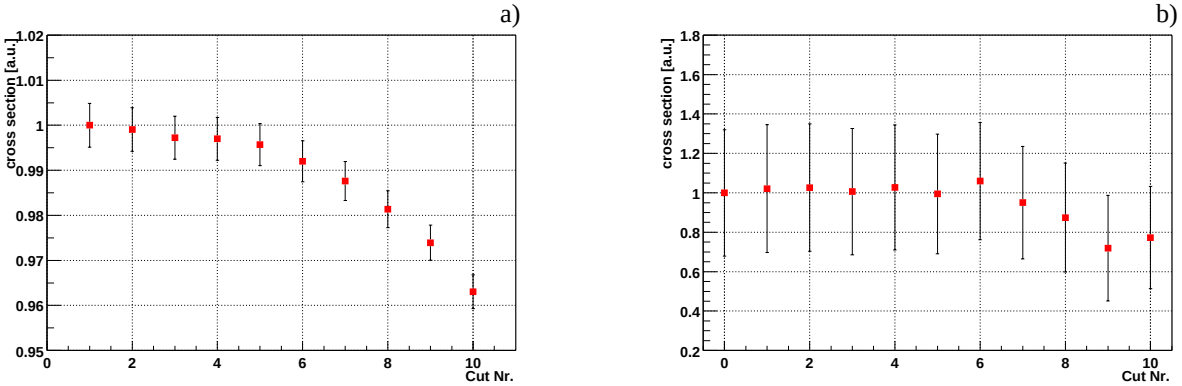

Figure 4.5: The influence of the QDC cuts for a) unpolarized cross sections and b) helicity dependent cross sections.

the relative unpolarized cross section is plotted versus the cut number. This ratio is taken relative to a cross section which has been extracted without the application of QDC cuts. It can be seen that from a certain cut value on the cross section decreases significantly as then also hadronic events are rejected. For the final analysis cut nr.'4' has been chosen, as the unpolarized cross section has not decreased within the statistical error of 0.5 %. In Fig 4.5 b) the same ratio is plotted for the helicity dependent cross section difference $\sigma_{3/2}(\nu) - \sigma_{1/2}(\nu)$ versus the cut number. As the statistics is worse in this case no significant deviation from one can be found in this case. However, also for the double polarized analysis, QDC cut nr. '4' has been used.

4.3 Extrapolation to missing solid angles

In forward direction the GDH-detector has an acceptance gap of $\vartheta = 1.5°$ for the passage of the primary photon beam. In backward direction 6° are not covered due to cryo components of the polarized target. The STAR-detector (Section 2.4.2) has been designed for an extrapolation of the measured cross sections to the uncovered region in forward direction ($\vartheta \to 0°$). The principle of the GDH-detector is to detect at least one hadron that was produced in a photohadronic interaction. The *critical* events are those where just one hadron is emitted in the forward direction. For the present investigation events are selected with a single track in the forward direction, i.e. just one hit in one of the 18 STAR segments and no hit in the BW-, CEN- and FW-modules is requested in the analysis. Under these conditions a cross section has been extracted for each of the 9 STAR rings. It has to be mentioned that the information of the STAR rings just has been used for the assignment of the ϑ angle to the event. For the timing information (prompt or random event) the (position independent) mean-TDC of the STP and/or the FFW_T has been used. An energy dependent cross section is obtained for every segment. Due to the limited statistics these cross sections are *rebinned* to a single energy bin for every segment and the entries of the two segments forming one ring are finally added together to obtain a ϑ-dependence of the cross section under the above mentioned conditions. Figure 4.6 a) shows the unpolarized differential cross section

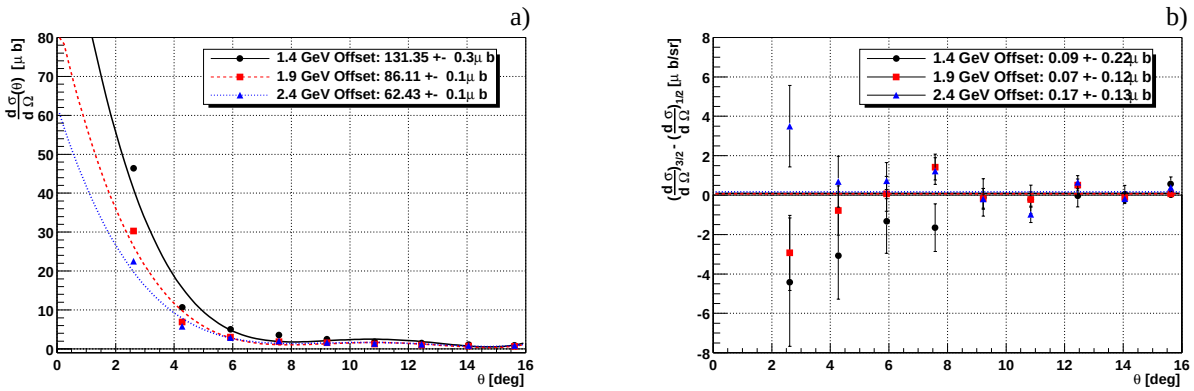

Figure 4.6: Differential cross sections for the special case of a single track in the forward direction; a) unpolarized b) polarized.

$d\sigma(\vartheta)/d\Omega$ versus the ϑ angles of the star rings, for three primary electron energies. For the extrapolation $\vartheta \to 0°$, polynomials are fitted to the data points. The cross section values at 0° are printed as *offset* values in the figure. Although these cross sections are in the order of 100 μb their contribution to the total cross section can be neglected as the uncovered solid angle in the forward direction is just 0.017% $\cdot 4\pi$. The contribution from the acceptance gap would therefore be about 0.02% of the total cross section.
In Figure 4.6 b) helicity dependent differential cross sections $(d\sigma/d\Omega)_{3/2} - (d\sigma/d\Omega)_{1/2}$ are plotted against the ϑ angles of the star rings, for three primary electron energies. Within the statistics no ϑ-dependence can be seen for this quantity and fitted straight lines are compatible with zero within error bars.
In the backward direction no segmented detector exists. For an estimate of the contribution that *escapes* through the hole in the BW detector, cross sections are calculated with events which have only hits in the BW_T and BW_S modules. Due to the Lorentz-boost it is clear

that the fraction that is missed in the backward direction is highest for the lowest primary electron energy of 1.0 GeV. For this energy the cross section calculated under the above mentioned conditions is 4.1±0.3 μb. Under the assumption of a flat differential cross section in this backward angular range, the cross section in the missing solid angle is estimated to 0.25 μb. As the unpolarized cross section is on the order of 180 μb, this is a relative contribution of 0.1 %. The double polarized cross section difference $\sigma_{3/2} - \sigma_{1/2}$ is zero within statistics, for the BW modules only. Therefore, it is assumed that the acceptance gap in the backward direction has no influence on this quantity.

4.4 Rate studies

During some beamtime periods the intensity of the electron beam was not constant but varied in a certain range. In Figure 3.18 the correction factor due to the veto deadtime was shown, where the tagging rate varied between 500 kHz and 1.5 MHz. The other correction directly dependent on the current of the electron beam is the pseudorandom correction (Section 3.4.1). For a systematic study and for a cross check of the analysis software, cross sections have been extracted for several intervals of the tagging rate, separately. Figure 4.7 a) shows

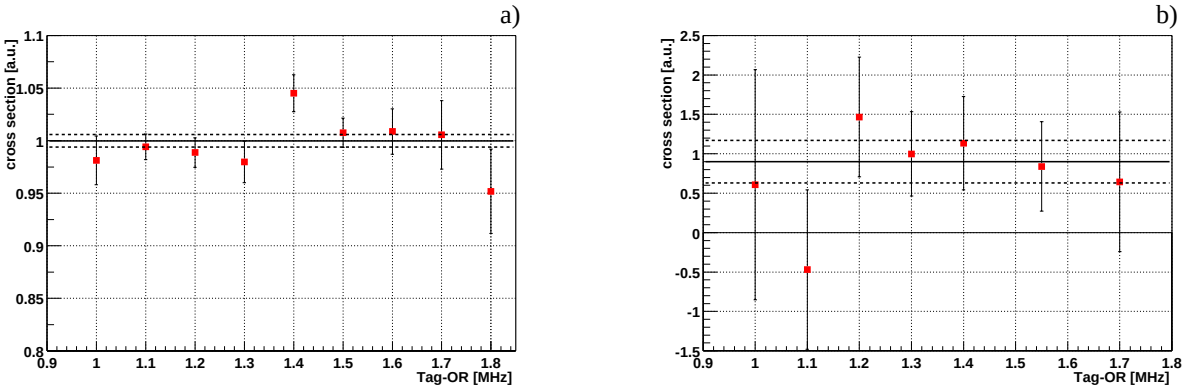

Figure 4.7: Unpolarized a) and double polarized cross sections b) versus the tagging rate relative to a reference cross sections which includes all tagging rates.

the rate dependence of the unpolarized cross section relative to a reference cross section which includes all tagging rates. Even at 1.8 MHz no deviation from one can be observed within error bars. The same also holds for the double polarized cross sections shown in Fig. 4.7 b).

Chapter 5

Results

In this chapter first the unpolarized results will be discussed in Section 5.1. After that the doubly polarized results will be presented in Section 5.2.
A detailed discussion about the sources of systematic uncertainties can be found in Appendix A.1.

5.1 Unpolarized results

This section starts with the presentation of total photoabsorption cross sections on carbon and beryllium targets (Sec.5.1.1). Thereafter, results for the identification of η-mesons via the missing mass technique will be given in Section 5.1.2.

5.1.1 Total photoabsorption cross sections

During each doubly polarized beamtime period several data-sets have been taken with carbon and beryllium targets. As the unpolarized total photoabsorption cross sections are well-known, the measurements with these external targets provide a systematic check of the experimental setup and the analysis method. Although just a few hours were used for these measurements during every beamtime period, the statistical precision of the present data surpasses published data.
For ^{9}Be the total photoabsorption cross section per nucleon is plotted versus the photon energy for several primary electron energies E_0 in Fig. 5.1. The data of each bin fit smoothly together and are in agreement with literature data [Hey71] [Ara83]. A comparison with carbon data [Muc99] indicates that already beryllium shows the *universal* behaviour [Ahr85] of the excitation function which has been confirmed for nuclei until lead [Muc99] and even uranium [Ara90] [Fro94].
Figure 5.2 shows the total photoabsorption cross section per nucleon for ^{12}C obtained with the present setup together with literature data [Bia96] compared to proton data [Arm72] [Mac96]. The comparison between the carbon and the proton data exhibits three major differences.

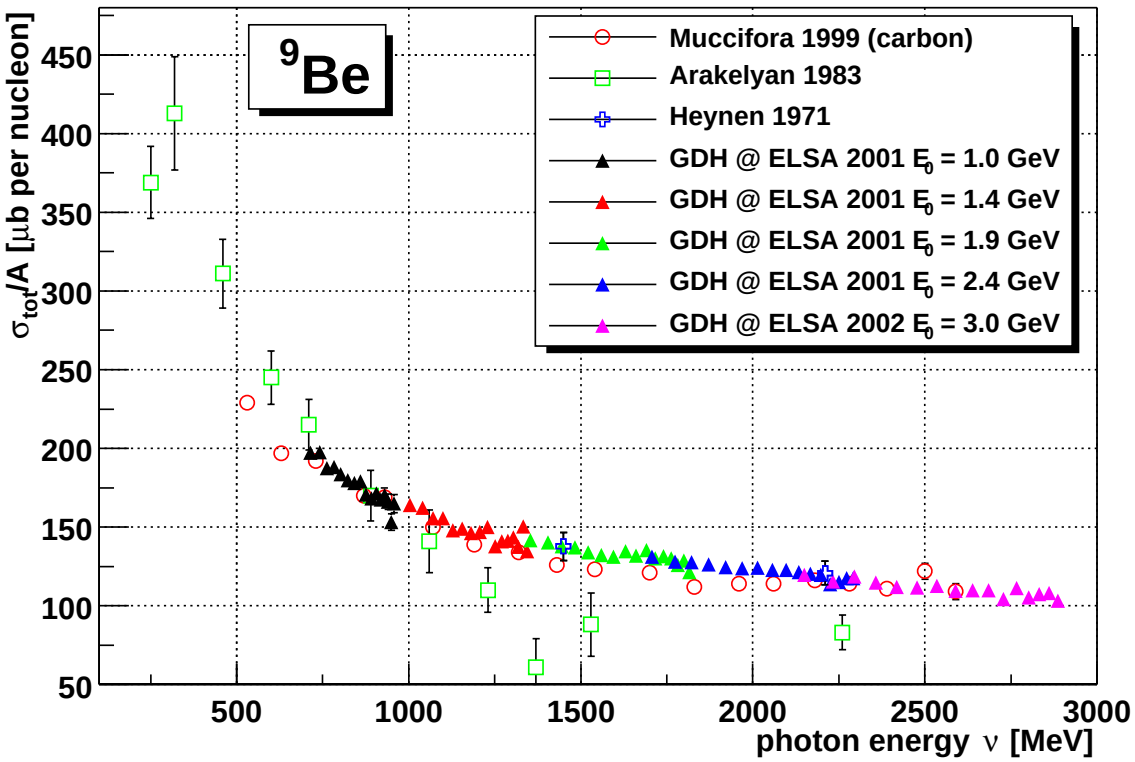

Figure 5.1: The total photoabsorption cross section per nucleon for ^{9}Be for several primary electron energies compared to literature data [Hey71] [Ara83] and data obtained from a carbon target [Muc99].

- The Δ resonance is damped and broadened.
- No N* resonances appear in the excitation functions of the nuclei.
- The photoabsorption cross sections on nuclei are *shadowed* for high energies, compared to the nucleon case.

A lot of theoretical work has been performed in the past decades to explain these effects. The damping of the cross section in the energy region of the Δ resonance can be explained by *Pauli blocking* [Car92]. In this case the phase space of forming a Δ is decreased through interaction with neighbouring nucleons according to the Pauli principle. Furthermore, the damping and the broadening of the Δ resonance is influenced by the Fermi motion of the nucleons and the propagation of a formed Δ trough the nucleus (see e.g. [Koc84] for a Δ-hole calculation).

The reason for the disappearance of the $D_{13}(1520)$-resonance and higher resonances in the photoexcitation spectra of nuclei has not finally been found. This effect cannot be explained by Fermi motion of the nucleons alone. Although generating a depletion of the $D_{13}(1520)$-resonance, a model [Gia94] assuming quark exchange between adjacent nucleons, cannot explain the complete absence of the $D_{13}(1520)$ and higher resonances in nuclei. The same holds for transport calculations using the BUU-model [Eff97].

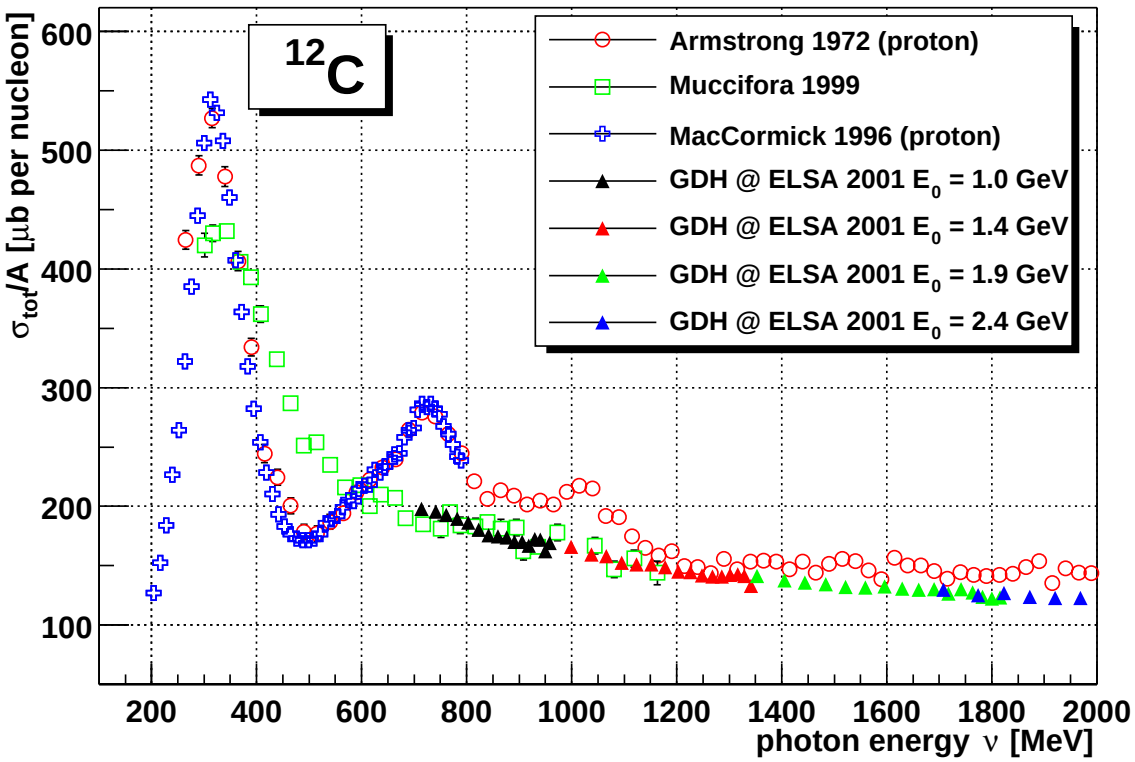

Figure 5.2: Comparison of the total photoabsorption cross section per nucleon on ^{12}C [Bia96] to the proton [Arm72] [Mac96].

For higher energies the cross section per nucleon is lower for nuclei than for the free proton. This so called *shadowing* has already been understood qualitatively in the early vector meson dominance models [Got69] [Bro69]. For a quantitative treatment an increase of the effective ρ mass in the nuclear medium has to be taken into account [Fal00].
In Figure 5.3 the high energy part of the photoabsorption cross sections is given. The shadowing effect is clearly visible for the case of carbon. Furthermore, the present data overshoot the most recent literature data [Muc99] by about 5% in the photon energy interval 1.3 - 2.0 GeV. This deviation is larger than the given systematic uncertainties. An older data set by Brookes et al. [Bro73] seems to confirm the trend of the present data.

5.1.2 Missing mass spectra for the η-meson

The missing mass technique has been discussed in Section 3.8. Here the missing mass spectra for the η-meson obtained with unpolarized targets will be shown.
If η-mesons are produced on free protons a sharp peak at the η-mass appears in the missing mass spectrum. If an η is produced, however, on protons bound in a nucleus, the peak in the missing mass spectrum is washed out due to the Fermi-motion.
Prior to the doubly polarized measurements, data have been taken with unpolarized carbon and CH_2 targets as a test for the detector setup. The missing mass on the proton M^p_{miss} can

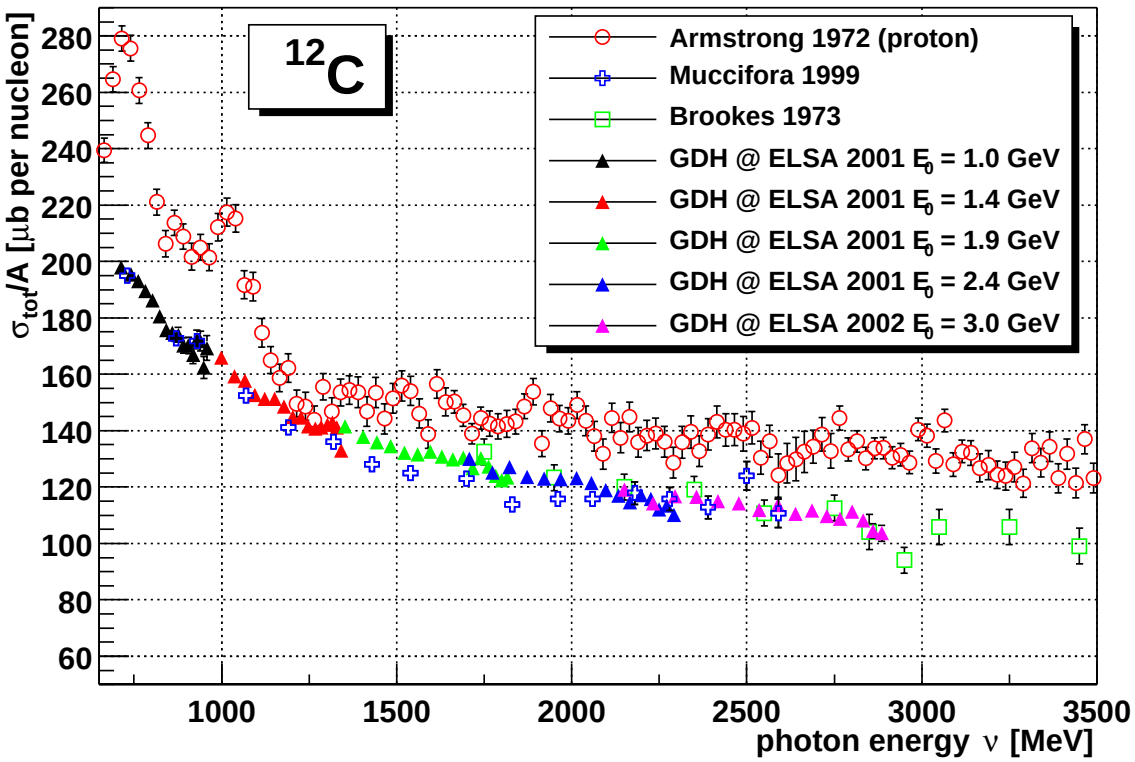

Figure 5.3: Total photoabsorption cross section per nucleon for ^{12}C compared to literature data for carbon [Muc99] [Bro73] and proton [Arm72].

be obtained from the difference of the missing mass on CH_2 $M_{miss}^{CH_2}$ and on carbon M_{miss}^{C}.

$$M_{miss}^{p} = \frac{1}{2}\left(M_{miss}^{CH_2} - M_{miss}^{C}\right) \tag{5.1}$$

In Figure 5.4 the missing mass spectra for both targets are given together with the spectrum for the free proton. The number of counts has been normalized to the incoming photon flux. In this figure the η-decay into two gammas has been selected[1]. Due to the Fermi motion broad missing mass distributions appear for carbon and CH_2. For the free proton this background is highly suppressed and a peak around the η-mass (547.3 MeV [PDG00]) remains. The experimental width of 10 MeV is by far larger than the intrinsic width of 1.2 keV [PDG00]. The missing mass spectra for the η-decay channel to $\pi^+\pi^-\pi^0$ are shown in Fig. 5.5. Due to the limited granularity of the detector system the background cannot be suppressed completely (cf. Section 3.8). A peak in the region of the η-mass remains, where the experimental width is again by far larger than the intrinsic width.
For the η-decay channel into three π^0's no statistical significant peak in the missing mass spectrum of the free proton can be observed. One reason is, that this decay channels exhibits a lower branching ratio than the decay into two gammas. Furthermore, the selection of the triple π^0 decay requires hits in three or more sandwich parts of the central detector in coincidence with a proton in the far forward part. Almost no events *survive* this restrictive condition.

[1]The hitpatterns of the detector modules for the different $\eta-$decay channels are given in Table 3.5.

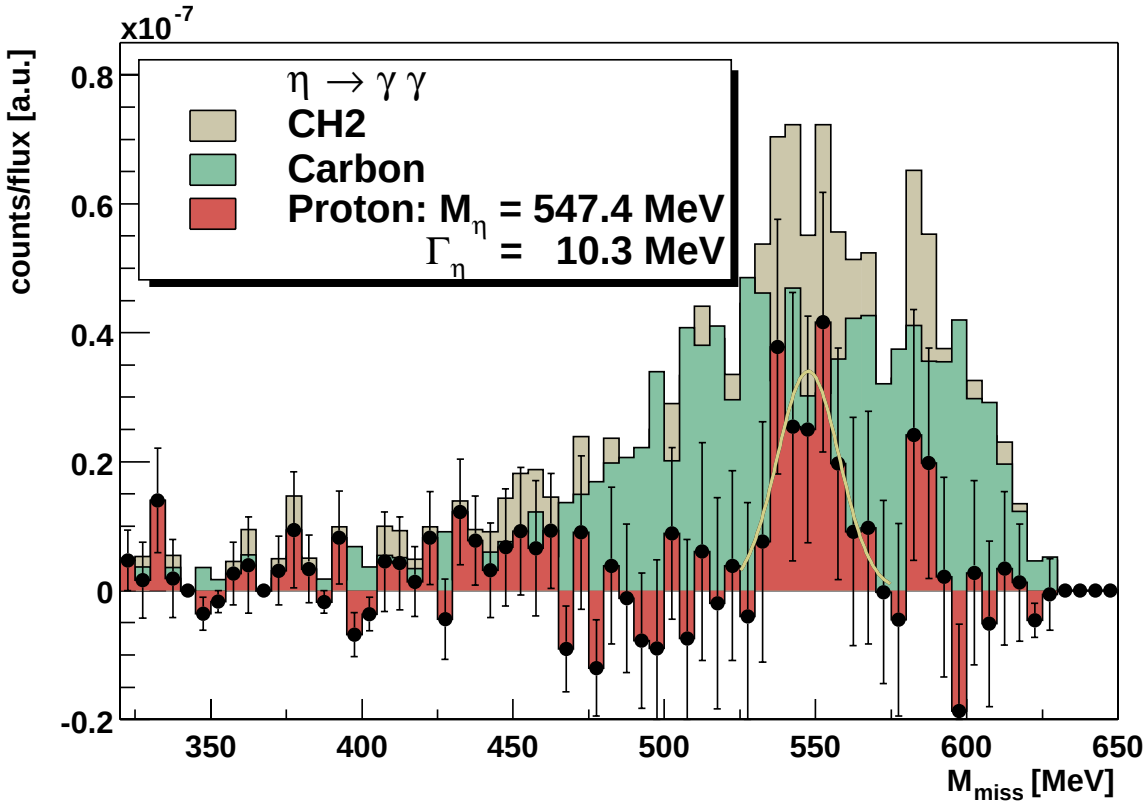

Figure 5.4: Missing mass spectrum for η-production on CH_2 and carbon. The result for the free proton is obtained from the difference. The selected decay channel is $\eta \to \gamma\gamma$.

5.2 Results from doubly polarized experiments

In Section 5.1.1 it has been shown that it is possible to measure total photoabsorption cross sections with the present experimental setup and the analysis method. No false asymmetries appear as has been demonstrated in Section 4.1. After this preparatory work has been completed, doubly polarized results will be presented in this section.
The difference $\Delta\sigma = \sigma_{3/2} - \sigma_{1/2}$ of helicity dependent total photoabsorption cross sections on the proton will be given in Section 5.2.1. With this information the separated cross sections $\sigma_{1/2}$ and $\sigma_{3/2}$ can be extracted (Section 5.2.3). Then, values for the GDH integral and the spin polarizability on the proton will be presented in Section 5.2.4. Finally, Section 5.2.5 deals with helicity dependent photoabsorption cross sections and their contribution to the GDH integral on the neutron.

5.2.1 $\Delta\sigma$ on the proton

During the GDH experiment at MAMI the helicity dependence of photoabsorption on the proton has been investigated in the photon energy range 200 MeV $\leq \nu \leq$ 800 MeV. The present experiment at ELSA has some overlap as its photon energy range covers 680 MeV - 2.9 GeV. The helicity dependent difference of total photoabsorption cross sections

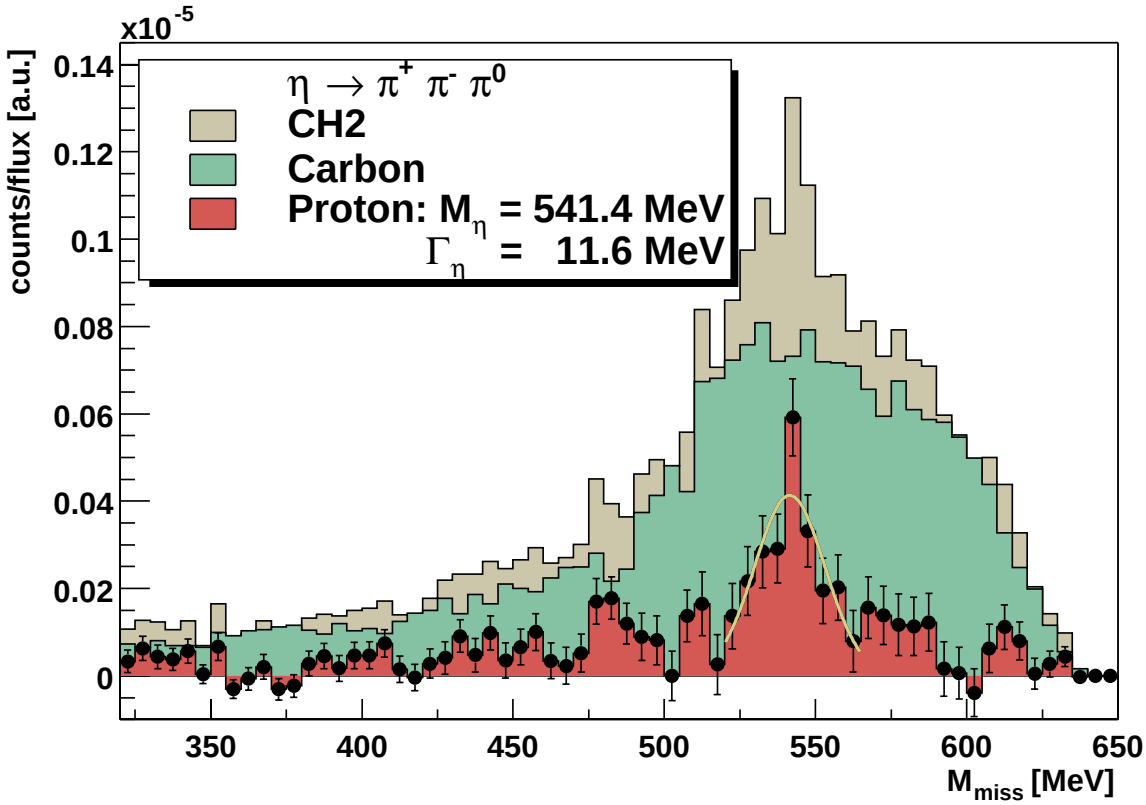

Figure 5.5: Same as Fig. 5.4 for the decay channel $\eta \to \pi^+\pi^-\pi^0$.

$\sigma_{3/2}(\nu) - \sigma_{1/2}(\nu)$ has already been published for the MAMI experiment [Ahr01]. Preliminary results from ELSA have been shown by the GDH collaboration on various conferences [Spe01] [Nau02] [Gra03] [Kri03] and data up to 1.82 GeV have been published recently [Dut03].
In Figure 5.6 the $\Delta\sigma$ data, as analysed in this thesis, are plotted for the six primary electron energies as a function of the photon energy. In the energy overlap regions the data fit smoothly together and they also agree with the MAMI data of [Ahr01]. The resonance structure known from the unpolarized total photoabsorption cross section on the proton [Arm72] is even more distinct in the doubly polarized case.
Figure 5.7 gives an overview of the resonances involved. In this figure just the contribution to the single pion photoproduction is shown. The resonances are calculated assuming a Breit-Wigner shape (Eq. 5.3 in Section 5.2.2) where the parameters have been taken from [PDG00].
The most prominent resonance is the Δ-resonance ($P_{33}(1232)$) with its large positive contribution to $\Delta\sigma$. In the second resonance region the positive contribution of the $D_{13}(1520)$ is partly compensated by that from the $S_{11}(1535)$. This resonance also couples to the η-meson, with comparable strength. The Roper-resonance ($P_{11}(1440)$) gives another negative contribution to $\Delta\sigma$. The third resonance region is dominated by the $F_{15}(1680)$, with small contributions of the $D_{33}(1700)$ and $S_{11}(1650)$, where the latter also couples to the η-meson. At higher energies the $F_{37}(1950)$ exhibits significant strength.

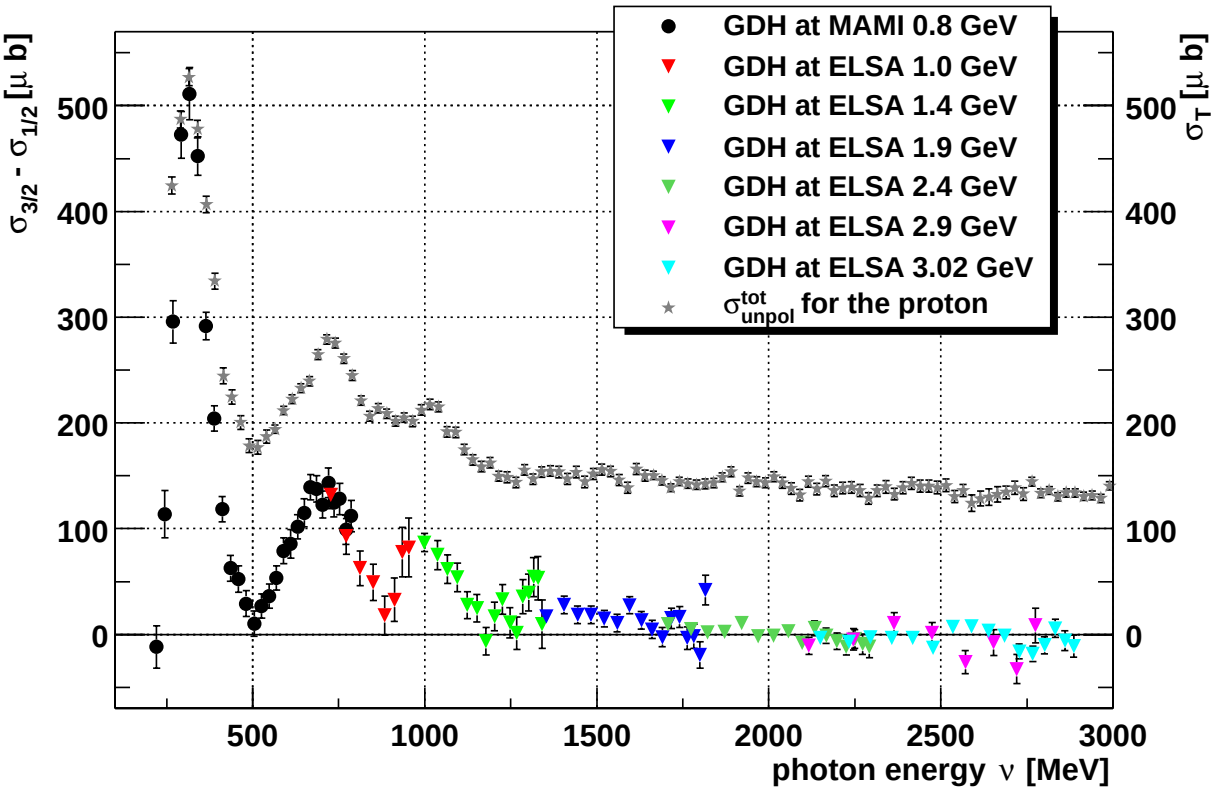

Figure 5.6: Difference of total photoabsorption cross sections $\sigma_{3/2}(\nu) - \sigma_{1/2}(\nu)$ for the proton versus the photon energy. Results for the six primary electron energies are compared to the low energy data from MAMI [Ahr01] and the unpolarized photoabsorption cross section [Arm72].

Rebinning

As the tagging system provides 64 channels, 64 data points are available for each primary electron energy. For practical purposes it is useful to group several channels together to new energy bins to obtain a better statistical precision. Usually 4 channels of the original data set with 64 channels are grouped together to form 16 new bins. The value of the rebinned data points y^{reb} is calculated from the weighted mean of the unbinned data points y_i

$$y^{reb} \;=\; \frac{1}{w}\sum_{i=1}^{N} w_i \; y_i \tag{5.2}$$

Where the weights w_i are obtained from the statistical errors σ_i of the original data points $w_i = 1/\sigma_i^2$, and $w = \sum w_i$. N is the number of data points that are grouped together to form a new bin, e.g. $N = 4$ in the above example. The statistical error of y^{reb} is $1/\sqrt{w}$.

Adding data sets

Since data have been taken at six primary electron energies, the data sets have a certain overlap covering the photon energy range 680 MeV $\leq \nu \leq$ 2.9 GeV without gaps. Figure 5.8

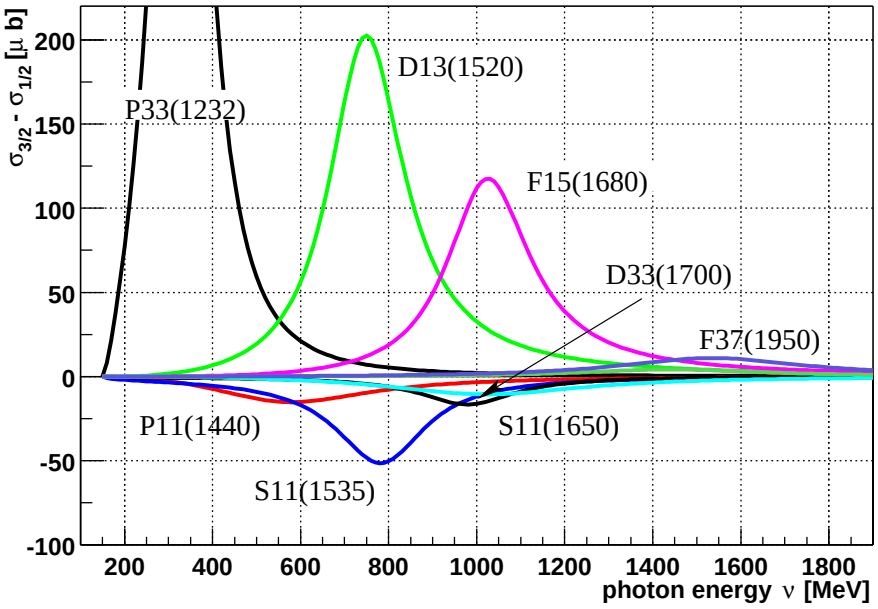

Figure 5.7: Single pion part of the resonances contributing to $\Delta\sigma$.

shows schematically the overlap region of two data sets, where data set 2 represents the higher primary electron energy. The width of the tagger channels decreases smoothly from

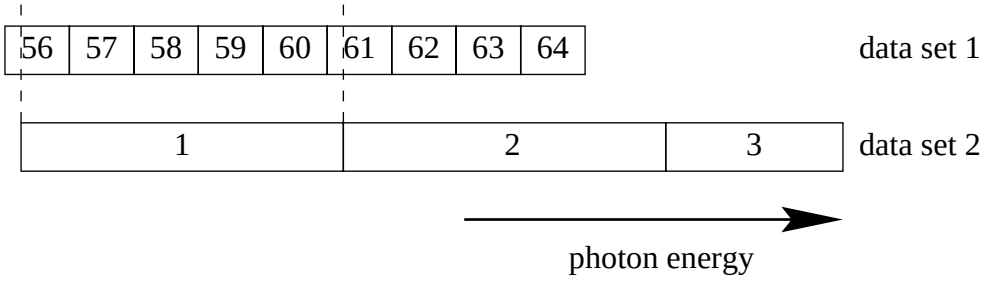

Figure 5.8: The overlap region of two data sets at different primary electron energies.

channel 1 to channel 64, however the first two channels are more than a factor 4 wider than the rest. Therefore, the set with the higher primary electron energy determines the bin widths in the overlap region when averaging the data sets.
In a first step the bins of data set 1 are grouped together according to the bins of set 2. For the example given in Fig. 5.8, tag channels 56 to 61 and 61 to 64 of set 1 are grouped together, using Equation 5.2 in order to form two new bins. The contributions of channels 56 and 61 are weighted in accordance with their overlap with the bins of data set 2.
In the next step the weighted mean (Eq. 5.2) of both data sets is calculated for the bins in the overlap region. Averaged data will be shown in the forthcoming figures when comparing to model predictions.

5.2.2 Theoretical descriptions

A Breit-Wigner parametrization

The resonant contribution to the total photoabsorption cross section can be described via a Breit-Wigner parametrization [Wal69]. In the following the notation of [Don98] is used. The helicity dependent photoabsorption cross sections $\sigma^{res}_{1/2}$ and $\sigma^{res}_{3/2}$ can be written in terms of the helicity amplitudes $A^R_{1/2}$ and $A^R_{3/2}$

$$\sigma^{res}_{1/2(3/2)} = \sum_R \left(\frac{k_R}{k}\right)^2 \cdot \frac{W^2\Gamma_G\Gamma_R}{(W^2-M_R^2)^2+W^2\Gamma_R^2} \cdot \frac{4M}{M_R\Gamma_R^{(0)}} \cdot \left(A^R_{1/2(3/2)}\right)^2 \tag{5.3}$$

where the sum runs over all resonances R. M denotes the mass of the proton, M_R the mass of the respective resonance and $W = \sqrt{M^2+2M\nu}$ is the total energy. k is the momentum of the incoming photon in the cm system, $k = (W^2-M^2)/2W$ and $k_R = k(W \equiv M_R)$. The W-dependence of the resonance widths is given by

$$\Gamma_G = \Gamma_R^{(0)} \cdot \left(\frac{k}{k_R}\right)^{j_1} \cdot \left(\frac{k_R^2+X_R^2}{k^2+X_R^2}\right)^{j_2} \tag{5.4}$$

$$\Gamma_R = \Gamma_R^{(0)} \cdot \left(\frac{q}{q_R}\right)^{2l_R+1} \cdot \left(\frac{q_R^2+X_R^2}{q^2+X_R^2}\right)^{l_R+1} \tag{5.5}$$

where the damping parameter X_R is 0.16 GeV for the Δ-resonance and 0.35 GeV for all other resonances. The three-momentum q of the outgoing pion in the cm system is given as $q = \sqrt{(W^2-(M+m_\pi)^2)(W^2-(M-m_\pi)^2)}/2W$, with m_π the pion mass ($q_R = q(W \equiv M_R)$). The resonance parameters M_R , $\Gamma_R^{(0)}$, j_1, j_2, l_R can be found found in [PDG00] [Eff97]. The following resonances have been taken into account: $P_{33}(1232)$, $P_{11}(1440)$, $D_{13}(1520)$, $S_{11}(1535)$, $S_{11}(1650)$, $F_{15}(1680)$, $D_{33}(1700)$, $F_{35}(1905)$, $F_{37}(1950)$.
Apart from the resonances, also nonresonant (nr) background contributes to $\Delta\sigma$. The following parametrization is taken from [Sim02]

$$(\sigma_{1/2}-\sigma_{3/2})^{nr} = \frac{8\pi^2\alpha_{em}}{M\nu} g^{\Delta\sigma} \tag{5.6}$$

with

$$g^{\Delta\sigma} = \frac{W^2-M^2}{2W^2} \sum_{j=1}^{2} a_j \left(1+\frac{W^2}{Q_R^2}\right)^{\alpha_j^{(0)}} \left(\frac{W^2-W_\pi^2}{W^2-W_\pi^2+W_T^2}\right)^{\beta_j^{(0)}} \tag{5.7}$$

where $W_\pi = M+m_\pi$ is the pion production threshold. The parameters a_j, $\alpha_j^{(0)}$, Q_R and W_T can be found in [Sim02]. The two exponents $\beta_j^{(0)}$ have not been taken from [Sim02]. These parameters have been determined by a fit to the doubly polarized photoabsorption data on the proton which resulted in $\beta_1^{(0)} = 0.356$ and $\beta_2^{(0)} = 2.23$.
The result of this Breit-Wigner parametrization is shown in Figure 5.9 together with data in the resonance region. For illustration, also the nonresonant background part is displayed separately. Although this parametrization just takes single pion decay widths into account and neglects interference effects between resonances, the description of the data is quite

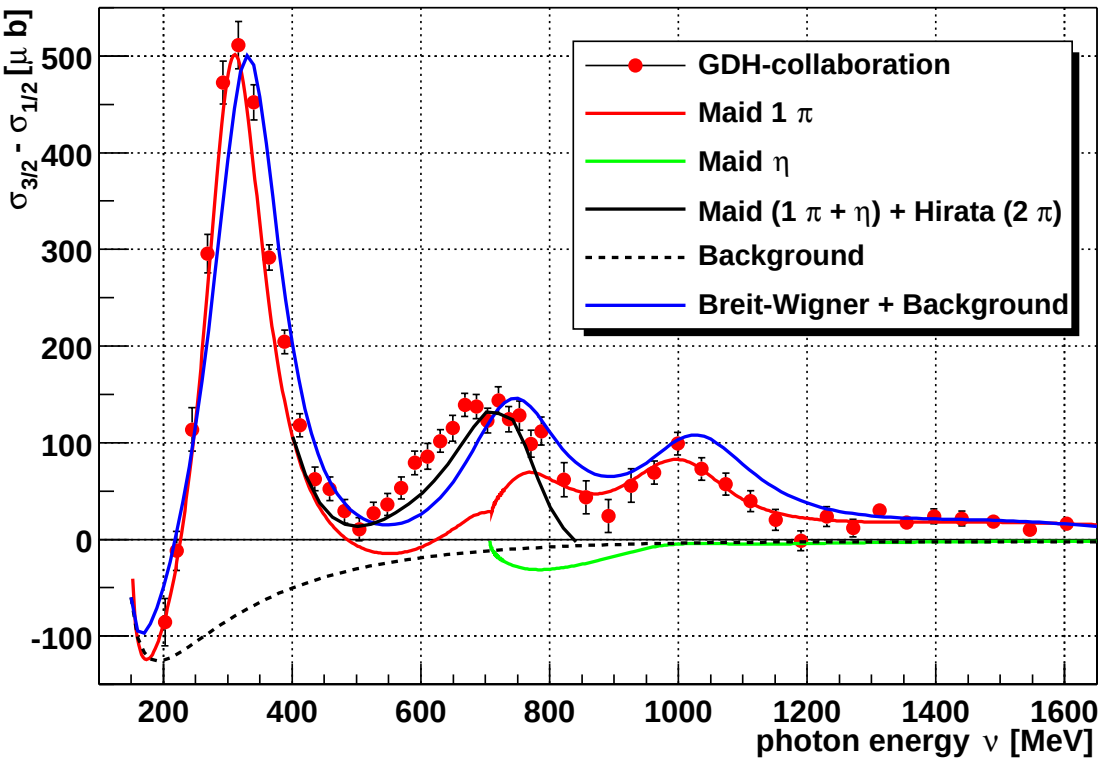

Figure 5.9: Data in the resonance region are compared to results from a simple Breit-Wigner parametrization with a phenomenological background (Eqs. 5.3 to 5.7). Furthermore, the single-pion and η partial reaction channels calculated by [MAID03] are shown. The MAID values are supplemented by the double pion contribution from [Hir03] and shown by the black line between 400 MeV and 850 MeV.

reasonable. Figure 5.10 presents a closer look to the 2nd and 3rd resonance regions. The two-pion production channel is already open in the second resonance region, furthermore, three resonances overlap almost completely in this energy regime (see Fig. 5.7). The shortcomings of the parametrization prevent a correct description of the data in this energy range. The $F_{15}(1680)$ dominates the 3rd resonance region, where the single pion production channel seems to be the most important process. Around 1500 MeV another resonant structure appears in the data. This *fourth* resonance region contains the $F_{35}(1905)$ and $F_{37}(1950)$ resonances. Looking at even higher energies the zero crossing of the data around 2100 MeV is well described by the given parametrization.

The unitary isobar model

In the unitary isobar model (UIM) [Dre99] the background is described by effective Lagrangians for Born terms and vector meson exchange. The resonances are modeled via Breit-Wigner functions with energy dependent widths. Unitarity is taken into account to obtain the correct phases of the pion photoproduction multipoles. The results of the UIM can be obtained from the program *MAID* which uses all four-star resonances of [PDG00] up

to W=2 GeV. In the current solution [MAID03] the resonances are parametrized in terms of the helicity amplitudes $A_{1/2(3/2)}$. The UIM describes the single-pion photo- and electroproduction, in a modified version also the η production is treated [Chi02]. The results are provided by the program *ETA-MAID* which is also available at [MAID03].

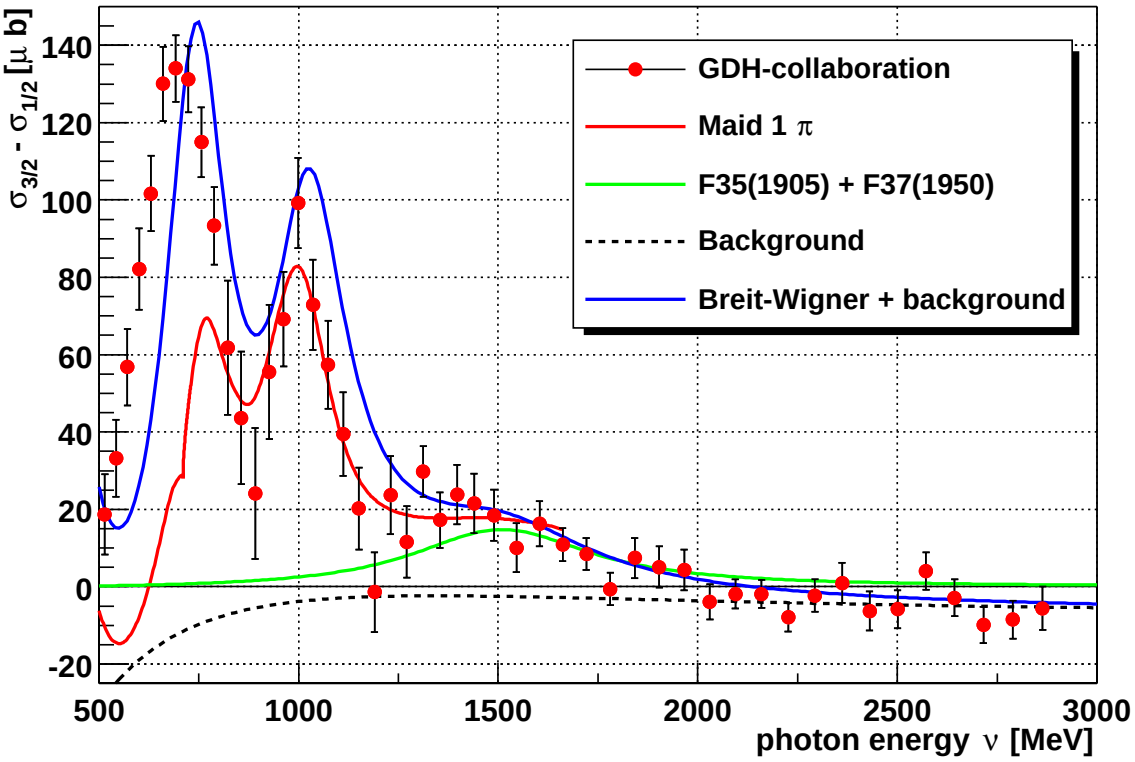

Figure 5.10: Data in the 2nd and 3rd resonance region are shown together with the single-pion contribution of [MAID03] and a Breit-Wigner parametrization. The $F_{35}(1905)$ and $F_{37}(1950)$ give rise to a *4th* resonance region around 1500 MeV before the data cross zero above 2000 MeV.

The approach of the UIM treats the physical processes generating background, and it takes into account interference effects of the contributing resonances and also interferences of background with resonances. This leads to a perfect description of the data in the Δ-resonance region (see Fig. 5.9). The deviation of the UIM and the data in the second resonance region is due to the two-pion production. A rough phenomenological approach of this partial reaction channel is given in [Dre99b]. More sophisticated calculations can be found in [Nac01] [Nac02] and in [Hol01] [Hol04] where the RPR[2]-model has been used. The sum of the single pion and η partial reaction channel from [MAID03] and the double pion contribution from [Hir03] leads to a better agreement with the data in the second resonance region (Fig. 5.9). The strength in the 3rd resonance region is almost completely generated by the single pion channel. In the current version of *MAID* also the $F_{35}(1905)$ and $F_{37}(1950)$ resonances are included which leads to a proper description of the data in this energy region (see also Fig. 5.10).

[2]Regge plus resonances

Regge phenomenology

The high energy behaviour of total cross sections σ_T is well described by $\sigma_T \sim s^{\alpha^0-1}$ where s is the center of mass energy squared and α^0 is the intercept of the leading Regge trajectory. The intercept α^0 is determined by the spin J and the mass m_t of the exchanged particle via $\alpha^0 = J - \alpha' m_t^2$ where the slope α' is about 0.8-0.9 GeV^{-2}. In [Bia99] a parametrization for the cross section difference $\sigma_{1/2} - \sigma_{3/2}$ of electron scattering is given. The data have been obtained from measurements with longitudinally polarized electrons and polarized ^{1}H, ^{2}H and ^{3}He targets, covering a large Q^2 and W^2 range. For real photons ($Q^2 = 0$) the parametrization simplifies to

$$\sigma_{1/2} - \sigma_{3/2} = \left[2aW^{2(\alpha^0_{a1}-1)}T + fW^{2(\alpha^0_{f1}-1)} + g\frac{lnW^2}{W^2} \right] F \tag{5.8}$$

where α^0_{a1} and α^0_{f1} are the intercepts of the a_1 and f_1 meson trajectories. All necessary parameters have been extracted from fits to the electron scattering data. T takes into account the isospin, $T = \pm 1/2$ for reactions on the proton or neutron, respectively. F is a threshold factor and reduces to a constant in the real photon case

$$F = \left[\frac{W^2 - W_\pi^2}{W^2 - W_\pi^2 + m_r^2} \right]^{1.5} \tag{5.9}$$

with $W^2 = M^2 + 2M\nu$, $W_\pi = 1.12$ GeV the pion electroproduction threshold, and $m_r = 1.26$ GeV a common mass scale which is close to the masses of the exchanged a_1 and f_1 mesons.
The result of this parametrization for the real photon case is shown for photon energies up to 50 GeV in Figure 5.11. The nonresonant background of equation 5.7 has been formulated in such a way that it also exhibits a Regge behaviour for high energies. The parameters $\alpha_j^{(0)}$ can be identified as the intercepts of the a_1 and f_1 trajectories. In [Sim02] these parameters have been obtained together with the factors a_j via fits to polarized deep inelastic electron scattering data. In the present work the parameters $\beta_j^{(0)}$ have been fitted to give a better description of the data in the resonance region. This modification leaves the high energy behaviour unaltered as can be seen in Fig. 5.11. Above ≈ 8 GeV the original and the modified version of [Sim02] are identical. Although the parametrization of [Bia99] fails to reproduce the available data up to 3 GeV, the high energy contribution to the GDH integral differs by less than 1 μb in comparison to the other parametrizations (Section 5.2.4).

5.2.3 Helicity dependent cross sections

The unpolarized carbon and oxygen nuclei in the butanol target prevent a direct determination of the helicity dependent photoabsorption cross sections $\sigma_{3/2}$ and $\sigma_{1/2}$. In the difference $\sigma_{3/2} - \sigma_{1/2}$ the contributions from the unpolarized nuclei cancel. By use of the unpolarized cross section $\sigma_T = (\sigma_{1/2} + \sigma_{3/2})/2$ the helicity dependent cross sections can be separated via

$$\sigma_{3/2} = \sigma_T + \frac{1}{2}(\sigma_{3/2} - \sigma_{1/2}) \tag{5.10}$$

$$\sigma_{1/2} = \sigma_T - \frac{1}{2}(\sigma_{3/2} - \sigma_{1/2}) \tag{5.11}$$

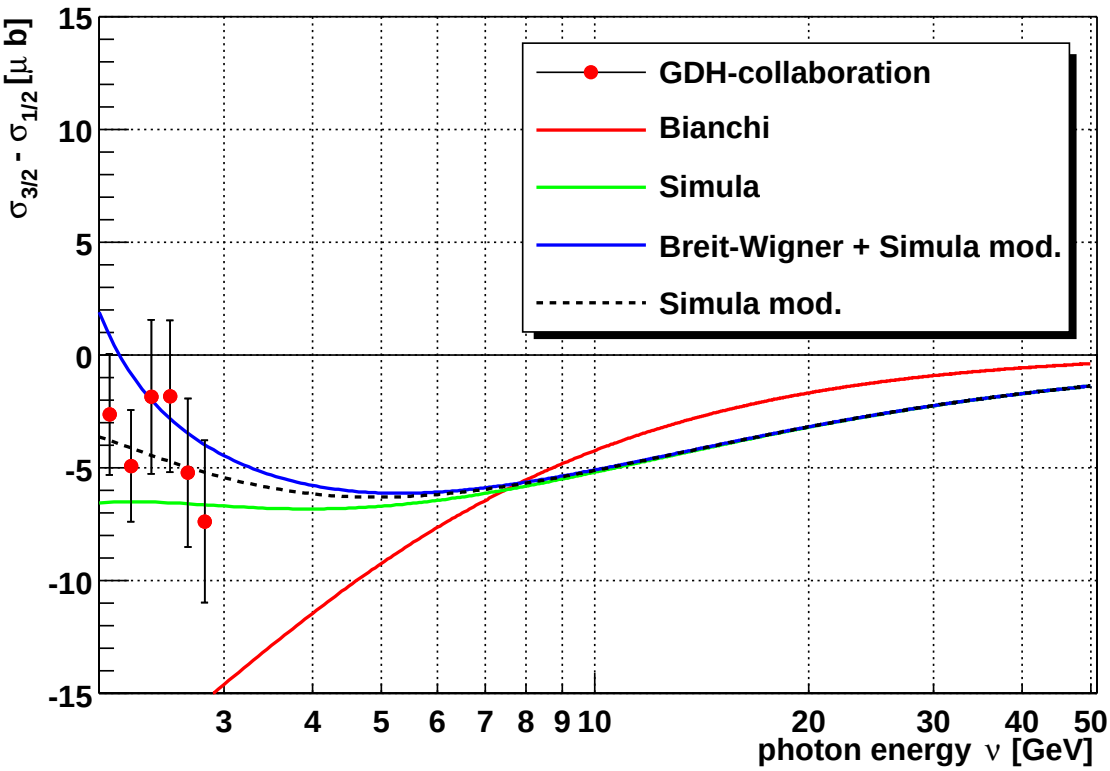

Figure 5.11: Data points above 2 GeV in comparison with Regge approaches of the original and of a modified version of [Sim02] and a parametrization by [Bia99].

The unpolarized photoabsorption cross section σ_T on the proton is experimentally well-known. The data from the particle data group [PDG00] are used, which mainly contain results from [Arm72] and [Blo69]. Furthermore, data from [Mac96] have been taken into account as they cover the energy range 200-800 MeV with the highest statistical precision. To become independent of the energy bins of the literature data, an analytic function has been fitted to the data points. This function includes resonances of the Breit-Wigner shape and background contributions.
Figure 5.12 shows the separated helicity dependent photoabsorption cross sections which have been extracted according to equations 5.10 and 5.11. $\sigma_{3/2}$ dominates the second and third resonance region, the contribution of $\sigma_{1/2}$ to the third resonance region can even be neglected. The $S_{11}(1535)$ contributes solely to $\sigma_{1/2}$, a strong rise of this quantity can be observed above the η-meson production threshold (707 MeV).

In a similar way the helicity asymmetry E can also be obtained with the above mentioned quantities. It is defined as

$$E = \frac{\sigma_{3/2} - \sigma_{1/2}}{\sigma_{3/2} + \sigma_{1/2}} = \frac{\sigma_{3/2} - \sigma_{1/2}}{2 \cdot \sigma_T} \tag{5.12}$$

This quantity is plotted versus the photon energy in Fig. 5.13. The resonant structure of the data is clearly visible up to the *fourth* resonance region around 1500 MeV before the data cross zero slightly above 2 GeV.

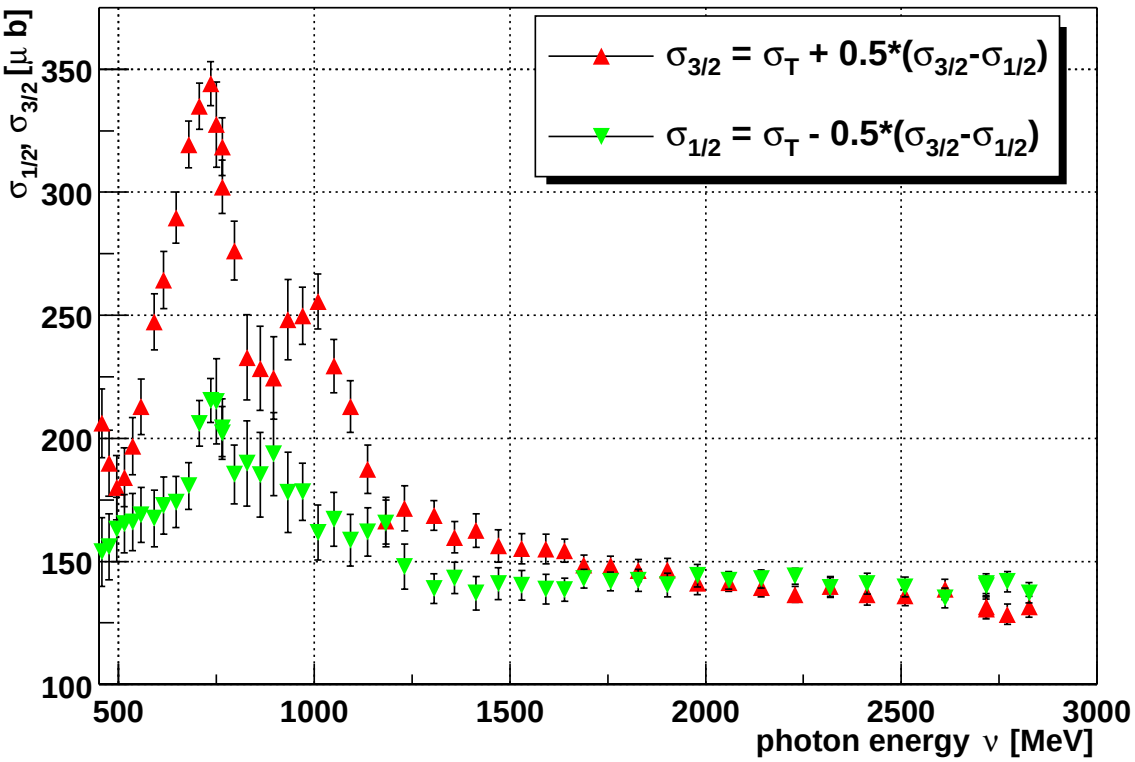

Figure 5.12: Separated helicity dependent photoabsorption cross sections $\sigma_{1/2}(\nu)$ and $\sigma_{3/2}(\nu)$.

5.2.4 GDH integral and spin polarizability

In this section the experimental contribution to the GDH integral and to the spin polarizability will be given and compared to theoretical models.
Together with the previous experiment at MAMI [Ahr01] doubly polarized photoabsorption data are now available in the energy range 200 MeV $\leq \nu \leq$ 2.9 GeV. To compare the experimental results with the GDH sum rule value, the *running* GDH integral I_{GDH} is defined as

$$I_{GDH} = \int_{\nu_0}^{\nu_{max}} \frac{\sigma_{3/2} - \sigma_{1/2}}{\nu} d\nu \tag{5.13}$$

This integral is plotted versus the upper integration limit ν_{max} in Figure 5.14. The contribution to this integral from the pion threshold ν_0 to the experimental threshold of 200 MeV has been obtained from the UIM which results in the current solution to -27.5 μb [Tia03]. The experimental contribution to the GDH integral in the energy range measured so far, overshoots the GDH sum rule value (horizontal line at 205 μb in Fig.5.14) significantly. In order to fulfill the sum rule, the integrand of equation 5.13 has to be negative for higher energies. The zero crossing of the integrand has been observed at a photon energy around 2.1 GeV (Fig. 5.10) and Regge phenomenology predicts that this quantity stays negative for $\nu \rightarrow \infty$ (Fig. 5.11). The various theoretical and experimental contributions to the GDH integral are summarized in Table 5.1.
In this thesis all available data from the GDH experiment at ELSA have been analyzed,

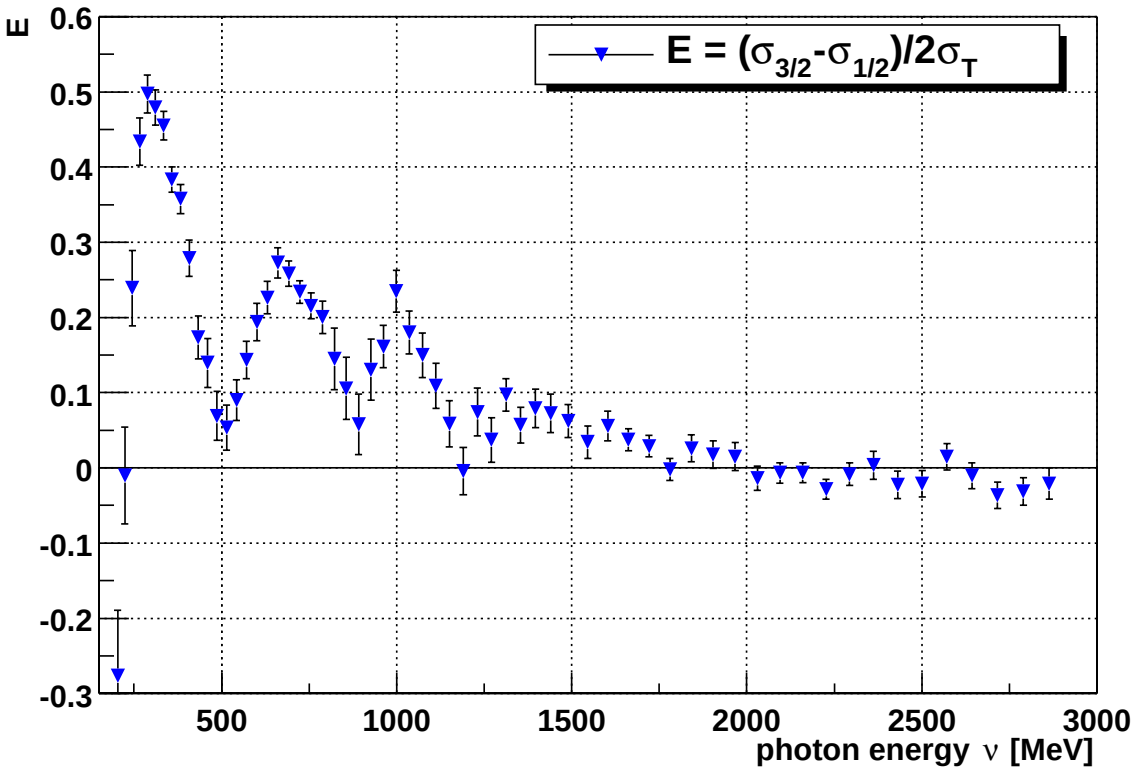

Figure 5.13: The helicity asymmetry E.

covering a photon energy range 680 MeV $\leq \nu \leq$ 2900 MeV. The contribution to the GDH integral is $(45.8 \pm 2.6$ (stat.) ± 2.3 (syst.)$)\mu$b. This value is compatible with an independent analysis from [Zei02] which resulted in $(49.6 \pm 2.6 \pm 2.2)\mu$b, where data in the photon energy range from 680 MeV to 2800 MeV have been available. In the present work an additional data set at a primary electron energy of 3.02 GeV is included which increases the statistical precision of the high energy data and confirms the zero crossing of $\sigma_{3/2} - \sigma_{1/2}$ around 2.1 GeV. With the inclusion of this data set [Zei03][Dut04] give $(48.3 \pm 2.5 \pm 2.1)\mu$b for 680 MeV $\leq \nu \leq$ 2900 MeV and $(27.5 \pm 2.0 \pm 1.2)\mu$b for the energy region between 800 MeV and 2900 MeV which is in good agreement with the results of the analysis presented here (see Table 5.1).
The deviations of both data analyses below 800 MeV can possibly be caused by the different correction methods that have been applied to tagging efficiency runs where the leadglass detector suffered radiation damage effects. A description of this correction method is given in Section 3.6.1, which is to be compared with chapter 3.3.3 of [Zei02]. Another difference is the treatment of the rate dependent corrections for the veto deadtime and the pseudorandom effect (cf. Section 3.4). Due to the variation of the tagging rate during one extraction phase (Fig. 3.14), veto deadtime and pseudorandom corrections have been calculated and applied for every single scaler block, whereas in [Zei02] mean values for a whole run have been used[3].

The experimental contribution to the GDH sum rule has been obtained by adding the results

[3]The independence of the extracted cross sections from the tagging rate (Section 4.4) demonstrates the functionality of the present analysis method.

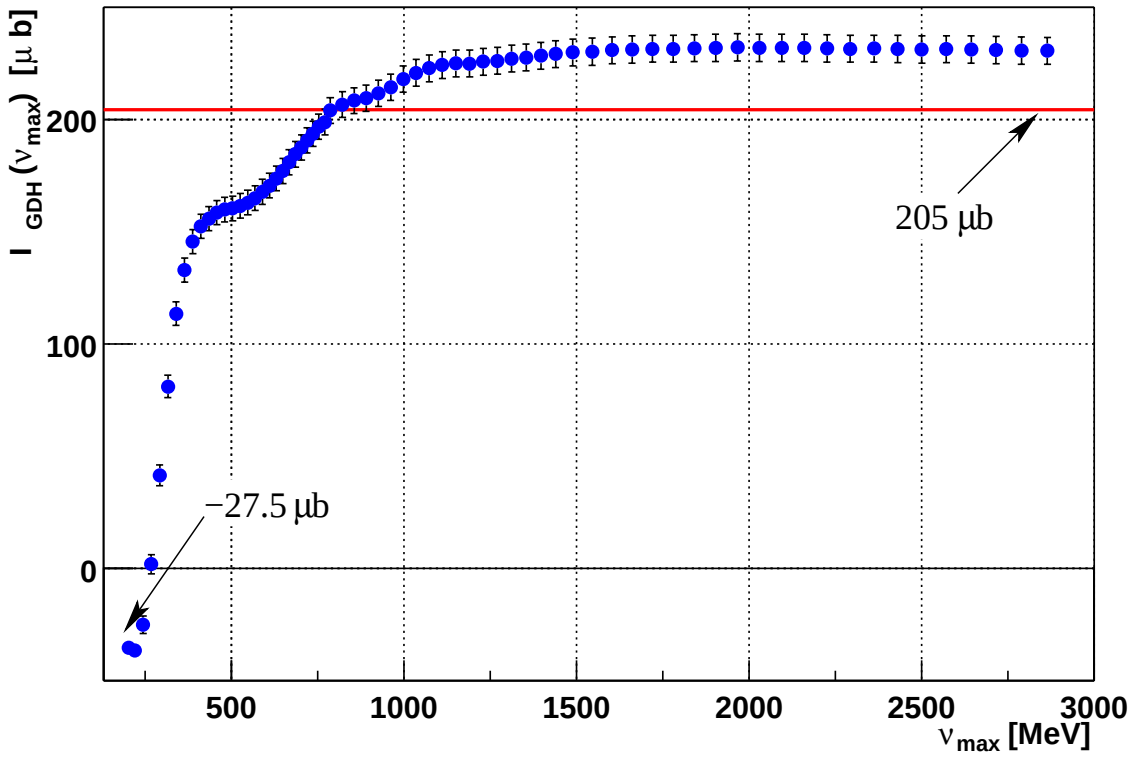

Figure 5.14: The running GDH integral as a function of the upper integration limit. The low energy contribution is from [Tia03]. For comparison also the GDH sum rule value is shown as a horizontal line.

of the MAMI experiment [Ahr01] below 800 MeV to the contribution from the ELSA experiment above 800 MeV resulting in $(253 \pm 5 \pm 12)\mu$b. Below the experimental threshold of 200 MeV the UIM predicts [Tia03] (-27.5 $\pm$ 3)μb for the GDH integral on the proton. Above 2.9 GeV Regge phenomenology can be used to describe cross sections. Parametrizations from [Bia99] and [Sim02] have been shown where the later has been modified to give a better description of the data. This modification caused only a minor change in the contribution to the GDH integral (Table 5.1) and even [Bia99] which does not describe the data in the measured energy range, results in a similar value of the GDH integral above 2.9 GeV. Adding the experimental parts to the theoretical estimates of the unmeasured energy regions one obtains approximately 212 μb which is, within error bars, in agreement with the GDH sum rule value for the proton of 205 μb.

The running integral I_{γ_0} **for the spin polarizability** shows a faster convergence than the GDH integral due to the ν^{-3} weighting.

$$I_{\gamma_0} = -\frac{1}{4\pi^2}\int_{\nu_0}^{\nu_{max}} \frac{\sigma_{3/2}-\sigma_{1/2}}{\nu^3} d\nu \tag{5.14}$$

On the other hand, this integral is more sensitive to model calculations in the experimentally uncovered photon energy range below 200 MeV. I_{γ_0} is shown as a function of the upper integration limit ν_{max} in Figure 5.15 where a low energy contribution of $90 \cdot 10^{-6}$ fm^4 [Tia03]

	ν [MeV]	I^p_{GDH} [μb]	$I^p_{\gamma_0}$ [10^{-6}fm^4]
Low energy			
MAID [Tia03]	< 200	-27.5 $\pm$ 3	90
Experiments			
MAMI [Ahr01]	200-800	226 $\pm$ 5 $\pm$ 12	-187 $\pm$ 8 $\pm$ 10
ELSA this work	680-2900	45.8 $\pm$ 2.6 $\pm$ 2.3	-6.2 $\pm$ 0.4 $\pm$ 0.3
ELSA this work	800-2900	27.3 $\pm$ 2.1 $\pm$ 1.4	-2.7 $\pm$ 0.2 $\pm$ 0.1
GDH-collaboration	200-2900	253 $\pm$ 5 $\pm$ 12	-190 $\pm$ 8 $\pm$ 10
High energy			
Bianchi [Bia99]	> 2900	-14.0	≈ 0
Simula [Sim02]	> 2900	-13.3	≈ 0
Simula modified	> 2900	-13.1	≈ 0

Table 5.1: Experimental and theoretical contributions to the GDH integral and the spin polarizability on the proton.

	$I^p_{\gamma_0}$ [10^{-6}fm^4]
Experiment + [Tia03]	-100 $\pm$ 8 $\pm$ 10
Dispersion relations:	
Babusci [Bab98]	-150
Drechsel [Dre00]	-80
χPT:	
Hemmert [Hem98]	+200
Ji [Ji00]	-380
Kumar [Kum00]	-390
Gellas [Gel00]	-110
Bernard [Ber03]	+464
K-Matrix model:	
Kondratyuk [Kon01] [Kon02]	+240

Table 5.2: The spin polarizability of the proton in comparison with results from various theoretical models.

has been used. The contribution from the present experiment at ELSA in the photon energy range from 680 MeV to 2900 MeV to the integral of the spin polarizability on the proton $I^p_{\gamma_0}$ is (-6.2 $\pm$ 0.4 $\pm$ 0.3) 10^{-6}fm^4. With the result from the MAMI experiment [Ahr01] and the contribution [Tia03] below the experimental threshold of 200 MeV γ^p_0 denotes -100 in the above mentioned units.

The spin polarizability can also be calculated via various theoretical models. The four spin polarizabilities γ_1 ...γ_4 [Rag93][Rag94] which can be calculated for example in the framework of chiral perturbation theory (χPT) are connected to the forward spin polarizability γ_0 via $\gamma_0 = \gamma_1 - \gamma_2 - 2\gamma_4$. The results of the different theoretical models, which are partly contradictory, are given in Table 5.2. The dispersion theoretical approaches come close to the experimental value while discrepancies exist in the chiral perturbation theories. In the most recent paper [Ber03] it is speculated that these discrepancies are possibly due to higher order effects. From the experimental site a measurement down to ν_0 would be desirable, to become independent of multipole analyses which have been used so far in this energy region.

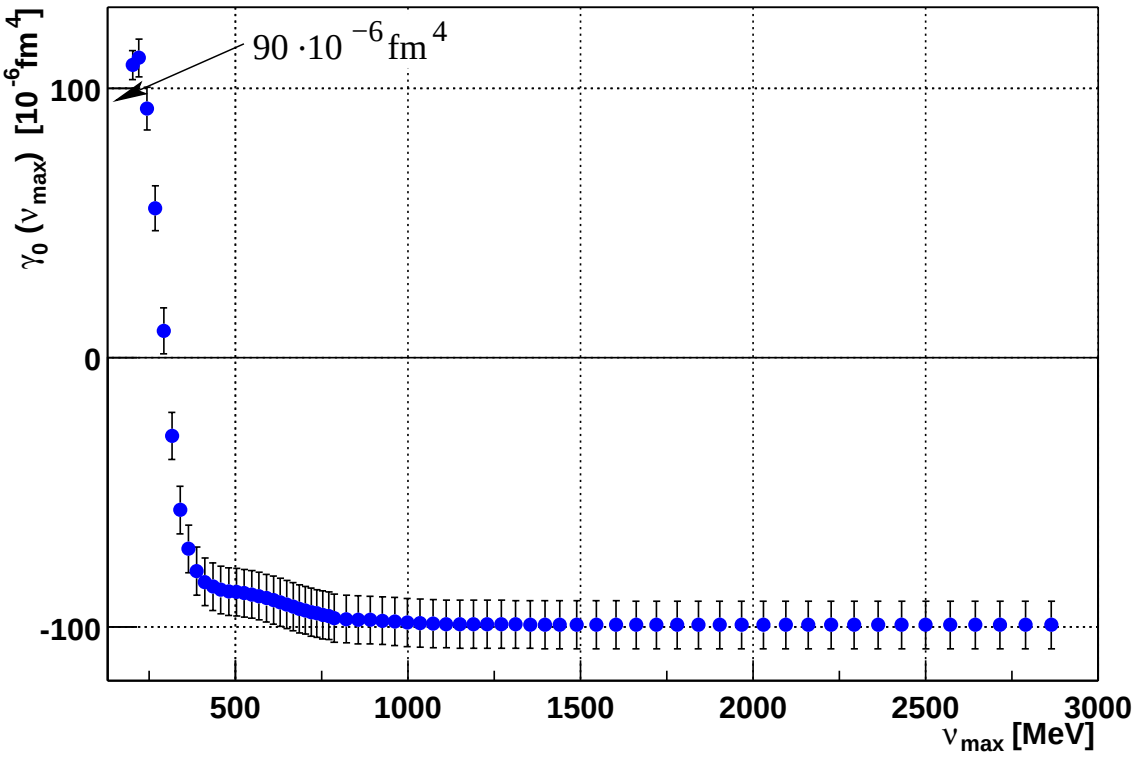

Figure 5.15: The running integral for the spin polarizability γ_0 as a function of the upper integration limit. The contribution below 200 MeV is from [Tia03].

5.2.5 $\Delta\sigma$ on the neutron

Motivations

Several motivations exist to measure also the helicity dependent photoabsorption cross sections on the neutron. The predictions of multipole analyses (Table 1.1) all fail to reproduce the sign of the so-called isovector sum rule $I^p_{GDH} - I^n_{GDH}$ which is the difference of the GDH integral on the proton and the neutron. A possible reason for this failure could be the $F_{15}(1680)$ resonance, which is very distinct in $\sigma_{3/2} - \sigma_{1/2}$ on the proton. As has been shown in Figure 5.10 this resonance can be well described by the single pion contribution of [MAID03]. This single pion contribution from [MAID03] is plotted for the proton and the neutron in Figure 5.16 (solid lines). As expected, both nucleons show an identical response in the Δ region but the $F_{15}(1680)$ resonance is not visible for the neutron. The helicity amplitudes for this resonance have first been extracted in 1996 [Arn96] but the data for the reactions on the neutron have been measured prior to 1993 [Arn96]. Therefore, the helicity amplitudes have not been changed significantly in the most recent partial-wave analysis [Arn02]. A direct measure of $\sigma_{3/2} - \sigma_{1/2}$ on the neutron in the third resonance region can be used as a test of the helicity amplitudes that have been extracted so far, and it can serve as an input to future multipole analyses.
Another point is the high energy behaviour which can be described by Regge phenomenology.

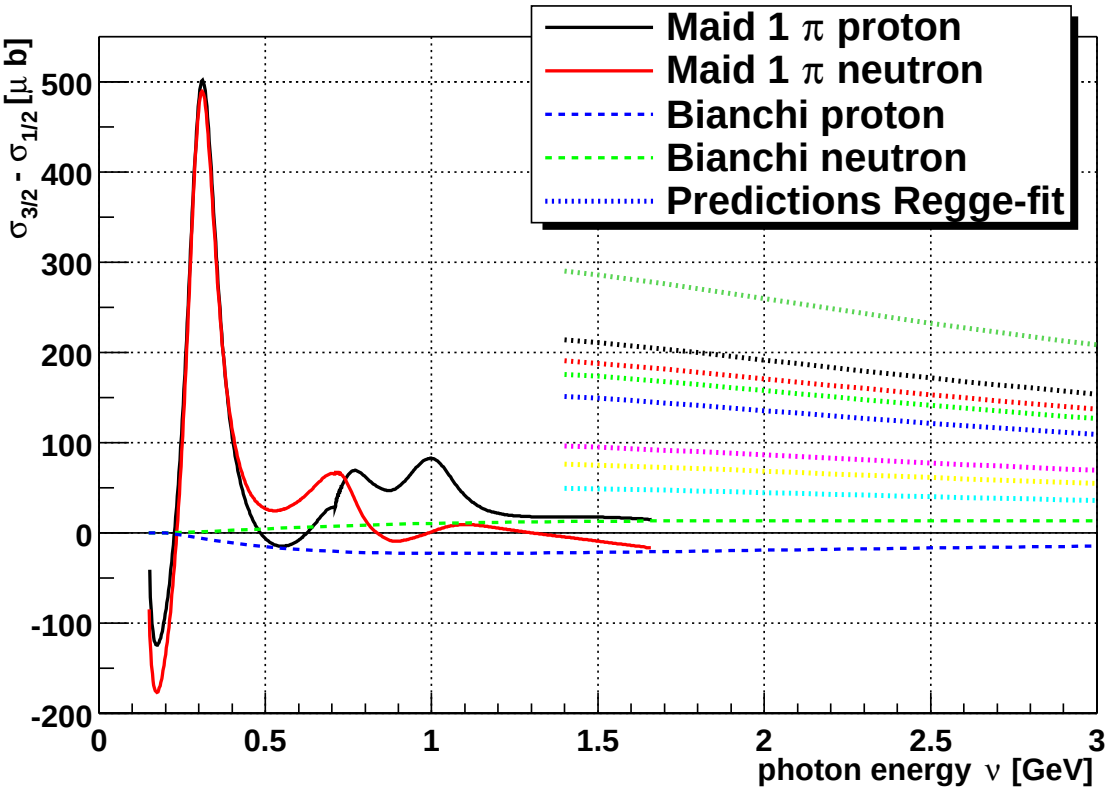

Figure 5.16: Theoretical estimates for $\sigma_{3/2} - \sigma_{1/2}$ for the proton and the neutron. The single pion contribution in the resonance region is from [MAID03] (solid lines) while the nonresonant and high energy behaviour is a parametrization from [Bia99] (dashed lines). The dotted lines are predictions for the neutron obtained from Regge-fits to the polarized proton data.

For the proton the parametrizations of [Bia99] [Sim02] predict a purely negative behaviour of $\Delta\sigma$ for $\nu \to \infty$. The data on the proton seem to follow this trend for photon energies above 2.1 GeV. For the neutron, however, a purely positive contribution is predicted from [Bia99] for higher energies. Both asymptotic behaviours are plotted as dashed lines in Figure 5.16. With the parameters given in [Bia99] the parametrization of equation 5.8 does not describe the proton data in the energy region measured so far (Fig. 5.11). Therefore, a Regge-fit has been performed using the doubly polarized photoabsorption cross section data of the proton. For this purpose equation 5.8 is used where the intercepts of the Regge trajectories α^0_{a1} and α^0_{f1} are taken from [Bia99]. g has been set to zero as the logarithmic term can be neglected at Q^2=0 (ref. [35] of [Hel03]) and a and f are free parameters of the fit. After a and f are fixed, one can make a prediction for $\Delta\sigma$ on the neutron by changing the isospin factor T from +1/2 to -1/2. These predictions are shown as dotted lines in Figure 5.16. The different lines represent different lower boundaries for the fit on the proton data. This lower boundary has been varied from 1.6 GeV to 2.3 GeV generating the 8 predictions for the neutron which vary in a very huge range. Some of these predictions for $\Delta\sigma$ even exceed the unpolarized cross section which is obviously impossible.
Resonances dominate the helicity dependent photoabsorption cross sections up to 2 GeV (Fig. 5.10) and Regge behaviour does appear not until 2.2 GeV. Extending the Regge-fit below the zero-crossing down to the resonance region generates these unbelievable large pre-

dictions for the neutron cross sections. The lower boundary for the fit should be at least 2.2 GeV or even higher, but the *leverarm* that is available with the data up to 2.9 GeV is too small to obtain a reliable Regge-fit.

Measurements

After the doubly polarized measurements on the proton were finished, a limited beamtime of about 10 days was available for measurements on the neutron. Due to the limited time the measurements have been restricted to two primary electron energies:

- 1.2 GeV: To cover the third resonance region.
- 1.9 GeV: To see a trend of the *high energy* behaviour, if there is a zero crossing or not.

The measurements have been performed with a polarized ^{6}LiD target. The polarization was about 27 % and the polarization loss during the measuring time was hardly detectable leading to relaxation times in the order of 10000 hours [Roh02].

Results

The helicity dependent photoabsorption cross sections on the neutron have been extracted according to equation 3.68[4]. Here the data from the double polarized measurements on LiD and on the proton enter. The data have been prepared in such a way that they have common energy bins. In Figure 5.17 the helicity dependent photoabsorption cross sections for all three data sets are plotted for the two primary electron energies. For clarity just the error bars are plotted, and the data points of LiD and of the proton have been shifted slightly to the right and to the left, respectively. The proton data exhibit the resonance structure in the third resonance region and the data from LiD seem to follow this behaviour. Extracting the neutron part from these two data sets leads to a nonzero contribution in this energy region, in contradiction to the result from [MAID03] (Fig.5.16).
At a primary electron energy of 1.9 GeV $\sigma_{3/2}-\sigma_{1/2}$ on the proton shows already the tendency to cross zero, whereas the neutron data stay positive at cross section values slightly higher than the proton.
In Figure 5.18 $\Delta\sigma$ on the neutron is shown after some rebinning. For comparison, the single pion contribution for the proton and the neutron from [MAID03] is plotted also. In the third resonance region the neutron data are not compatible with the neutron result from [MAID03]. From this plot one gets the impression that the excitation of the $F_{15}(1680)$ resonance is very similar in the proton and the neutron case.
At higher photon energies the neutron data do not show a tendency for zero crossing. The Regge approach of [Bia99] does not give a perfect but at least a reasonable description of the data. For comparison also one expectation from a Regge-fit is given in Fig. 5.18. Such a prediction from a Regge-fit to the proton data has also been given in [Hel03] where the lower boundary for the fit was about 1350 MeV. With the present neutron data such predictions

[4]Owing to the high photon energies no corrections due to the nuclear structure of the deuteron have been applied (see also Sec. 3.7).

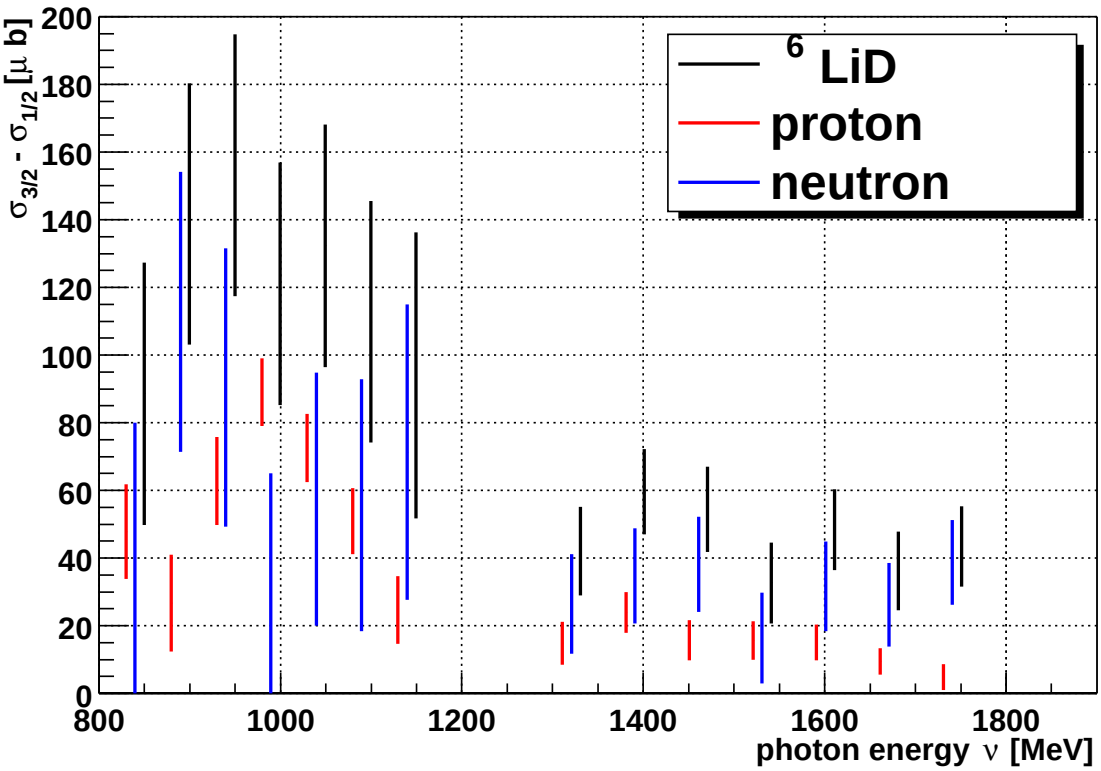

Figure 5.17: Helicity dependent photoabsorption cross sections on LiD, the proton and the neutron. For clearness just the error bars are plotted and the data points of LiD and the proton have been shifted slightly to the right and to the left, respectively.

are definitely ruled out. It has already been discussed that for a reliable Regge-fit on the proton one needs data at higher photon energies and one should not include data below 2.2 GeV in such a fit.

The helicity dependent photoabsorption cross sections $\sigma_{3/2}$ and $\sigma_{1/2}$ have also been separated for the neutron according to Eqs. 5.10 and 5.11. The necessary unpolarized photoabsorption cross section on the neutron has been extracted from deuteron and proton data as described in [Bia96]. In Fig. 5.19 a) $\sigma_{3/2}$ and $\sigma_{1/2}$ are shown as a function of the photon energy ν. The resonant structure in the third resonance region is even more distinct in the helicity asymmetry E (Eq. 5.12) which is plotted in Fig. 5.19 b). This plot also indicates that, in contrast to the proton, E stays positive for higher photon energies.

Estimates for the GDH sum rule on the neutron

Due to the short beamtime available, data on the neutron could only be taken at two primary electron energies with a limited statistical precision. In the present section these data will be used together with theoretical information in the unmeasured energy regions to obtain an estimate for the GDH sum rule on the neutron.
With the two primary electron energies 1.2 GeV and 1.9 GeV, photon energy ranges 815 MeV

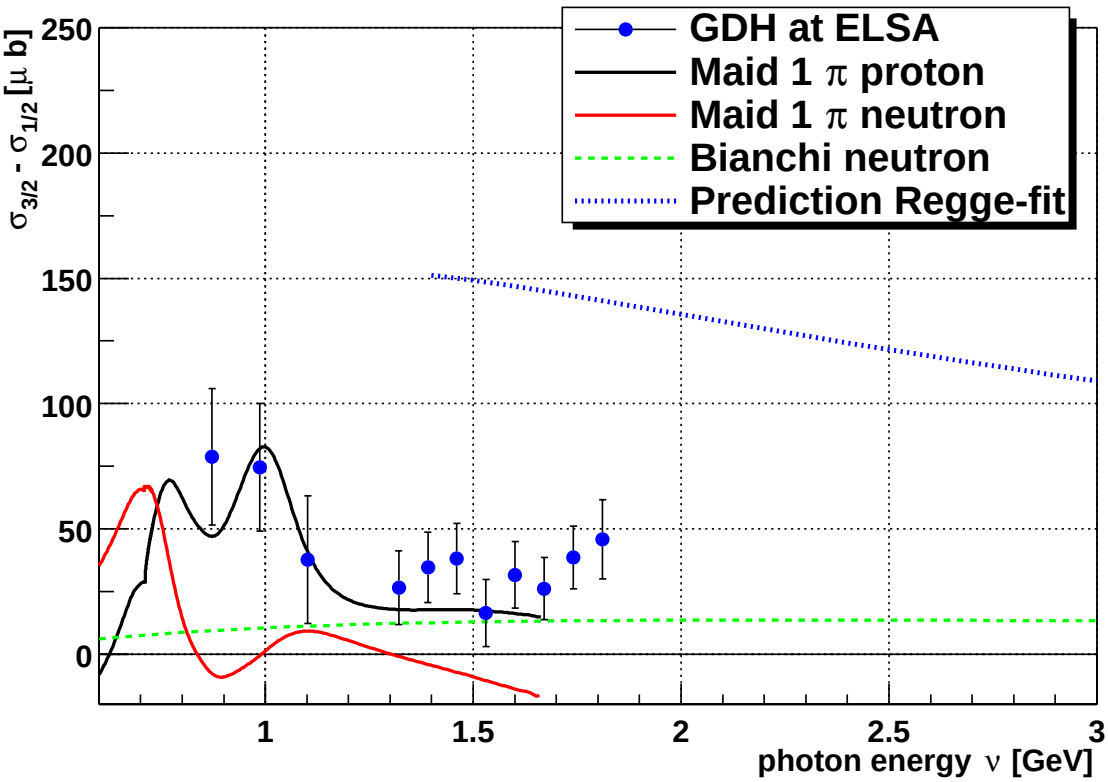

Figure 5.18: $\Delta\sigma$ for the neutron in comparison with the single pion contribution of [MAID03], a Regge approach from [Bia99] and a prediction from a Regge-fit to the proton data.

- 1155 MeV and 1285 MeV - 1825 MeV are covered, respectively. Outside these energy ranges one has to rely on theoretical predictions. The largest contribution to the single-pion part of the GDH integral will come from the Δ-resonance. This resonance is perfectly described by [MAID03] in the proton case. For the neutron the description should be equally good. Dedicated calculations for the double-pion partial reaction channels are on the way [Hol04] also for the neutron. As a rough estimate the double-pion contribution is assumed to be equal for proton and neutron. A value of ≈ 40 μb has been extracted from Figs. 7.22-7.24 of [Hol01] for the energy range below 815 MeV. In the energy gap of the two data sets, between 1155 MeV and 1285 MeV, a smooth continuation of the data is assumed. Above 1825 MeV the Regge parametrization from [Bia99] is used. All experimental and theoretical contributions to the GDH integral on the neutron I^n_{GDH} are summarized in Table 5.3. The experimental contribution between 815 and 1825 MeV is $(36.8 \pm 5.6(\text{stat.}) \pm 4.0(\text{syst.}))\mu$b where the assumed value of 3.4 μb in the energy gap between the two data sets is already included. Adding up all experimental and theoretical contributions one comes very close to the sum rule value of 233 μb[5]. Although the statistical and the systematic errors of the experiment are large, a significant contribution to the GDH integral can be observed. Especially the third resonance region contributes to $\approx 20\mu$b (which is identical to the proton value) in contradiction to multipole analyses which predict zero in this energy range.

[5]Note that in Tab. 5.3 just the experimental errors are given, for the double pion channel one can assume an uncertainty on the order of 20 μb.

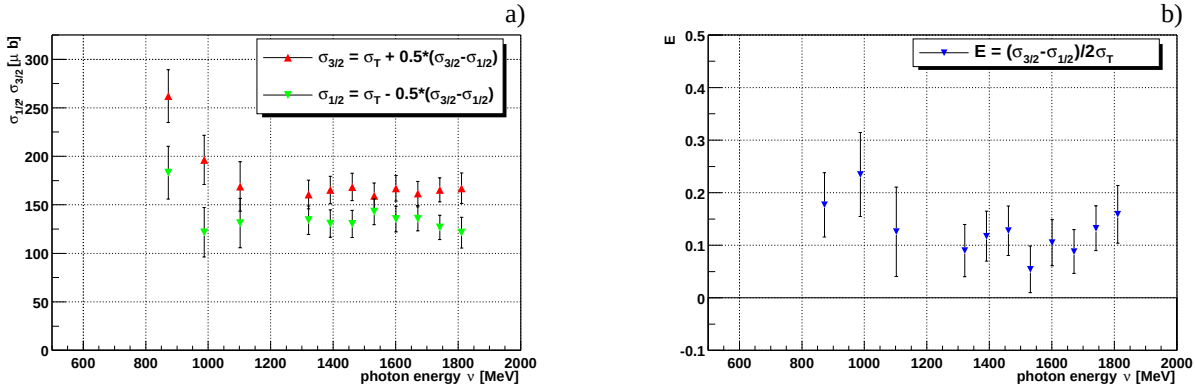

Figure 5.19: a) The separated helicity dependent photoabsorption cross sections $\sigma_{3/2}(\nu)$ and $\sigma_{1/2}(\nu)$ and b) the helicity asymmetry E on the neutron.

		ν [MeV]	I^n_{GDH} [μb]	$I^n_{\gamma_0}$ [10^{-6}fm^4]
Low energy				
MAID [MAID03]	π	< 815	125	8
Holvoet et al. [Hol01] [Hol04]	$\pi\pi$	< 815	≈ 40	-8
ETA-MAID [MAID03]	η	< 815	-2.5	0.2
Experiment				
ELSA this work		815-1155	$22.8 \pm 5.4 \pm 2.8$	$-2.5 \pm 0.6 \pm 0.3$
Assumption		1155-1285	3.4	-0.2
ELSA this work		1285-1825	$10.6 \pm 1.7 \pm 1.2$	$-0.5 \pm 0.1 \pm 0.1$
Experimental sum		815-1825	$36.8 \pm 5.6 \pm 4.0$	$-3.2 \pm 0.6 \pm 0.4$
High energy				
Bianchi [Bia99]		> 1825	30	-0.2
theory + experiment		150 - ∞	$229.3 \pm 5.6 \pm 4.0$	$-3.2 \pm 0.6 \pm 0.4$
GDH sum rule		150 - ∞	233	

Table 5.3: Experimental and theoretical contributions to the GDH integral and the spin polarizability on the neutron.

The present data show that the missing strength in the multipole analyses for the neutron comes from the third resonance region. Two scenarios are now possible:

- Change of the helicity amplitudes of the $F_{15}(1680)$ resonance for the neutron,
- Double pion contributions.

A change of the helicity amplitudes of the $F_{15}(1680)$ resonance for the neutron in order to reproduce the strength of the doubly polarized neutron data is not compatible with differential π^- production cross sections on the neutron [Tia04]. These data are, however, from 1974 and one might think about a remeasurement.
To decide if the second scenario is correct one has to wait for new experiments which can identify double pion partial reaction channels at these energies. Theoretical calculations still do not give a perfect description of the double pion production data on the proton (see e.g.

[Lan03]) and the current upper limit of all calculations is 800 MeV.
Kaon and vector meson photoproduction cannot account for the missing strength on the neutron as it contributes only -0.25 μb (+4.2 μb for the proton) to the GDH sum rule [Zha02] [Sum99].

Comparison with proton data

Figure 5.20 shows a comparison of $\Delta\sigma$-data on the proton and on the neutron that have been obtained so far. It seems that in the resonance region up to 1.6 GeV both nuclei behave very

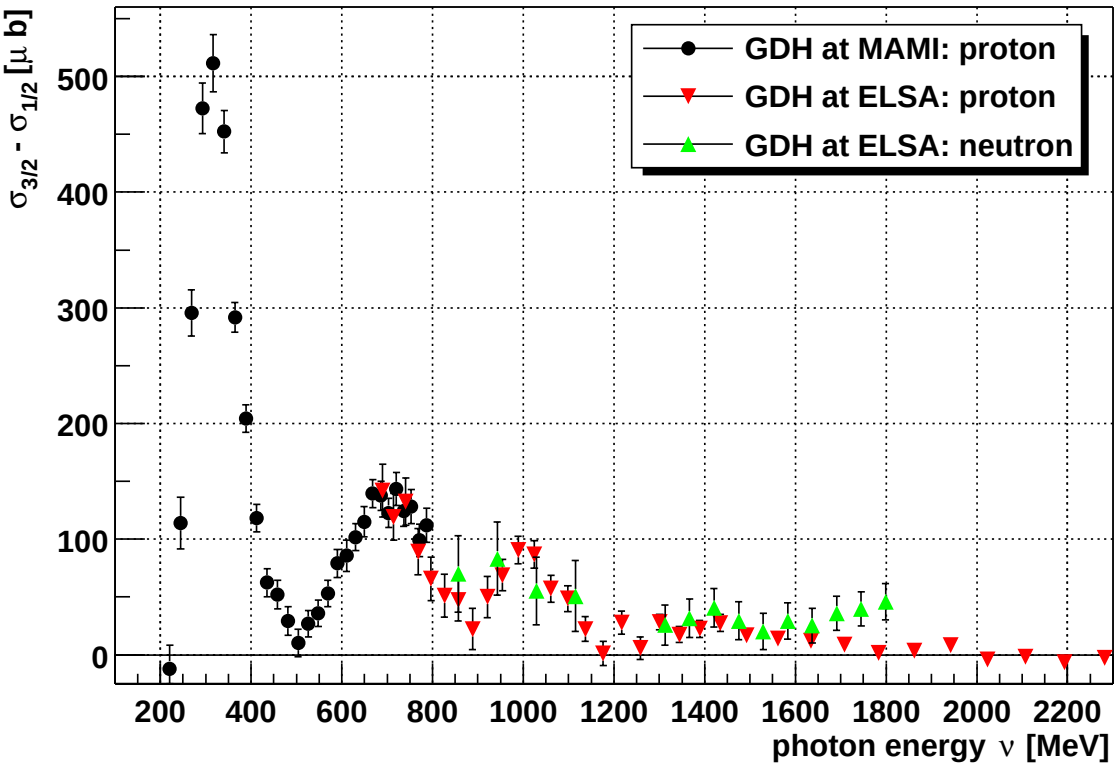

Figure 5.20: Comparison of the experimentally obtained $\Delta\sigma$ on the proton ([Ahr01] and this work) and the neutron (this work). Tabulated results of the ELSA data shown in this plot can be found in Tables B.9 and B.10.

similar. Above this energy the proton data exhibit already a trend to cross zero, whereas the neutron data stay positive.
Below 800 MeV data on the neutron have been taken with a polarized deuterated butanol target at MAMI in the year 2003. These data are currently being analysed [Ros04] and they will provide more information about the validity of the theoretical predictions that have been used so far in this energy range.
Of special interest is also the spin polarizability of the neutron where the threshold contribution to $I^n_{\gamma_0}$ cancels the contribution from the Δ-resonance almost completely, leading to a very small number after integration (Tab. 5.3). This value deviates significantly from the spin polarizability of the proton, denoted in Table 5.1.

Chapter 6

Summary and outlook

The measurement of doubly polarized total photoabsorption cross sections is required for a direct experimental check of the GDH sum rule. These measurements have been performed at the tagged photon facilities of the electron accelerators MAMI in Mainz and ELSA in Bonn. The experiment at MAMI covered the photon energy range from 200 MeV to 800 MeV whereas at ELSA the range from 680 MeV to 2.9 GeV was covered.
The experiment at MAMI was carried out between 1996 and 1998. Besides the total photoabsorption cross sections, also the helicity dependence of all partial reaction channels was investigated.

The topic of the present thesis is the experiment at ELSA. It has been built up and put into operation in the years 1999 - 2000 after a pilot run in 1995. Due to the stringent requirements for the GDH experiment progress in the quality and the stability of the beam at ELSA has been made during this time. One component to monitor the position and the intensity of the photon beam is the photon camera, setup by the nuclear physics group of the university of Tübingen. The results of this device have been used as a feedback signal to ELSA control. Together with a stabilization system that became available in 2002, the relative intensity variation was less than 1% and the position could be kept stable to better than 0.1 mm during a period of several days.
As a check of the detector system and the analysis method, data have been taken with (unpolarized) carbon and beryllium targets. For the determination of total photoabsorption cross sections the photon flux at the target has to be known precisely. During the present experiment the tagging efficiency has been determined under the same experimental conditions as during ordinary data taking, i.e. at tagged photon rates of 1.0 - 1.3 MHz. A method to extract the tagging efficiency at these high rates, developed in [Zei98] and [Zei02], has also been used in the present work. Furthermore, deadtime effects have to be taken into account. These are directly dependent on the beam intensity. Due to the structure of the ELSA accelerator the beam intensity varies during one extraction phase. To account for this effect, the analysis method presented in this thesis uses a deadtime correction factor for every single scaler block (100 events). The independence of the extracted cross sections on the tagging rate demonstrates the functionality of this analysis method. The STAR detector has been used for an extrapolation of the measured cross sections to the acceptance gap in the forward direction. Less than 0.02 % of the cross section is missed by this acceptance gap in the forward direction and less than 0.1 % by the hole in the backward direction.

The complete detector covers a solid angle of 99.6%·4π, furthermore, its detection efficiency for charged particles and decay photons is close to 100 %. The unpolarized photoabsorption cross sections obtained with the present detector setup and analysis method are in agreement with published data.

Doubly polarized data on the proton and the neutron have been taken 2001 and 2002. Circularly polarized photons were produced by bremsstrahlung of longitudinally polarized electrons. A horizontal *frozen spin* target provided longitudinally polarized nucleons. Due to the horizontal arrangement of the target cryostat, the detector system covered almost 4π of the solid angle. Systematic studies have been performed for searches of *false asymmetries* inherent to the experimental setup. No such *false asymmetries* could be found, and no significant loss of acceptance due to the holes in the detector was found. The result for the difference of helicity dependent photoabsorption cross sections $\sigma_{3/2} - \sigma_{1/2}$ agrees in the overlap region with the data from the experiment at MAMI [Ahr01]. The contribution to the GDH integral on the proton is (45.8 $\pm$ 2.6 $\pm$ 2.3)μb for 680 MeV $\leq \nu \leq$ 2.9 GeV and (27.3 $\pm$ 2.1 $\pm$ 1.4)μb for 800 MeV $\leq \nu \leq$ 2.9 GeV, respectively. Adding the experimental contribution to the GDH integral below 800 MeV from MAMI to the present results, one obtains (253 $\pm$ 5 $\pm$ 12)μb. Including the negative contributions below the experimental threshold of 200 MeV from [Tia03] and the estimates from Regge-approaches above 2.9 GeV [Bia99] [Sim02] one obtains 212 μb which is, within error bars, in agreement with the GDH sum rule value for the proton of 205 μb.
Doubly polarized photoabsorption data on the neutron have been taken with a polarized ^{6}LiD target in the photon energy range 815 MeV $\leq \nu \leq$ 1825 MeV. The extracted helicity dependent cross section difference shows a significant contribution in the third resonance region in contradiction to all present multipole analyses. For higher energies no tendency for a zero crossing can be observed in contrast to the proton data. The Regge prediction from [Bia99] gives a reasonable description of the neutron data for higher energies. The experimental contribution to the GDH sum rule on the neutron is (36.8 $\pm$ 5.6 $\pm$ 4.0)μb. Adding the single [MAID03] and double pion [Hol01] contributions below 815 MeV and the estimate from the Regge approach [Bia99] above 1825 MeV one obtains 229 μb which is, within error bars, very close to the GDH sum rule value for the neutron of 233 μb. The strength missing in the multipole analyses comes from the third resonance region. A possible solution of this problem can either be a modification of the helicity amplitudes of the $F_{15}(1680)$ resonance, which would be in contradiction to existing differential π^- cross sections, or a large double pion contribution. Such a large double pion contribution is not expected from the proton data, where the third resonance region is almost completely saturated by the single pion part.

To summarize: The GDH integral on the proton has been measured for the first time over a large photon energy range from 200 MeV to 2.9 GeV. Including the theoretical estimates outside the experimentally covered energy range, no deviation from the sum rule value has been found.
The GDH integral on the neutron has always been a problem for multipole analyses. The present measurement gives a significant contribution to the GDH integral on the neutron from the third resonance region. Therefore, also for the neutron no deviation from the GDH sum rule value has been found.

The experimental program of the GDH collaboration has been finished in 2003 with the

measurement on a polarized deuterated butanol target at MAMI in Mainz. The data are currently being analyzed [Ros04], and will provide new informations for the theoretical models that have been used so far in this energy range.
For higher energies one has to rely on Regge-approaches up to now. Experimental programs to check the high energy behaviour of the GDH integral are on the way. At Jefferson-Lab real photons can be used to cover the energy range 2.5 GeV $\leq \nu \leq$ 5.3 GeV [Sob03]. Furthermore, a proposal exists from the same laboratory to use *nearly real photons* to study the Q^2 dependence of the generalized GDH integral very close to the real photon point (0.02 GeV$^2 \leq Q^2 \leq$ 0.5 GeV^2)[Che97].
The photon energy range up to 40 GeV will be covered by an experiment at SLAC [Bos03] which will serve as a test of the predictions from Regge-approaches and of the *no subtraction hypothesis*, the weakest point in the derivation of the GDH sum rule.
After the upgrade to 1.5 GeV, it will be possible to solve the neutron puzzle in the third resonance region with the Crystal Ball detector at MAMI-C [Bec04].

Appendix A

Calculation of uncertainties

This section deals with the calculation of the *systematic* (Section A.1) and the *statistical* uncertainties (Section A.2). While the statistical error can in principle be decreased by an increase of the measuring time, the systematic error is inherent to the experimental setup in use. Its sources have to be investigated and the different contributions have to be calculated or estimated, respectively.

A.1 Systematic errors

The major quantities entering the calculation of an absolute cross section (see Section 3.7) are: the hadronic rate, the photon flux, the target density and for the double polarized cross sections, the polarization values. Each of these quantities provides several sources of systematic uncertainties:

- Hadronic rate: Cuts in the TDC and QDC spectra, veto deadtime correction, pseudo-random correction, absorption of reaction products in the target, acceptance gaps.
- Target: target density, target polarization
- Photon flux: tagging efficiency (stability of the photon beam), attenuation of the photon flux in the target, photon polarization

As the size of the uncertainty of the experimental result is of paramount importance, all contributions to the relative error of the unpolarized ($\frac{\Delta\sigma_{C,Be}}{\sigma_{C,Be}}$) and double polarized cross sections ($\frac{\Delta(\sigma_{3/2}-\sigma_{1/2})}{\sigma_{3/2}-\sigma_{1/2}}$) are given in detail.

Hadronic rate

It has already been discussed in Section 4.2 that the choice of the **cuts in the timing spectra** have no systematic influence on the value of the cross sections.
In contrast, the choice of the **QDC cuts** can decrease the unpolarized cross sections (see Fig.

4.5 a)). With the used cut values no decrease of the cross section has been observed within the statistical error of 0.5%. As the QDC cuts can only decrease the unpolarized carbon and beryllium cross sections the systematic uncertainty reads

$$\left(\frac{\Delta\sigma_{C,Be}}{\sigma_{C,Be}}\right)_{QDC-cuts} = +0.5\% \tag{A.1}$$

For the double polarized cross sections the QDC-cuts can effect both helicity states, the relative systematic error denotes here

$$\left(\frac{\Delta(\sigma_{3/2}-\sigma_{1/2})}{\sigma_{3/2}-\sigma_{1/2}}\right)_{QDC-cuts} = \pm 0.5\% \tag{A.2}$$

The measurement of the **veto deadtime** is based on a coincidence measurement of the veto signal with the delayed TAG-OR signal (Section 3.4.2). The task of the electronics for measuring the veto deadtime is to simulate the conditions at the experimental-trigger coincidence. A hypothetical source for systematic errors are different coincidence widths at the experimental trigger and the coincidence of the veto-signal with the delayed TAG-OR. As the veto signals come from the same coincidence units and as identical cables are used it is assumed that the widths of the veto signals are identical. The width of the delayed TAG-OR signal is adjusted via an oscilloscope to the width of the TAG-OR signal t_{TAG-OR} = 13 ns with an accuracy Δt_{TAG-OR} = 0.5 ns. The ratio $\Delta t_{TAG-OR}/t_{TAG-OR}$ corresponds to the uncertainty of the measurement of the deadtime $R_{dead} = 1 - R_{live}$. For the relative systematic error of the cross section generated by the measurement of the veto deadtime it follows

$$\left(\frac{\Delta\sigma}{\sigma}\right)_{veto} = \frac{\Delta R_{dead}}{R_{live}} = \pm\frac{\Delta t_{TAG-OR}}{t_{TAG-OR}}\cdot\frac{1-R_{live}}{R_{live}} \tag{A.3}$$

With $\Delta R_{dead} = R_{dead}\cdot\frac{\Delta t_{TAG-OR}}{t_{TAG-OR}}$.

For the determination of the **pseudorandom correction** the tagging radiator, the tagging rate, the time between two successive electron bunches and the tagging range have to be known (Section 3.4.1). The thickness d of the tagging radiator is known with a relative precision $\Delta d = \pm$ 10%, for all other quantities no systematic uncertainties are assumed. The systematic error generated by the pseudorandom (pr) correction can then be obtained by comparing the hadronic rates extracted with the two extreme values of the radiator thickness $Y(d \pm \Delta d)$ to the nominal value $Y(d)$

$$\left(\frac{\Delta\sigma}{\sigma}\right)_{pr} = \frac{Y(d+\Delta d)-Y(d-\Delta d)}{Y(d)} \tag{A.4}$$

The **absorption of reaction products in the target** is most important for reaction channels with a single meson in the exit channel, as for the GDH-detector the detection of a single hadron is sufficient to identify a photohadronic reaction. In the energy region of the $\Delta(1232)$ resonance single-pion photoproduction is the dominant process. The pilot experiment with the GDH-detector in the PHOENIX-areal has shown[1] that the systematic error caused by the absorption of reaction products in the target is less than 2% in the

[1] by using carbon targets of various target densities

Δ-resonance region [Hel97] [Sau98].
At 680 MeV (the lowest photon energy at the present experiment) the single pion production is not the dominant process any more, in the energy range 680 MeV $\leq \nu \leq$ 1000 MeV it contributes to about 40 % to the total unpolarized photoabsorption cross section [Fuj77]. The relative systematic error $(\Delta\sigma/\sigma)_{absorb}$ is here 1%. For a primary electron energy of 1.4 GeV this error is estimated to be 0.5 % and for even higher energies it is set to zero.
The absorption of reaction products in the target can only cause a decrease in the unpolarized cross sections, the systematic error has therefore a distinct direction. For the double polarized cross sections the sign of the systematic error is not defined, as the absorption in the target can be helicity dependent.

The contribution from the **acceptance gaps** of the detector in the forward and backward direction have been estimated in Section 4.3. It has been shown that for the double polarized cross sections no contribution is expected from these holes and that the unpolarized cross section might be modified by 0.1% for the lowest photon energies.

Target

The **target density** F_t for a solid state target is $F_t = \rho_{eff} \cdot L \cdot N_A/M$. The quantity $\rho_{eff} \cdot L$ can be written in terms of the masses $m_{C,Be}$ of the external carbon and beryllium targets

$$\rho_{eff} \cdot L_{C,Be} = \frac{m_{C,Be}}{V_{C,Be}} \cdot L_{C,Be} \tag{A.5}$$

The carbon target has a cylindrical shape, whereas the beryllium target is a cuboid. The volumes can be determined by measuring the diameter d_C or the length of one edge d_{Be} of the carbon or the beryllium target, respectively.

$$V_C = \frac{1}{4} \cdot \pi \cdot d_C^2 \cdot L_C \quad \text{and} \quad V_{Be} = d_{Be}^2 \cdot L_{Be} \tag{A.6}$$

The target density F_t can now be calculated. The mass can be measured to $\Delta m = \pm 5$ mg. As the masses are $m_C = 18.08$ g and $m_{Be} = 11.55$ g [Zei02] the error of the mass measurement is on the order of 10^{-4} and can therefore be neglected.
The measurement of $d_C = 30$ mm and $d_{Be} = 25$ mm [Zei02] can be performed with a precision $\Delta d = 0.1$ mm. The error in the target density due to these length measurements is

$$\left(\frac{\Delta F_t}{F_t}\right)_d = -\frac{2\Delta d}{d} \tag{A.7}$$

The external targets have been placed behind the tip of the polarized target inside the detector. It is assumed that the targets can be placed with a tilting angle α of less than 5°. A tilted target has a larger effective length, i.e. a larger effective target density. This can only lead to an increase of the measured cross section in comparison to a correctly placed target. The systematic error reads

$$\left(\frac{\Delta F_t}{F_t}\right)_{tilt} = \frac{\Delta l}{l} = \frac{1}{\cos\alpha} - 1 = -0.38\% \tag{A.8}$$

E_0 [GeV]	1.0	1.4	1.9	2.4	2.9	3.02	1.2	1.9
$(\frac{\Delta P_t}{P_t})^{b,e}$ [%]	0.1	0.2	0.2	0.9	0.8	0.4	0.3	0.9
$(\frac{\Delta P_t}{P_t})^{TE}$ [%]	2.8	2.8	1.1	0.9	1.0	2.4	1.8	1.8
$(\frac{\Delta P_t}{P_t})$ [%]	2.8	2.8	1.1	1.3	1.3	2.4	1.8	2.1

Table A.1: Systematic error of the target polarization. The primary energy E_0 is given to separate the different beamtime periods. The two rightmost columns denote the periods with the ^{6}LiD target.

The systematic error for the unpolarized cross section caused by the target density has two different bounds

$$\left(\frac{\Delta\sigma_{C,Be}}{\sigma_{C,Be}}\right)_{F_t+} = +\left(\frac{\Delta F_t}{F_t}\right)_d \tag{A.9}$$

$$\left(\frac{\Delta\sigma_{C,Be}}{\sigma_{C,Be}}\right)_{F_t-} = -\sqrt{\left(\frac{\Delta F_t}{F_t}\right)_d^2 + \left(\frac{\Delta F_t}{F_t}\right)_{tilt}^2} \tag{A.10}$$

Numerical values for the carbon and beryllium targets are given in table A.4.
The target density of the butanol target has been given in Section 2.3.3, its systematic uncertainties are described in [Roh03]. The systematic error for the helicity dependent double polarized cross sections reads

$$\left(\frac{\Delta(\sigma_{3/2}-\sigma_{1/2})}{\sigma_{3/2}-\sigma_{1/2}}\right)_{F_t} = -\frac{\Delta F_t}{F_t} = \pm 2.3\% \tag{A.11}$$

For the ^{6}LiD target the dilution factor is included in the effective nucleon polarizations. The target density F_t' has the following relative systematic uncertainty [Roh03]

$$\frac{\Delta F_t'}{F_t'} = \pm 3.4\% \tag{A.12}$$

The **target polarization** is measured with a NMR-system. The systematic error $\Delta P_t/P_t$ consists of two parts. One comes from the calibration measurement in thermal equilibrium $(\Delta P_t/P_t)^{TE}$, the other from the uncertainty of measuring the begin and end values $(\Delta P_t/P_t)^{b,e}$ of one polarization period. The different sources of systematic errors are described in [Roh03]. One beamtime period consists of one TE-measurement and several polarization periods. To obtain a single value for the systematic error of one beamtime period, the weighted mean of all polarization periods is taken. Results are given in table A.1 where the input values are from [Roh02]. The primary energy E_0 is given in table A.1 to specify the different beamtime periods. The two rightmost columns denote the periods with the polarized ^{6}LiD target.

Photon flux

The flux of tagged photons $\phi^i_{\gamma,tag}$ at the target is given by

$$\phi^i_{\gamma,tag} = \epsilon^i_{tag} \cdot \phi^i_{el} \tag{A.13}$$

As the electron flux ϕ_{el}^i is measured via scalers, no systematic uncertainty is assumed here. In contrast the **tagging efficiency** ϵ_{tag}^i (Section 3.6.1) provides several sources for systematic errors. It is measured every few hours, and for analysis the tagging efficiency run which is next to the data run is used. Drifts in the electron beam can cause deviations of the tagging efficiency larger than the statistical error. Figure A.1 shows an example of a beamtime period

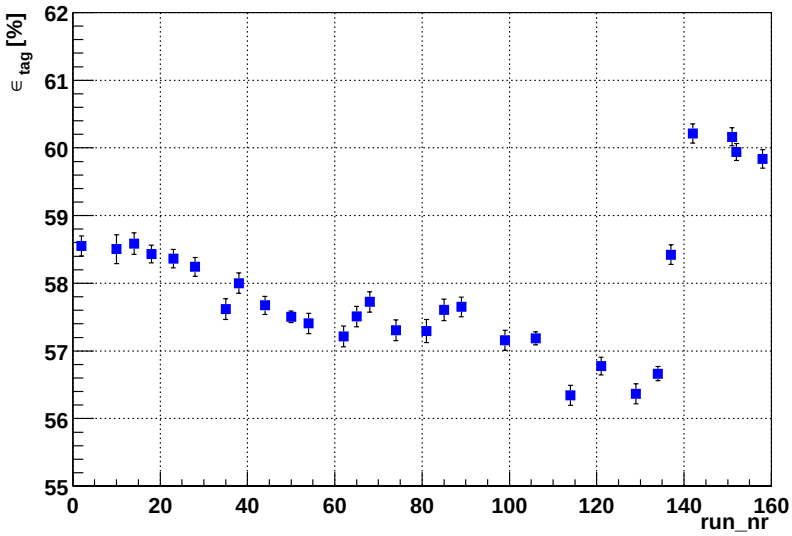

Figure A.1: The tagging efficiency versus the run number during a beamtime period at 1.4 GeV

at 1.4 GeV. The tagging efficiency is plotted versus the run number, a systematic drift is clearly visible. Around run number 140 the beam position has been readjusted to its nominal position. For the systematic error of the tagging efficiency $(\Delta\epsilon_{tag}/\epsilon_{tag})_{drift}$ due to this drift, the variance is taken between two successive tagging efficiency runs.

$$\left(\frac{\Delta\epsilon_{tag}}{\epsilon}\right)^j_{drift} = \left(\frac{1}{N_j}\sum_{i=1}^{N_j}\epsilon_{tag}(i)\right)^{-1}\sqrt{\sum_{i=1}^{N_j-1}\left(\epsilon_{tag}(i+1)-\epsilon_{tag}(i)\right)^2} \tag{A.14}$$

All runs are divided into j periods where during one period no changes in the beam parameters are made. N_j denotes the number of tagging efficiency runs during one period, the shown example (Fig. A.1) consists of two such periods. Finally, all periods are summed up

$$\left(\frac{\Delta\epsilon_{tag}}{\epsilon}\right)_{drift} = \left(\sum_{i=1}^{j}N_i\right)^{-1}\cdot\sum_{i=1}^{j}N_i\cdot\left(\frac{\Delta\epsilon_{tag}}{\epsilon}\right)^i_{drift} \tag{A.15}$$

The pseudorandom effect has also to be taken into account for the determination of the tagging efficiency. Similarly to the calculation of the systematic error for the hadronic rate, the tagging efficiency has been extracted using the two extreme values for the thickness of the tagging radiator $d \pm \Delta d$ ($\Delta d = \pm 10\%$).

$$\left(\frac{\Delta\epsilon_{tag}}{\epsilon}\right)_{pr} = \frac{\epsilon_{tag}(d+\Delta d)-\epsilon_{tag}(d-\Delta d)}{\epsilon_{tag}(d)} \tag{A.16}$$

E_0 [GeV]	1.0	1.4	1.9	2.4	2.9	3.02
radiator	CU15	CU15	CU15	CU15	CU15	CU15
$(\frac{\Delta\epsilon_{tag}}{\epsilon})_{drift}$	± 2.3 %	± 0.5 %	± 1.4 %	± 1.1 %	± 2.1 %	± 0.4 %
$(\frac{\Delta\epsilon_{tag}}{\epsilon})_{pr}$	± 0.02 %	± 0.02 %	± 0.01 %	± 0.01 %	± 0.01 %	± 0.01 %
$(\frac{\Delta\epsilon_{tag}}{\epsilon})_{rd}$	± 0.06 %	0 %	± 0.12 %	± 0.24 %	± 0.1 %	± 0.31 %
$(\frac{\Delta\epsilon_{tag}}{\epsilon})_{shad}$	± 0.5 %	± 0.5 %	± 0.5 %	± 0.5 %	± 0.5 %	± 0.5 %
$(\frac{\Delta\sigma}{\sigma})_{\epsilon_{tag}}$	± 2.4 %	± 0.7 %	± 1.5 %	± 1.2 %	± 2.1 %	± 0.7 %

Table A.2: Contributions to the systematic error of the tagging efficiency for the measurements with the butanol target.

E_0 [GeV]	1.2	1.2	1.9
radiator	CU15	CU50	CU15
$(\frac{\Delta\epsilon_{tag}}{\epsilon})_{drift}$	± 0.9 %	± 1.2 %	± 0.5 %
$(\frac{\Delta\epsilon_{tag}}{\epsilon})_{pr}$	± 0.02 %	± 0.04 %	± 0.01 %
$(\frac{\Delta\epsilon_{tag}}{\epsilon})_{rd}$	0 %	0 %	0 %
$(\frac{\Delta\epsilon_{tag}}{\epsilon})_{shad}$	± 0.5 %	± 0.5 %	± 0.5 %
$(\frac{\Delta\sigma}{\sigma})_{\epsilon_{tag}}$	± 1.0 %	± 1.3 %	± 0.7 %

Table A.3: Same as Tab. A.2 for the measurements with the ^{6}LiD target.

This systematic uncertainty is at maximum 0.04% for a limited number of runs which have been taken with a 50 μm copper radiator and it is less than 0.02% for the majority of runs which have been measured with a 15 μm copper tagging radiator.
The correction for radiation damage of the leadglass detector via the analysis software requires a polynomial fit to the data points (see Figure 3.23). The accuracy of the fit determines the systematic error of the tagging efficiency caused by radiation damage (rd) of the leadglass detector.

$$\left(\frac{\Delta\epsilon_{tag}}{\epsilon}\right)_{rd} = \pm 0.5\% \tag{A.17}$$

This correction was just necessary for a limited number of runs and the contribution to the systematic error is obtained by multiplying the above mentioned error by the number of files which have been corrected, and dividing it by the total number of tagging efficiency runs of this beamtime period.
Finally, the contribution due to the shadowing effect ($shad$) and the analysis method for extracting the tagging efficiency, to the systematic error is estimated to ± 0.5%.

$$\left(\frac{\Delta\epsilon_{tag}}{\epsilon}\right)_{shad} = \pm 0.5\% \tag{A.18}$$

All sources contributing to the systematic error of the tagging efficiency are not directed and are independent from each other. The total systematic error can be calculated via

$$\left(\frac{\Delta\epsilon_{tag}}{\epsilon}\right) = \sqrt{\left(\frac{\Delta\epsilon_{tag}}{\epsilon}\right)^2_{drift} + \left(\frac{\Delta\epsilon_{tag}}{\epsilon}\right)^2_{pr} + \left(\frac{\Delta\epsilon_{tag}}{\epsilon}\right)^2_{rd} + \left(\frac{\Delta\epsilon_{tag}}{\epsilon}\right)^2_{shad}} \tag{A.19}$$

The systematic error of the **attenuation of the photon flux** is dominated by the uncertainty in the effective density ρ_{eff}. This uncertainty is about 2% for the butanol target (see Section 2.3.3) and even smaller for the external carbon and beryllium targets. As the correction factor c_ϕ (see Table 3.4) is about 2%, a 2% uncertainty causes a systematic error for the cross section on the order 10^{-4} and can therefore be neglected.

The **photon polarization** is directly connected to the electron polarization P_e via equation 2.6. In [Spe02] the systematic error of the electron polarization ΔP_e is discussed. For the double polarized cross sections it follows

$$\left(\frac{\Delta(\sigma_{3/2}-\sigma_{1/2})}{\sigma_{3/2}-\sigma_{1/2}}\right)_{P_e} = \pm\frac{\Delta P_e}{P_e} \tag{A.20}$$

Total systematic error

The total systematic error of the **unpolarized** cross section contains some contributions which can only cause a decrease of the cross section. The sum of these parts $(\Delta\sigma_{C,Be}/\sigma_{C,Be})_{\Sigma+}$ can be obtained by quadratic summation as the different contributions are independent from each other.

$$\left(\frac{\Delta\sigma_{C,Be}}{\sigma_{C,Be}}\right)_{\Sigma+} = \sqrt{\left(\frac{\Delta\sigma_{C,Be}}{\sigma_{C,Be}}\right)^2_{QDC-cuts} + \left(\frac{\Delta\sigma_{C,Be}}{\sigma_{C,Be}}\right)^2_{F_t+} + \left(\frac{\Delta\sigma_{C,Be}}{\sigma_{C,Be}}\right)^2_{absorb}} \tag{A.21}$$

The other contributions $(\Delta\sigma_{C,Be}/\sigma_{C,Be})_{\Sigma\pm}$ which can cause an increase or a decrease of the cross section are given by

$$\left(\frac{\Delta\sigma_{C,Be}}{\sigma_{C,Be}}\right)_{\Sigma\pm} = \sqrt{\left(\frac{\Delta\sigma_{C,Be}}{\sigma_{C,Be}}\right)^2_{veto} + \left(\frac{\Delta\sigma_{C,Be}}{\sigma_{C,Be}}\right)^2_{pr} + \left(\frac{\Delta\sigma_{C,Be}}{\sigma_{C,Be}}\right)^2_{\epsilon_{tag}}} \tag{A.22}$$

The total systematic error which corresponds to an underestimation of the cross section $(\Delta\sigma_{C,Be}/\sigma_{C,Be})_+$ reads

$$\left(\frac{\Delta\sigma_{C,Be}}{\sigma_{C,Be}}\right)_{+} = +\sqrt{\left(\frac{\Delta\sigma_{C,Be}}{\sigma_{C,Be}}\right)^2_{\Sigma+} + \left(\frac{\Delta\sigma_{C,Be}}{\sigma_{C,Be}}\right)^2_{\Sigma\pm}} \tag{A.23}$$

correspondingly the part which causes an overestimation

$$\left(\frac{\Delta\sigma_{C,Be}}{\sigma_{C,Be}}\right)_{-} = -\sqrt{\left(\frac{\Delta\sigma_{C,Be}}{\sigma_{C,Be}}\right)^2_{\Sigma\pm} + \left(\frac{\Delta\sigma_{C,Be}}{\sigma_{C,Be}}\right)^2_{F_t-}} \tag{A.24}$$

In Table A.4 all contributions to the systematic error of the unpolarized photoabsorption cross section measurement with the beryllium and carbon targets are given.

The discussed sources for systematic errors of the **double polarized** cross sections are helicity independent, i.e. the influence to $\sigma_{3/2}$ and $\sigma_{1/2}$ is the same. In the systematic error of the cross section difference $(\Delta(\sigma_{3/2}-\sigma_{1/2})/\sigma_{3/2}-\sigma_{1/2})_\pm$ all parts have therefore just to be treated once, and as all contributions are independent from each each other they can be added

E_0 [GeV]	1.0	1.4	1.9	2.4	2.9	3.02
Carbon σ_C						
Hadronic rate						
$(\frac{\Delta\sigma_C}{\sigma_C})_{QDC-cuts}$	+ 0.5 %	+ 0.5 %	+ 0.5 %	+ 0.5 %	+ 0.5 %	+ 0.5 %
$(\frac{\Delta\sigma_C}{\sigma_C})_{pr}$	± 0.05 %	± 0.02 %	± 0.01 %	± 0.01 %	± 0.01 %	± 0.01 %
$(\frac{\Delta\sigma_C}{\sigma_C})_{veto}$	± 1.2 %	± 1.3 %	± 1.5 %	± 1.3 %	± 1.6 %	± 1.3 %
$(\frac{\Delta\sigma_C}{\sigma_C})_{absorb}$	± 1.0 %	± 0.5 %	0 %	0 %	0 %	0 %
Target						
$(\frac{\Delta\sigma_C}{\sigma_C})_{F_t+}$	+ 0.4 %	+ 0.4 %	+ 0.4 %	+ 0.4 %	+ 0.4 %	+ 0.4 %
$(\frac{\Delta\sigma_C}{\sigma_C})_{F_t-}$	- 0.5 %	- 0.5 %	- 0.5 %	- 0.5 %	- 0.5 %	- 0.5 %
Photon flux						
$(\frac{\Delta\sigma_C}{\sigma_C})_{\epsilon_{tag}}$	± 2.4 %	± 0.7 %	± 1.5 %	± 1.2 %	± 2.1 %	± 0.7 %
Sum						
$(\frac{\Delta\sigma_C}{\sigma_C})_+$	+ 2.9 %	+ 1.6 %	+ 2.2 %	+ 1.8 %	+ 2.7 %	+ 1.5 %
$(\frac{\Delta\sigma_C}{\sigma_C})_-$	- 3.0 %	- 1.7 %	- 2.2 %	- 1.9 %	- 2.7 %	- 1.6 %
Beryllium σ_{Be}						
Hadronic rate						
$(\frac{\Delta\sigma_{Be}}{\sigma_{Be}})_{QDC-cuts}$	+ 0.5 %	+ 0.5 %	+ 0.5 %	+ 0.5 %	+ 0.5 %	+ 0.5 %
$(\frac{\Delta\sigma_{Be}}{\sigma_{Be}})_{pr}$	± 0.05 %	± 0.02 %	± 0.01 %	± 0.01 %	± 0.01 %	± 0.01 %
$(\frac{\Delta\sigma_{Be}}{\sigma_{Be}})_{veto}$	± 1.1 %	± 0.8 %	± 1.3 %	± 1.2 %	± 1.3 %	± 1.5 %
$(\frac{\Delta\sigma_{Be}}{\sigma_{Be}})_{absorb}$	± 1.0 %	± 0.5 %	0 %	0 %	0 %	0 %
Target						
$(\frac{\Delta\sigma_{Be}}{\sigma_{Be}})_{F_t+}$	+0.5 %	+0.5 %	+0.5 %	+0.5 %	+0.5 %	+0.5 %
$(\frac{\Delta\sigma_{Be}}{\sigma_{Be}})_{F_t-}$	-0.6 %	-0.6 %	-0.6 %	-0.6 %	-0.6 %	-0.6 %
Photon flux						
$(\frac{\Delta\sigma_{Be}}{\sigma_{Be}})_{\epsilon_{tag}}$	± 2.4 %	± 0.7 %	± 1.5 %	± 1.2 %	± 2.1 %	± 0.7 %
Sum						
$(\frac{\Delta\sigma_{Be}}{\sigma_{Be}})_+$	+ 2.9 %	+ 1.3 %	+ 2.0 %	+ 1.8 %	+ 2.5 %	+ 1.7 %
$(\frac{\Delta\sigma_{Be}}{\sigma_{Be}})_-$	- 2.9 %	- 1.4 %	- 2.1 %	- 1.9 %	- 2.6 %	- 1.8 %

Table A.4: Contributions to the systematic error for the unpolarized cross sections.

E_0 [GeV]	1.0	1.4	1.9	2.4	2.9	3.02
Butanol $(\sigma_{3/2}-\sigma_{1/2})^p$						
Hadronic rate						
$(\frac{\Delta(\sigma_{3/2}-\sigma_{1/2})}{\sigma_{3/2}-\sigma_{1/2}})^p_{QDC-cuts}$	± 0.5 %	± 0.5 %	± 0.5 %	± 0.5 %	± 0.5 %	± 0.5 %
$(\frac{\Delta(\sigma_{3/2}-\sigma_{1/2})}{\sigma_{3/2}-\sigma_{1/2}})^p_{pr}$	± 0.05 %	± 0.02 %	± 0.01 %	± 0.01 %	± 0.01 %	± 0.01 %
$(\frac{\Delta(\sigma_{3/2}-\sigma_{1/2})}{\sigma_{3/2}-\sigma_{1/2}})^p_{veto}$	± 1.0 %	± 1.1 %	± 1.0 %	± 0.8 %	± 1.3 %	± 1.0 %
$(\frac{\Delta(\sigma_{3/2}-\sigma_{1/2})}{\sigma_{3/2}-\sigma_{1/2}})^p_{absorb}$	± 1.0 %	± 0.5 %	0 %	0 %	0 %	0 %
Target						
$(\frac{\Delta(\sigma_{3/2}-\sigma_{1/2})}{\sigma_{3/2}-\sigma_{1/2}})^p_{F_t\pm}$	± 2.3 %	± 2.3 %	± 2.3 %	± 2.3 %	± 2.3 %	± 2.3 %
$(\frac{\Delta(\sigma_{3/2}-\sigma_{1/2})}{\sigma_{3/2}-\sigma_{1/2}})^p_{P_t\pm}$	± 2.8 %	± 2.8 %	± 1.1 %	± 1.3 %	± 1.3 %	± 2.4 %
Photon flux						
$(\frac{\Delta(\sigma_{3/2}-\sigma_{1/2})}{\sigma_{3/2}-\sigma_{1/2}})^p_{\epsilon_{tag}}$	± 2.4 %	± 0.7 %	± 1.5 %	± 1.2 %	± 2.1 %	± 0.7 %
$(\frac{\Delta(\sigma_{3/2}-\sigma_{1/2})}{\sigma_{3/2}-\sigma_{1/2}})^p_{P_e}$	± 2.0%	± 2.0 %	± 2.1 %	± 2.3 %	± 3.6 %	± 4.4 %
Sum						
$(\frac{\Delta(\sigma_{3/2}-\sigma_{1/2})}{\sigma_{3/2}-\sigma_{1/2}})^p_{\pm}$	± 5.0 %	± 4.4 %	± 3.8 %	± 3.8 %	± 5.1 %	± 5.7 %

Table A.5: Contributions to the systematic error of the double polarized cross sections measured with the butanol target.

up quadratically. Numerical values for the double polarized cross section measurements on the proton which have been obtained with the butanol target are displayed in Table A.5.

The helicity dependent cross section difference on the neutron $(\sigma_{3/2}-\sigma_{1/2})^n$ has been defined in Section 3.7 Eq. 3.68, where the helicity dependent hadronic rates $Y_{3/2,(1/2)}$ are obtained experimentally from a polarized ^{6}LiD target. These hadronic rates contain proton and neutron contributions $Y_{3/2,(1/2)} = Y^p_{3/2,(1/2)} + Y^n_{3/2,(1/2)}$. Equation 3.68 can be written in a shorter form in terms of $(\sigma_{3/2}-\sigma_{1/2})^{LiD}$

$$\left(\sigma_{3/2}-\sigma_{1/2}\right)^n \;=\; \left(\sigma_{3/2}-\sigma_{1/2}\right)^{LiD} \;-\; \left(\sigma_{3/2}-\sigma_{1/2}\right)^p \cdot \frac{P^p_{eff}}{P^n_{eff}} \tag{A.25}$$

The contributions to the systematic error $(\Delta(\sigma_{3/2}-\sigma_{1/2})/\sigma_{3/2}-\sigma_{1/2})^{LiD}$ are given in Table A.6.

The systematic error for $(\sigma_{3/2}-\sigma_{1/2})^n$ has some contributions which occur independently for the LiD and for the proton part. These are:

- The target densities
- The target polarizations
- The tagging efficiencies
- The photon polarizations

E_0 [GeV]	1.2	1.2	1.9
radiator	Cu15	Cu50	Cu15
Lithium deuteride $(\sigma_{3/2}-\sigma_{1/2})^{LiD}$			
Hadronic rate			
$(\frac{\Delta(\sigma_{3/2}-\sigma_{1/2})}{\sigma_{3/2}-\sigma_{1/2}})^{LiD}_{QDC-cuts}$	± 0.5 %	± 0.5 %	± 0.5 %
$(\frac{\Delta(\sigma_{3/2}-\sigma_{1/2})}{\sigma_{3/2}-\sigma_{1/2}})^{LiD}_{pr}$	± 0.03 %	± 0.06 %	± 0.01 %
$(\frac{\Delta(\sigma_{3/2}-\sigma_{1/2})}{\sigma_{3/2}-\sigma_{1/2}})^{LiD}_{veto}$	± 0.7 %	± 0.7 %	± 0.9 %
$(\frac{\Delta(\sigma_{3/2}-\sigma_{1/2})}{\sigma_{3/2}-\sigma_{1/2}})^{LiD}_{absorb}$	± 0.7 %	± 0.7 %	0 %
Target			
$(\frac{\Delta(\sigma_{3/2}-\sigma_{1/2})}{\sigma_{3/2}-\sigma_{1/2}})^{LiD}_{F_t'\pm}$	± 3.4 %	± 3.4 %	± 3.4 %
$(\frac{\Delta(\sigma_{3/2}-\sigma_{1/2})}{\sigma_{3/2}-\sigma_{1/2}})^{LiD}_{P_t\pm}$	± 1.8 %	± 1.8 %	± 2.1 %
Photon flux			
$(\frac{\Delta(\sigma_{3/2}-\sigma_{1/2})}{\sigma_{3/2}-\sigma_{1/2}})^{LiD}_{\epsilon_{tag}}$	± 1.0 %	± 1.3 %	± 0.7 %
$(\frac{\Delta(\sigma_{3/2}-\sigma_{1/2})}{\sigma_{3/2}-\sigma_{1/2}})^{LiD}_{P_e}$	± 2.0 %	± 2.0 %	± 2.1 %
Sum			
$(\frac{\Delta(\sigma_{3/2}-\sigma_{1/2})}{\sigma_{3/2}-\sigma_{1/2}})^{LiD}_{\pm}$	± 4.6 %	± 4.7 %	± 4.7 %

Table A.6: Contributions to the systematic error of the double polarized cross sections obtained from the ^{6}LiD target.

- The pseudorandom corrections
- The veto deadtime corrections

The systematic errors of these parts are

$$\left(\frac{\Delta(\sigma_{3/2}-\sigma_{1/2})}{\sigma_{3/2}-\sigma_{1/2}}\right)^{p,LiD}_{indep} = \sqrt{\sum_i \left(\left(\frac{\Delta(\sigma_{3/2}-\sigma_{1/2})}{\sigma_{3/2}-\sigma_{1/2}}\right)^{p,LiD}_{i}\right)^2} \tag{A.26}$$

With $i = \{F_t, P_t, \epsilon_{tag}, P_e, pr, veto\}$. From Equation A.25 it follows for the independent part of the systematic error $\Delta(\sigma_{3/2}-\sigma_{1/2})^n_{indep}$:

$$\Delta(\sigma_{3/2}-\sigma_{1/2})^n_{indep} = \sqrt{\left(\Delta(\sigma_{3/2}-\sigma_{1/2})^{LiD}_{indep}\right)^2 + \left(\Delta(\sigma_{3/2}-\sigma_{1/2})^p_{indep}\cdot\frac{P^p_{eff}}{P^n_{eff}}\right)^2} \tag{A.27}$$

and the relative error reads

$$\left(\frac{\Delta(\sigma_{3/2}-\sigma_{1/2})}{\sigma_{3/2}-\sigma_{1/2}}\right)^{n}_{indep} = \sqrt{\left(\frac{\Delta(\sigma_{3/2}-\sigma_{1/2})^{LiD}_{indep}}{(\sigma_{3/2}-\sigma_{1/2})^n}\right)^2 + \left(\frac{\Delta(\sigma_{3/2}-\sigma_{1/2})^{p}_{indep}}{(\sigma_{3/2}-\sigma_{1/2})^n}\cdot\frac{P^p_{eff}}{P^n_{eff}}\right)^2} \tag{A.28}$$

With $P^p_{eff}/P^n_{eff} \approx 1$ it follows

$$\left(\frac{\Delta(\sigma_{3/2}-\sigma_{1/2})}{\sigma_{3/2}-\sigma_{1/2}}\right)^n_{indep} = \sqrt{2^2 \cdot \left(\frac{\Delta(\sigma_{3/2}-\sigma_{1/2})^{LiD}_{indep}}{2\cdot(\sigma_{3/2}-\sigma_{1/2})^n}\right)^2 + \left(\frac{\Delta(\sigma_{3/2}-\sigma_{1/2})^{p}_{indep}}{(\sigma_{3/2}-\sigma_{1/2})^n}\right)^2} \quad \text{(A.29)}$$

Using

$$(\sigma_{3/2}-\sigma_{1/2})^p \approx (\sigma_{3/2}-\sigma_{1/2})^n \approx \frac{1}{2}\cdot(\sigma_{3/2}-\sigma_{1/2})^{LiD} \quad \text{(A.30)}$$

One obtains

$$\left(\frac{\Delta(\sigma_{3/2}-\sigma_{1/2})}{\sigma_{3/2}-\sigma_{1/2}}\right)^n_{indep} = \sqrt{4\cdot\left(\left(\frac{\Delta(\sigma_{3/2}-\sigma_{1/2})}{\sigma_{3/2}-\sigma_{1/2}}\right)^{LiD}_{indep}\right)^2 + \left(\left(\frac{\Delta(\sigma_{3/2}-\sigma_{1/2})}{\sigma_{3/2}-\sigma_{1/2}}\right)^{p}_{indep}\right)^2} \quad \text{(A.31)}$$

The other contributions to the systematic error effect the LiD and the proton measurement in the same way and are therefore treated just once. These contributions are

- The QDC-cuts
- Absorption of reaction products in the target

The systematic error for this part is given by

$$\left(\frac{\Delta(\sigma_{3/2}-\sigma_{1/2})}{\sigma_{3/2}-\sigma_{1/2}}\right)^n_{dep} = \sqrt{\left(\left(\frac{\Delta(\sigma_{3/2}-\sigma_{1/2})}{\sigma_{3/2}-\sigma_{1/2}}\right)_{QDC-cuts}\right)^2 + \left(\left(\frac{\Delta(\sigma_{3/2}-\sigma_{1/2})}{\sigma_{3/2}-\sigma_{1/2}}\right)_{absorb}\right)^2} \quad \text{(A.32)}$$

The final systematic error for the helicity dependent cross section on the neutron denotes

$$\left(\frac{\Delta(\sigma_{3/2}-\sigma_{1/2})}{\sigma_{3/2}-\sigma_{1/2}}\right)^n = \sqrt{\left(\left(\frac{\Delta(\sigma_{3/2}-\sigma_{1/2})}{\sigma_{3/2}-\sigma_{1/2}}\right)^n_{indep}\right)^2 + \left(\left(\frac{\Delta(\sigma_{3/2}-\sigma_{1/2})}{\sigma_{3/2}-\sigma_{1/2}}\right)^n_{dep}\right)^2} \quad \text{(A.33)}$$

The different contributions and the sum which has been calculated according to Eqs. A.31 and A.33, are given in Table A.7.

A.2 Statistical error

The number of hadronic events N_{hadr} obeys a Poisson statistic. The statistical error ΔN_{hadr} is given as

$$\Delta N_{hadr} = \sqrt{N_{hadr}} \quad \text{(A.34)}$$

For the determination of a cross section the *true* number of hadronic events has to be separated from random background events. In the analysis this is done by applying cuts in the TDC spectra. This is illustrated in Figure A.2, where w_L and w_R denote the widths of

E_0 [GeV]	1.2	1.2	1.9
radiator	Cu15	CU50	CU15
$\left(\frac{\Delta(\sigma_{3/2}-\sigma_{1/2})}{\sigma_{3/2}-\sigma_{1/2}}\right)^{LiD}_{indep}$	± 4.5 %	± 4.6 %	± 4.7 %
$\left(\frac{\Delta(\sigma_{3/2}-\sigma_{1/2})}{\sigma_{3/2}-\sigma_{1/2}}\right)^{p}_{indep}$	± 4.5 %	± 4.5 %	± 3.8 %
$\left(\frac{\Delta(\sigma_{3/2}-\sigma_{1/2})}{\sigma_{3/2}-\sigma_{1/2}}\right)_{dep}$	± 0.9 %	± 0.9 %	± 0.5 %
$\left(\frac{\Delta(\sigma_{3/2}-\sigma_{1/2})}{\sigma_{3/2}-\sigma_{1/2}}\right)^{n}$	± 10.1 %	± 10.3 %	± 10.2 %

Table A.7: Systematic error of the double polarized cross section measurement on the neutron

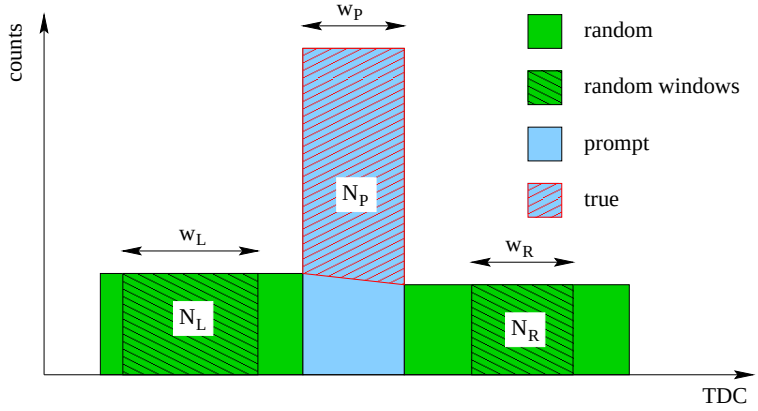

Figure A.2: Illustration of the TDC cuts to obtain the true number of hadronic events.

the left and right random regions and w_P the width of the prompt region. $N_x(x = L, R, P)$ is the number of events in these regions. The true number of events N_{true} is then given by

$$N_{true} = N_P - \frac{1}{2} \cdot \left(\frac{N_L}{w_L} + \frac{N_R}{w_R} \right) \cdot w_P \tag{A.35}$$

Slightly different background left and right to the prompt peak owing to shadowing is taken into account by this formula. The numbers $N_x(x = L, R, P)$ include the corrections due to the veto deadtime and the pseudorandom effect.
For the statistical error ΔN_{true} it follows

$$\Delta N_{true} = \sqrt{N_P + 0.25 \cdot w_P^2 \cdot \left(\frac{N_L}{w_L^2} + \frac{N_R}{w_R^2} \right)} \tag{A.36}$$

By taking into account the statistical error of the tagging efficiency measurement $\Delta\epsilon_{tag}$ the total statistical error of an unpolarized cross section $\Delta\sigma$ now reads

$$\Delta\sigma = \sqrt{\left(\frac{d\sigma}{dN_{true}} \Delta N_{true} \right)^2 + \left(\frac{d\sigma}{d\epsilon_{tag}} \Delta\epsilon_{tag} \right)^2} \tag{A.37}$$

With the definition of the cross section in Section 3.7 it follows

$$\Delta\sigma = \frac{1}{\phi_{el} \cdot \epsilon_{tag} \cdot c_\phi \cdot F_t} \sqrt{(\Delta N_{true})^2 + \left(\frac{1}{\epsilon_{tag}} \Delta\epsilon_{tag} \right)^2} \tag{A.38}$$

In complete analogy, the statistical error of the helicity dependent cross sections $\Delta\sigma_{3/2,(1/2)}$ reads

$$\Delta\sigma_{3/2,(1/2)} = \frac{1}{\phi_{el}\cdot\epsilon_{tag}\cdot c_\phi\cdot F_t\cdot P_t\cdot P_{circ}}\sqrt{\left(\Delta N_{3/2,(1/2)}\right)^2+\left(\frac{1}{\epsilon_{tag}}\Delta\epsilon_{tag}\right)^2+\left(\frac{1}{P_{circ}}\Delta P_{circ}\right)^2} \tag{A.39}$$

With ΔP_{circ} the statistical error of the photon polarization which is directly connected to the statistical error of the electron polarization via Equation 2.6. The statistical error of the NMR-measurement of the target polarization is treated as a systematic error and has been considered there (see Table A.1).

Appendix B

Tabulated results

On the following pages the tabulated results for the doubly polarized photoabsorption cross sections on the proton and on the neutron will be given. Each table represents one primary electron energy. The photon energy ν is given together with the width of the corresponding bin in MeV. The cross section differences $\sigma_{3/2} - \sigma_{1/2}$ and the statistical errors $\Delta\left(\sigma_{3/2} - \sigma_{1/2}\right)$ are denoted in μb. The relative systematic errors can be found in Tables A.5 and A.7 for the proton and the neutron, respectively.
Rebinned data of the proton and the neutron (as shown in Fig. 5.20), including all primary electron energies, will be given in Tables B.9 and B.10.

ν [MeV]	width [MeV]	$\sigma_{3/2} - \sigma_{1/2}$ [μb]	$\Delta(\sigma_{3/2} - \sigma_{1/2})$ [μb]	ν [MeV]	width [MeV]	$\sigma_{3/2} - \sigma_{1/2}$ [μb]	$\Delta(\sigma_{3/2} - \sigma_{1/2})$ [μb]
689.7	23.2	145.5	23.4	870.0	4.1	28.3	50.9
711.5	20.2	123.7	23.9	874.0	3.9	-12.9	50.9
724.1	4.9	109.1	45.1	878.1	4.2	-20.3	50.6
728.7	4.4	186.3	51.1	881.9	3.6	99.7	53.9
733.5	5.3	159.2	48.3	885.8	4.2	77.2	50.8
738.4	4.4	121.2	51.5	889.6	3.4	-5.7	55.2
743.5	5.8	87.4	45.2	893.2	3.8	19.9	53.0
748.6	4.5	117.3	50.9	896.9	3.5	-46.7	54.6
753.8	5.8	175.2	45.8	900.4	3.5	66.6	55.2
758.9	4.5	130.2	50.6	903.8	3.2	31.4	55.5
764.1	5.9	11.0	44.8	907.2	3.5	24.6	55.8
769.3	4.5	132.5	49.7	910.4	3.1	103.7	60.8
774.5	5.9	149.9	44.1	913.6	3.3	-24.8	58.1
779.6	4.2	-8.8	52.5	916.8	2.9	-44.3	59.0
784.8	6.2	69.2	43.9	919.8	3.2	23.0	59.2
790.0	4.1	66.9	53.0	922.7	2.6	94.6	64.7
794.9	5.8	52.2	42.8	925.6	3.2	162.5	59.8
800.1	4.6	22.7	45.0	928.4	2.5	112.3	66.7
805.0	5.3	97.7	44.9	931.2	3.0	34.5	63.8
810.2	5.0	113.1	47.1	933.9	2.4	40.3	67.9
815.1	4.9	82.1	47.0	936.4	2.7	84.3	65.7
820.1	5.0	32.2	45.6	938.9	2.3	183.2	69.9
825.0	4.9	28.2	47.7	941.3	2.5	4.2	69.0
829.6	4.3	77.8	49.9	943.7	2.3	-21.7	70.5
834.4	5.4	49.1	44.7	946.0	2.3	72.7	73.6
839.1	4.1	33.0	51.1	948.2	2.2	154.2	73.2
843.7	4.9	-47.4	47.1	950.5	2.2	190.8	73.6
848.3	4.4	47.9	48.7	952.7	2.1	108.1	78.1
852.9	4.7	82.6	48.4	954.8	2.1	-12.4	78.1
857.3	4.2	139.1	50.3	956.7	1.8	16.8	84.0
861.6	4.4	25.9	48.4	958.7	2.1	-38.4	81.4
865.9	4.1	75.7	49.6	960.8	1.9	139.7	90.1

Table B.1: Helicity dependent cross sections on the proton, primary energy 1.0 GeV.

ν [MeV]	width [MeV]	$\sigma_{3/2} - \sigma_{1/2}$ [μb]	$\Delta(\sigma_{3/2} - \sigma_{1/2})$ [μb]	ν [MeV]	width [MeV]	$\sigma_{3/2} - \sigma_{1/2}$ [μb]	$\Delta(\sigma_{3/2} - \sigma_{1/2})$ [μb]
965.6	32.5	69.2	13.7	1218.0	5.8	35.5	27.7
996.1	28.3	103.8	13.9	1223.6	5.5	74.3	27.7
1013.7	6.8	101.2	26.1	1229.3	5.8	16.6	27.6
1020.2	6.2	74.7	29.2	1234.7	5.0	2.9	29.2
1027.0	7.4	84.6	27.5	1240.2	5.8	23.3	27.5
1033.8	6.2	104.2	29.3	1245.5	4.8	-15.9	29.9
1040.9	8.1	67.2	25.7	1250.5	5.3	-2.5	28.8
1048.1	6.3	46.0	28.9	1255.7	4.9	37.7	29.7
1055.3	8.1	72.9	25.9	1260.6	4.9	-37.2	30.0
1062.5	6.3	58.5	28.6	1265.3	4.6	-31.5	30.0
1069.8	8.3	31.0	25.1	1270.0	4.9	52.5	30.2
1077.1	6.3	90.1	28.1	1274.6	4.3	26.1	32.8
1084.4	8.3	56.1	24.8	1279.1	4.6	-1.5	31.2
1091.5	5.9	55.7	29.4	1283.5	4.1	-11.6	31.9
1098.8	8.7	56.3	24.6	1287.8	4.4	32.9	32.0
1106.0	5.7	45.0	29.6	1291.8	3.7	142.4	35.0
1112.9	8.0	32.9	23.8	1295.9	4.4	63.8	32.3
1120.1	6.5	64.8	25.7	1299.8	3.5	-33.4	36.1
1127.1	7.4	3.8	25.4	1303.6	4.1	53.9	34.5
1134.2	7.0	8.0	26.3	1307.4	3.4	66.8	36.8
1141.2	6.9	28.3	26.0	1311.0	3.8	26.5	35.5
1148.1	7.0	-6.6	25.2	1314.5	3.3	83.2	37.8
1155.0	6.8	53.4	26.3	1317.9	3.4	37.2	37.4
1161.4	6.0	27.3	27.5	1321.2	3.2	74.8	38.3
1168.2	7.5	15.8	24.5	1324.4	3.2	47.9	40.1
1174.8	5.8	-27.1	28.0	1327.6	3.1	36.9	40.4
1181.1	6.9	-44.4	25.7	1330.7	3.2	86.3	40.4
1187.6	6.1	25.9	26.6	1333.7	2.9	40.4	42.6
1194.0	6.6	-7.1	26.4	1336.7	3.0	-39.8	42.7
1200.3	5.9	16.5	27.5	1339.4	2.6	41.2	46.1
1206.3	6.2	19.1	26.4	1342.2	3.0	48.5	44.5
1212.3	5.7	40.5	27.1	1345.1	2.7	-8.0	49.8

Table B.2: Helicity dependent cross sections on the proton, primary energy 1.4 GeV.

ν [MeV]	width [MeV]	$\sigma_{3/2} - \sigma_{1/2}$ [μb]	$\Delta(\sigma_{3/2} - \sigma_{1/2})$ [μb]	ν [MeV]	width [MeV]	$\sigma_{3/2} - \sigma_{1/2}$ [μb]	$\Delta(\sigma_{3/2} - \sigma_{1/2})$ [μb]
1307.8	44.0	17.5	8.4	1649.7	7.8	23.3	17.2
1349.1	38.3	11.9	8.5	1657.3	7.5	8.0	17.4
1373.0	9.2	33.4	15.9	1665.0	7.9	5.0	17.1
1381.8	8.3	15.5	17.8	1672.3	6.8	-20.3	18.3
1390.9	10.0	19.6	16.9	1679.7	7.9	2.6	17.1
1400.1	8.3	6.6	17.8	1686.9	6.5	-11.5	18.8
1409.8	11.0	44.0	15.7	1693.7	7.2	0.3	17.9
1419.6	8.6	38.0	17.7	1700.7	6.6	-3.1	18.6
1429.3	10.9	32.1	15.9	1707.3	6.7	19.6	18.7
1439.0	8.6	10.8	17.5	1713.8	6.2	-2.8	18.6
1449.0	11.2	35.2	15.5	1720.1	6.6	2.5	18.8
1458.8	8.5	-9.9	17.2	1726.4	5.9	47.2	20.5
1468.7	11.3	2.4	15.3	1732.4	6.3	55.9	19.4
1478.3	8.0	-12.4	18.2	1738.3	5.6	3.4	19.9
1488.2	11.7	39.4	15.2	1744.2	6.0	5.0	19.9
1497.9	7.8	43.0	18.4	1749.7	5.0	-3.6	21.7
1507.3	10.9	21.1	14.7	1755.2	6.0	5.1	20.0
1517.1	8.8	24.2	15.9	1760.5	4.7	-3.7	22.6
1526.5	10.0	19.3	15.8	1765.7	5.6	1.3	21.4
1536.2	9.5	-7.7	16.3	1770.8	4.6	-20.1	22.9
1545.6	9.3	15.6	16.1	1775.7	5.1	-11.6	21.9
1555.0	9.4	11.4	15.6	1780.4	4.4	-9.7	23.6
1564.4	9.2	7.7	16.4	1784.9	4.7	21.1	23.1
1573.1	8.1	7.8	17.1	1789.5	4.4	-5.9	23.8
1582.2	10.2	9.0	15.2	1793.8	4.3	-16.6	24.6
1591.2	7.8	54.9	17.5	1798.1	4.2	-61.2	25.0
1599.7	9.3	39.9	16.0	1802.3	4.3	-8.4	25.1
1608.6	8.3	11.8	16.6	1806.4	3.9	11.7	26.4
1617.2	9.0	-16.3	16.4	1810.4	4.1	41.0	25.9
1625.7	8.0	38.4	17.1	1814.2	3.5	41.1	28.4
1633.8	8.4	21.8	16.5	1817.9	4.0	41.0	27.4
1641.9	7.8	10.7	16.9	1821.8	3.7	45.4	30.7

Table B.3: Helicity dependent cross sections on the proton, primary energy 1.9 GeV.

ν [MeV]	width [MeV]	$\sigma_{3/2} - \sigma_{1/2}$ [μb]	$\Delta(\sigma_{3/2} - \sigma_{1/2})$ [μb]	ν [MeV]	width [MeV]	$\sigma_{3/2} - \sigma_{1/2}$ [μb]	$\Delta(\sigma_{3/2} - \sigma_{1/2})$ [μb]
1650.8	55.5	14.0	6.5	2082.2	9.9	-1.6	13.3
1702.8	48.4	5.6	6.5	2091.9	9.4	-20.1	13.4
1733.0	11.6	16.0	12.3	2101.6	9.9	5.6	13.2
1744.1	10.5	1.6	13.7	2110.8	8.6	-17.9	14.1
1755.7	12.6	-8.8	13.0	2120.1	9.9	2.1	13.2
1767.2	10.5	-7.4	13.8	2129.2	8.2	-0.9	14.4
1779.4	13.9	14.6	11.9	2137.8	9.1	0.1	13.8
1791.8	10.8	20.6	13.7	2146.6	8.3	23.1	14.3
1804.1	13.8	-5.1	12.3	2155.0	8.5	10.1	14.3
1816.4	10.9	-1.0	13.6	2163.1	7.8	-21.0	14.4
1828.9	14.1	0.2	11.9	2171.2	8.3	1.7	14.4
1841.3	10.7	16.1	13.3	2179.0	7.4	5.3	15.7
1853.8	14.2	2.0	11.8	2186.7	7.9	-8.6	14.9
1866.0	10.1	-1.5	14.1	2194.1	7.0	-0.6	15.3
1878.4	14.8	2.0	11.7	2201.5	7.6	-2.2	15.4
1890.7	9.8	6.7	14.2	2208.4	6.3	-15.2	16.7
1902.5	13.8	-8.7	11.4	2215.4	7.6	-21.3	15.3
1914.9	11.1	7.9	12.3	2222.1	6.0	-7.7	17.3
1926.8	12.6	16.9	12.2	2228.6	7.1	-6.3	16.4
1939.0	12.0	31.4	12.6	2235.1	5.8	-8.0	17.6
1950.9	11.8	4.4	12.5	2241.2	6.4	-32.3	16.8
1962.8	11.9	5.7	12.1	2247.2	5.6	-8.5	18.1
1974.5	11.7	-12.2	12.6	2253.0	5.9	17.3	17.7
1985.5	10.2	-7.1	13.2	2258.7	5.6	9.6	18.2
1997.0	12.9	-14.8	11.7	2264.2	5.5	-17.3	18.8
2008.4	9.9	3.1	13.5	2269.5	5.3	-6.7	19.3
2019.2	11.8	-0.6	12.4	2274.9	5.4	-17.5	19.2
2030.3	10.5	11.1	12.8	2280.1	4.9	6.9	20.2
2041.2	11.3	-0.4	12.7	2285.1	5.1	-23.4	20.2
2051.9	10.1	-1.3	13.3	2289.8	4.4	13.3	21.7
2062.2	10.6	1.7	12.7	2294.6	5.1	-20.6	20.9
2072.4	9.8	12.8	13.0	2299.5	4.7	-12.5	23.6

Table B.4: Helicity dependent cross sections on the proton, primary energy 2.4 GeV.

ν [MeV]	width [MeV]	$\sigma_{3/2} - \sigma_{1/2}$ [μb]	$\Delta(\sigma_{3/2} - \sigma_{1/2})$ [μb]	ν [MeV]	width [MeV]	$\sigma_{3/2} - \sigma_{1/2}$ [μb]	$\Delta(\sigma_{3/2} - \sigma_{1/2})$ [μb]
2007.1	67.6	-24.8	14.6	2531.7	12.0	-14.0	30.0
2070.4	58.8	-13.4	14.7	2543.4	11.4	-52.4	30.3
2107.1	14.2	-0.6	27.7	2555.2	12.1	-19.5	29.7
2120.6	12.8	-50.3	31.0	2566.5	10.4	-56.8	31.9
2134.6	15.4	26.8	29.3	2577.8	12.1	-14.3	29.7
2148.7	12.8	-20.8	30.9	2588.8	10.0	-13.6	32.6
2163.6	16.8	6.1	27.3	2599.3	11.1	3.6	31.0
2178.5	13.2	35.7	30.7	2610.0	10.1	-46.9	32.3
2193.5	16.7	-13.0	27.6	2620.2	10.3	-37.1	32.2
2208.5	13.2	12.5	30.5	2630.1	9.5	2.7	32.4
2223.7	17.2	-34.3	26.9	2639.9	10.1	-24.0	32.5
2238.8	13.1	-12.0	29.9	2649.4	9.0	6.2	35.6
2254.0	17.3	-25.8	26.7	2658.7	9.6	-16.7	33.5
2268.8	12.3	-17.2	31.7	2667.8	8.5	-25.9	34.5
2283.9	18.0	25.4	26.4	2676.7	9.2	23.0	34.5
2298.9	11.9	37.0	32.0	2685.1	7.7	21.7	37.9
2313.2	16.7	34.7	25.6	2693.6	9.2	7.2	34.5
2328.3	13.5	18.4	27.8	2701.8	7.3	-30.0	39.0
2342.7	15.3	9.4	27.5	2709.7	8.6	-37.4	37.0
2357.6	14.5	41.6	28.4	2717.6	7.1	-22.1	39.7
2372.1	14.3	18.6	28.1	2725.1	7.8	-58.3	38.1
2386.5	14.5	-41.5	27.2	2732.4	6.8	-70.1	40.8
2400.8	14.2	19.1	28.4	2739.3	7.1	-33.1	39.9
2414.1	12.4	-18.5	29.9	2746.2	6.8	-30.4	41.1
2428.1	15.6	-2.8	26.4	2752.9	6.6	-14.6	42.5
2441.9	12.0	-12.3	30.5	2759.5	6.4	17.2	43.7
2455.1	14.3	40.9	27.8	2766.0	6.6	-15.3	43.4
2468.6	12.8	-8.5	29.0	2772.3	6.0	-2.7	45.6
2481.9	13.8	16.9	28.5	2778.4	6.2	64.9	45.5
2494.9	12.2	-0.4	29.9	2784.1	5.3	50.6	49.0
2507.4	12.8	-14.6	28.6	2789.9	6.2	14.6	47.1
2519.8	11.9	-13.6	29.5	2795.9	5.7	-52.0	53.3

Table B.5: Helicity dependent cross sections on the proton, primary energy 2.9 GeV.

ν [MeV]	width [MeV]	$\sigma_{3/2} - \sigma_{1/2}$ [μb]	$\Delta(\sigma_{3/2} - \sigma_{1/2})$ [μb]	ν [MeV]	width [MeV]	$\sigma_{3/2} - \sigma_{1/2}$ [μb]	$\Delta(\sigma_{3/2} - \sigma_{1/2})$ [μb]
2078.2	69.9	-0.2	6.4	2621.4	12.4	-20.7	12.9
2143.8	60.9	-5.4	6.4	2633.5	11.9	22.4	13.0
2181.8	14.7	-9.9	12.1	2645.7	12.5	6.9	12.8
2195.7	13.2	0.4	13.5	2657.4	10.8	5.6	13.7
2210.3	15.9	-31.1	12.8	2669.1	12.5	-17.8	12.8
2224.9	13.2	0.5	13.5	2680.5	10.3	-2.6	14.0
2240.2	17.4	0.9	12.0	2691.4	11.5	8.2	13.3
2255.7	13.6	3.4	13.5	2702.4	10.5	8.9	13.8
2271.2	17.3	-4.1	12.1	2713.0	10.6	-2.5	13.9
2286.7	13.7	2.7	13.4	2723.2	9.8	-7.4	13.9
2302.4	17.8	-1.7	11.7	2733.4	10.5	-46.8	13.9
2318.1	13.5	-6.9	13.1	2743.3	9.3	-6.4	15.2
2333.8	17.9	-6.1	11.6	2752.9	10.0	-16.2	14.4
2349.2	12.7	4.3	13.8	2762.3	8.8	-1.3	14.7
2364.8	18.6	-3.6	11.5	2771.5	9.5	-25.3	14.7
2380.3	12.3	-7.8	13.9	2780.3	7.9	-33.7	16.1
2395.1	17.3	10.9	11.2	2789.0	9.5	-13.9	14.8
2410.8	14.0	-18.7	12.0	2797.5	7.5	-17.8	16.7
2425.7	15.9	-6.0	11.9	2805.7	8.9	-16.9	15.8
2441.1	15.1	-1.6	12.3	2813.9	7.4	10.1	16.9
2456.1	14.8	-15.2	12.2	2821.6	8.1	20.1	16.2
2471.0	15.0	-15.1	11.8	2829.2	7.0	6.2	17.4
2485.8	14.7	-13.5	12.4	2836.4	7.4	14.6	17.0
2499.6	12.9	-6.4	12.9	2843.5	7.0	-20.9	17.5
2514.1	16.2	-6.3	11.5	2850.5	6.9	-12.5	18.1
2528.4	12.4	11.6	13.2	2857.2	6.6	5.0	18.6
2542.1	14.8	9.0	12.1	2863.9	6.8	-19.4	18.6
2556.1	13.2	16.4	12.5	2870.5	6.2	3.7	19.5
2569.8	14.3	22.3	12.4	2876.8	6.4	2.4	19.4
2583.3	12.7	-1.8	12.9	2882.8	5.5	-6.9	20.8
2596.3	13.3	6.8	12.4	2888.8	6.4	-22.3	20.1
2609.1	12.3	2.2	12.7	2894.9	5.8	-19.4	22.2

Table B.6: Helicity dependent cross sections on the proton, primary energy 3.02 GeV.

ν [MeV]	width [MeV]	$\sigma_{3/2} - \sigma_{1/2}$ [μb]	$\Delta(\sigma_{3/2} - \sigma_{1/2})$ [μb]	ν [MeV]	width [MeV]	$\sigma_{3/2} - \sigma_{1/2}$ [μb]	$\Delta(\sigma_{3/2} - \sigma_{1/2})$ [μb]
827.7	27.9	38.9	58.7	1027.0	7.4	140.9	101.2
853.8	24.3	37.0	59.6	1033.8	6.2	122.1	107.4
868.9	5.8	23.8	114.0	1040.9	8.1	160.5	92.6
874.5	5.3	172.3	124.5	1048.1	6.3	-112.7	99.6
880.2	6.3	244.6	119.0	1055.3	8.1	-15.3	93.6
886.1	5.3	-44.4	126.3	1062.5	6.3	-102.8	108.3
892.2	6.9	145.3	112.3	1069.8	8.3	261.5	93.4
898.3	5.4	119.6	124.3	1077.1	6.3	-8.6	100.2
904.5	6.9	153.4	113.1	1084.4	8.3	26.6	92.3
910.7	5.4	74.5	123.7	1091.5	5.9	13.0	110.7
917.0	7.1	110.9	110.5	1098.8	8.7	65.2	88.7
923.2	5.4	42.5	123.3	1106.0	5.7	49.1	119.0
929.5	7.1	157.2	108.2	1112.9	8.0	-50.8	94.9
935.6	5.1	37.0	128.1	1120.1	6.5	-44.3	103.2
941.8	7.4	165.6	108.3	1127.1	7.4	-13.1	102.4
965.6	32.5	54.4	47.2	1134.2	7.0	251.4	104.1
996.1	28.3	-5.9	49.8	1141.2	6.9	91.1	106.0
1013.7	6.8	124.2	100.6	1148.1	7.0	35.3	108.4
1020.2	6.2	144.3	108.8	1152.9	2.5	298.1	177.9

Table B.7: Helicity dependent cross sections on the neutron, primary energy 1.2 GeV.

ν [MeV]	width [MeV]	$\sigma_{3/2} - \sigma_{1/2}$ [μb]	$\Delta(\sigma_{3/2} - \sigma_{1/2})$ [μb]	ν [MeV]	width [MeV]	$\sigma_{3/2} - \sigma_{1/2}$ [μb]	$\Delta(\sigma_{3/2} - \sigma_{1/2})$ [μb]
1307.8	44.0	23.7	19.2	1545.6	9.3	9.6	37.2
1349.1	38.3	30.5	19.4	1555.0	9.4	15.5	35.9
1373.0	9.2	63.5	36.7	1564.4	9.2	31.4	37.8
1381.8	8.3	-13.1	40.9	1573.1	8.1	41.6	39.6
1390.9	10.0	36.5	38.8	1582.2	10.2	28.2	35.2
1400.1	8.3	72.2	40.8	1591.2	7.8	28.0	40.3
1409.8	11.0	35.6	36.8	1599.7	9.3	18.4	37.0
1419.6	8.6	18.1	40.6	1608.6	8.3	33.3	38.3
1429.3	10.9	0.3	36.7	1617.2	9.0	68.3	37.8
1439.0	8.6	103.7	40.6	1650.8	55.5	16.0	14.0
1449.0	11.2	-1.4	35.9	1702.8	48.4	42.2	15.0
1458.8	8.5	92.8	39.6	1733.0	11.6	17.3	30.6
1468.7	11.3	63.3	35.3	1744.1	10.5	56.4	32.2
1478.3	8.0	55.6	41.6	1755.7	12.6	34.6	29.7
1488.2	11.7	-13.4	35.0	1767.2	10.5	48.0	33.3
1497.9	7.8	-35.2	42.2	1779.4	13.9	26.4	28.6
1507.3	10.9	27.7	34.0	1791.8	10.8	-19.5	32.8
1517.1	8.8	-17.6	36.6	1804.1	13.8	95.3	29.9
1526.5	10.0	-8.5	36.3	1816.4	10.9	68.2	34.8
1536.2	9.5	92.5	37.5	1822.7	1.8	91.2	88.0

Table B.8: Helicity dependent cross sections on the neutron, primary energy 1.9 GeV.

ν [MeV]	$\sigma_{3/2} - \sigma_{1/2}$ [μb]	$\Delta(\sigma_{3/2} - \sigma_{1/2})$ [μb]	ν [MeV]	$\sigma_{3/2} - \sigma_{1/2}$ [μb]	$\Delta(\sigma_{3/2} - \sigma_{1/2})$ [μb]
689.7	145.5	23.4	1388.8	23.0	7.6
714.3	122.5	20.8	1434.3	28.2	7.6
740.8	136.1	21.0	1491.8	17.5	6.0
768.3	91.5	20.4	1561.8	14.5	5.8
796.8	67.6	19.3	1633.8	12.3	4.4
826.3	52.5	18.9	1707.8	9.0	3.8
856.8	48.5	18.5	1783.8	1.7	3.8
888.3	23.0	18.1	1861.8	3.5	5.0
920.8	51.4	18.4	1941.8	8.4	4.8
954.3	70.8	13.8	2023.8	-4.2	4.1
988.8	93.0	12.4	2107.8	-1.8	3.4
1024.3	89.2	12.1	2193.8	-6.4	3.3
1060.8	58.7	11.9	2281.8	-2.6	3.6
1098.3	50.0	11.5	2371.8	-1.4	4.6
1136.8	22.9	10.9	2463.8	-7.4	4.4
1176.3	1.4	10.6	2557.8	3.2	4.3
1216.8	28.7	10.3	2653.8	-1.0	4.2
1258.3	5.9	10.2	2751.8	-15.8	4.2
1300.8	29.0	6.9	2851.8	-3.0	4.9
1344.3	18.0	7.1			

Table B.9: Rebinned helicity dependent cross sections on the proton.

ν [MeV]	$\sigma_{3/2} - \sigma_{1/2}$ [μb]	$\Delta(\sigma_{3/2} - \sigma_{1/2})$ [μb]	ν [MeV]	$\sigma_{3/2} - \sigma_{1/2}$ [μb]	$\Delta(\sigma_{3/2} - \sigma_{1/2})$ [μb]
856.7	68.2	32.0	1474.8	28.7	16.1
942.7	81.1	31.0	1528.8	19.8	15.3
1028.7	53.8	28.7	1582.8	28.6	15.3
1114.7	49.5	29.8	1636.8	24.7	14.6
1312.8	25.1	17.1	1690.8	35.0	14.2
1366.8	30.9	16.1	1744.8	38.8	14.4
1420.8	39.6	16.3	1798.8	44.8	15.3

Table B.10: Rebinned helicity dependent cross sections on the neutron.

Bibliography

[Aba68] H.D.I. Abarbanel and M.L. Goldberger, Phys. Rev. **165** (1968) 1594

[Ade98] E143 Collaboration; B. Adeva *et al.* Phys. Rev. **D 58** (1998) 112003

[Ahr85] J. Ahrens, Nucl. Phys. **A 446** (1985) 229c

[Ahr00] GDH-Collaboration; J. Ahrens *et al.*, Phys. Rev. Lett. **84** (2000) 5950

[Ahr01] GDH-Collaboration; J. Ahrens *et al.*, Phys. Rev. Lett. **87** (2001) 022003

[Ahr02] GDH and A2 Collaboration; J. Ahrens *et al.*, Phys. Rev. Lett. **88** (2002) 232002

[Ahr03] GDH-Collaboration; J. Ahrens *et al.*, Phys. Lett. **B 551** (2003) 49

[Ahr03b] GDH-Collaboration; J. Ahrens *et al.*, Eur. Phys. J. **A 17** (2003) 241

[Aid95] H1-Collaboration; S. Aid *et al.*, Z. Phys. **C 69** (1995) 27

[Air03] HERMES Collaboration; A. Airapetian *et al.*, Eur. Phys. J. **C 26** (2003) 527

[Ama02] E94010 Collaboration; M. Amarian *et al.* Phys. Rev. Lett. **89** (2002) 242301

[Ama04] E94010 Collaboration; M. Amarian *et al.* Phys. Rev. Lett. **92** (2004) 022301

[Ann96] J.R.M. Annand, I. Anthony, B. Oussena, Nucl. Instr. Meth. **A 368** (1996) 385

[Ans89] M. Anselmino, B.L. Ioffe and E. Leader, Yad. Fiz. **49** (1989) 214

[Ant95] G. Anton, Prog. Part. Nucl. Phys. **34** (1995) 173

[Ant03] E155 Collaboration; P.L. Anthony *et al.* Phys. Lett. **B 553** (2003) 18

[Ara90] Y. Arankov *et al.*, Sov. J. Nucl. Phys. **52** (1990) 878

[Ara83] Arakelyan *et al.*, Sov. J. Nucl. Phys. **38** (1983) 589

[Are91] J. Arends *et al.*, Nucl. Instr. Meth. **A 306** (1991) 89

[Are97] H. Ahrenövel *eta al.*, Phys. Lett. **B 407** (1997) 1

[Are98] H. Arenhövel *et al.*, Nucl. Phys. **A 631** (1998) 612

[Are00] H. Arenhövel in D. Drechsel and L. Tiator (Eds.) *Proceedings of the Symposium on the Gerasimov-Drell-Hearn Sum Rule and the Nucleon Spin Structure in the Resonance Region* (GDH 2000), Mainz, World Scientific (2000) 67

[Ash89] European Muon Collaboration; J. Ashman *et al.*, Nucl. Phys. **B 328** (1989) 1

[Arm72] T.A. Armstrong *et al.*, Phys. Rev. **D 5** (1972) 1640

[Arn90] R.A. Arndt *et al.*, Phys. Rev. **C 42** (1990) 1864

[Arn96] R.A. Arndt *et al.*. Phys. Rev. **C 53** (1996) 430

[Arn02] R.A. Arndt *et al.*, Phys. Rev. **C 66** (2002) 055213

[Aud91] G. Audit *et al.*, Nucl. Instr. Meth. **A 301** (1991) 473

[Bab91] D. Babusci *et al.*, Nucl. Instr. Meth. **A 305** (1991) 19

[Bab98] D. Babusci, G. Giordano and G. Matoni, Phys. Rev. **C 57** (1998) 291

[Bab98b] D. Babusci *et al.*, Phys. Rev. **C 58** (1998) 1013

[Bal60] A.M. Baldin, Nucl. Phys. **18** (1960) 310

[Bal03] J. Ball *et al.*, Nucl. Instr. Meth. **A 498** (2003) 101

[Bau83] E130 Collaboration, G. Baum *et al.*, Phys. Rev. Lett. **51** (1983) 1135

[Bec04] R. Beck and A. Starosin, Eur. Phys. J. **A 19** (2004) 279

[Ber93] V. Bernard, N. Kaiser and U.G. Meissner, Phys. Rev. **D 48** (1993) 3062

[Ber03] V. Bernard, T.R. Hemmert and U.G. Meißner, Phys. Rev. **D 67** (2003) 076008

[Bia96] N. Bianchi *et al.*, Phys. Rev. **C 54** (1996) 1688

[Bia99] N. Bianchi, E. Thomas, Phys. Lett. **B 450** (1999) 439

[Bjo66] J.D. Bjorken, Phys. Rev. **148** (1966) 1467

[Blo69] E.D. Bloom *et al.*, *Determination of the total photon-proton cross section from high energy inelastic electron scattering*, SLAC-PUB-0653 (1969)

[Bos03] P.E. Bosted in M. Anghinolfi, M. Battaglieri, R. De Vita (Eds.) *Proceedings of the Second International Symposium on the Gerasimov-Drell-Hearn Sum Rule and the Spin Structure of the Nucleon*, GDH 2002, World Scientific (2003) 157

[Bur70] H. Burkhardt and W.N. Cottingham, Ann. Phys. (N.Y.) **56** (1970) 453

[Bur93] V. Burkert and Z. Li, Phys. Rev. **D 47** (1993) 46

[Bue99] S. Bueltmann *et al.*, Nucl. Instr. Meth. **A 425** (1999) 23

[Bra99] Ch. Bradtke *et al.*, Nucl. Instr. Meth. **A 436** (1999) 430

[Bro69] S.J. Brodsky and J. Pumplin, Phys. Rev. **D 47** (1969) 1794

[Bro73] G.R. Brookes *et al.*, Phys. Rev. **D 8** (1973) 2826

[Car92] R.C. Carrasco, E. Oset, Nucl. Phys. **A 536** (1992) 445

[Cha94] L.N. Chang, Y. Liang, R. Workman, Phys. Lett. **B 329** (1994) 514

[Che97] Jefferson Laboratory Proposal E97-110, J.P. Chen, A. Deur, and F. Garibaldi spokesperson

[Chi02] W.-T. Chiang, S.-N. Yang, L. Tiator, D. Drechsel, Nucl. Phys. **A 700** (2002) 429

[Dar03] E.M. Darwish, H. Arenhövel and M. Schwamb, Eur. J. Phys. **A 17** (2003) 513

[Der92] ZEUS-Collaboration; M. Derek *et al.*, Phys. Lett. **B 293** (1992) 465

[Der94] ZEUS-Collaboration; M. Derek *et al.*, Z. Phys. **C 63** (1994) 391

[Dic72] Duane A. Dicus and David R. Palmer, Phys. Rev. **D 6** (1972) 720

[Don92] A. Donnachie and P. Landshoff, Phys. Lett. **B 296** (1992) 227

[Don98] Y.-B. Dong, Eur. Phys. J. **A 1** (1998) 347

[Dre66] S.D.Drell und A.C.Hearn, Phys. Rev. Lett. **16** (1966)908

[Dre94] D. Drechsel, Prog. Part. Nucl. Phys. **34** (1994) 181

[Dre98] D. Drechsel and K. Krein, Phys. Rev. **D 58** (1998) 116009

[Dre99] D. Drechsel, O. Hanstein, S.S. Kamalov and L. Tiator, Nucl. Phys. **A 645** (1999) 145

[Dre99b] D. Drechsel, S.S. Kamalov, G. Krein and L. Tiator, Phys. Rev. **D 59** (1999) 094021

[Dre00] D. Drechsel, M. Gorchtein, B. Pasquini and M. Vanderhaeghen, Phys. Rev. **C 61** (2000) 015204

[Dre01] D. Drechsel, S.S. Kamalov and L. Tiator, Phys. Rev. **D 63** (2001) 114010

[Dre03] D. Drechsel, B. Pasquini, M. Vanderhaeghen, Phys. Rept. **378** (2003) 99

[Dut95] H. Dutz *et al.*, Nucl. Instr. Meth. **A 356** (1999) 111

[Dut03] GDH-Collaboration; H. Dutz *et al.*, Phys. Rev. Lett. **91** (2003) 192001

[Dut04] GDH-Collaboration; H. Dutz *et al.* in preparation

[Drv96] Linux driver for the MV-1000 ftp://sunsite.unc.edu/pub/Linux/apps/video/mv1000drv-0.33.tgz

[Eff97] M. Effenberger *et al.*, Nucl. Phys. **A 613** (1997) 353; **A 614** (1997) 353

[Ell74] J. Ellis and R.L. Jaffe, Phys. Rev. **D 9** (1974) 1444; **D 10** (1974) 1669

[EPD97] D.E. Cullen, J.H. Hubbel, L. Kissel *EPDL97: the Evaluated Photon Data Library*, UCRL-50400, Vol. 6, Rev. 5, Lawrence Livermore National Laboratory 1997

[Fal00] T. Falter, S. Leupold and U. Mosel, Phys. Rev. **C 62** (2000) 031602

[Fat03] CLAS Collaboration; R. Fatemi *et al.*, Phys. Rev. Lett. **91** (2003) 222002

[Fil01] B.W. Fillipone and X. Ji, Adv. Nucl. Phys. **26** (2001) 1

[Fix04] A. Fix, *private communication*, (2004); A. Fix *et al.* in preparation

[Fri33] R. Frisch and O. Stern, Z. Phys. **85** (1933) 4, I. Estermann and O. Stern, *ibid.* p. 17

[Fri77] J.L. Friar, Phys. Rev. **C 16** (1977) 1504

[Fro02] F. Frommberger, *private communication*, (2002)

[Fro94] Th. Frommhold *et al*, Z. Phys. **A 350** (1994) 249

[Fuc94] A. Fuchs, *Entwicklung des STAR Detektors für die exoerimentelle Überprüfung der Gerasimov-Drell-Hearn-Summenregel*, diploma thesis, Tübingen 1994

[Fuj77] T. Fuji *et al.*, Nucl. Phys. **B 120** (1977) 395

[Gel00] G.C. Gellas *et al.*, Phys. Rev. Lett. **85** (2000) 14

[Gel54] M. Gell-Mann and M.L. Goldberger, Phys. Rev. **96** (1954) 1433

[Ger65] S.B. Gerasimov, Yad. Fiz. **2** (1965) 598

[Ger66] S.B. Gerasimov, Sov. J. Nucl. Phys. **2** (1966) 430

[Gia94] M.M. Giannini and E. Santopinto, Phys. Rev. **C 49** (1994) 1258

[God02] M. Godo, *Messung der Polarisationsasymmetrie der Eta-Photoproduktion am Proton am GDH-Experiment an ELSA*, diploma thesis, Erlangen 2002

[Goe95] St. Goertz *et al*, Nucl. Instr. Meth. **A 356** (1995) 20

[Goe02] St. Goertz, W. Meyer and G. Reichertz, Prog. Part. Nucl. Phys. 49 (2002) 403

[Got69] K. Gottfried *et al.* , Phys. Rev. **182** (1969) 1595

[Gow01] M. Gowin, *Optimierung der laserinduzierten Photoemission zur Erzeugung polarisierter Elektronenstrahlen an der 50 keV-Quelle der Bonner Beschleunigeranlage ELSA*, Ph.D. thesis IR-2001-11, Bonn 2001

[Gra03] P. Grabmayr, in M. Anghinolfi, M. Battaglieri, R. De Vita (Eds.) *Proceedings of the Second International Symposium on the Gerasimov-Drell-Hearn Sum Rule and the Spin Structure of the Nucleon*, GDH 2002, World Scientific (2003) 85

[Hei54] W. Heitler, *The Quantum Theory of Radiation*, Clarendon Press, Oxford 1954

[Hel93] K. Helbing, *Konzeption eines Detektors zur Überprüfung der Drell-Hearn-Gerasimov Summenregel*, diploma thesis IR-93-27 , Bonn 1993

[Hel97] K. Helbing, *Messung von totalen Photoabsorptionsquerschnitten mit dem GDH-Detektor*, Ph.D. thesis IR-97-14, Bonn 1997

[Hel02] K. Helbing *et al.*, Nucl. Instr. Meth. **A 484** (2002) 129

[Hel02b] K. Helbing, AIP American Institute of Physics Conference Proceedings no.675 (2003) 33

[Hel03] K. Helbing, Prog. Part. Nucl. Phys. **50** (2003) 451

[Hem98] T.R. Hemmert, B.R. Holstein, J. Kambor, G. Knöchlein, Phys. Rev. **D 57** (1998) 5746

[Hey71] V. Heynen *et al.*, Phys. Lett. **B 34** (1971) 651

[Hil00] W. Hillert *et al.* in D. Drechsel and L. Tiator (Eds.) *Proceedings of the Symposium on the Gerasimov-Drell-Hearn Sum Rule and the Nucleon Spin Structure in the Resonance Region* (GDH 2000), Mainz, World Scientific (2000) 283

[Hir03] M. Hirata, N. Katagiri and T. Takaki, Phys. Rev. **C 67** (2003) 034601

[Hof01] M. Hoffmann, *Beschleunigung polarisierter Elektronen in der Bonner Elektron-Beschleunigeranalage ELSA*, Ph.D. thesis IR-2001-17, Bonn 2001

[Hof01b] M. Hoffmann *et al.*, SPIN 2000, Osaka, AIP Conf. Proc. 570 (2001) 756

[Hol01] H. Holvoet, *Study of the helicity dependence of double pion photoproduction on the proton*, Ph.D. thesis, Gent 2001

[Hol04] H. Holvoet and M. Vanderhaeghen in preparation

[Hos66] M. Hosoda and K. Yamamoto, Prog. Theor. Phys. **35** (1966) 425

[Hug99] E.W. Hughes and R. Voss, Annu. Rev. Nucl. Part. Sci. **49** (1999) 303

[Ji00] X. Ji, C.-W. Kao, J. Osborne, Phys. Rev. **D 61** (2000) 074003

[Ji01] X. Ji and J. Osborne, J. Phys. **G 27** (2001) 127

[Kar73] I. Karliner, Phys. Rev. **D 7** (1973) 2717

[Kar96] J. Karrer, diploma thesis, Würzburg, 1996

[Kie96] B. Kiel, *Untersuchungen zur Strahlführung des Gerasimov-Drell-Hearn-Experimentes*, diploma thesis, Bonn, 1996

[Kie99] B. Kiel, *Ein Møllerpolarimeter für das Experiment zur Verifizierung der Gerasimov-Drell-Hearn Summenregel an ELSA*, Ph.D. thesis, Erlangen 1999

[Koc84] J.H. Koch, E.J. Moniz and N. Ohtsuka, Ann. Phys. **154** (1984) 99

[Kon01] S. Kondratyuk and O. Scholten, Phys. Rev. **C 64** (2001) 024005

[Kon02] S. Kondratyuk and O. Scholten, Phys. Rev. **C 65** (2002) 038201

[Kos03] K. Kosstert *et al*, Eur. Phys. J. **A 16** (2003) 259

[Kri98] J. Krimmer, *Aufbau eines Überwachungssystems für den Photonenstrahl für das GDH-Experiment an ELSA Bonn*, diploma thesis, Tübingen, 1998

[Kri02] J. Krimmer, P. Grabmayr and M. Sauer, Nucl. Instr. Meth. **A 481** (2002) 57

[Kri03] J. Krimmer *Experimental verification of the GDH sum rule up to 3 GeV*, PaNIC 2002, Osaka, Nucl. Phys. **A 721** (2003) 384c

[Kum00] K.B.V. Kumar, J.A. McGovern and M.C. Birse, Phys. Lett. **B 479** (2000) 167

[Lam00] B. Lampe and E. Reya, Phys. Rep. **332** (2000) 1

[Lan86] Landau-Lifschitz, Lehrbuch der Theoretischen Physik, Band 4, Quantenelektrodynamik, Akademie Verlag, Berlin 1986

[Lan03] M. Lang in M. Anghinolfi, M. Battaglieri, R. De Vita (Eds.) *Proceedings of the Second International Symposium on the Gerasimov-Drell-Hearn Sum Rule and the Spin Structure of the Nucleon*, GDH 2002, World Scientific (2003) 309

[Lan00] B. Lannoy, *Experimental verifaction of the Gerasimov-Drell-Hearn sum rule*, Ph.D. thesis, Gent 2000

[Lap61] L.I. Lapidus and Chou Kuang-Khao, Zh. Eksp. Teor. Fiz. **39** (1960) 1286 (Sov. JETP **12** (1961) 898)

[Lap63] L.I. Lapidus, Sov. Phys. JETP **16** (1963) 964

[Low54] F.E. Low, Phys. Rev. **96** (1954) 1428

[Lun03] M. Lundin *et al.*, Phys. Rev. Lett. **90** (2003) 192501

[Mac96] M. MacCormic *et al*, Phys. Rev. **C 53** (1996) 41

[MAID03] http://www.kph.uni-mainz.de/MAID/

[McG97] C. McGeorge, *private communication*, (1997)

[Mic96] T. Michel, *Konzeption eines Møllerpolarimeters für das GDH-Experiment zur Überprüfung der Gerasimov-Drell-Hearn Summenregel*, diploma thesis IB-96-09, Bonn 1996

[Mic01] T. Michel, *Messung von totalen Photoabsorptionsquerschnitten als Vorbereitung des GDH-Experiments an ELSA*, Ph.D. thesis, Erlangen 2001

[Muc99] V. Muccifora, *et al.*, Phys. Rev. **C 60** (1999) 064616

[Nac01] J.C. Nacher, *et al.*, Nucl. Phys. **A 695** (2001) 295

[Nac02] J.C. Nacher and E. Oset, Nucl. Phys. **A 697** (2002) 372

[Nag95] A. Nagel, *Aufbau und Test eines Detektors für die experimentelle Überprüfung der Gerasimov-Drell-Hearn Summenregel*, diploma thesis IB-95-44, Bonn 1995

[Nak98] S. Nakamura *et al.*, Nucl. Instr. Meth. **A 411** (1998) 93

[Nat00] F.A. Natter Prog. Part. Nucl. Physics 44 (2000) 461

[Nat03] F.A. Natter *et al.*, Nucl. Instr. Meth. **B 211** (2003) 465

[Nau01] J. Naumann, *Tagging-System, Datennahme und Strahlüberwachung des GDH-Experiments an ELSA*, Ph.D. thesis, Erlangen 2001

[Nau02] J. Naumann, *First measurement of the GDH integral for protons from 200 to 1800 MeV at MAMI and ELSA*, INPC 2001, San Francisco, AIP Conf. Proc. 610 (2002) 371

[Nau03] J. Naumann, *et al.*, Nucl. Instr. Meth. **A 498** (2003) 211

[Ols59] H. Olsen and L.C. Maximon, Phys. Rev. **114** (1959) 887

[Olm01] V. Olmos de León, F. Wissmann *et al.*, Eur. Phys. J. **A 10** (2001) 207

[Ous94] J.K. Ousterhout, *Tcl and the Tk Toolkit*, Addison- Wesleym Reading, MA, 1994

[Owe90] R.O. Owens, Nucl. Instr. Meth. **A 288** (1990) 574

[Pan98] R. Pantförder, *Investigations on the Foundation and Possible Modifications of the Gerasimov-Drell-Hearn Sum Rule*, Ph.D. thesis IR-98-6, Bonn 1998; hep-ph/9805434

[PDG00] Particle Data Group; D.E. Groom *et al.*, Eur. Phys. J. **C 15** (2000) 1

[Pov94] Povh, Rith, Scholz, Zetsche, *Teilchen und Kerne*, Springer Berlin, 1994

[Pud97] B.S. Pudliner *et al.*, Phys. Rev. **C 56**, 1720 (1997)

[Rag93] S. Ragusa, Phys. Rev. **D 47** (1993) 3757

[Rag94] S. Ragusa, Phys. Rev. **D 49** (1994) 3157

[Rei95] G. Reichertz *et al.* Nucl. Instr. Meth. **A 356** (1995) 74

[Rob90] S. Robinson *et al.* Proceedings of High Energy Spin Physics, 385 (1990)

[Roh02] Ch, Rohlof, *private communication*, (2002)

[Roh03] Ch. Rohlof, *Entwicklung polarisierter Targets zur Messung der Gerasimov-Drell-Hearn-Summenregel an ELSA*, Ph.D. thesis, Bonn 2003

[Ron99] O.A. Rondon, Phys. Rev. **C 60** (1999) 035201

[Ros04] T. Rostomyan, Ph.D. thesis in preparation, Gent 2004

[Roy68] S.M. Roy and V. Singh, Phys. Rev. Lett. **21** (1968) 861

[Sai69] S. Saito, Phys. Rev. **184** (1969) 1894

[San94] A.M. Sandorfi, C.S. Whisnant, M. Khandaker, Phys. Rev. **D 50** (1994) 6681

[Sau96] M. Sauer *et al.*, Nucl. Instr. Meth. **A 378** (1996) 143

[Sau98] M.Sauer, *Inklusive Messung von Wirkungsquerschnitten der totalen Photoabsorption am Proton und Neutron als Vorbereitung für das GDH-Experiment*, Ph.D. thesis, Tübingen, 1998

[Sch93] N.W. Schellingerhout *et al.* Phys. Rev. **C 48** (1993) 2741, Phys. Rev. **C 52** (1995) 439

[Sim02] S. Simula, *et al.*, Phys. Rev. **D 65** (2002) 034017

[Sob03] CLAS Collaboration; D.I. Sober, L. Todor, P.E. Bosted, S.E. Kuhn in M. Anghinolfi, M. Battaglieri, R. De Vita (Eds.) *Proceedings of the Second International Symposium on the Gerasimov-Drell-Hearn Sum Rule and the Spin Structure of the Nucleon*, GDH 2002, World Scientific (2003) 253

[Spe98] T. Speckner, *Simulation eines Compton-Polarimeters sowie Konzeption, Bau und Test von Detektoren für das GDH-Experiment an ELSA* , diploma thesis, Erlangen 1998

[Spe01] T. Speckner, *The GDH experiment at ELSA*, Meson 2001, Prag, AIP Conf. Proc. 603 (2001) 385

[Spe02] T. Speckner, *Møllerpolarimetrie am GDH-Experiment sowie Bestimmung helizitätsabhängiger Photoabsorptionswirkungsquerschnitte an ELSA*, Ph.D. thesis, Erlangen 2002

[Spe04] T. Speckner *et al.*, Nucl. Instr. Meth. **A 519** (2004) 518

[Sum99] S. Sumowidago and T. Mart, Phys. Rev. **C 60** (1999) 028201

[Tho01] A.W. Thomas and W. Weise, *The structure of the nucleon*, Wiley-VCH, Berlin 2001

[Tia03] L. Tiator in M. Anghinolfi, M. Battaglieri, R. De Vita (Eds.) *Proceedings of the Second International Symposium on the Gerasimov-Drell-Hearn Sum Rule and the Spin Structure of the Nucleon*, GDH 2002, World Scientific (2003) 27

[Tia04] L. Tiator, *private communication*, 2004

[Tsa74] Y.S. Tsai, Rev. Mod. Phys. **46**, 815 (1974)

[TUNL03] W. Tornow, M. Ahmed and H.R. Weller, Triangle Universities Nuclear Laboratory Progress Report - XLII (2003) 126

[Wal69] R.L. Walker, Phys. Rev. **182** (1969) 1729

[Wal85] H. Walliser and T. Fliessbach, Phys. Rev. **C 31**, 2242 (1985)

[Wei96] L. Weitemeyer, *Untersuchung von 9 HE VME-Bus QDC und TDC Modules für die Messung der GDH Summenregel*, diploma thesis, Tübingen 1996

[Wei97] W. Weihofen, *Konfiguration und Erprobung eines neuen Datennahmesystems auf VME-Basis zur Erfassung kernphysikalischer Experimentdaten*, diploma thesis, Göttingen, 1997

[Wei02] W. Weihofen, *Apparative Entwicklungen zur experimentellen Überprüfung der Gerasimov-Drell-Hearn-Summenregel am Elektronenbeschleuniger ELSA in Bonn*, Ph.D. thesis, Göttingen 2002

[Wel03] H.R. Weller in M. Anghinolfi, M. Battaglieri, R. De Vita (Eds.) *Proceedings of the Second International Symposium on the Gerasimov-Drell-Hearn Sum Rule and the Spin Structure of the Nucleon*, GDH 2002, World Scientific (2003) 173

[Wis04] F. Wissmann, *Compton Scattering. Investigating the Structure of the Nucleon with Real Photons*, Springer Heidelberg Berlin, 2004

[Wol01] S. Wolf *et al.*, Eur. Phys. J. **A 12** (2001) 231

[Wor92] R. Workman and R. Arndt, Phys. Rev. **D 45** (1992) 1789

[Zei98] G. Zeitler, *Simulation, Konzeption, Bau und Test eines aktiven Kollimatorsystems sowie von Detektoren für das GDH-Experiment an ELSA*, diploma thesis, Erlangen 1998

[Zei01] G. Zeitler *et al.*, Nucl. Instr. Meth. **A 459** (2001) 6

[Zei02] G. Zeitler, *Messung helizitätsabhängiger Photoabsorptionswirkungsquerschnitte zur experimentellen Überprüfung der GDH-Summenregel an ELSA*, Ph.D. thesis, Erlangen 2002

[Zei03] G. Zeitler, *private communication*, (2003)

[Zha02] Q. Zhao, J.S. Al-Khalili and C. Bennhold, Phys. Rev. **C 65** (2002) 032201

Danksagung

Hiermit möchte ich mich bei allen bedanken, die zum Gelingen dieser Arbeit beigetragen haben:

- An erster Stelle sei Prof. Dr. Peter Grabmayr genannt, für das Vertrauen und die Freiheiten bei der Bearbeitung des Themas, wobei er immer ein offenes Ohr für Fragen und Probleme hatte.
- Prof. Dr. Heinz Clement für die Begutachtung der Arbeit und für die anregenden Diskussionen im *Kaffeeseminar*.
- Dr. Markus Sauer, der mir den Einstieg in das *GDH-Buisiness* erleichtert hat und der mir auch den Mountainbike-Sport näher gebracht hat.
- Den Mitgliedern der Arbeitsgruppe aus Erlangen, die maßgeblich an der Durchführung des GDH-Experiments an ELSA beteiligt waren und die mit mir die Feinheiten der Analyse diskutiert haben, Prof. Dr. Gisela Anton, Dr. Klaus Helbing, Dr. Jakob Naumann, Dr. Thorsten Speckner und Dr. Günter Zeitler.
- Den Mitgliedern der GDH-Kollaboration aus Bochum, Gent, Göttingen, Lund, Mainz, Pavia und Saclay, die durch ihren Einsatz den Erfolg des Experiments ermöglicht haben.
- Den Mitarbeitern des Physikalischen Instituts in Bonn und dem damaligen Direktor Prof. Dr. Berthold Schoch, insbesondere der ELSA-Beschleunigermannschaft, für die polarisierten Elektronen zu jeder Tages- und Nachtzeit. Stellvertretend seien Dr. Frank Frommberger und Dr. Wolther von Drachenfels genannt.
- Dr. Hartmut Dutz und Dr. Christian Rohlof für ihren harten aber letztendlich doch erfolgreichen Kampf mit dem polarisierten Target.
- Den Kolleginnen und Kollegen der Tübinger Arbeitsgruppe für die angenehme Arbeitsatmosphäre und die gemeinsamen Aktivitäten ausserhalb der Physik.
- Der DFG und dem Europäischen Graduiertenkolleg 'Hadronen im Vakuum, in Kernen und Sternen' für die finanzielle Unterstützung.
- Meinen Eltern, die mir das Studium ermöglicht haben.
- Allen Freunden und Bekannten und Sonstigen, die ich noch vergessen habe.